Development of Novel Energy-Transferring Nanomaterials which Enhance the Photophysical Properties of Light-Harvesting Proteins

Ashley Mark Hancock

Submitted in accordance with the requirements for the degree of Doctor of Philosophy

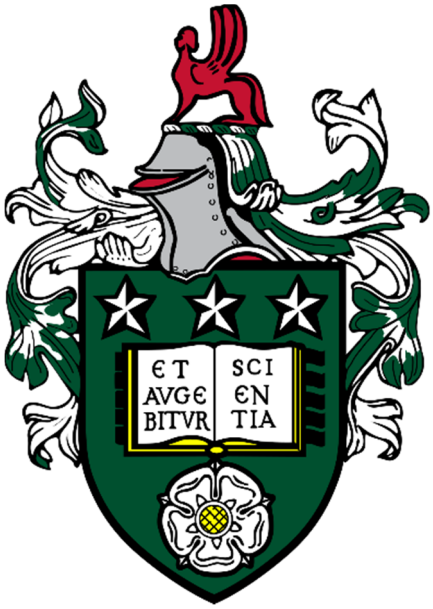

University of Leeds

School of Physics and Astronomy

September 2020

Declaration

The candidate confirms that the work submitted is his own, except where work has formed part of jointly authored publications and has been included. The contribution of the candidate and the other authors of this work have been explicitly indicated below. The candidate confirms that appropriate credit has been given within the thesis where reference has been made to the work of others.

The work discussed in chapters 3 & 4 of these thesis has appeared in publication as follows:
HANCOCK, A. M., MEREDITH, S. A., CONNELL, S. D., JEUKEN, L. J. C. & ADAMS, P. G. 2019. Proteoliposomes as energy transferring nanomaterials: enhancing the spectral range of light-harvesting proteins using lipid-linked chromophores. *Nanoscale*, 11, 16284-16292.

AMH was responsible for sample preparation, protein purification, UV-vis spectroscopy, fluorescence spectroscopy, TCSPC measurements, DLS, epifluorescence microscopy, data analysis and writing the manuscript. The contribution of the other authors involved FLIM measurements, FLIM data analysis, discussions and assisting with writing the manuscript.

Acknowledgements

Firstly, I would like to thank my supervisor, Peter Adams, for his unwavering support, guidance, and literally hundreds of hours of time spent helping me at every stage of my PhD. This research is as much yours as it is mine. I am sure that if I inherit only half of your passion and commitment to research, I will be in excellent stead for the rest of my career. I would also like to thank my other supervisors, Lars Jeuken and Simon Connell, for their encouragement and expertise. You kept me on the straight and narrow with both excellent technical knowledge and an invaluable 'big picture' view of the project which guided me throughout. A special thanks is also due to Sophie Meredith. Aside from my supervisors, you have had a larger impact on this project than anyone else and I thank you for it.

Thank you to Hope, Anna, and Declan from the Jeuken group who happily persisted in the noble goal of trying to teach biology to a physicist. Much of this research would not have been possible without your help and patience while showing me the ropes.

I have been lucky enough to work with and visit several fantastic collaborators during my PhD. I would especially like to thank Minjung and Muath from the Schlau-Cohen group at MIT, and Takuro from the Morigaki group at the University of Kobe. These visits were both high points for me, and I cannot thank you enough for your warm hospitality and allowing me to share in some truly awesome research.

I owe enormous thanks to every single member of the MNP research group who have graced the department with their presence while I have been here. You are all truly wonderful people and I know that I would not have completed this PhD without your help. The support provided both in the Fenton and the lab has been invaluable. I cannot possibly list every one of you but between gliding lessons with Twig, a stag do for Harry, Matt's wedding, a week in Hirschegg, and literally countless other occasions that I have been lucky enough to share with you, I have made memories that I will never forget.

I want to thank everyone from outside of work who has made the last eight years in Leeds an absolute blast. Jack, Olivia, Abi, Foz, Clare, and Fiona, you have been such an enormous part of what has made Leeds my home. Sam and Miley, we have been on this journey together from the first year of undergrad to finally becoming doctors, I could not imagine a funnier, kinder, or more talented pair of people to have spent it with. My biggest thanks are to Meghan. You have supported me through thick and thin - including being stuck in our flat during a pandemic, as I endeavoured to write a thesis - there are not sufficient words to thank you enough for all you have done for me over the last few years.

My final thanks are for my family. I could not be luckier to have a set of people so supportive and encouraging in all aspects of my life.

Abstract

Bio-hybrid nanomaterials have great potential for combining the most desirable aspects of biomolecules with the conceptual aspects of nanotechnology, both to potentially develop new technology for applications such as light harvesting, but also to understand fundamental properties of natural systems. The photosynthetic plant antenna protein light-harvesting complex II (LHCII) is extremely efficient at solar energy absorption and subsequent energy transfer in nature and has been demonstrated to perform effectively when incorporated into artificial nanoscale assemblies for light absorption. Here, we show that the effective absorption range of LHCII can be enhanced by interfacing the complementary lipid tagged chromophore, Texas Red DHPE, alongside LHCII in a model lipid membrane system which is self-assembled, modular, and readily adsorbed onto surfaces.

Chapter 1 contains an overview of: photosynthesis in plants, the photo-physics of energy capture and transfer in antenna proteins, background on model lipid bilayers, and the development of bio-hybrid light harvesting materials. Chapter 2 summaries the methodology used in my PhD studies. Chapter 3 details the formation and spectroscopic characterisation of a new type of proteoliposome which were developed to interface the synthetic chromophore Texas Red to LHCII within a model lipid membrane. This successfully enhanced the overall absorption cross-section of the system. The proteoliposomes' modularity was shown as the ability to incorporate a range of chosen concentrations of both Texas Red and LHCII and the energy transfer efficiency and enhancement of LHCII's spectral range was quantified. In Chapter 4, proteoliposomes were deposited onto solid surfaces to allow the properties of individual membrane vesicles to be assessed and the population distribution to be quantified. This included measuring individual particle size, the co-localisation of LHCII and Texas Red, and energy transfer efficiency. Furthermore, membranes deposited on solid surfaces retained their energy transfer properties, demonstrating the potential for device-based applications for this concept. Finally, Chapter 5 details the adaptation of the LHCII and Texas Red system into lipid nanodiscs, which allowed the interactions between diffusing Texas Red molecules and single LHCII proteins to be investigated with ultrafast spectroscopy. This led to the quantification of the timescale of Texas Red to LHCII energy transfer and identification of sub-populations of energy donor molecules.

Contents

List of Figures

List of Abbreviations and Acronyms

α -DDM - Detergent n-dodecyl α-D-maltoside

Abs – Absorption

ADP/ATP – Adenosine diphosphate/ Adenosine triphosphate

AFM – Atomic force microscopy

Car – Carotenoid

CCD – Charge coupled device

Chl – Chlorophyll

Conc – Concentration

Cyt – Cytochrome

DAS – Decay associated spectra

DGDG – Digalactosyldiacylglycerol

DLS – Dynamic light scattering

DOPC – 1,2-dioleoyl-sn-glycero-3-phosphocholine

EDTA – Ethylenediaminitetraacetic acid

ETE – Energy transfer efficiency

Fd – Ferredoxin

FLIM – Fluorescence lifetime imaging microscopy

FNR – Ferredoxin NADP+ reductase

FPLC – Fast protein liquid chromatography

FRET – Förster Resonance Energy Transfer

HEPES – 4-(2-hydroxyethyl)-1-piperazineethanesulfonic acid

His – Histidine

HOMO – Highest occupied molecular orbital

IPTG – Isopropyl β-d-1-thiogalactopyranoside

IRF – Instrument response function

LB – Lysogeny broth

LHC – Light-harvesting complex

LUMO – Lowest unoccupied molecular orbital

MES – 2-(N-morpholino)ethanesulfonic acid

MGDG – Monogalactosyldiacylglycerol

MWCO – Molecular weight cut off

NA – Numerical aperture

NADH/NADPH – Nicotinamide adenine dinucleotide/ Nicotinamide adenine dinucleotide phosphate

ND – Neutral density

Ni-NTA – Nickle-Nitrilotracetic acid

NPQ – Non-photochemical quenching

PAGE – Polyacrylamide gel electrophoresis

PC – Plastocyanin

PG – Phosphatidylglycerol

PMT – Photomultiplier tube

PQH – Plastoquinol

PS – Photosystem

RC – Reaction centre

SDS – Sodium dodecyl sulphate

SEC – Size exclusion chromatography

SPAD – Single photon avalanche diode

SQPG – Sulfoquinovosyldiacylglycerol

T – Temperature

t – Time

TA – Transient absorption

TB – Terrific broth

TCSPC – Time correlated single photon counting

TEM – Transmission electron microscopy

TR DHPE – Texas Red 1,2-dihexadecanoyl-sn-glycero-3-phosphoethanolamine

TRFS – Time resolved fluorescence spectra

TRIS – Tris(hydroxymethyl)aminomethane

UV-Vis-NIR – Ultraviolet-visible-near infrared

1 Introduction

This chapter will introduce the concepts of photosynthesis, photon absorption, photosynthetic pigments, Förster resonance energy transfer, and the function of antenna proteins in higher order plants. The use of photosynthetic proteins in bio-hybrid light-harvesting systems will also be reviewed. Finally, the previous works in the field on the use of complementary non-native chromophores to effectively enhance the natural light-harvesting ability of photosynthetic proteins will be summarised. This will put into context the motivation and scope of the work described in this thesis.

1.1 Photosynthesis and the role of Light-Harvesting Proteins

1.1.1 Photosynthesis overview in higher order plants

Photosynthesis is the primary or secondary source of energy for almost every living organism on the planet. It is defined as the biological process in which energy provided by light from the sun is converted into chemical energy which can be stored and used (Blankenship, 2014). The majority of the solar light which illuminates the earth's surface is in the visible and infrared regions of the electromagnetic spectrum (350 - 2000 nm). However, 47 % of the irradiance energy which penetrates the atmosphere is in the wavelength range of 380 - 700 nm (Thekaekara, 1973).Solar irradiance in this wavelength range is the primary energy source for plants. Plants utilise photosynthesis to convert this absorbed energy to biomass, which accounts for ~80 % of the total biomass on the planet (Bar-On et al., 2018). The initial photosynthetic processes of energy capture, transfer, and stabilisation are far more efficient than any equivalent renewable human-fabricated process. For this reason, understanding the nature of photosynthesis on both molecular and macro levels is hugely important for the development of renewable energy systems which are necessary to alleviate the worldwide demand for non-renewable fossil fuels (Hoffert et al., 2002).

All photosynthetic plants and algae utilise organelles called chloroplasts to perform the primary functions of photosynthesis, a schematic of a chloroplast is shown in Figure 1 (A). These organelles share many features with, and are thought to have evolved from, prokaryotic cyanobacteria which perform photosynthesis with a similar mechanism to plants (Cavalier-Smith, 2000). The chloroplast envelope contains a fluid called the stroma. This contains many soluble proteins crucial for the latter stages of photosynthesis and so-called 'dark-reactions 'in which energy is converted to sugars for long-term storage (i.e., carbon fixation, etc.). Also contained within the chloroplast is a complex system of bio-membranes called the thylakoid, which is the location of solar energy capture, transfer and initial chemical stabilisation, the so-called 'light-reactions' of photosynthesis (Daum and Kühlbrandt, 2011). Thylakoids are made up of an interconnected membrane (transmembrane proteins within lipid bilayers) which surround an inner space, or lumen, which is separated from the Stromal liquid by the thylakoid bilayer membrane. The thylakoid is organised into densely packed stacks of discs called Grana which are connected to one another by single layer thylakoids called stromal lamellae (Figure 1 (A)). The granal and lamellar parts of the thylakoid membrane contain different photosynthetic membrane proteins allowing many processes to take place in various regions of the membrane simultaneously (Dekker and Boekema, 2005).

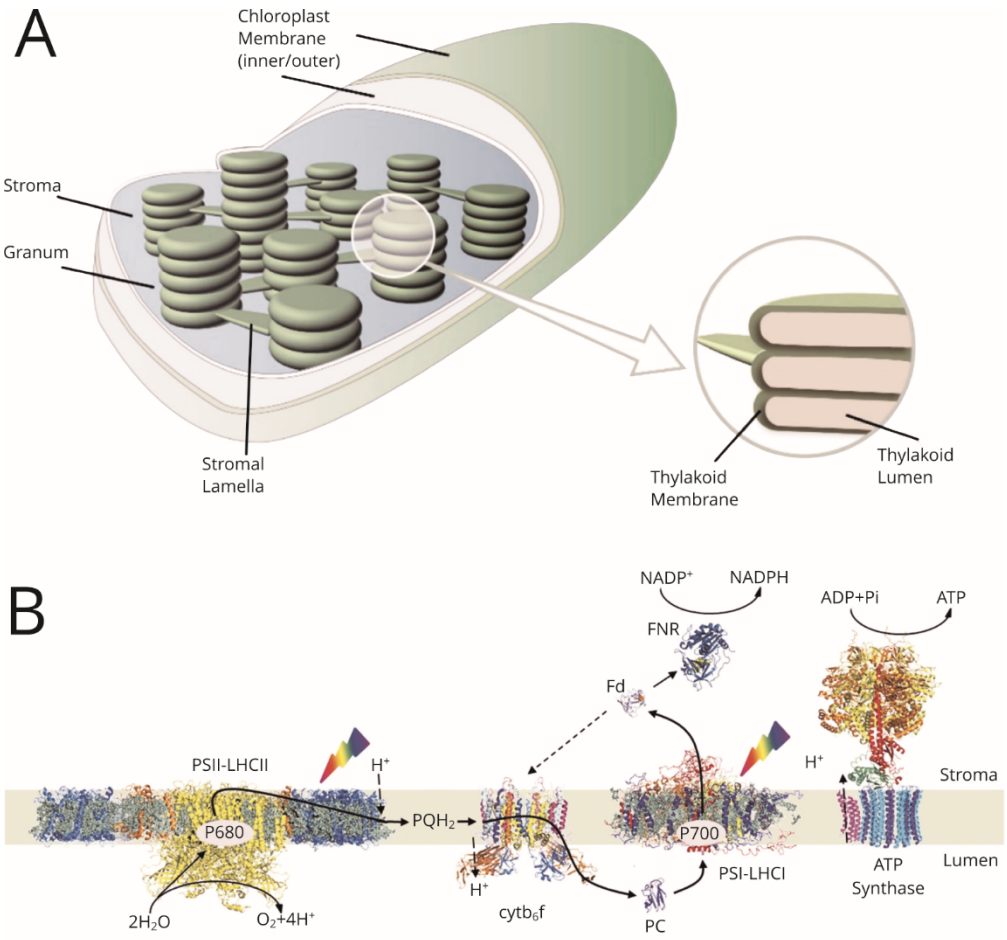

Figure 1 Schematics of thylakoid membrane and photosynthetic electron transport chain

(A) Cartoon showing the cross-section of a chloroplast and thylakoid membrane. Reprinted (adapted) with permission from Croc Mirkovic et al, (2016). Copyright (2014) American Chemical Society. (B) Schematic of the membrane proteins found in the thylakoid membrane and the chemical pathways, adapted from Croce and van Amerongen (2014).

Within the thylakoid membrane, which separates the stromal and lamellar regions within the grana stacks, there are several proteins crucial to the initial stages of photosynthesis. Figure 1 (B) shows a schematic of these proteins with electron pathways (Croce and van Amerongen, 2014). Energy is initially absorbed by pigments confined within various antenna proteins, or light-harvesting complexes (LHCs), and directed towards photosystems in the form of excited electronic states or 'excitons'. The starting point of the electron transport chain in photosynthesis is the membrane protein photosystem II (PSII). After initial absorption of a photon either by PSII or its associated antenna protein LHCII an exciton is formed. The exciton then migrates towards the central PSII reaction

centre (RC) on the luminal side of the membrane. The core PSII reaction centre contains a 'special pair' of two chlorophyll molecules called P680 (with an associated energy relating to photons of 680 nm), in close proximity to monomeric chlorophylls and pheophytins where charge separation takes place (recent evidence has shown that a monomeric Chl is the primary site of charge separation rather than P680 (Cardona et al., 2012). Four excitons are required to perform the water splitting reaction. Excitons build up sequentially within the PSII leading to five possible states, S_0 to S_4, with the number representing the number of excitons. Once PSII reaches the S_4 state the water splitting reaction takes place in the oxygen-evolving complex, in which two water molecules (H_2O) are split into molecular oxygen (O_2), four protons (H^+), and four electrons (Lubitz et al., 2019). The protons produced by this reaction (and by proton pumping in transmembrane cytochromes) build up on the luminal side of the thylakoid membrane, creating a proton gradient across the membrane. Two of the electrons produced in the reaction reduce quinone molecules, plastoquinone is reduced by an electron with the concomitant uptake of H^+ to form plastoquinol (PQH^+). The other two electrons produced in the water splitting re-reduce primary donor molecules (monomeric Chl/$P680^+$) which are oxidised during charge separation. These processes do not occur simultaneously but rather as multiple cycles of electron transfer, eventually producing one O_2 molecule and four protons. PQH^+ is an electron transporter located exclusively in the inner envelope of the thylakoid membrane bilayer and transports electrons to the cytochrome *b*$_6$*f* complex (cyt *b*$_6$*f*). The role of cyt *b*$_6$*f* is to transfer the electrons from the reduced plastoquinol to the soluble electron transporter protein plastocyanin (PC), in this process protons are released from the plastoquinol as it is oxidised back to plastoquinone, which builds up in the lumen to add to the proton gradient formed by the water splitting reaction. PC then binds with the membrane protein photosystem I (PSI) and the electrons are transferred through an electron transfer chain to the soluble protein ferredoxin (Fd) on the stoma side of the membrane (Blankenship, 2014).

The electron transport from plastocyanin to ferredoxin via PSI an energetically 'uphill' process. Additional energy is provided by the absorption of photons by the PSI or its associated antenna proteins LHCI. The reaction centre of PSI consists of a 'special pair' of chlorophylls with a corresponding absorption wavelength of 700 nm. Energy from PSI, or LHCI, photon absorption is used to further excite the electrons from PC to a higher energy level, allowing them to be transferred to the stroma side of the membrane and

reduce Fd. The Fd is then oxidised by the enzyme ferredoxin-NADP+ reductase (FNR), which utilises the electrons in ferredoxin to produce NADPH by reducing NADP+ in the stroma. NADPH is a stable reducing agent used in many cellular reactions including molecular synthesis and the 'dark reactions' of photosynthesis. This includes the Calvin cycle, where long chain sugars are formed to store chemical energy in plants. The proton gradient formed by protons being produced on the lumen side of the membrane, via the oxidation of plastoquinol and the water splitting reaction, is utilised by the protein ATP synthase which is located in the lamella stroma region of the thylakoid. ATP synthase uses the energy from the protein gradient to convert ADP to ATP which is used as the standard 'energy currency' in cells for processes such as the Calvin cycle and complex molecule synthesis (Blankenship, 2014).

1.1.2 Light absorption and fluorescence in photosynthetic systems

The first process of photosynthesis is the absorption of light at specific wavelengths by pigments in the photosystems and light-harvesting complexes. Absorbance occurs when a photon interacts with an atom or molecule causing it to enter an excited vibrational state. The photon energy is transferred to an electron which is excited to a higher-energy electronic state orbital. The energy of a photon is directly proportional to its frequency and inversely proportional to its associated wavelength (Equation 1) (Lakowicz, 2006).

$$E = h\upsilon = hc\frac{1}{\lambda}$$

Equation 1 Energy of a photon. E: Photon energy, λ: photon wavelength, h: Planck's constant (6.626×10^{-34} J s), υ: photon frequency, c: speed of light (2.998×10^{8} ms^{-1}).

A photon can be absorbed by an atom or molecule if its energy corresponds to the gap between the molecule's ground state energy level (S_0), or highest occupied molecular orbital (HOMO), and the energy level of the first (S_1) or second (S_2) electronic vibrational state orbitals. It is also possible for higher energy photons to excite electrons from the higher electronic states to other orbitals, but this is typically not the case with photons in the visible range. A Jablonski diagram of these states and sub-states is shown in Figure 2 with electron excitation due to photon absorption displayed as blue arrows (Lakowicz, 2006).

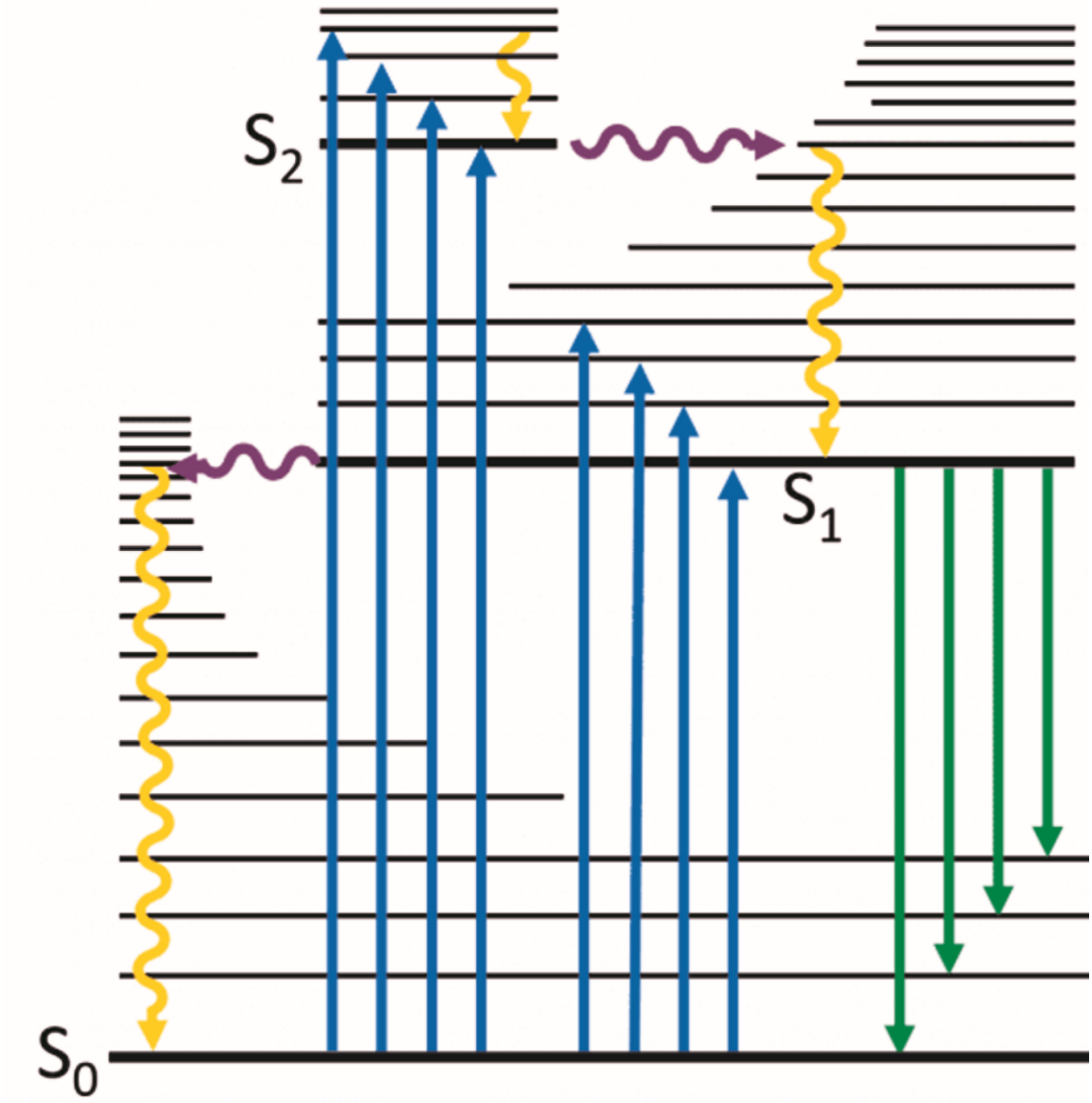

Figure 2 Jablonski diagram showing excited states of a fluorescence molecule

Electronic energy states (thick black lines) and vibrational sub-states (thin black lines). Blue: photon absorption, Yellow: vibrational relaxation, Purple: internal conversion, Green: Fluorescence. Adapted from Edinburgh instruments F980 fluorescence spectrometer manual.

The timescale of photon absorption and electron excitation to higher energy levels is on the order of femtoseconds (10^{-15} s). Due to the dependency of photon energy on wavelength, absorption of shorter 'high energy' photons results in electrons being excited to higher energy levels. Conversely, when longer wavelength 'lower energy' photons are absorbed, electrons will be excited to lower energy levels. If the energy of a photon does

not correspond to any transitions between energy levels for an atom or molecule it will not be absorbed at all. For molecules with multiple interacting atoms the energy levels are more complex due to a dynamic system with many electron orbitals interacting. This results in many vibrational sub-states at each electronic state, which greatly broadens the energy levels available. The lowest vibrational sub-state will be the lowest energy S_1 or S_2 electronic state, and if an electron is excited to a higher vibrational state by initial photon absorption it will return to the S_1 or S_2 level through "vibrational relaxation" where excess energy is dissipated to the environment as heat. The timescale of this relaxation process is on the order of picoseconds to hundreds of picoseconds (10^{-12} – 10^{-10} s) and is displayed as yellow arrows in Figure 2. The energy gap between the electronic states S_1 and S_0 is typically much larger than the energy gap between vibrational excited states. However, it is possible that vibrational states of a higher electronic state will overlap with those of a lower state, making energy transfer between them possible. This process is known as internal conversion and is displayed as purple arrows in Figure 2. Internal conversion typically occurs between the higher states at a timescale of tens of picoseconds to nanoseconds (10^{-11} – 10^{-9} s). From the S_1 state, or Lowest Occupied Molecular Orbital (LUMO), excitons can relax to the ground state or its associated vibrational states via fluorescence emission as is displayed with green arrows in Figure 2. As the exciton relaxes a photon is emitted with a wavelength corresponding to the difference in energy levels. The timescale of fluorescence typically between hundreds of picoseconds and nanoseconds (10^{-10} – 10^{-7} s) (Lakowicz, 2006). If the exciton relaxes to a vibrational state it will further relax to the S_0 ground state though vibrational relaxation. Due to energy loss via internal conversion and vibrational relaxation the emitted photon is always lower energy than the initially absorbed photon. This means that the wavelength of the emitted photon is always shorter than those absorbed; this is called the Stokes shift.

In photosynthetic systems the most common form of excited states are singlet states, where the electron in the excited orbital is paired with an electron of opposite spin in the ground state. Triplet states also occur, where electrons in the excited state and ground state have the same spin orientation. The Pauli Exclusion Principle forbids two electrons with the same spin to occupy the same energy level so triplet states cannot recombine with the ground state. This results in an extended excited state lifetime (10^{-1} – 10^{3} s) as the electron must change spin direction before returning to the ground state. Fluorescence emission from electrons returning to the ground state from the triplet state is termed

phosphorescence. Triplet states can cause damage in biological systems as they can be highly reactive and have a long lifetime; photosynthetic systems have pathways to dissipate excited triplet states which will be discussed later (Lakowicz, 2006, Niedzwiedzki and Blankenship, 2010).

The most common pigments in plants are chlorophylls, planar molecules with a 'head group' which have a magnesium atom at the centre ligated by four nitrogen atoms, each of which is part of a cyclic pyrrole ring containing four carbons. The structure is shown in Figure 3 (B) for chlorophyll *a*, the most common chlorophyll in nature which absorbs strongly in the visible wavelength regions of 380 – 450 nm ($S_0 – S_2$ transition) and 625 - 725 nm ($S_0 – S_1$ transition). Chlorophyll molecules also have a hydrocarbon 'tail' which provides stability and allows the pigment to be incorporated into complex structures such as proteins, denoted by R in Figure 3 (B).

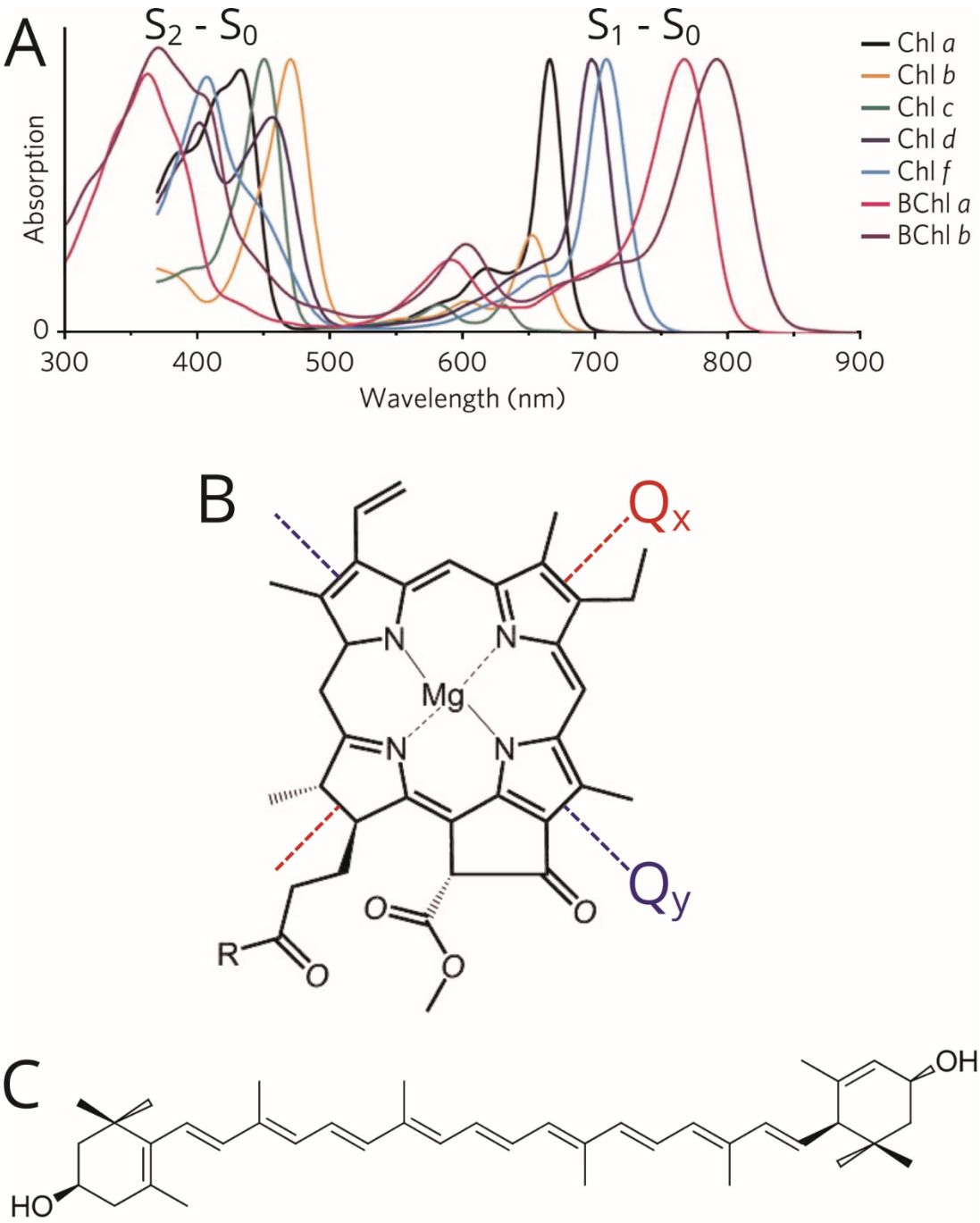

Figure 3 Absorption spectra of chlorophyll and example structures of photosynthetic pigments

(A) Absorption spectra of all known chlorophyll molecules, adapted from Croce and van Amerongen (2014). (B) Chemical structure of chlorophyll a, the Q_x and Q_y axis (dipole transitions) are denoted by the dotted lines. (C) Chemical structure of a lutein molecule.

The four cyclic carbon rings in the chlorophyll 'head' provide a delocalised π bond structure, called a macrocycle, which allows different vibration energy states across molecules. The two vibrational dipoles across the chlorophyll, labelled Q_x and Q_y in Figure 3 (B), relate to the $S_0 - S_1$ transitions of the molecule; two other vibrational dipoles called B_x and B_y relate to the $S_0 - S_2$ transition (the latter B states are often also referred to as "Soret" transitions). Q_y is the lowest energy of all transitions in the molecule. This means that energy absorbed by either of the B transitions will relax to the Q transitions via internal conversion followed by vibrational relaxation to Q_y. There are seven variations of the chlorophyll molecule found in different photosynthetic organisms, five in plants and two in bacteria, each with a slightly different molecular structure around the macrocycle. Variations in the chemical composition around the macrocycle change the length and orientation of the transitions resulting in slightly different electronic and vibrational states. The absorption spectra for all known chlorophyll molecules are shown in Figure 3 (A) (Croce and van Amerongen, 2014, Lakowicz, 2006). Chlorophyll molecules typically absorb strongly in the blue and red regions of the visible spectrum and have excited fluorescence lifetimes on the order of nanoseconds, the wavelengths of absorption maxima and fluorescence lifetimes of known plant chlorophylls and examples of the two most common bacteriochlorophyll pigments are shown in Table 1 (Niedzwiedzki and Blankenship, 2010). Bacteriochlorophylls are found in prokaryotic phototrophs (such as purple and green bacteria) instead of chlorophylls, due to different biosynthetic pathways in the particular organisms. Bacteriochlorophylls have different substituent groups attached to the pyrrole ring compared to chlorophylls, which red-shift Soret and Q transitions. These shifts, along with pigment-pigment interactions, lead to absorption for the Q bands in the near-infrared, often at 850 to 900 nm, and up to a longest reported 1050 nm (Qian et al., 2018).

Pigment	Absorption peak positions λ (nm)	Fluorescence lifetime τ (ns)
Chlorophyll *a*	**430, 578, 662**	**6.3**
Chlorophyll *b*	**455, 549, 644**	**3.2**
Chlorophyll *c*	**640, 593, 462**	**6.3**
Chlorophyll *d*	**400, 456, 697**	**6.2**
Chlorophyll *f*	**393, 440, 707**	**-**
Bacteriochlorophyll *a*	**358, 577, 773**	**2.9**
Bacteriochlorophyll *b*	**572, 592, 791**	**2.4**

Table 1 Absorption peak positions and fluorescence lifetime for photosynthetic pigments, data taken from Niedzwiedzki and Blankenship (2010)

Chlorophylls and bacteriochlorophylls are not the only pigments found in photosynthetic proteins. Typically, a combination of different chlorophyll types is present alongside additional carotenoids to maximise the absorption range of the protein. Carotenoids are extended molecules with many double bonds which provide a delocalised π bond electron system across the molecules, some contain cyclic carbon rings at either end of the carbon chain which further extends the π bond system. The chemical structure of lutein, the most common carotenoid found in plant light-harvesting proteins, is shown in Figure 3 (C). Carotenoids typically absorb strongly in the 400-500 nm range of the visible spectrum related to the S_0 – S_2 transition. Due to the symmetry of the elongated molecules absorption directly to the S_1 state is "forbidden" (i.e., does not occur in normal conditions in nature). Internal conversion from the S_2 to S_1 state is very efficient and occurs on a femtosecond timescale (10^{-15} s). Due to the forbidden nature of the S_1 state, the internal conversion from S_1– S_0 is also very efficient, taking place on a picosecond timescale (10^{-12} s). Carotenoids have multiple roles in photosynthetic systems: first, energy absorbed by carotenoids in the blue part of the visible spectrum can be transferred to chlorophylls for eventual use in photochemical reactions. Second, the ability of carotenoids to quickly dissipate electron energy as heat through internal conversion and vibrational relaxation make them crucial for the rapid quenching of potentially damaging triplet states which can form if photosynthetic proteins are excited by multiple photons in a short time period. Thirdly, carotenoids appear to have important structural roles in stabilizing the 3-D structure of many pigment-protein complexes (Blankenship, 2014).

1.1.3 Non-radiative energy transfer and light-harvesting proteins

Förster theory and resonance energy transfer

The initial stages of photosynthesis involve photons being absorbed by a number of different pigments in both photosystems and their associated light-harvesting proteins. As discussed in section 1.1.1, to perform photochemistry the energy of excited electrons, or excitons, must be transferred to specific chlorophyll pairs (with corresponding energy levels of 680 nm and 700 nm) which are located in the reaction centres of PSII and PSI, respectively. The principal mode of energy transportation between pigments in photosynthetic proteins is Förster Resonance Energy Transfer (FRET) (Sener et al., 2011). The requirements for the energy of an excited state in one molecule to be non-radiatively transferred to another are (1) overlapping spectral properties, (2) their vibrational dipoles are not oriented perpendicular to each other, and (3) they are in close enough proximity to exhibit dipole-dipole coupling (Förster, 1965). Dipole-dipole coupling occurs when two electromagnetic dipoles, such as vibrational electronic dipole states in chlorophylls, are aligned with each other and are in close proximity (e.g., within 10 nm). If the dipoles are of a similar frequency then the vibronic dipoles will become coupled, if this is the case and one dipole is in an excited state (donor) then exciton energy will be transferred to the non-excited dipole (acceptor) causing it to become excited, while the first relaxes to the ground state. This can only occur if it is an energetically downhill transfer; energy must be lost in the transfer and not gained in accordance with the first law of thermodynamics (although thermal energy from the local environment, k_BT, can allow flexibility via access to higher vibrational states). An energy level diagram of this process is shown in Figure 4 (A) with the electronic states of the donor shown in blue, and of the acceptor in orange. After initial absorption of a photon by the donor molecule (1) an electron is excited to an S_1 vibrational state (2), which then returns to the S_1 electronic state through vibrational relaxation (3). As the donor and acceptor molecules are coupled FRET takes place and the energy of the excited state in the donor is transferred to the acceptor (4). In this process, the excited electron in the donor molecule relaxes to the ground state without photon emission. Simultaneously an electron is excited from acceptor molecule ground state to an S_1 vibrational state without photon absorption (red arrows). The excited electron in the donor then returns to the S_1 state through vibrational relaxation (5), before further relaxing to the ground state as a photon is emitted

via fluorescence (6). The process of energy transfer is non-radiative as there is no emission or absorption of photons and the coupling of dipoles is due to the Coulombic interactions between two vibrational states (Mirkovic et al., 2016).

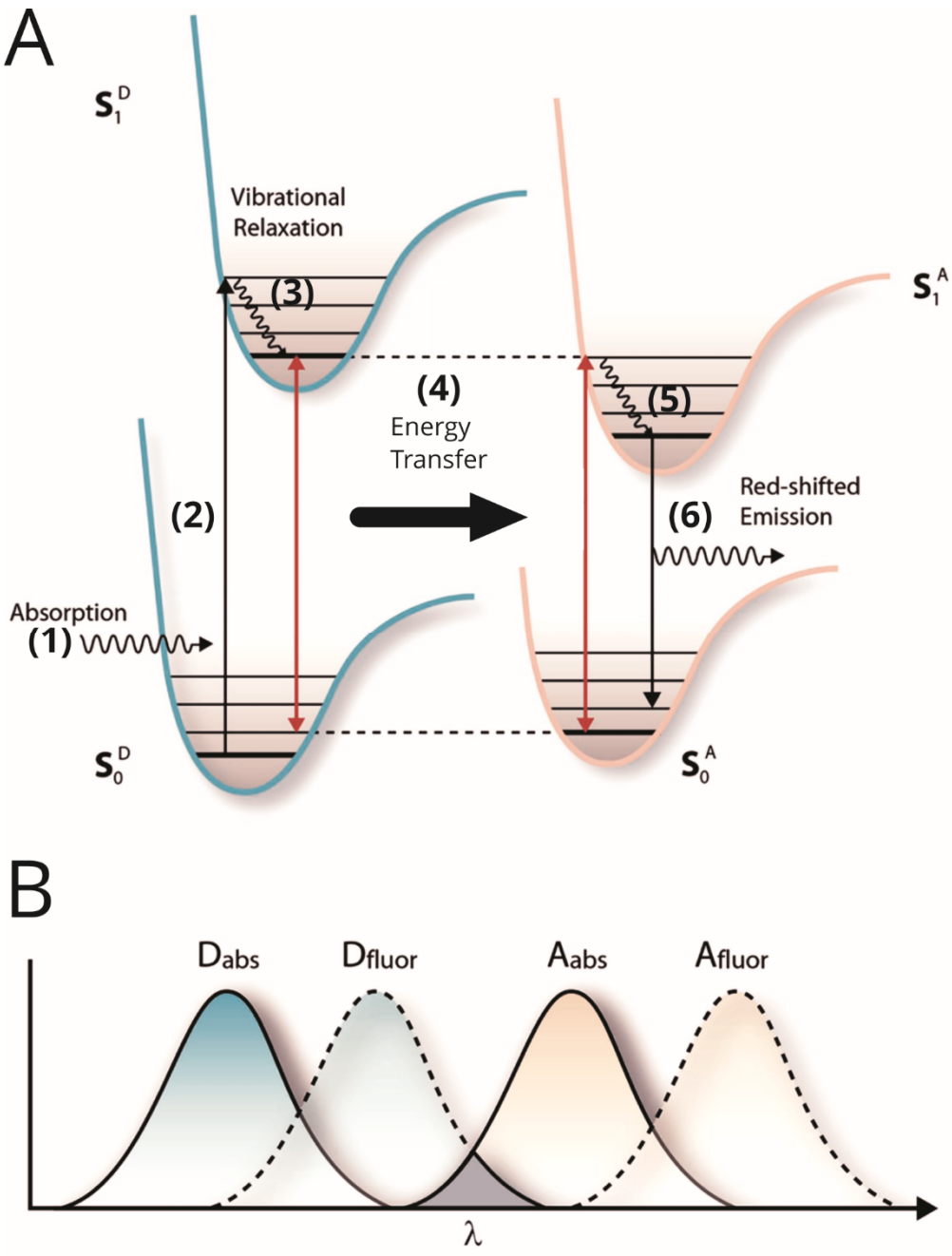

Figure 4 Jablonski diagram showing donor-acceptor FRET and required spectra overlap

(A) Energy level diagram for donor to acceptor FRET: S_0^D and S_0^A are ground states of the donor and acceptor. S_1^D and S_1^A are excited singlet states of donor and

acceptor, respectively. (B) Spectral conditions needed for donor to acceptor FRET to take place. D_{abs} and A_{abs} are the absorption spectra of donor and acceptor. D_{fluor} and A_{fluor} are the fluorescence emission spectra of donor and acceptor, respectively. The grey shaded area is the overlap defined by the overlap integral J. (A+B). Reprinted (adapted) with permission from Croc Mirkovic et al, (2016). Copyright (2014) American Chemical Society.

The conditions for the 'downhill' energy transfer can be defined by the donor molecule emission and acceptor molecule absorption. The wavelengths of photon emission from the donor must overlap with the photon absorption wavelengths of the acceptor; this condition must be met so that the energies of vibronic states are sufficiently similar for dipole-dipole coupling to take place and the transfer is occurring 'downhill'. This overlap of donor emission and acceptor absorption is defined by a spectral overlap factor, J. The overlap factor J correlates to the area of overlap the donor's fluorescence emission spectra and the acceptor's absorption spectra, which is the integral with respect to wavelength of the molar extinction coefficient of the acceptor, $\varepsilon(\lambda)$, and the normalised emission spectrum of the acceptor, $F_D(\lambda)$. The equation for the overlap integral is shown in Equation 2 and a spectral representation in Figure 4 (B, grey shaded area) D: donor, A: acceptor. The orientation of dipoles relative to each other is also crucial to the efficiency of energy transfer; if the dipoles are parallel then energy transfer will be most effective due to maximised Coulombic interactions, whereas if they are perpendicular coupling is not possible. The orientation of dipoles relative to one another is given by an orientation factor, κ. The orientation factor is defined by the angle between the planes of the dipoles α, and the angle of each of the dipoles relative to a vector joining them $\beta_{1,2}$. The interaction factor has a value 2/3 on average for randomly oriented dipoles. The equation for the orientation factor is shown in Equation 3 (Loura, 2012, Blankenship, 2014).

$$J = \int \varepsilon(\lambda) F_D(\lambda) \lambda^4 d\lambda$$

Equation 2 J: Overlap integral. $\varepsilon(\lambda)$: the molar extinction coefficient of the acceptor as a function of wavelength, $F_D(\lambda)$: normalised emission spectrum of the acceptor as a function of wavelength, λ: wavelength.

$$\kappa^2 = (cos\alpha - 3cos\beta_1 cos\beta_2)^2$$

Equation 3 k^2: Orientation factor. α: angle between planes of dipoles, β: angle between dipole direction and a vector linking to the other dipole.

The rate of energy transfer from donor to acceptor can be defined by an adaptation of Fermi's golden rule (Equation 4) which is used to define the transition rate ($k_{D\rightarrow A}$) of a quantum system based on the coupling of the two states (V_{DA}) and the difference in state energy $\delta(E_D - E_A)$. The difference in state energy of the FRET system is defined by the overlap interval, J. The coupling of states in a FRET system is simply the Coulombic interaction between the donor and acceptor dipoles taking into account the Coulombic strength of the donor (μ_D) and acceptor (μ_A) dipoles, and their relative orientation factor (k); interaction energy is defined in Equation 5. These equations can be combined to give an equation for the rate of energy transfer between donor and acceptor dipoles, Equation 6 (Blankenship, 2014).

$$k_{D\rightarrow A} = \frac{2\pi}{\hbar}|V_{DA}|^2\delta(E_D - E_A)$$

Equation 4 Fermi's golden rule. $k_{D\rightarrow A}$: rate of energy transfer between states, ħ: Reduced Planck's constant ($\frac{h}{2\pi}$), V_{DA}: Interaction energy, V_{DA}: Interaction energy, $\delta(E_D - E_A)$: difference in state energy defined as overlap integral J

$$V_{DA} = k_e \frac{\mu_D \mu_A k}{r_{DA}^3}$$

Equation 5 Interaction energy of dipole-dipole coupling. V_{DA}: Interaction energy, k_e: Coulomb's constant (8.99 x10^9 Nm^2C^{-2}), μ_x: transition dipole strength, κ: orientation factor, r_{DA}^3: distance between transition dipoles

$$k_{D\rightarrow A} = \frac{2\pi k_e^2}{\hbar}\frac{\mu_D^2 \mu_A^2 k^2}{r_{DA}^6}J$$

Equation 6 FRET equation for the rate of energy transfer from combined Equation 4 and Equation 5.

The rate of energy transfer ($k_{D\rightarrow A}$) can be calculated by defining a critical distance between two pigments where energy transfer is 50 % efficient (R_0). The critical distance considers the rate of fluorescence of the donor dipole in the absence of energy transfer (k_d) (which is equal to 1/donor fluorescence lifetime (τ_D)). The R_0 equation and a simplified version with a single constant are shown in Equation 7. The value for R_0 varies from pigment to pigment but is generally between 60 Å and 100Å (Van Grondelle, 1985). Molecules must be separated by at least 10Å for FRET to take place, due to the Pauli Exclusion Principle which limits massive particles from occupying the same space and comes into effect at sub-nanometre separation (Blankenship, 2014).

$$R_0^6 = \left(\frac{2\pi k_e^2}{\hbar}\mu_D^2\mu_A^2 k^2 \tau_D J\right) = 8.79 \times 10^{-5} J k^2 n^{-4} \text{Å}$$

Equation 7 Förster distance equation

The rate of energy transfer in a system can also be defined by the rate of fluorescence of the donor (k_D), donor – acceptor dipole separation (r_{DA}) and the critical distance (R_0), as shown in Equation 8. The rate of energy transfer is proportional to r^{-6} meaning that FRET is extremely sensitive to distance between molecules, this has been utilised in many nano-technological applications which involve measuring when two molecules are sufficiently close for FRET to occur (Schuler and Eaton, 2008).

$$k_{D\rightarrow A} = \frac{1}{\tau_f}(R_0/r_{DA})^6 = k_D(R_0/r_{DA})^6$$

Equation 8 Rate of energy transfer defined by Förster distance and donor-acceptor separation

Finally, the efficiency of energy transfer between donor and acceptor dipoles (ETE) can be defined by the relative rates of energy transfer from the donor due to dipole-dipole coupling ($k_{D\rightarrow A}$) and the rate of natural donor fluorescence (k_D). This can be combined with Equation 8 for the rate of energy transfer defined by donor-acceptor separation (r_{DA}) and R_0 to give energy transfer efficiency in these terms. This is defined in Equation 9 (Blankenship, 2014).

$$ETE(r_{DA}) = \frac{k_{D\rightarrow A}}{k_{D\rightarrow A} + k_D} = \frac{R_0^6}{R_0^6 + r_{DA}^6}$$

Equation 9 energy transfer efficiency.

The concept of light-harvesting and role of light-harvesting antenna proteins

The two proteins in the photosynthetic system described in 1.1.1 are the photosystems (PS) and their associated light-harvesting complexes (LHC). The pigments in these proteins are arranged to allow energy to be transferred via FRET to the 'special pairs' of chlorophylls located in the reaction centres of the PSs where photochemical reactions take place. Carotenoids absorb the highest energy (lowest wavelength) photons and transfer the resulting excitons energetically 'downhill' to the chlorophylls which have lower associated energy levels via FRET. The chlorophyll pigments within LHCs and PSs, including the 'special pairs', have similar associated excited state energy levels. FRET can therefore occur between all chlorophyll molecules in the proteins and that excitons are effectively de-localised across the system (slight "uphill" energy transfers are feasible at room temperature due to the energy available to molecules from vibrations and heat, i.e., k_BT). This allows energy absorbed by any pigment to be eventually transferred to the reaction centres. (Blankenship, 2014).

The primary function of antenna proteins is to increase the spatial and optical area that light can be absorbed over in the thylakoid membrane. Calculations show that solar energy is relatively dilute, with individual chlorophyll molecules absorbing a photon every ~100 μs (Blankenship, 2014). Four cycles of photon absorption, photochemistry and subsequent electron transfer are required in the PSII reaction centre for the water splitting reaction to take place, by relying on the absorption of these chlorophylls alone the maximum rate of water splitting would be once every ~200 μs. This would be extremely slow relative to the maximum rate that reaction centres are capable of, which is charge separation on the order of once every few hundreds of picoseconds under ideal conditions (van Amerongen and Croce, 2013). The outcome would be uneconomical to have the entire area of the thylakoid covered in reaction centres as the low photon flux

would render them inactive for the majority of the time. It is more efficient to have large areas of the thylakoid membrane acting as an antenna which can transfer any energy absorbed to a central photosystem at a rate which delivers sufficient excitation to the reaction centres to allow regular photochemistry to take place, antenna proteins serve this purpose. Figure 5 (A) shows a 2D cartoon demonstrating the large surface area available for energy absorption due to additional pigments. Pigments in both photosystems and antenna proteins act to increase the effective absorption area of the reaction centre, and antenna pigments can refer to the pigments in both types of protein. Antenna proteins and photosystems are organised so that the pigments which absorb the highest energy photons are typically furthest away from the photosystem reaction centre, and pigments with a lower characteristic energy are closer. Due to the similar energy levels of chlorophylls, excitons are effectively de-localised across the system allowing them to eventually reach the central reaction centres (Croce and van Amerongen, 2011). One way of visualising the energy transfer in antenna proteins is the concept of a funnel or satellite dish shown in Figure 5 (B). The outermost carotenoid pigments absorb the highest energy photons (lowest wavelengths), excitons are transferred to the orange and then red-absorbing pigments, chlorophyll *b* and *a,* respectively, before reaching the reaction centre 'special pair' of chlorophyll *a* molecules with an associated energy of 680 nm. In reality, at room temperature the energy funnel is extremely shallow. Thermal energy from the local environment, k_BT, can provide additional energy to excitons which allows them to transfer to pigments with higher corresponding energies, which means that there can be a certain amount of exciton delocalisation in the system before reaching the reaction centre (Mirkovic et al., 2016).

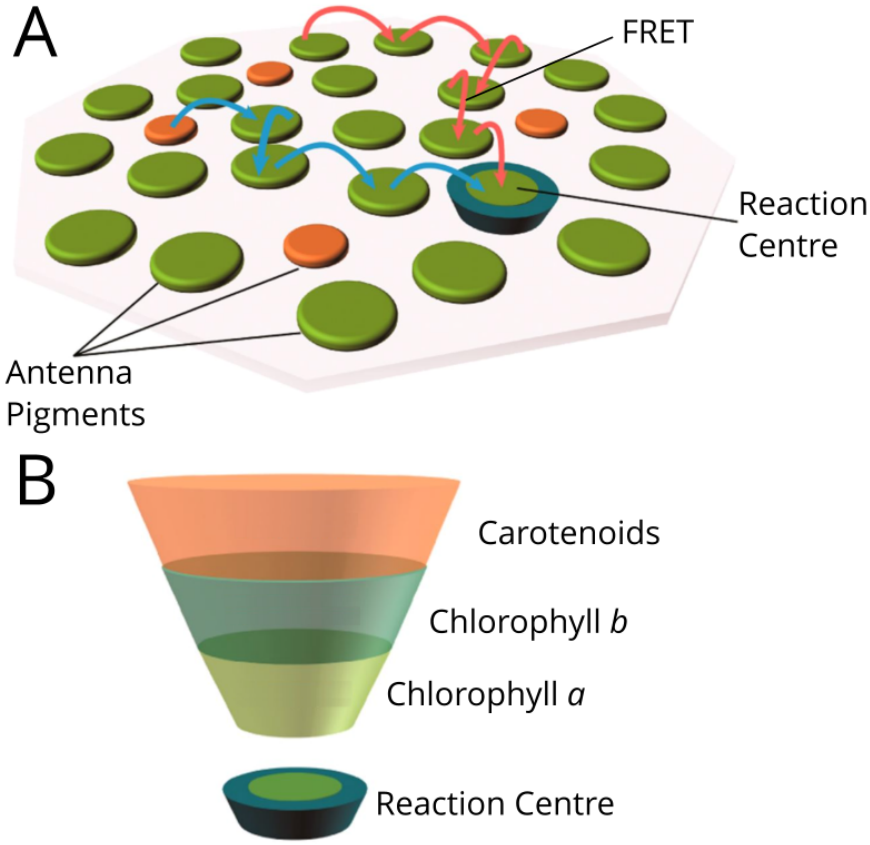

Figure 5 Cartoons demonstrating the function of antenna proteins and the directionality of inter-pigment energy transfer

(A) Cartoon showing the pathway of excitation energy from antenna protein pigments to the reaction centre (B) Visualisation of the 'funnel' of pigments with different characteristic energy levels and the direction of excitations. Reprinted (adapted) with permission from Croc Mirkovic et al, (2016). Copyright (2014) American Chemical Society.

The Light-Harvesting Complex II (LHCII) protein

The light harvesting protein LHCII is the most abundant antenna complex found in nature. It was first identified in 1993 as a protein in thylakoid grana membranes and acts as the antenna protein for the water splitting photosystem II (Grossman et al., 1993). A model for its structure was first determined to a maximum resolution of 3.4 Å in 1994 using electron crystallography (Kühlbrandt et al., 1994). The next major update to the structure was in the mid-2000s using X-ray crystallography to achieve a resolution of up to 2.5 Å; top and side views of an LHCII trimer are shown in Figure 6 (A+B) (Standfuss et al.,

2005, Liu et al., 2004). In nature LHCII functions both as a monomer and in a trimeric form. Both are found in the dimeric PCII-LHCII supercomplex shown in Figure 6 (D), with monomers labelled CP29 and CP24 (Wei et al., 2016). A monomer of LHCII contains three transmembrane alpha helices, 8 chlorophyll *a* pigments, 6 chlorophyll *b* pigments, 4 carotenoids and 2 bound lipids (Standfuss et al., 2005). This combination of pigments gives the complex strong absorption in the blue region of the visible spectrum (400 -500 nm), due to the combined absorption of the chlorophyll and carotenoid $S_2 - S_0$ transitions, and it also has a strong absorption in the red (650 – 700 nm) due to the chlorophyll $S_1 - S_0$ transitions. Energy absorbed by any of the pigments in LHCII is transferred energetically downhill via FRET to a 'terminal' chlorophyll *a* molecule at the periphery of the complex. LHCII then equilibrates to the lowest energy level, corresponding to a wavelength of 680nm, ready to be transferred to PSII in a few picoseconds on average (Van Amerongen and Van Grondelle, 2001). The energy rapidly directed to a 'terminal' chlorophyll *a* results in a single emission peak for isolated LHCII trimers at 681 nm corresponding to emission from a single type of pigment. Absorption and emission spectra of LHCII isolated in detergent are shown in Figure 6 (D). There are three isoforms of the LHCII polypeptides, each of which are produced from separate genes, which combine to make up the trimeric complex: Lhcb1, Lhcb2 and Lhcb3. Lhcb1 and 2 are very similar while Lhcb3 differs due to its lack of phosphorylation sites and one less chlorophyll *b* pigment. It is thought that Lhcb1 and 2 act as the main antenna complexes and Lhcb3 contains the lowest energy chlorophyll that acts as an intermediate between Lhcb1, Lhcb2 and PSII in the FRET energy transfer chain (Standfuss and Kuhlbrandt, 2004).

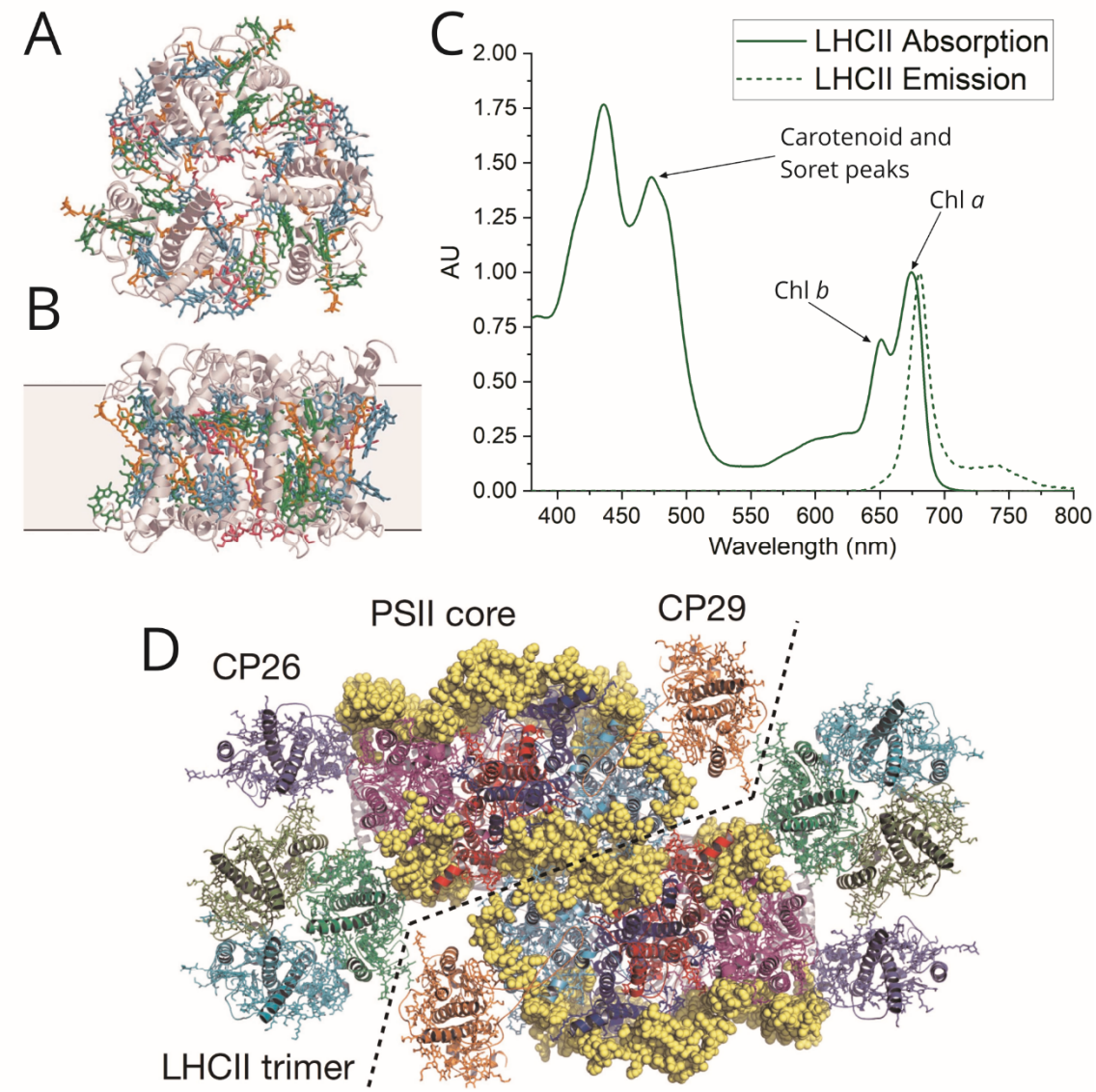

Figure 6 Structures of isolated LHCII and PSII-LHCII supercomplexes

(A + B) Top and side views of an LHCII trimer complex respectively; the membrane has a thickness of 35Å. Colour key: Grey; polypeptide chain, Cyan; chlorophyll *a*, Green; chlorophyll *b*, Orange; Carotenoids, Red; Lipids. Adapted from Standfuss et al. (2005). (C) Absorption and emission spectra of isolated LHCII in detergent (D) PSII-LHCII super-complex, showing the positions of the PSII core dimer, LHCII trimers and supplementary antenna proteins. Adapted from Wei et al. (2016).

Regulation of light-harvesting proteins and non-photochemical quenching

Having a large effective absorption area allows photosystems to perform photochemistry at an efficient rate, under most conditions the photon flux is the limiting factor of photosynthesis. However, there is a limit to the rate of photochemical reactions and under high light intensity the large area of antenna proteins and photosystems can absorb an excess of photons, which results in an excess of delocalised excitons in the system (many singlet excited states). A build-up of excitations within the antenna proteins can produce chlorophyll triplet states, which occur when the spin of the excited electron in a chlorophyll molecule changes. This is a random process which is far more likely to happen if there are many excitons in a system not being immediately used for photochemistry (Krieger-Liszkay, 2005). Triplet chlorophyll states are highly reactive and long-lived, and they can react with stable triplet oxygen molecules to form highly reactive oxygen singlet states that will oxidise molecules in their immediate vicinity and damage the protein (Ruban, 2016). These potentially damaging triplet states of chlorophyll and reactive singlet states of oxygen can both be effectively quenched by the carotenoid pigments found in antenna proteins. These protective mechanisms which limit damage from these reactive states, or photoinhibition, when under high photon flux are termed "photo-protection" and are typically manifested as the non-photochemical quenching (NPQ) of chlorophyll fluorescence.

There are several changes which occur in photosynthetic systems when under high-light conditions which promote NPQ in the system. This is not necessarily a specific quenching of potentially damaging states but a general quenching of excited states in the system. There is evidence that the trigger of NPQ is a pH change across the thylakoid membrane due a high concentration of protons accumulating in the lumen (i.e., decreased pH) from a high rate of water splitting reactions in PSII and conversion of plastoquinol to plastocyanin by cytochrome b_6f. This change in cross-membrane pH may act as a feedback loop and initiates quenching when there is a large proton gradient (Horton et al., 1996). Many of the changes occur specifically within the LHCII antenna protein which is believed to have a crucial role in the process. The "xanthophyll cycle" is a process that occurs whereby the carotenoid violaxanthin in LHCII is converted to the carotenoid zeaxanthin under high light conditions and results in a quenching of fluorescence either

directly by the violaxanthin or by stabilising a quenching site (Duffy and Ruban, 2015). Under low light conditions this process is reversed suggesting that zeaxanthin has an active role in the quenching of excess energy or stabilizing a state that does (Demmig-Adams, 1990). The presence of a minor antenna subunit called PsbS, a peripheral protein in the PSII supercomplex, has been shown to directly relate to the amount of quenching a photosynthetic system will undergo under high light conditions. This small protein does not have a role in efficient light harvesting so is also considered to have an intrinsic role in NPQ (Li et al., 2000). It has also been demonstrated that the aggregation of LHCII causes a quenching of fluorescence even in the absence of other photosynthetic proteins, suggesting that inter-protein interactions, specifically those involving LHCII, may lead to energy dissipation (Moya et al., 2001, Crisafi and Pandit, 2017). This is supported by evidence of large scale conformational changes in supercomplexes of many photosynthetic proteins taking place under different light conditions (Betterle et al., 2009). Crucially, when in an energy dissipative state LHCII experiences a slight change in conformation (Belgio et al., 2013), the cause of which could be due to a combination of the discussed mechanisms. The change in conformation allows a favourable transfer of energy from chlorophylls to carotenoids where internal relaxation dissipates the energy as heat (Ruban et al., 2007).

Much of the current research on photosynthetic systems involves trying to determine the mechanism of NPQ, understanding the process has potential applications in both bio-hybrid light-harvesting and optimising crop growth in agriculture (Ruban, 2017a). Many studies investigate the effect of large scale reorganisation of proteins in the thylakoid membrane under high and low light conditions (Ruban, 2016). LHCII trimers have been shown to rapidly reorganise in order to balance excitation levels between the two photosystems and divert excess energy away from the one which is energetically saturated and unable to utilise excitons (Minagawa, 2011). Both LHCII and PSII have been demonstrated to aggregate during NPQ to change organisation from the highly efficient LHCII-PSII supercomplexes (Figure 7 (A)) to a state where proteins are more closely aggregated and capable of inter-protein energy dissipation (Figure 7(B)) (Kouril et al., 2011, Johnson et al., 2011). This most likely coincides with changes in the conformation of LHCII to open energy transfer pathways to carotenoids as previously discussed. The effect of reorganisation on energy dissipation has been demonstrated with LHCII-only systems on surfaces. Comparison between LHCII trimers reconstituted into membranes

on surfaces with a degree inter-protein separation and aggregated LHCII trimers on surfaces with no inter-protein separation shows a significant decrease in excited state lifetime as protein-protein interactions are minimised. This suggests that the LHCII-LHCII interactions mediate the dissipative pathway (Adams et al., 2018). LHCII has also been shown to exhibit 'blinking' of fluorescence both when isolated in detergent (Krüger et al., 2014, Schlau-Cohen et al., 2015), and when incorporated into model-lipid bilayers (Natali et al., 2016). This suggests that the switching between dissipative states is a transition which occurs with relatively low energy input, occurring naturally on the timescale of seconds. Molecular dynamics simulations have been used to demonstrate how flexibility of LHCII allows structural changes to occur in quenched states which heavily involve the carotenoids proposed to be involved in energy dissipation (Liguori et al., 2015). Recently, ultrafast spectroscopy techniques have been used to study the conditions for and speed of exciton transfer from chlorophylls to carotenoid 'dark' states in the final stages of energy dissipation as heat into the environment (Liguori et al., 2017, Son et al., 2020).

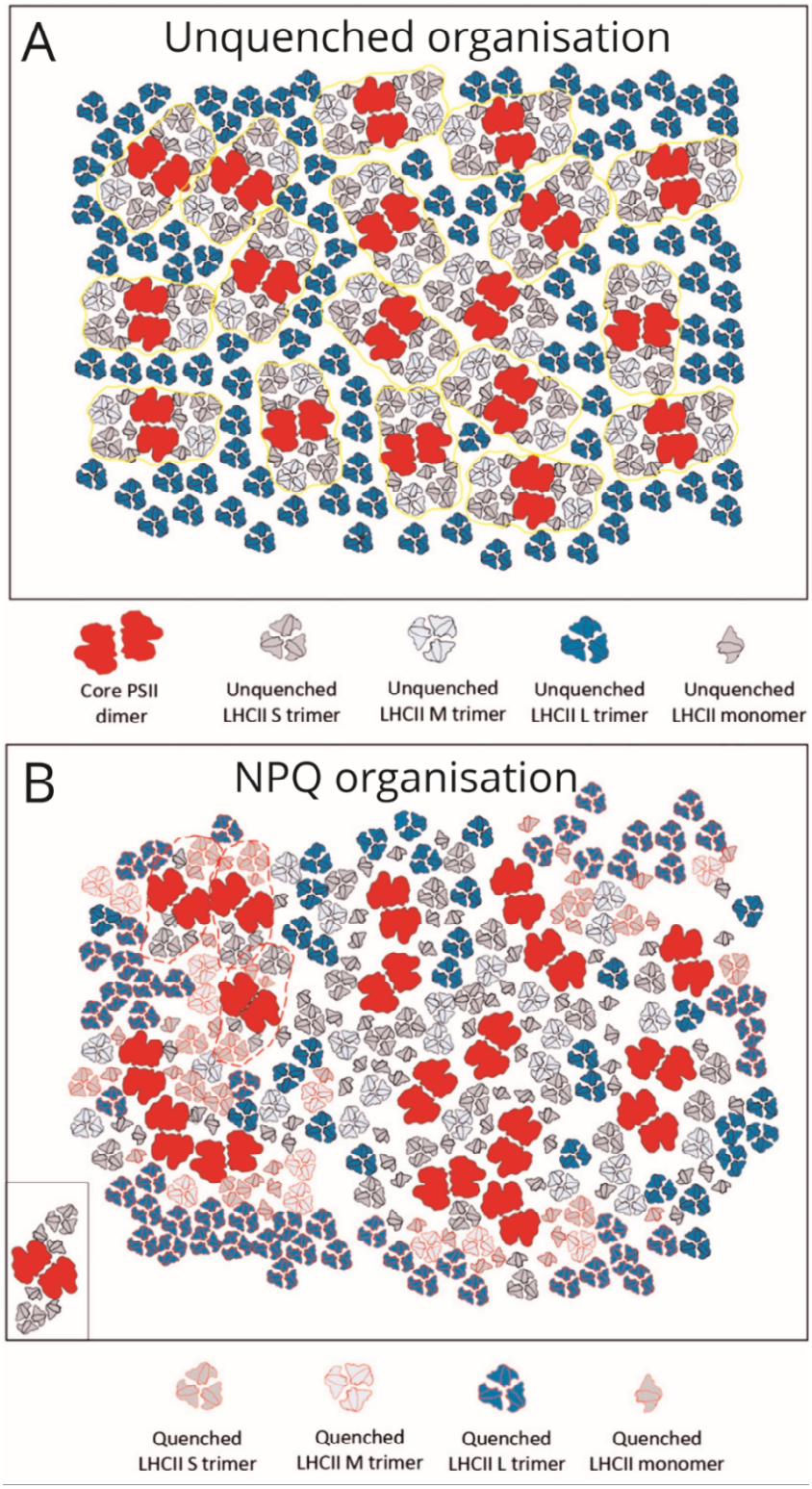

Figure 7 Schematic showing re-organisation of photosynthetic membrane proteins during NPQ

Organisation of photosynthetic membrane proteins in thylakoids under low light conditions (unquenched) and high light conditions (NPQ). Adapted from Ruban (2016). Note that this cartoon does not include cyt *b*$_6$*f* which is known to be present in these membranes (Johnson et al., 2014).

1.2 Lipid Bilayers

1.2.1 Lipids and the thylakoid membrane

The site of many of the initial phases of photosynthesis in plants is the thylakoid membrane. The thylakoid membrane consists of a folded and stacked lipid bilayer with a high density (~70 % surface area) of photosynthetic membrane proteins (Daum and Kühlbrandt, 2011). Lipids are amphiphilic molecules formed of a hydrophilic head group connected to a pair of hydrophobic fatty acid tails, as shown in Figure 8 (A). Due to the amphiphilic nature of lipids, they will self-assemble when they are in a polar solvent, such as water, to reduce the system's free energy. This is achieved by minimising the exposure of the hydrophobic tails to the solvent and maximising the exposure of the hydrophilic heads of the lipids. The structures formed by self-assembly are dependent on the relative shape of lipid head and tail groups (Bitounis et al., 2012). If the head group is wider than the tail then spherical structures will tend to form with all tails together and heads exposed. These structures, termed "micelles" commonly form from the self-assembly of detergent molecules, which are analogous to lipids in that they have a single hydrophobic fatty acid tail and hydrophilic head (Figure 8 (D)). Micelles will only self-assemble if above a critical concentration, termed the critical micelle concentration (CMC), where it is energetically favourable to self-associate and reduce the exposure of hydrophobic tails to the aqueous solution (Chakraborty et al., 2011). If the width of the head group is equal to that of the tails then lipids will form into planar lipid bilayers, as shown by stacks of bi-layers in Figure 8 (B), with two layers of lipids arranged with tails facing each other to minimise exposure to the solvent. These bilayers can form large spheres called "liposomes" or "lipid vesicles" (Figure 8 (D)) which separates an aqueous core from the aqueous solvent with at least one lipid bilayer. The size of liposomes is often dependent on the curvature of the lipids forming them. Other more complex structures can form if the tail group is significantly wider than the head, which includes the inverse hexagonal packing phases where lipid arrange to form stacks of highly curved cylinders with head groups forming the internal cylinder surface (Figure 8 (F)) (Tresset, 2009).

The structure of lipids, and the manner in which they interact with each other, are based on their chemical composition. Typically, a lipid consists of a polar head group connected to 1-3 fatty acid tails either directly or via a scaffold sugar molecule such as glycerol. The

fatty acid tails are a carboxylic acid with an aliphatic chain of carbon atoms. Fatty acids can be either saturated or unsaturated, where “unsaturated” means that they contain one or more carbon-carbon double bonds, causing the chain to be bent. The number of carbons and double bonds in a fatty acid tail are denoted by a pair of numbers X:Y, with the first representing the number of carbons and the second the number of double bonds. Lipids with tail groups containing many double bonds will have a tail group wider than the head and can therefore lead to the formation of non-planar structures such as the aforementioned inverse hexagonal phase. The lipid head group is the hydrophilic portion of the molecule, it often contains a phosphate group, which is the case in phospholipids, but also other chemical compounds such as sugars. A common bilayer forming lipid is 1,2-dioleoyl-sn-glycero-3-phosphocholine (DOPC), the structure of which is shown in Figure 8 (C). It has a phosphate and choline head group connected, via a glycerol and ester bonds, to two 18:1 fatty acid tails. DOPC is a common lipid used to form model lipid membranes as it readily forms planar lipid bilayers in the form of liposomes which can be deposited onto surfaces (Richter et al., 2006).

The plant thylakoid membrane is made up of four different types of lipid; monogalactosyldiacylglycerol (MGDG), digalactosyldiacylglycerol (DGDG), sulfoquinovosyldiacylglycerol (SQDG) and phosphatidylglycerol (PG). Figure 8 (G) shows the structure of each of the lipids (Boudiere et al., 2014). These lipids are most commonly present in a ratio of 40 % MGDG, 32 % DGDG, 15 % SQDG and 13 % PG. MGDG, DGDG and SQDG are unusual compared to most biological lipids due to their galactose based head groups, each lipid has a different role in the thylakoid membrane and different conformational properties (Sakurai et al., 2006, Deme et al., 2014). The ratio of lipid types often changes between different species of plants and algae. PG and SQDG are negatively charged and bilayer-forming; DGDG is also bilayer forming but has an essential role in forming bilayer stacks due to strong hydrogen bonding between lipid heads. MGDG would form inverse-hexagonally arranged membranes if it is was alone, and due to its cone like shape with a small head group and wide tail, it introduces curvature into the thylakoid allowing the stacked membranes to be formed (Jouhet, 2013).

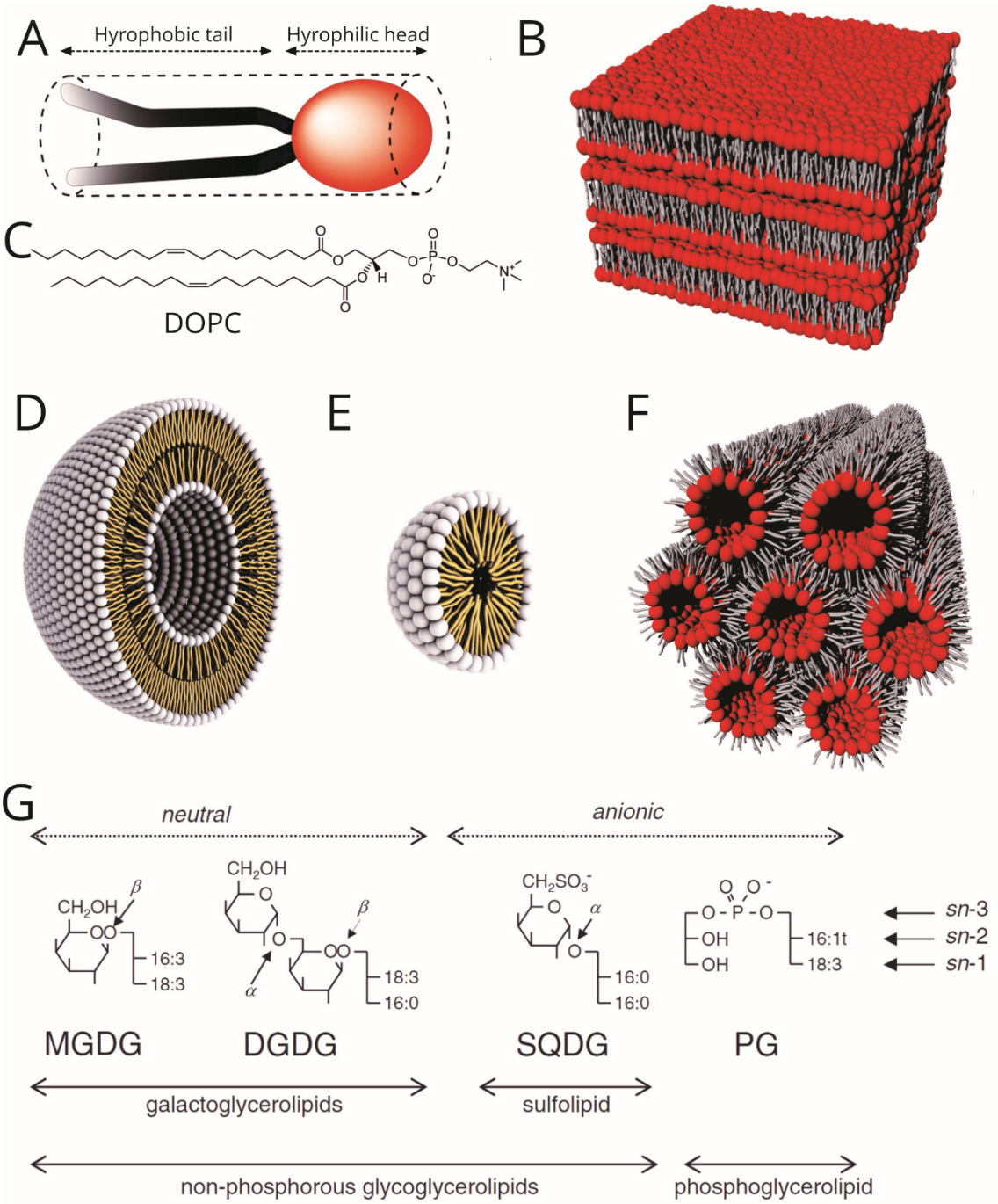

Figure 8 Chemical structures of lipids and possible self-assembled structures

(A) Cartoon of a lipid molecule with equal head and tail width, (B) Cartoon of stacks of lipid bilayers, (C) Chemical structure of DOPC, (D) Cartoon of a single membrane liposome (E) Cartoon of a lipid micelle, (F) Cartoon of an inverse-hexagonal arranged lipids, (G) Chemical structures of common thylakoid lipids. (A,B,F) Adapted from Tresset (2009), (D,E) adapted from Bitounis et al. (2012), (G) adapted from Boudiere et al. (2014).

1.2.2 Model lipid bilayers and membrane protein reconstitution

In natural systems lipid bilayers are often densely packed with proteins which have crucial biological functions such as trans-membrane transport, molecular synthesis and signalling (Blankenship, 2014). In photosynthetic thylakoid bilayers, membrane proteins such as those involved in solar energy capture (introduced in section 1.1.1), are estimated to make up ~70 % of membrane surface area (Daum and Kühlbrandt, 2011). The large number of proteins performing a multitude of functions in biological membranes make it extremely difficult to study the properties of the lipid bilayer itself or any specific protein in the system. To effectively study the properties of lipids and/or membrane proteins in a controlled environment, model lipid membranes can be formed in vitro. Lipid bilayers, most often in the form of small liposomes of ~100 nm in diameter, can be prepared from specific lipids arranged into nanoscale assemblies which are stable in aqueous solutions. This is often achieved by the gradual hydration of lipids dried onto a surface (Nogueira et al., 2015),through disrupting aggregates of liposomes in solution by applying a force through sonication (Shashi et al., 2012), or by solubilising lipids into detergent micelles and gently removing the detergent (Ollivon et al., 2000). All of these methods involve breaking up any preformed aggregates of lipids and allowing self-assembly into the simple structures of planar bilayers. Model lipid bilayers can also be deposited onto surfaces, most commonly by the adsorption of pre-formed liposomes onto hydrophilic substrates. Supported lipid bilayers (SLBs) are a form of planar lipid bilayer on such a solid substrate, and have advantage of a far larger flat area than liposomes (10-100s of microns), long term stability, and the capacity to be studied via microscopy techniques. Supported lipid bilayers can be formed onto solid surfaces such as glass or mica or onto other complex surfaces such as polymer cushions to limit lipid-surface interactions (Richter et al., 2006). Lipid dyes are often utilised in both liposomes and supported lipid bilayers, allowing these bilayers to be labelled and also be environmentally sensitive to changes in local conditions (Demchenko et al., 2009). Dyes are often directly covalently tagged to lipid head or tail groups which will either freely diffuse laterally in the bilayer or be localised to specific lipid types or phases (Kaiser et al., 2009). Dyes can also be tagged to hydrophobic molecules which will sit in the membranes hydrophobic envelope between the fatty acid tails.

Model lipid bilayers can also be used as a platform to study proteins and their function. Such "proteoliposomes" can be studied in solution and can also be deposited onto surfaces to form supported lipid-protein bilayers. Many membrane proteins are solubilised into detergent micelles during the isolation procedure from their natural membranes. When forming proteoliposomes detergent must be removed to allow reconstitution of the proteins into lipid bilayers, which is often done by rapidly diluting the solution to lower detergent concentration or by the gradual removal of detergent by porous polystyrene beads (Liguori et al., 2015). This reduces the concentration of detergent in solution below the CMC causing micelles to disassociate, and the membrane proteins will then reconstitute into lipid bilayers to minimise free energy by removing their hydrophobic regions from contact with the aqueous solution. Proteoliposomes can be used to study the effect of in-membrane protein aggregation (Crisafi and Pandit, 2017), changes in environmental conditions (Yang et al., 2006), and even utilise differences in chemical conditions on the interior and exterior of the liposome (Li et al., 2017). One potential issue with the use of proteoliposomes is the interactions that may occur between many proteins reconstituted within the bilayer, which complicate specific functions being measured; this can be especially challenging when studying proteins with known conformational and functionality changes related to aggregation (Moya et al., 2001). Lipid nanodiscs have been developed in order to study individual membrane proteins independently of protein-protein interactions. These amphiphilic scaffold proteins form discs of defined radius which can encapsulate a section of lipid bilayer and a single membrane protein, so that measurements on truly isolated membrane proteins reconstituted into their native membrane environment are possible (Rouck et al., 2017).

A suite of photosynthetic proteins have been incorporated into model lipid membranes, such as proteoliposomes, in order to study them in a near native lipid environment from both bacterial (Swainsbury et al., 2018), and plant systems (Bhaduri et al., 2019). LHCII and PSII have been co-reconstituted into proteoliposomes in order to quantify the enhancing effect of LHCII to PSII energy transfer by observing the increase in PSII oxygen evolution with the incorporation of the antenna protein (Zhou et al., 2009). PSII and ATP synthase have also been co-reconstituted into proteoliposomes in order to create an 'artificial chloroplast' where the cross-membrane proton gradient produced by PSII in the water splitting reaction is used to drive ATP synthase in an in vitro system (Feng et al., 2016). The deposition of proteoliposomes onto solid surfaces as supported lipid

bilayers allows the effect of different lipid compositions on the stacking of membranes containing photosynthetic protein to be studied (Seiwert et al., 2017). It also allows physical measurements such as single molecule force spectroscopy to be performed on proteins and reveal the stabilising effects of different lipids (Seiwert et al., 2018). LHCII aggregation is known to be a driving force in the process of non-photochemical quenching, and LHCII reconstitution into proteoliposomes is an established method of studying both the effect of different lipids and of protein aggregation on the photophysical properties of the protein (Tutkus et al., 2018). The closeness of in-membrane LHCII-LHCII interactions can be mediated by altering the lipid: protein ratio in proteoliposomes, which reveals a gradual change of the system towards an energy dissipative state LHCII-LHCII interactions are increased (Crisafi and Pandit, 2017, Natali et al., 2016) Lipid nanodiscs are able to provide a membrane environment with minimal LHCII-LHCII interactions, resulting in a significant reduction in the quenching of LHCII fluorescence and further enforcing the idea that the dissipative state is strongly related to aggregation (Crisafi and Pandit, 2017, Natali et al., 2016, Pandit et al., 2011). The minimised dissipative pathways of LHCII reconstituted into nanodiscs also allow the inter-chromophore photo-physics of energy transfer in the non-quenched system to be investigated using ultrafast spectroscopy techniques (Son et al., 2020).

1.3 Bio-hybrid light harvesting systems

1.3.1 Using photosynthetic proteins in nanotechnology for light-harvesting

While the overall solar energy conversion efficiency of a photosynthetic system from absorbed photons to biomass is typically between 1-3 %, ~1 % in crops(Zhu et al., 2010), and up to 3 % in cyanobacteria farm reactors, specific processes such as photon absorption and energy transfer within and between light-harvesting (LH) proteins are over 95 % efficient (Blankenship et al., 2011). Light-harvesting complexes may have potential future industrial applications due to their perspective as components in renewable energy systems. Rooftop photovoltaic solar cells are typically 10-20 % efficient, with a theoretical upper limit of 47.7 % (Hanna and Nozik, 2006), significantly lower than the

absorption and energy transfer efficiency of a photosynthetic protein such as LHCII under optimal conditions.

It has been demonstrated that LHCII antenna proteins can be nano-patterned onto glass surfaces and retain high photon absorptivity and fluorescence properties (Vasilev et al., 2014). These nano-patterns have also been shown to be capable of long range energy propagation with bacterial LH antenna proteins proving that inter-protein energy transfer is retained in a non-native environment (Escalante et al., 2010). It has also been shown that it is possible for light-harvesting complexes to retain at least a portion of their ability to transfer exciton energy to other synthetic exciton acceptors to produce electrical current. An energy transfer efficiency of up to 32 % from incident photons to excited electrons has been achieved by depositing a densely packed monolayer of LHCII-PSII supercomplexes from photosynthetic bacteria onto gold electrodes. Here, the complexes were self-assembled onto electrodes using the Langmuir-Blodgett deposition method to achieve consistent orientation. The light-driven electron transfer in PSI was then utilised to produce photocurrent through the electrode under illumination (Kamran et al., 2014). Depositing multiple layers of plant PSI proteins onto electrodes has shown that the photochemical activity of the protein increases linearly with the number of layers deposited (Figure 9 (A+B)). This means that the natural photosynthetic strategy of increasing effective photon absorption by multiple layers of light-harvesting proteins, such as in the thylakoid grana, can be applied to bio-hybrid light-harvesting devices. The increased absorption of the multilayers was also shown to translate to a proportional increase in photo-current produced under illumination (Ciesielski et al., 2010). Another effective method of depositing high concentrations of photosynthetic proteins onto surfaces has been the use of columnar titanium dioxide nano-pillars (Figure 9 (C)). Here, depositing PSI directly onto these nano-pillars yields effective a fourfold increase in produced electrical current when under visible light illumination. The use of nanostructures such as nano-pillars significantly increases the surface area which proteins can be deposited onto a surface (Henson et al., 2013).

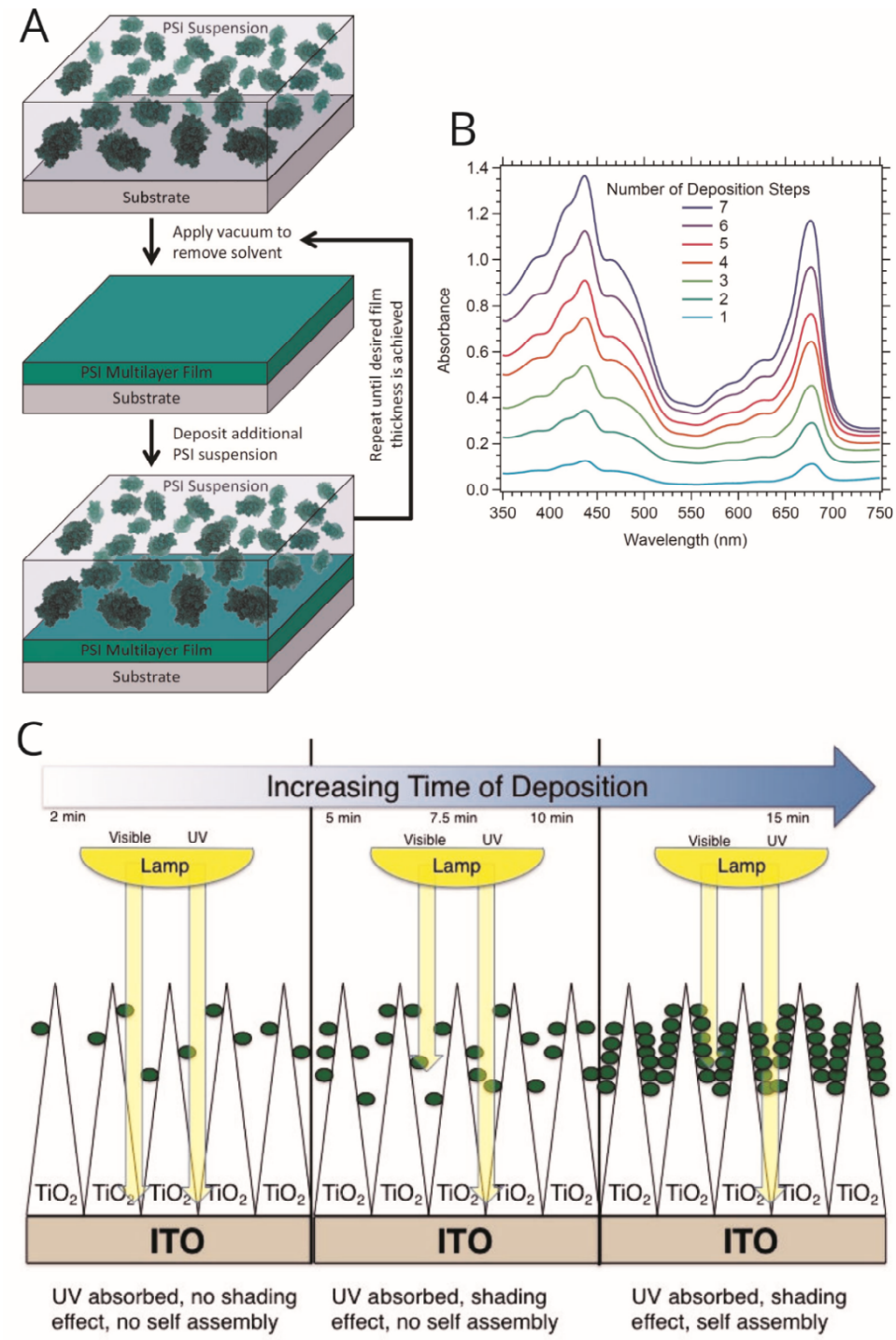

Figure 9 Example of bio-hybrid light-harvesting devices

(A) Schematic of PSI multilayers being formed onto substrates, (B) Absorption of PSI multilayers, (A+B) adapted from Ciesielski et al. (2010) (C) Schematic of deposition of PSI protein (green) onto TiO_2 nano-pillars, adapted from Henson et al. (2013) © [2013] IEEE.

1.3.2 Artificially increasing the efficiency of photosynthetic systems

Light-harvesting proteins only efficiently absorb a fraction of the solar irradiation that reaches the Earth's surface, due to the limited spectral range of the particular complement of pigments which are incorporated into the light-harvesting antenna and photosystem proteins in both bacterial and plant photosynthetic systems (Blankenship et al., 2011). LHCII has a characteristic 'green gap' of minimal absorption between 500 - 600 nm, which corresponds to the highest intensity of solar irradiation not being utilised for photochemistry. This gap of absorption efficiency is present in all chlorophyll based photosynthetic proteins. One of the most promising aspects of bio-hybrid light-harvesting research is the concept of increasing the amount of energy that the photosynthetic system can take up by increasing their effective absorption cross section over the wavelengths of minimal natural absorption. This is often done by attempting to fill the aforementioned 'green gap' with pigments which absorb in this range and can effectively transfer energy to chlorophyll molecules. This gap is sometimes filled by natural photosynthetic organisms in extreme environments. For example, light with wavelengths of above 600 nm cannot penetrate to depths of over 10 m of water due to scattering effects, so for cyanobacteria living at these depths the 'green gap' between 500-600 nm is a huge limitation to their overall absorbance. These organisms often have an abundance of red pigments capable of absorbing in the 500-600 nm range and transferring their energy to the lower energy chlorophyll *a* and *b* molecules (Croce and van Amerongen, 2014).

The first instance of artificially attempting to fill the 'green gap' of LHCII trimers was done by site-specific covalent attachment of one Rhodamine Red dye per monomer. The dyes added an absorption peak at 573nm to the modified LHCII absorption spectra, as shown in Figure 10 (A), partially filling the green gap of natural minimal absorption. When the combined LHCII-dye system was excited at the excitation wavelength of the dye, and minimal absorption of LHCII, the fluorescence emission of the dye was almost completely quenched and the fluorescence emission of the LHCII more than twofold increased. The concomitant reduction in Rhodamine Red fluorescence emission intensity and increase in LHCII intensity confirmed that energy was being successfully transferred from the covalent attached dye to the LHCII, and manifesting as 'extra' excitation energy (Gundlach et al., 2009). This enhancement of effective protein absorption has also been

achieved using the light-harvesting complexes from purple bacteria, both isolated in detergent (Yoneda et al., 2015), and then reconstituted into bilayers (Yoneda et al., 2020b).

The covalent attachment of Alexa647 dye to bacterial LH2 monomers at a ratio of 9: 1 resulted in a significantly enhanced absorption range of the combined system as shown in Figure 10 (B). In this study both the efficiency and ultra-fast photophilic energy transfer were investigated. The quenching of donor fluorescence emission intensity and excited state lifetime revealed that ~85 % of energy absorbed by the additional dye is transferred to the protein. Transient absorption spectroscopy shows that the timescales of energy transfer from additional synthetic dyes are in the range of 440 fs to 23 ps. This is on a similar timescale to the 700 fs timescale of energy transfer between natural pigments in the LH2, showing that additional synthetic chromophores can emulate the role of natural pigments (Yoneda et al., 2015). A method of further enhancing the effective absorption range of photosynthetic systems is to use multiple additional dyes. Bio-hybrid analogues of bacterial LH2 monomers, formed of two α-helices and a single bacteriochlorophyll *a* molecule, can be spectrally enhanced by the covalent attachment of several different dyes (Figure 10 (C)). These monomers then self-assemble in solution to form oligomers analogous to LH2 complexes. Figure 10 (E) shows the absorption of the bacteriochlorophyll *a* containing oligomers with different additional chromophores labelled BC1, 2 and 3. A combination of these monomers can be used to create a heterogeneous oligomer with the combined absorption enhancement of the three different addition dyes, a schematic of this combination is shown in Figure 10 (D) and the combined spectra in Figure 10 (F) (Harris et al., 2014a, Harris et al., 2013). In vivo covalent attachment is not the only method of directly interfacing complementary pigments with light-harvesting proteins. It has been demonstrated that complementary yellow fluorescent protein (YFP) can be genetically encoded with a cluster of genes which produce a hybrid bacterial reaction centre with enhanced absorption as shown in Figure 10 (G+H). This has been shown to directly improve the growth rate of bacterial cultures with direct YFP to reaction centre energy transfer observed through transient absorption spectroscopy on isolated YFP/RC complexes (Grayson et al., 2017).

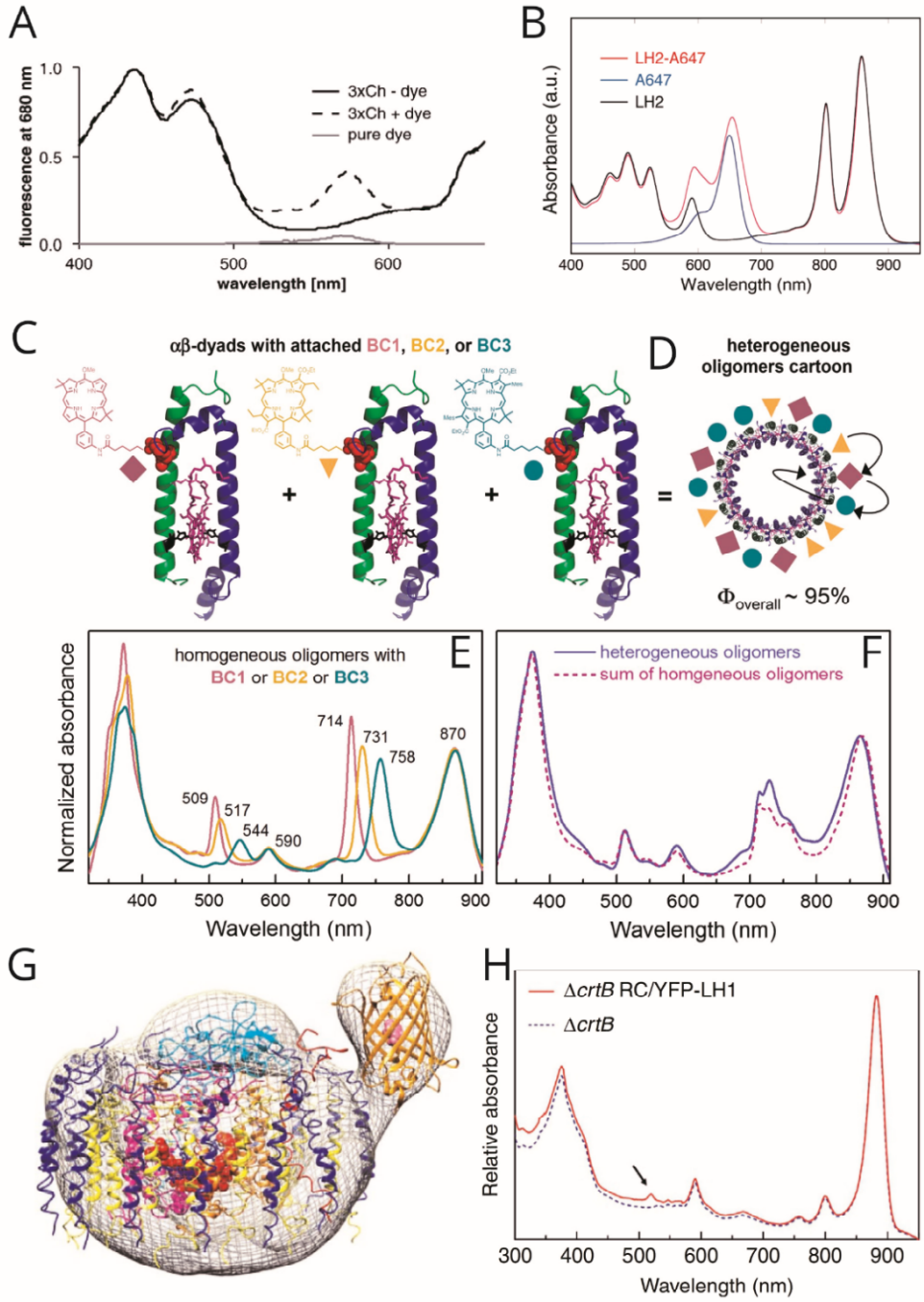

Figure 10 Example spectra and structures of pigment enhanced photosynthetic light-harvesting proteins

(A) Selective LHCII fluorescence excitation spectra of: isolated LHCII monomers (solid black line), isolated Rhodamine Red dye (solid grey line), LHCII-Rhodamine Red complex (dashed grey line) adapted from Gundlach et al. (2009). (B) Absorbance spectra of: isolated bacterial LH2 (solid black line), isolated Alexa647 dye (solid blue line), LH2-Alexa647 complex (solid red line) adapted from Yoneda et al. (2015). (C) Structure of bio-hybrid light-harvesting subunits containing

bacteriochlorophyll *a* (purple) with different additional dyes (purple, orange and green). (D) Top-down view of heterogeneous oligomer formed of self-assembled subunits. (E) Absorption spectra of homogenous oligomers formed from single types of light-harvesting subunits. (F) Absorption spectra of heterogeneous oligomers formed from multiple types of types of light-harvesting subunits. (C-F) Adapted from Harris et al. (2014a) (G) Reconstructed structure of YFP-LH1-RC complex, electron density is shown as grey mesh, LH1 units (blue + yellow), RC special pair (red). The low resolution structure of the complex shows YFP attached to the side of the circular LH/RC complex (gold). (H) Absorbance of LH/RC complex (black solid line) and YFP-LH/RC complex (red solid line). Adapted from Grayson et al. (2017).

The effective enhancement of absorption has been shown to directly result in an increase of photochemistry. Individual detergent-isolated bacterial LH2 reaction centres with five bio-conjugated AE_{800} dyes were found to have increased overall photosynthetic activity by 30 % with energy transfer efficiency via FRET quantified to be 62 % when excited in the region of natural minimal absorption compared to LH2 only samples (Hassan Omar et al., 2016). Following reconstitution of LH1 reaction centres into lipid bilayers alongside dye-enhanced LH2 antenna, the addition of a covalently tagged ATTO647N dye to the antenna protein increased the effective absorption of the dye/protein system at 650 nm by 700 % compared to the natural protein. When excited at 650 nm there was a sevenfold increase in photocurrent generation across the membrane compared to the system without the addition dye. This observation suggests that all of the additional energy absorbed by the dye is effectively transferred to the LHC1 reaction centre to be used in photochemical reactions (Yoneda et al., 2020b). These studies show that the addition of complementary chromophores directly attached to the antenna proteins significantly increases the effective absorption of the system and subsequent photochemistry. An advantage of directly bonding a complementary fluorescent dye to a light-harvesting complex at a known position is that the dye is always close enough for FRET to take place. A disadvantage is that the covalent attachment of dyes is not very modular, with the synthesis of the complex-dye component needed for each combination of dye and photosynthetic protein by genetic modification (Grayson et al., 2017), or the addition of chemical cross-linkers (Yoneda et al., 2020b, Springer et al., 2012).

An alternative method of getting a complementary dye close enough to a photosynthetic pigment for FRET to occur, which does not involve binding them to one another, is by enclosing them in a matrix favourable for both components. Simple diblock copolymer micelles can be used to incorporate both photosynthetic bacteriochlorin chromophores and complementary BODIPY dyes in close enough proximity for FRET to occur. This is achieved by designing the co-polymer so that the chromophores each favourably entered one of the micelle phases. This effectively increased the bacteriochlorin absorption cross section in a system where both donor and acceptor concentration could be easily modulated. The use of polymer micelles also has the advantage of being able to be deposited onto a surface to create monolayers or bilayers and retain energy transfer (Adams et al., 2015a). Polymer micelles with associated complementary dyes have also been used to support full light-harvesting antenna proteins. Light-harvesting Complex 1 (LH1) from purple bacteria incorporated into a polymer micelle with free chromophores has been shown to have a FRET efficiency comparable to using covertly bound systems (Harris et al., 2014b). These polymers which associate specific chromophores are not restricted to encompassing single proteins in micelles but can also be used to encapsulate large volumes of photosynthetic material mimicking bacterial chromosomes (Orf et al., 2017, Collins et al., 2016). Another system that can be used to interface complementary chromophores with light-harvesting proteins, close enough to allow energy transfer via FRET, is proteoliposomes. It has been demonstrated that the compartmentation of chromophores into different areas of liposomes via self-assembly allows FRET to occur with up to 85 % efficiency without covalently bonding (Sahin et al., 2015). Another advantage of using liposomes is that multiple photosynthetic membrane proteins can be simultaneously reconstituted allowing multi-protein photosynthetic processes to take place (Yoneda et al., 2020b). Lipid bilayers can also be deposited onto substrates as multilayers and are permeable to electron transfer, which is a crucial component in potential light-harvesting applications (Heath et al., 2016).

1.4 Summary and motivation for this thesis

This introduction has reviewed the basics of photosynthesis and how it is optimised for extremely efficient energy capture over most of the visible spectrum. It has been demonstrated that the proteins which make up the photosynthetic electron transfer pathway can be utilised for bio-hybrid light-harvesting applications. They are very well adapted for these systems due to their natural ability to perform photon absorption and energy transfer with extremely high efficiency. Due to the natural limitation in the absorption range of photosynthetic proteins, caused by restraints in pigment composition, efforts have been made to enhance the effective absorption range of these proteins through the use of complementary chromophores. These spectrally complementary chromophores can be interfaced with photosynthetic proteins such that energy absorbed by the chromophores is transferred to the proteins via FRET. In this thesis, the concept of reconstituting lipid-tagged complementary chromophores alongside photosynthetic antenna proteins into model lipid membranes will be explored as a method of effectively enhancing the protein absorption range. This system takes advantage of self-assembly driven formation not requiring chemical or biological modifications to the protein, these modifications can be complex and have restrictions due to the number of potential binding sites. The system is also highly modular with the potential to be adapted with different photosynthetic proteins and corresponding complementary dyes. A membrane-based system also has the benefit of being amenable to surfaces, an essential property for any future device-based applications. The development of this method will be vital for furthering the field of artificially enhanced light-harvesting proteins, potentially leading to advances in renewable energy systems.

2 Experimental Procedures and Theory

2.1 Materials and aqueous buffer preparation

2.1.1 Materials

All solvents and chemical solids were purchased from Sigma-Aldrich, UK. Solvents were BioUlta analytical grade or higher, chemical solids were HPLC grade or higher, unless otherwise stated.

2.1.2 Standard buffers

All buffers were prepared as stock solutions, typically 1 M, by weighing solids to ±1 mg accuracy and dissolving in ultrapure water. All water used was deionized and filtered by a milli-Q water purification system. Buffers were purified through 0.22 μm filters before use and typically stored at 4 °C. pH buffers were prepared to be within 0.1 of the intended final pH by the dropwise addition of 1-10 M hydrochloric acid or sodium hydroxide. All growth media and glassware used for bacterial growth were autoclaved for at least 20 minutes and allowed to cool before use.

2.2 Protein Biochemistry

2.2.1 LHCII isolation and purification

Trimeric LHCII complexes were biochemically purified directly from plant material (spinach) using a previously established procedure for isolating photosynthetic light harvesting proteins from thylakoid membranes and solubilising in detergent (Adams et al., 2018). 400 g of spinach leaves (purchased from a local supermarket) were macerated in 400 ml of ice-cold buffer A (300 mM sucrose, 5 mM EDTA, 50 mM HEPES, pH 7.5) using a high power pre-cooled blender. Liquid was then filtered through a double layer of muslin cloth followed by filtering through a second double layer sandwiching a ~1 cm layer of cotton wool. ~ 350 ml of liquid was recovered and centrifuged at 3000 g for 20 minutes at 4 °C to collect chloroplasts as a pellet, and the supernatant was discarded. The pellet was resuspended in 25 ml of buffer B using a soft paintbrush (5 mM EDTA, 10

mM Tricine pH 7.4) and osmotically lyzed by adding an equal volume of buffer C (400 mM sucrose, 5 mM EDTA, 10 mM Tricine, pH 7.4). The lyzed chloroplasts were then centrifuged at 3000 g for 15 minutes at 4 °C to collect thylakoid membranes as pellet, and the supernatant was discarded. The thylakoid membranes were then washed by re-suspending the thylakoid pellet in a series of buffers and re-centrifuging at 3000 g for 20 minutes at 4 °C. Two washes were performed re-suspending the pellet in 35 ml of high EDTA buffer D (50 mM EDTA, 20 mM HEPES pH 8.0) followed by two more washes in 35 ml of high NaBr buffer E (2 M NaBr, 20 mM HEPES pH 8.0). Isolated thylakoid membranes were adjusted to 0.5 mg Chl/mL in a buffer F (20 mM HEPES pH 8.0) and then solubilized with 0.5 % (w/v) detergent n-dodecyl α-D-maltoside (α-DDM ≥99 % purity. Anagrade High Alpha, Generon) for 1 hour on ice mixing every 15 minutes. Thylakoid membrane proteins were then loaded onto freshly poured 8 -13 % continuous sucrose density gradients in a buffer in buffer G (20 mM HEPES pH 7.5, 0.03 % α-DDM, 8-13 % w/w sucrose) and ultracentrifuge at 100,000 g for 36 hr, 4 °C. 2 ml of α-DDM - solubilized thylakoids were loaded onto each 32 ml sucrose gradient (in disposable SW32 tubes from Beckman Coulter). The dense green band of LHCII trimers in the centre of gradient was then collected and concentrated using a 30 kDa Amicon Ultra centrifugal filter (Merck Millipore, UK).

LHCII trimers were further purified using high-resolution size exclusion chromatography, concentrated protein was loaded onto a 16/600 Superdex 200 prep grade column on an refrigerated (4 °C) AKTA Prime FPLC system (GE Healthcare Life Sciences, PA, USA) in the buffer 150 mM NaCl, 0.03 % α-DDM, 20 mM HEPES (pH 7.5). After pooling the appropriate eluted fractions and concentrating using Amicon centrifugal filters, LHCII trimers were at a concentration of approx. 100 nM (corresponding to an absorbance of ~20 at 675 nm), as estimated by absorption spectroscopy as described in 2.4.2, in buffer of 20 mM HEPES (pH 7.5) and estimated 0.3 % α-DDM. SDS-PAGE and Native-PAGE was used to confirm protein purity and oligomerisation state.

2.2.2 Lipid nanodisc scaffold protein production and purification

The ApoE422k membrane scaffold protein was purified directly from the plasmid pD451-SR provided by collaborators (Son et al., 2020). The plasmid included genes encoding a fusion of the nanodisc peptide to a model protein, Thioredoxin-ApoE422k (termed the "full length fusion protein") tagged with 6x Histidine residues, and a kanamycin antibiotic resistance gene. 1 µL of the plasmid was injected into a 50 µL vial of *E. coli* LB21 cells, which was then heat shocked using a water bath at 42 °C for 42 seconds before being incubated on ice for five minutes. The cells were then added to 950 µL of LB broth (for 1 L: ultrapure water, 10 g Tryptone, 5 g yeast extract, 10 g NaCl, autoclaved before use) and incubated a in a 200 ml conical flask at 37 °C and 150 rpm for one hour. This was then spread onto agar plates to allow colonies to grow. Three plates are prepared in parallel. (i) Positive control: LB21 cells without plasmid + LB agar without Kanamycin (antibacterial) (ii) Negative control LB21 cells without plasmid + LB agar with Kanamycin (antibacterial) (iii) Transformation: B21 cells with plasmid + LB agar with Kanamycin (antibacterial). Plates were inverted and incubated at 37 °C overnight and colonies appeared in the positive control and transformation plates. To increase the number of cells for freezing a higher volume culture was grown. One colony from the transformation plate was added to 5 ml of LB broth (with x1 Kanamycin) and incubated in a 15 ml Falcon tube at 37 °C and 150 rpm overnight. Cells were then spun down at 12500 g for 5 minutes to collect cell pellet. This pellet was suspended in the same volume of 100 % glycerol and flash frozen in liquid nitrogen for storage at – 80 °C.

A 50 ml starter culture was grown overnight at in a 200 ml conical flask at 37 °C and 150 rpm using a small amount of frozen cells from a stock, and prepared as described above, in LB buffer with 1x kanamycin. The starter culture was then split into eight 2 L conical beakers containing 500 ml TB broth each (for 1L: ultrapure water, 12.5 g Tryptone, 24 g yeast extract, 4 g glycerol, 2.31 g KH_2PO_4, 12.55 g K_2HPO_4, autoclaved before use) and incubated at 37 °C and 150 rpm. The absorbance of the TB buffer was checked every 30 minutes until it reached an optical density of 0.6-0.8 (~2-3 hours). IPTG was added to induce overexpression of the Thioredoxin-ApoE422k protein. After further growth (~5 hours) cells were spun down at 6000 g for 20 minutes at 4 °C to collect the cell pellet. Cells were resuspended in 20 mM TRIS, pH 8.0, 50 mM NaCl, 40 mM imidazole and an

EDTA free protease inhibitor tablet added. Cells were lyzed by two passes through a multi-shot cell disruptor at 30 kpsi. (Constant Systems, UK) Disrupted cells were and spun down at 30000 g for 30 minutes to remove any debris, then the supernatant containing the protein Thioredoxin-ApoE422k was collected.

The supernatant of disrupted cells was then purified through a Ni-NTA affinity column to remove any non-His tagged material leaving only Thioredoxin-ApoE422k fusion proteins. The Ni-NTA affinity column (5ml HisTrap HP, GE Healthcare Life Sciences, USA) was attached to an AKTA (GE Healthcare Life Sciences, USA) controlled flow protein purification system. Columns were washed with 25 ml of ultrapure water and 25 ml of 20 mM TRIS (pH 8.0), 0.5 M NaCl, 40 mM imidazole at 5 ml/min before use. The supernatant was loaded onto the column at 2.5 ml/min. The column was then washed with 50 ml of 20 mM TRIS (pH 8.0), 0.5 M NaCl, 40 mM imidazole at 5 ml/min to remove any unbound material. The column was then eluted with 25 ml of 20 mM TRIS (pH 8.0), 0.5 M NaCl, 400 mM imidazole at 2.5 ml/min to remove His-tagged samples from the column. The eluted sample was collected with a fraction collector so that fractions containing the protein (as indicated by increased UV absorption trace) could be selected. Proteins were then incubated overnight with the cleaving enzyme Thrombin (x2 tablets) (T7513 Thrombin from Bovine Plasma, Sigma-Aldrich, USA) which separated Thioredoxin and ApoE422k components of the full-length protein. The cleaved Thioredoxin and ApoE422k mixture is then passed again through a Ni-NTA affinity column, exactly the same protocol as above, removing the Thioredoxin and leaving only the His-tagged ApoE422k. The protein was dialysed into 20 mM HEPES (pH 7.5), 150 mM NaCl using 10K MWCO dialysis cassettes (Thermo Scientific, USA) to remove any residual elution buffer from Ni-NTA purification. Protein concentration was then assessed using absorbance at 280 nm (extinction coefficient ε = 30940 M^{-1} cm^{-1}) and by SDS-PAGE before being frozen in liquid nitrogen and stored at -80°C for use when forming nanodiscs. This protocol was adapted from Morrow et al. (1999).

2.2.3 Gel electrophoresis of protein samples

Protein purity was assessed via denaturing SDS-PAGE with Coomassie (Coomassie(r) Brilliant Blue, Bio-Rad, USA) or Sypro Ruby (SYPRO Ruby Protein Gel Stain, Bio-Rad, USA) staining using pre-made gels (NuPAGE Novex 12 % Bis-Tris, ThermoFisher Scientific, USA). Samples were solubilised in LDS (NuPAGE® LDS Sample Buffer (4X), ThermoFisher Scientific, USA) for 1 hour before being loaded onto gels with a pre-stained protein ladder (Precision Plus Protein Dual Colour Standards, BioRad, USA). A running buffer of x1 MES was used for both anode and cathode chambers. (NuPAGE® MES SDS Running Buffer, ThermoFisher Scientific, USA).

Protein oligomeric state was assessed via non-denaturing Clear Native PAGE with Coomassie staining using pre-made gels (NativePAGE Novex 4–16 % Bis-Tris, respectively, ThermoFisher Scientific, USA) and pre-stained protein ladder (Precision Plus Protein Dual Colour Standards, BioRad, CA, USA). A running buffer of x1 native buffer (NativePAGE running buffer, ThermoFisher Scientific, USA) was used for anode and cathode chambers with additional 0.02 % α-DDM (α-DDM ≥99 % purity. Anagrade High Alpha, Generon) in cathode chamber.

2.3 Formation of model lipid membranes

2.3.1 Lipid preparation and storage

Plant thylakoid lipids monogalactosyldiacylglycerol (MGDG), digalactosyldiacylglycerol (DGDG), sulphoquinovosyldiacylglycerol (SQDG) and L-α-phosphatidylglycerol (Soy PG), and the synthetic lipid 1,2-dioleoyl-sn-glycero-3-phosphocholine (DOPC) were purchased from Avanti Polar Lipids as lyophilized solids (received as ampules sealed under dry nitrogen). The lipid mixture used for lipid nanodisc formation was Asolectin lipid extract from soybeans (Soy Asolectin), which was purchased from Sigma-Aldrich in a dry granulated form. The fluorescently-tagged lipid Texas Red 1,2-dihexadecanoyl-sn-glycero-3-phosphoethanolamine (TR-DHPE) was purchased as a solid from Life Technologies (Invitrogen). Lipid mixtures were prepared by solubilising dry lipids with a 2:1 chloroform: methanol and mixing to obtain the

desired ratios and final mass for sample formation. TR-DHPE was dissolved in chloroform and added as required to aliquots of lipid mixture before drying. Solubilised lipids were then subsequently dried under dry nitrogen gas flow for 40 minutes and then placed in vacuum desiccator for 3-16 hours to remove any residual traces of solvents (room temperature, in the dark). Lipid aliquots were then either used immediately or stored under argon gas at -80 °C until use. Single use glass vials were used throughout when working with lipids in organic solvents.

Our standard thylakoid lipid mixture used for proteoliposome samples contained 35 % MGDG, 20 % DGDG, 12 % SQDG, 8 % Soy PG and 25 % DOPC (% wt/wt), adapted from Grab et al., (2016). The lipid mixture known as Soy Asolectin was used for all nanodisc samples due to previous reports of it providing excellent stability to reconstituted LHCII in lipid nanodiscs (Son et al., 2020) .

2.3.2 Liposomes

Aliquots of dry lipid mixture are solubilised in a buffer solution of 20 mM HEPES (pH 7.5) 40 mM NaCl to reach a final lipid concentration of 1 mM. This is achieved by a combination of vortex mixing and bath sonication until there is no visible lipid film in the vial and the solution is semi-translucent (cloudy). The lipid solution is then loaded into a temperature-controlled glass sample holder (pre-cooled to 4 °C) and tip sonicated for 20 minutes at 20 % power (Sonifier 250, Branson, USA) to form small unilamellar vesicles. Samples are then centrifuged at 10,000 g for three minutes to remove any titanium residue from the sonicator tip before being transferred into fresh vials and used for characterisation.

2.3.3 Proteoliposomes

Aliquots of dry thylakoid lipid mixture (Grab mix as prepared above) were solubilised with 0.5 % α-DDM, 20 mM HEPES (pH 7.5) at room temperature for approx. 12-16 hours with agitation via a pinwheel rotator to generate a mixed micellar lipid-DDM solution (approx. 9:1 molar ratio of detergent-to-lipid). For example, typically 0.4 mL of this buffer would be added to 1 mg DOPC to give approx. 2.5 mM DOPC and 22 mM DDM

in final volume of 0.4 mL (lower masses of thylakoid lipids were often used due to their cost and a lower final volume). The starting protein-lipid-detergent suspension was prepared in plastic microfuge tubes by mixing calculated volumes of the following: the pre-solubilized lipid-DDM suspension, aqueous buffers, and purified LHCII trimers to a final concentration of: 1 mM total lipid, 0.2 % α-DDM, 20 mM HEPES (pH 7.5), 40 mM NaCl and the desired LHCII concentration. The desired LHCII concentration is achieved by calculating the volume of isolated LHCII trimers required to reach a defined lipid-to-protein (mol/mol) ratio for each sample (with molar concentration of lipids calculated from known masses and molecular weights and LHCII protein concentration determined from absorption as stated above). The lipid-DDM-protein mixture was then incubated with Bio-Beads SM-2 Adsorbents (Bio-Rad) to gradually remove the detergent and allow proteoliposome formation via self-assembly, as follows: four incubation cycles with increasing quantities of fresh Bio-Beads (8 mg/mL, 20 mg/mL and 40 mg/mL and 100 mg/mL) for 90 min, 90 min, 90 min, and ~16 hours, respectively. Proteoliposome samples were prepared in parallel, typically in sets of 5 to 7 samples, stored in the dark at 4 °C when not in use, and diluted samples from these immediately were characterised by ensemble spectroscopies (within 16 hours) and by microscopies (within 24-72 hours). Sample volumes were varied based on the required quantity of material needed (generally governed by the characterisation to be performed), typically volumes of 300-500 μL were used to allow good mixing of BioBeads in the detergent removal stage and provide enough volume to be diluted for both cuvette based spectroscopy and microscopy. Samples were diluted by the desired factor for the characterization method, typically using a buffer solution of 20 mM HEPES (pH 7.5) 40 mM NaCl, unless any other additives were required.

2.3.4 Lipid nanodiscs

Aliquots of dry lipid mixture were brought to room temperature and re-solubilised overnight in an α-DDM detergent solution (20 mM HEPES (pH 7.5), 100 mM NaCl, 0.5 % α-DDM) to solubilise lipids into detergent micelles. ApoE422k monomers, detergent solubilised lipids and LHCII trimers were mixed in a 12.5: 3000: 1 ratio and incubated while shaking at 4°C for one hour. Initial sample volumes were prepared to achieve a final lipid concentration of 4.8 mM. Absorbent Bio Beads were then added to samples (2/3 sample volume) and incubated for a further hour to remove detergent and allow lipid

LHCII nanodiscs to self-assemble. Nanodisc samples were then purified through a Ni-NTA affinity column (5ml HisTrap HP, GE Healthcare Life Sciences, USA) using an AKTA (GE Healthcare Life Sciences, USA) controlled flow protein purification system to remove any sample that was not incorporated into the His-tagged nanodiscs. Columns were washed with 25 ml of ultrapure water and 25 ml of 20 mM HEPES (pH 7.5), 0.5 M NaCl 40 mM imidazole at 5 ml/min before use. Samples were diluted to a final volume of 10 ml in a buffer of 20 mM HEPES (pH 7.5) 0.5 M NaCl 40 mM imidazole before being loaded onto the column at 2.5 ml/min. The column was then washed with 50 ml of 20 mM HEPES (pH 7.5), 0.5 M NaCl, 40 mM imidazole at 5 ml/min to remove any unbound material. The column was then eluted with 25 ml of 20 mM HEPES (pH 7.5), 0.5 M NaCl, 400 mM imidazole at 2.5 ml/min to remove His-tagged samples from the column. The eluted sample was collected with a fraction collector so that fractions containing nanodiscs (as indicated by colour and increased UV absorption trace) could be selected. The selected fractions were then dialysed against 5 L of 20 mM HEPES (pH 7.5), 100 mM NaCl for 3 hours total with two buffer changes, using either 10K MWCO dialysis cassettes (Thermo Scientific, USA) or 10K MWCO dialysis tubing (Generon, UK) to remove any residual elution buffer from Ni-NTA purification before further characterisation. Samples were prepared at a range of volumes depending on the characterisation being performed, 500 μL samples were prepared for cuvette-based absorption and fluorescence spectroscopy while volumes of up to 3 ml were required for transient absorption measurements.

2.4 Optical spectroscopy

2.4.1 General theory and use of cuvettes

Optical spectroscopy techniques study the interaction of light with matter such as absorption, reflection, and fluorescence. Spectroscopic techniques were extensively used in this research to characterise the absorption and fluorescence properties of biological and synthetic chromophores in solution. Chromophores are investigated both when isolated in solution and when reconstituted into nanomaterials such as proteoliposomes or lipid nanodiscs. For most spectroscopic techniques' samples must be suspended in

solution in a clear sided sample holder or 'cuvette' to allow light to initially interact with the sample and then be collected and measured.

Before all cuvette based optical spectroscopy measurements, proteoliposome samples were diluted in a buffer of 40 mM NaCl, 20 mM HEPES (pH 7.5), and nanodisc samples in a buffer of 100 mM NaCl, 20 mM HEPES (pH 7.5), to obtain a volume of 3 ml for use in a 10 x10 mm quartz cuvette (Hellma). All samples were diluted to obtain a low enough absorbance (≤0.1) to avoid inner filter effects where light emitted from one chromophore may be reabsorbed by another before detection (Yuan and Walt, 1957).

2.4.2 Absorption spectroscopy

Theory

Absorption spectroscopy is a steady-state technique which measures how much light is absorbed by a sample at a particular wavelength. Chromophores and systems made up of many chromophores, such as light-harvesting proteins, often have complex absorption spectra due to different absorption efficiencies at different wavelengths. Changes in a chromophore local environment, such as charge, solvent or interactions with other chromophores, often manifest as changes in the absorption spectra that can be measured with absorption spectroscopy. The absorbance of a sample is proportional to the concentration in accordance with the Beer-Lambert law, meaning that the concentration of a sample can be calculated from its absorbance if the extinction coefficient (constant relating chromophore concentration and absorption) and path length of light through the sample are known.

$$\boldsymbol{A = \varepsilon l c}$$

Equation 10 Beer-Lambert law relating, A: Sample absorbance, Ɛ: Molar extinction coefficient of relevant component, l: optical path length of absorption spectroscopy measurement, c: Molar concentration of relevant component.

An absorption spectrometer uses a white light lamp with a wide wavelength range to create an initial beam of light. This then passes through an adjustable monochromator which utilises concave mirrors and a diffraction grating to produce light centred at a specific wavelength; this beam will have a controllable 'slit width' which defines the wavelength range of light produced. The beam will pass through the sample to a detector

which the wavelength is iteratively changed through a pre-defined range allowing the amount of light transmitted to the detector, and therefore absorbed by the sample, at each wavelength to be determined. To take into account the absorption of the cuvette and solution the sample is suspended in a 'blank' measurement must be taken of the solution and cuvette without the sample. This can be done with a parallel cuvette and beam-splitter or a 'matched' cuvette as used for the sample measurement. This measurement of 'blank' absorption is subtracted from the sample measurement to provide a spectra of the sample absorption only.

Instrumentation and typical parameters

All cuvette-based absorption spectroscopy for proteoliposomes and nanodisc samples was performed using an Agilent Technologies Cary 5000 UV-Vis-NIR absorption spectrophotometer equipped with an "integrating sphere" (also called a Diffuse Reflectance Accessory, Agilent) to remove any minor scattering effects. Absorption scans were taken with a wavelength range of 380-800 nm, 0.5 nm step size, 0.5 s dwell time. 'Blank' measurements of the absorption of buffer-only samples to be automatically subtracted from sample absorption spectra were made before each set of measurements were taken. New 'blank' measurements were made each time there was a buffer change in samples being characterised.

2.4.3 Steady state fluorescence spectroscopy

Theory

Steady-state fluorescence spectroscopy is a technique used to determine the level of fluorescence emission from a sample at a particular wavelength after excitation at another wavelength. Typically there are two kinds of steady-state fluorescence measurements that can be made with a standard fluorescence spectrometer:

1) Fluorescence emission spectroscopy: samples are excited at a constant wavelength while the emission at different wavelengths is measured. This produces an "emission spectrum".
2) Fluorescence excitation spectroscopy: emission is collected at a set wavelength while the excitation wavelength is changed. This produces an "excitation spectrum".

In a fluorescence spectrometer a white light lamp with a wide wavelength range is used to create an initial beam of light. This beam is then passed through an adjustable monochromator which produces a beam of light centred at a specific wavelength to excite the sample. This excitation beam will have a 'slit width' with defines the range wavelengths in the beam that exits the slit. This light will be directed towards the sample, often though an iris which can open or close to mediate beam intensity, where it will interact with the sample. Fluorescence emission from the sample is then collected at 90° from the excitation beam. The emission beam passes through a second adjustable monochromator which will allow a defined wavelength range, again with a defined emission 'slit width', to reach a detector that records the fluorescence intensity of the sample for those specific excitation and emission wavelengths. Typically the excitation or emission monochromator is kept at one wavelength while the other scans through a predefined range to measure emission or excitation spectra respectively.

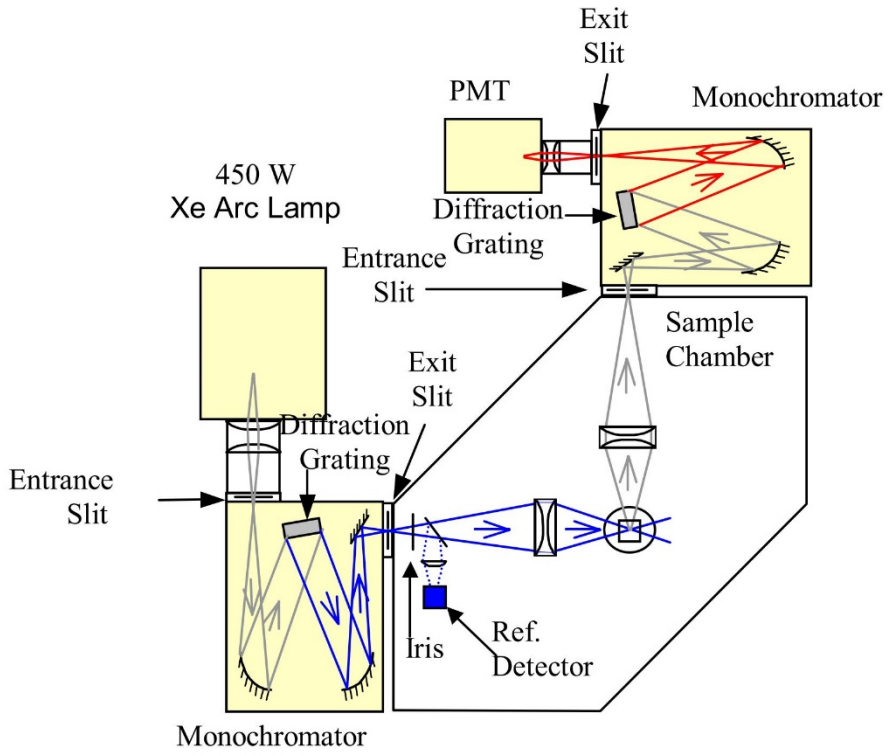

Figure 11 Fluorescence spectrometer schematic, adapted from Edinburgh Instruments FLS980 fluorescence spectrophotometer manual

Instrumentation and typical parameters

All cuvette-based steady-state fluorescence spectroscopy on proteoliposomes and nanodiscs was performed using an Edinburgh Instruments FLS980 fluorescence spectrophotometer equipped with dual excitation monochromators and dual emission monochromators. Samples were maintained at 20 °C and gently stirred at 500-1000 rpm during all measurements using a thermoelectrically-cooled cuvette-holder with magnetic stirring capabilities (Quantum Northwest TC 1 Temperature Controller). A 450W Xenon arc lamp was used for excitation and a red-sensitive-PMT for detection (Hamamatsu R928 PMT). Emission scans with selective excitation of LHCII were acquired with excitation at 473 nm, collecting emission between 500-800 nm (2 nm and 1 nm bandwidth excitation and emission slits, respectively). Emission scans with selective excitation of Texas Red were acquired with excitation at 540 nm, collecting emission between 550-800 nm (1 nm bandwidth for both excitation and emission slits). Data acquisition parameters were 0.5 nm steps, integrating 0.1 s/ step and five scans averaged for all samples. LHCII fluorescence excitation measurements were acquired with emission collected at 686 nm scanning over the excitation range of 380-380 nm (1 nm and 2 nm

bandwidth excitation and emission slits, respectively. Data acquisition parameters were 1 nm steps, integrating 0.1 s/ step and a single scan for all samples. All ensemble spectroscopy data were further analysed in Origin Pro (v.9) graphing software.

2.4.4 Time correlated single photon counting (TCSPC)

Theory

Time correlated single photon counting (TCSPC) is a spectroscopic technique used to determine the average fluorescence lifetime of chromophores. Samples are excited by a high-frequency pulsed laser at a set wavelength. At the time of the initial pulse an effective 'stopwatch' is started which, through fast electronics and photomultiplier detector, will record the time between initial pulse and emission of the sample. A very large number of events results in large numbers of measured delays between the initial excitation and emission being recorded, which are used to build up a histogram. The histogram produced will have the shape of an exponential decay with the frequency density of each bin relating to the probability of recording emission at that time after initial excitation. The time with maximum probability of emission after excitation, and therefore peak maximum, is normally shortly after excitation as most chromophores are in the excited state and most likely to fluoresce. The experiment is stopped when the maximum reaches a pre-defined number of counts. The curve can be described as the sum of exponential decays with the number of time constants depending on the system being measured. The amplitude-weighted average time constant (τ_{av}) for a sample is the typically quoted fluorescence lifetime. This is calculated by taking each of the time constants (τ_i) of a multi-component fit and averaging them with each component weighted in accordance with its associated amplitude (β_i). The fluorescence lifetime of a sample represents the stability of the excited state under the measurement conditions, specifically that τ_{av} represents the time required for the excited state population to decrease to 1/e (~37 % of the maximum population).

$$I = \sum_i \beta_i e^{-\frac{t}{\tau_i}}$$

Equation 11 Sum of exponential decays: I: Intensity, β_i: Amplitude of component (1 if single exponential decay), τ_i: Time constant, t: Time

TCSPC are often made on the exact same instrument as steady-state fluorescence measurements as previously described, aside from the excitation source of a pulsed laser being required. As the laser is at very narrow set wavelength range (FWHM typically ~1 nm) then the excitation monochromator is not required to select excitation wavelength. Emission is collected at a set wavelength bandwidth using the emission monochromator and slits.

Instrumentation and typical parameters

Fluorescence lifetime measurements on LHCII in detergent, proteoliposomes and in nanodiscs were made using an Edinburgh Instruments FLS980 fluorescence spectrophotometer. Samples were maintained at 20 °C and gently stirred during all measurements using a thermoelectrically-cooled cuvette-holder with magnetic stirring capabilities (Quantum Northwest TC 1 Temperature Controller). A 473 nm pulsed diode laser (EPL-475, Edinburgh Instruments, pulse width of ~100 ps) was used for selective excitation of LHCII, collecting emission at 681 nm with 10 nm bandwidth emission slits. A laser repetition rate of 0.5 MHz was always used. A dedicated high-speed red-sensitive PMT was used for detection (Hamamatsu H10720-20 PMT). A built-in neutral density (ND) filter wheel was applied to the pulsed laser for LHCII lifetime measurements to set excitation power as desired, an average power of approximately 1.5 μW for LHCII (pulse energy of 3.0 pJ). Control measurements for excitation power versus fluorescence lifetime showed that singlet-singlet annihilation effects are likely to be avoided using these settings. Decay curves from the Edinburgh FLS980 system were fitting using the manufacturer's supplied software. The instrument response function (IRF) was determined by measuring scattered excitation light using a dilute solution of colloidal silica (Ludox, MilliporeSigma) and has a width of ~270 ps.

Fluorescence lifetime measurements on Texas Red in solvents, detergent, proteoliposomes and in nanodiscs were made using a Horiba PTI Quantamaster 8000 fluorescence spectrometer equipped with a higher power supercontinuum 75 W excitation laser (pulse width of ~100 ps). This was because the 560 nm laser on the Edinburgh system was an LED (rather than a "true" laser source) which had relatively low power and relatively broader pulse so we found that the Quantamaster produced higher quality data. Samples were maintained at 20 °C and gently stirred during all measurements using a thermoelectrically-cooled cuvette-holder with magnetic stirring capabilities (Quantum

Northwest TC 1 Temperature Controller). Here the acquisition parameters were: 0.5 MHz laser repetition rate, excitation set to 540 nm (1 nm slit) and emission collected at 610 nm (5 nm slit) with a dedicated PPD-900 PMT detector. Decay curves from the Edinburgh FLS980 system were fitting using open source DecayFit TCSPC analysis software. The instrument response function (IRF) was determined by measuring scattered excitation light using a dilute solution of colloidal silica (Ludox, MilliporeSigma) and has a width of ~225 ps.

2.4.5 Time resolved fluorescence spectra

Theory

Time-resolved fluorescence spectra (TRFS) are conceptually the same as time-correlated single photo counting (TCSPC) measurements which have been described in 2.4.4. The difference with TRFS measurements is the addition of an interferometer to collect the emission beam which is capable of determining the wavelength of detected photons. This allows a TRFS map to be produced which both wavelength and emission time information for samples.

Instrumentation and typical parameters

TRFS measurements were made using a home-built spectroscopy setup by our collaborators in the group of Prof. Gabriela Schlau-Cohen (MIT, USA), which is described here. The excitation source was generated by coupling the output of a Ti:sapphire oscillator (MaiTai BB, SpectraPhysics; centred at 800 nm, 80 MHz repetition rate, pulse width ~80 fs) into a nonlinear photonic crystal fibre (FemtoWhite 800, NKT Photonics), and then passing the generated white light through a bandpass filter (ET550/15x, Chroma) to selectively excite Texas Red. The excitation beam was focused into a 100 μm spot on a 1 cm path length quartz cuvette containing the sample at an optical density of 0.08 per cm at 550 nm. The emission from the sample was detected by a single-photon-detecting avalanche photodiode (PDM Series, Micro Photon Devices), and the arrival time of each photon was recorded by a timing module (PicoHarp 300, PicoQuant, Inc.). Two different emission filters were used to selectively monitor the fluorescence of

the Texas Red (Em1: 560–600 nm; RPE560LP, Omega and FES0600, Thorlabs) and LHCII (Em2: >665 nm; BLP01-647R-25, Semrock).

The data were measured in two different modes. Individual fluorescence decay traces presented were measured by integrating the fluorescence signal over each emission wavelength range (Em1 or Em2) for a higher signal-to-noise ratio. Spectrally-resolved fluorescence data were obtained with spectral interferometry (Gemini, NIREOS), and then Fourier transformed to yield the time-resolved fluorescence spectra (TRFS). For TRFS measurements, a long pass emission filter (RPE560LP, Thorlabs) was used. The resolution of the wavelength axis was 0.7 nm. The interferometer was combined with the timing module described above to give fluorescence decay traces at each wavelength.

The excitation power was 30 fJ for all three samples. The experiment was repeated at 10 fJ and 100 fJ, and no power dependence was observed. The instrument response function (IRF) was determined by measuring scattered excitation light using a dilute solution of colloidal silica (Ludox, MilliporeSigma), and has a width of 50 ps. Fluorescence decay traces were fitted with a mono- or bi-exponential function using iterative re-convolution with the IRF.

Note on contributions: all TRFS data were collected and analysed by my collaborators Minjung Son and Dr Muath Nairat from the group of Gabriela Schlau-Cohen, Department of Chemistry, MIT, USA. All samples were prepared and initially characterised by AMH before shipping.

2.4.6 Transient absorption spectroscopy

Theory

Transient absorption spectroscopy is an ultrafast spectroscopy technique used to determine the excited state of systems and energy transfer by measuring changes in a sample's absorption at the picosecond timescale. The Pauli Exclusion Principle states that two identical fermions cannot exist in the same quantum state in a single system, which is the reason why two electrons cannot share the same excited state (Tipler and Mosca, 2007). If a molecule is in an excited state due to photon absorption and is then excited

again by another photon it will not interact in the same manner as the first, due to an electron not being able to enter the same excited state as the first. Transient absorption spectroscopy uses this principle to determine changes in the excited state of a system at very short timescales (Berera et al., 2009).

Samples are excited by an initial 'pump' pulse which measures the absorption of the sample and puts molecules into an excited state. A second 'probe' pulse then measures the absorption of the sample again after a defined delay. The pump and probe pulses are normally from the same initial laser diode pulse which is split with a beam splitter, a mechanical delay stage is then used to extend the path length of the 'probe' pulse before it is directed onto the sample. The change in absorbance of the sample between the 'pump' and 'pulse' pulses is calculated as in Equation 12, the ΔAbs value therefore gives information about the state of the system at different times directly after the initial excitation.

$$\Delta \boldsymbol{Abs} = \boldsymbol{Absorbance}\ (\boldsymbol{After\ probe}) - \boldsymbol{Absorbance}\ (\boldsymbol{After\ pump})$$

Equation 12 ΔAbs calculated from absorption before and after pump pulse.

The difference in the absorption, or ΔAbs, at different pump/probe intervals and wavelengths are used to produce TA maps which contain information on the excited state of a system. There are two main components of transient absorption spectra which produce a negative ΔAbs signal. (i) Ground state bleaching reduces the ΔAbs due to molecules being excited by the initial pump pulse; fewer molecules in the ground state mean that the probe pulse cannot be absorbed as effectively as the pump. (ii) Stimulated emission signal is caused by the probe pulse interacting with molecules already in the excited state due to the initial pump, which causes a photon to be emitted at the same wavelength of the incident photon and is observed as reduced absorption or negative ΔAbs. Both ground state bleaching and stimulated emission are directly caused by molecules being in an excited state and produce a negative ΔAbs signal. Therefore, the negative ΔAbs signal indicates when samples are in an excited state, and when plotted against time can indicate the decay and transfer of excited states.

Instrumentation and typical parameters

Transient absorption spectroscopy measurements were made using a home-built spectroscopy setup by our collaborators in the group of Prof. Gabriela Schlau-Cohen (MIT, USA). The setup of this custom system is described here. The pump and probe pulses were produced by white light generation by focusing the output of a Ti:sapphire regenerative amplifier (Libra, Coherent; centred at 800 nm, 5 kHz repetition rate) into a chamber filled with pressurized argon gas at 20 psi. The residual fundamental and near-infrared region of the white light were filtered out with the combination of a dichroic mirror (DMSP805, Thorlabs) and a bandpass filter (FGS600, Thorlabs). For preferential excitation of Texas Red, the pump pulse was further passed through a bandpass filter (FES0600, Thorlabs), and resulted in the spectrum shown in Figure 12(A). With this pump spectrum, we estimate a 20.5 % direct excitation of the higher vibronic bands of chlorophyll Qx/Qy states in LHCII. The spectrally filtered pulses were compressed with chirped mirrors (PC70, Ultrafast Innovations). The temporal width of the pump pulse was measured to be 26 fs by autocorrelation (Figure 12(B)), and the dispersion in the probe was corrected for after data collection. The pump and probe pulses were focused into a 150 μm spot on a 1 mm path length quartz cuvette containing the sample at an optical density of 0.25/mm at the absorption peak. The pump pulse was modulated with a chopper at 2.5 kHz, and the change in probe intensity was collected shot by shot at 5 kHz with a linear CCD (Aviiva EM4-BA8, e2v Imaging). The excitation power was 6 nJ, which corresponds to 2.26×10^{13} photons per pulse per cm^2, previously reported to be in the linear regime. The sample was continuously recirculated with a peristaltic pump to prevent photo-degradation and repetitive excitation of the same spot. The sample reservoir was kept at 4°C throughout the measurement. Global analysis of the transient absorption data was performed using the Glotaran software.

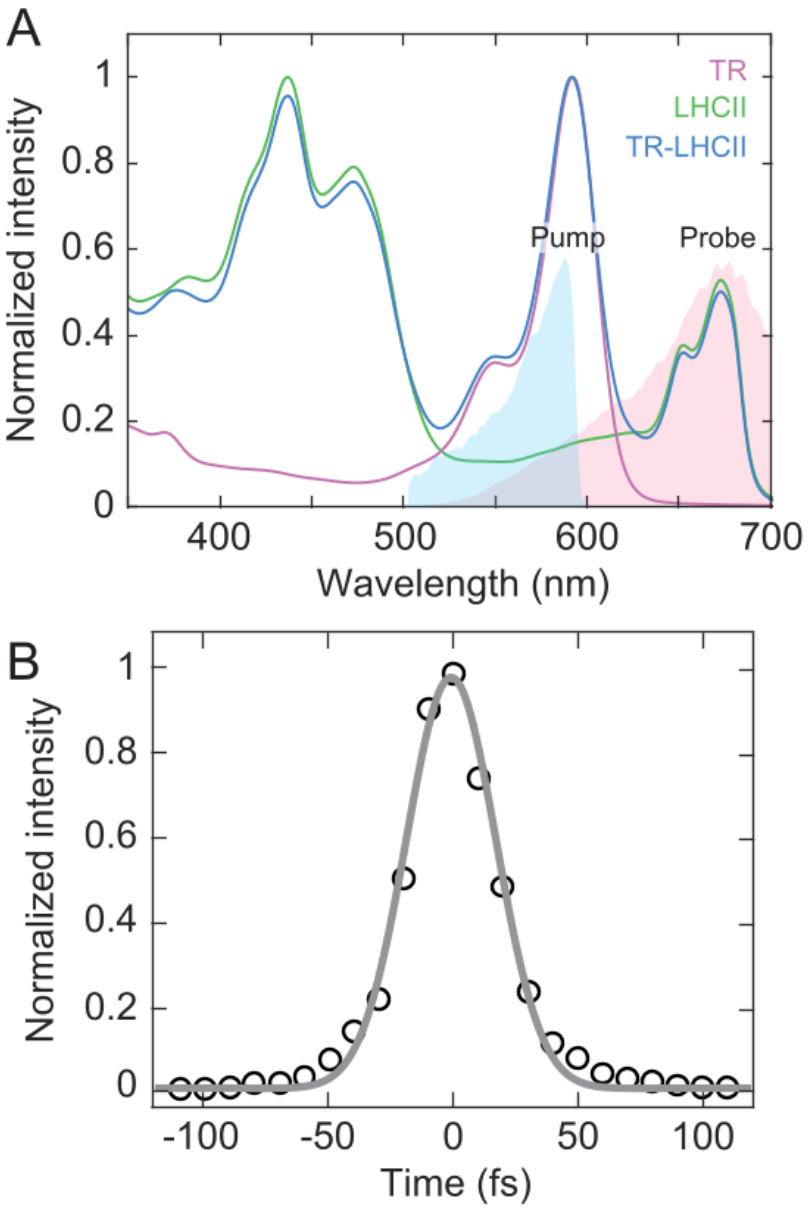

Figure 12 Experimental conditions for transient absorption spectroscopy measurements

(A) Pump/probe wavelengths for transient absorption spectroscopy measurements. The steady-state absorption spectra of the samples are overlaid (TR: Texas Red). (B) Autocorrelation trace showing the width of pump probe. This figure was produced by my collaborator Minjung Son, Department of Chemistry, MIT, USA.

Note on contributions: all TRFS data were collected and analysed by my collaborators Minjung Son and Dr Muath Nairat from the group of Gabriela Schlau-Cohen, Department of Chemistry, MIT, USA. All samples were prepared and initially characterised by AMH before shipping.

2.5 Fluorescence microscopy

Preparation of substrates and adsorption of samples for fluorescence microscopy

Substrates used for florescence microscopy were glass coverslips 50 x 25 mm (#1.5 thickness). These were always cleaned and made hydrophilic by "piranha cleaning": incubation in a 3:7 mixture of sulphuric acid (H_2SO_4) and hydrogen peroxide (H_2O_2) for 40 min, rinsed with ultrapure water ten times and subsequently stored in ultrapure water at room temperature. Glass coverslips were used within 5 days of cleaning, by carefully removing from the water with clean tweezers and drying with nitrogen gas. Hydrophobic ultrathin adhesive imaging spacers (0.12 mm depth, 9 mm diameter) were immediately attached to dry substrates, to create small wells to confine a droplet of buffer (Electron Microscopy Sciences, Hatfield, PA), for an open sample setup to allow multiple buffer exchanges. Samples were incubated with the glass within 2 minutes of drying the substrate.

Proteoliposome samples (~1 mM initial lipid concentration with various amount of additional reconstituted Texas Red DHPE and LHCII) were diluted using a buffer of 10 mM MES (pH 6.0) 150 mM NaCl and incubated with clean glass for 30 minutes in the dark (lower pH buffer was used here during membrane adsorption in an attempt to promote interactions with the highly electronegative glass). A 1/5 dilution was typically used when we were aiming for high density of surface-attached particles and a 1/50 for low density. Samples were then washed with seven changes of 10 mM MES (pH 6.0) 150 mM NaCl buffer in order to remove any loosely associated membranes, before being washed a final time with three changes of 20 mM HEPES (pH 7.5) 20 mM NaCl to keep imaging conditions consistent with spectroscopy, returning the pH to the standard 7.5.

2.5.1 Epifluorescence microscopy

Theory

Epifluorescence microscopy is a form of microscopy where excitation light illuminates a sample at an angle of 90° from the surface and emission is collected along the same path as the excitation. Fluorescence microscopes can be used to image different fluorescence components by having selective excitation and emission filters which control the wavelengths of excitation light that reaches the sample and the wavelengths of emission light collected, respectively. The excitation and emission filters are paired with a dichroic mirror, which will reflect shorter wavelengths and transmit longer ones with a defined cut off, to form a 'filter cube'. The dichroic cut off is typically designed to separate excitation and emission wavelength. Filter cubes are designed to excite and collect emission from a specific chromophore or group of chromophores with similar spectroscopic properties.

In a typical epifluorescence microscopy system, a white light lamp with a wide wavelength range provides a beam of light. This beam initially passes through a mechanical aperture which can open and close to block the beam or mediate its width. The beam then passes through the excitation filter only allowing the desired excitation wavelengths through. This excitation beam is then reflected 90° towards to the sample by the dichroic mirror, through a magnifying objective, and onto the sample stage. The excitation light will cause fluorescence emission of chromophores in the sample; some of this emission will be at 180° to the emission and travel back through the objective. The emission light, which is above the cut off wavelength, will then travel though the dichroic mirror though a final emission filter and onto the CCD detector where an image is recorded.

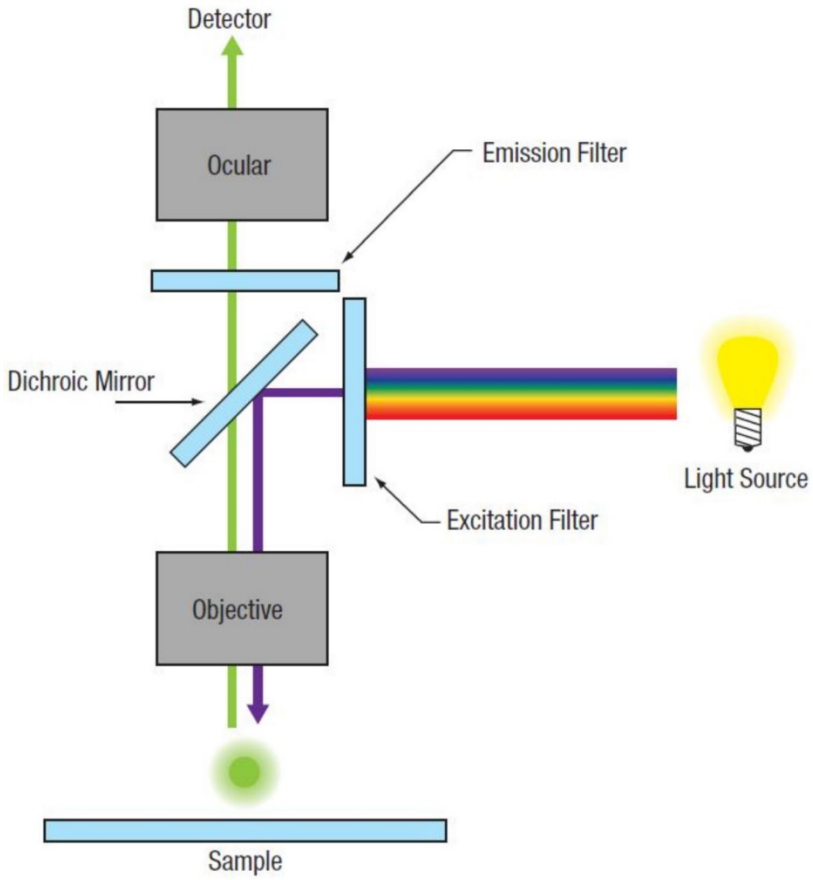

Figure 13 Fluorescence microscopy schematic. Adapted from ThorLabs user manual

Instrumentation and typical parameters

Epifluorescence microscopy was performed using a Nikon E600 microscope equipped with a Andor Zyla 4.2 sCMOS detector and appropriate filter cubes (LHCII cube: excitation 450-475 nm, dichroic 500 nm, emission 650-800 nm; Texas Red cube: excitation 540-580 nm, dichroic 595, emission 600-660 nm). Images were taken using a x40 air objective (NA 0.6), 1 s exposure and with appropriate ND filters inserted to maintain the maximum number of counts at a level for good detector signal-to-noise and linearity (10-75 % of detector saturation). Two-channel imaging (Texas Red + LHCII) of a field of view was performed sequentially by switching between cubes and ND filters as appropriate.

For photo-bleaching experiments, an aperture was inserted to expose an approx. 30 μm diameter region of the sample for a continuous period of 120 s through the LHCII filter cube at full power (i.e. no ND filters). During the bleaching, the aperture diameter was

increased incrementally by approx. 10 μm every 30 s to bleach multiple regions by different amounts. Subsequently, full-field images were acquired sequentially with LHCII and Texas Red filter cubes, to visualize the effect of photo-bleaching.

2.5.2 Fluorescence lifetime imaging microscopy (FLIM)

Theory

Fluorescence lifetime imaging microscopy (FLIM) is a microscopy technique which allows TCSPC fluorescence decay measurements to be taken on individual pixels to build up an image which contains information on both fluorescence intensity and lifetime. The system excitation is in the form of a pulsed laser, which passes through an excitation filter to select excitation wavelengths and a mechanical aperture before a magnifying objective that scans across the sample stage in a confocal manner. Emission from the sample then passes through a dichroic mirror which selects the desired emission wavelengths. The emission beam is then directed though an emission filter towards a single detector, or through a beam splitter and to two emission filters and detectors if two fluorescent components are being imaged. As the system uses pulsed lasers, two excitation sources can also be used. TCSPC measurements are made by tracking the time between each pulse of laser excitation and the emission collected by the detectors, building up decay curves for each chromophore being measured in each pixel, and allowing an image containing fluorescence lifetime information to be obtained.

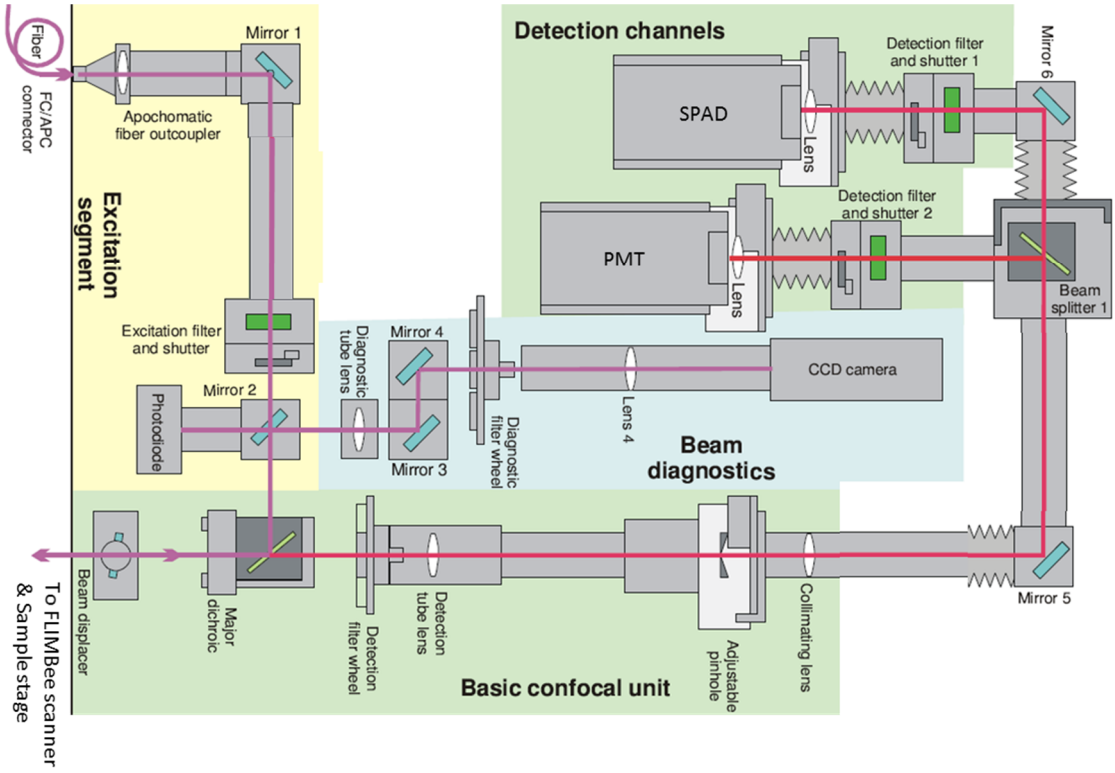

Figure 14 FLIM schematic, adapted from the PicoQuant FLIM manual

Instrumentation and typical parameters

FLIM measurements were performed on a "Microtime 200 time-resolved confocal fluorescence microscope" (PicoQuant GmbH). This system uses an Olympus IX73 inverted optical microscope effectively just as a sample holder, with light passing into and exciting various filter units for excitation, laser scanning and emission detection (as shown in Figure 14, with associated timing electronics. Excitation lasers were reflected toward the sample by a 488/561 (dual band) dichroic mirror. Prior to the dichroic mirror, a small portion of the beam is deflected towards a photodiode that provides an average power readout for the excitation source before the objective lens. The excitation beam is focused through a 100X oil objective (NA 1.4) (UPlanSApo, Olympus). For calculating excitation power, we estimate that there is ~85 % transmission efficiency at the excitation wavelengths of 485 nm and 561 nm.

The excitation sources, LDH 485 nm and LDH 561 nm laser heads (PicoQuant), were driven in Pulsed Interleaved Excitation (PIE) mode by a PDL 828 Sepia II burst generator module (PicoQuant) at a pulse rate of 10 MHz per laser (i.e. 20 MHz overall). The pulse widths for the LDH 485 nm and LDH 561 nm lasers were 90 ps and 70 ps respectively.

The voltage supplied to each laser was set at the minimum required to allow lasing and kept constant for all measurements (this maintains the shortest possible pulse FWHM and provides the best temporal resolution). Laser power was set to the desired output using a combination of neutral density filters and a micro blade cut-off that partially blocks the laser beam. An excitation fluence of 0.026 mJ/cm^2 was used in order to limit any damage to the samples; this value was selected after trailing a series of excitation powers on control samples.

Emission from the sample was passed through the same objective lens and dichroic mirror, towards a detection arm of the optical path. LHCII emission and Texas Red emission were separated by a 635LP filter in a beam splitter tower that directed the emission towards two detectors. Emission wavelengths shorter than 635 nm, were directed though a 620/60 emission filter before being detected by a hybrid Photomultiplier Tube (PMT) detector (PicoQuant). Emission wavelengths longer than 635 nm, were directed though a 690/70 emission filter before being detected by a Single Photon Avalanche Diode (SPAD) detector (PicoQuant). With this arrangement of detectors, the PMT was optimised to detect Texas Red emission, and SPAD detected emission from LHCII. Timing electronics were a time-correlated single photon counting (TCSPC) TimeHarp 260 module (PicoQuant).

The PIE beam was directed across the sample using a "FLIMBee" mirror-based galvanometer scanner (PicoQuant). FLIM measurements were generally taken for 256 x 256 pixels across a 25 x 25 μm field of view. The dwell time for each pixel was set to 25 μs, such that an entire frame was captured in 1.64 s, and 500 frames were accumulated for each field of view. Collecting the data in this manner allowed for the quantification of fluorophore bleaching, and the separation of frames into subgroups such that the lifetimes can be analysed at different times during the measurement. Analysis of fluorescence decay curves were performed using inbuilt fitting functions in the SymPhoTime software (PicoQuant GmbH) to fit a bi-exponential decay that was re-convoluted with measured Instrument Response Functions (IRFs). A good fit was confirmed when residuals were minimized, and Chi2 was <1.1.

Note on contributions: all FLIM data were collected by my colleague Sophie Meredith and data analysis was performed jointly.

2.6 Dynamic light scattering

Theory

Dynamic light scattering (DLS) is a light scattering technique used to assess the hydrodynamic radius of nanoscale to microscale particles suspended in solution. Particles in solution undergo random movement due to collisions with solute particles, movement that is termed 'Brownian motion'. The mean squared displacement of a particle from its original position over time is dependent on its diffusivity in a particular solution, as shown in Equation 13. Diffusivity is dependent on the size of the particle and the solute conditions as shown in Equation 14.

$$\overline{x^2} = 2Dt$$

Equation 13 $\overline{x}$: mean squared displacement, D: diffusivity, t: time

$$D = \frac{RT}{6\pi\eta r N_A}$$

Equation 14 D: Diffusivity, R: Ideal gas constant (8.314 J K^{-1} mol^{-1}), η: Solute viscosity, r: particle radius, N_A: Avogadro's number (6.022 x 10^{23})

Therefore, if the mean squared displacement of a particle over time is measured and the properties of the solvent are known then the particle radius can be determined.

In DLS a laser is used to measure the random motion of particles in solution. The laser passes through the sample and is scattered in all directions due to diffracting upon interaction with the particles, the diffracted light forms a speckle pattern which is measured by a CCD detector. As particles move in the sample the measured speckle pattern will change, which is measured at nanosecond intervals and autocorrelation function analyses can describe the rate of changes to the pattern. The autocorrelation function is a measure of the random movement of particles and can be used to calculate diffusivity and therefore particle radius.

Instrumentation and typical parameters

DLS measurements of proteoliposomes and nanodiscs were performed using a ZetaSizer Nano (Malvern, UK). When acquiring data on a sample set, DLS was typically performed after absorption and fluorescence spectroscopy measurements had been acquired, in standard sample buffers, using 80 µL polystyrene disposable cuvettes. Temperature was set to 20 °C and at least three independent DLS runs were performed for each sample.

2.7 Atomic force microscopy

Theory

Atomic force microscopy (AFM) is a form of scanning probe microscopy, an imaging technique which scans a probe over the surface of a sample to measure surface topography. In AFM samples are placed onto a piezoelectric motor driven sample stage which can translate the stage relative to the probe with sub-nanometer accuracy. The probe for AFM measurements is a spring-like cantilever which has a nanometer sharp tip on one side and is reflective on the other. A laser is aligned onto the top of the cantilever so that it reflects onto the centre of a four-quadrant photodetector. As the tip scans over the sample, or more commonly the sample scans relative to the stationary tip, the cantilever will be deflected by topological features keeping in contact with the surface. The cantilever deflection is measured by the changing position of the laser reflecting onto the photodetector. An electronic feedback loop allows the deflection of the cantilever to be taken into account as the sample is scanned, to adjust to large changes in the sample surface. A simplified schematic of an AFM is shown in Figure 15. There are two main modes of AFM, which are: (i) contact mode, where the cantilever is ‘dragged’ across the surface and remains in constant contact with the surface with tip deflection building up an image for surface topography. (ii) Tapping mode, where the cantilever is oscillated at high frequency as it scans over the surface close enough for interactions with the surface (electrostatic, Van der Waals, etc.) to affect the oscillation. As the distance between the oscillating cantilever and surface changes so will the frequency of oscillation, which is fed into a feedback loop, similar to tip deflection in contact mode, to build up an image. Due to the extremely small topological features being measured samples are deposited onto atomically flat surfaces.

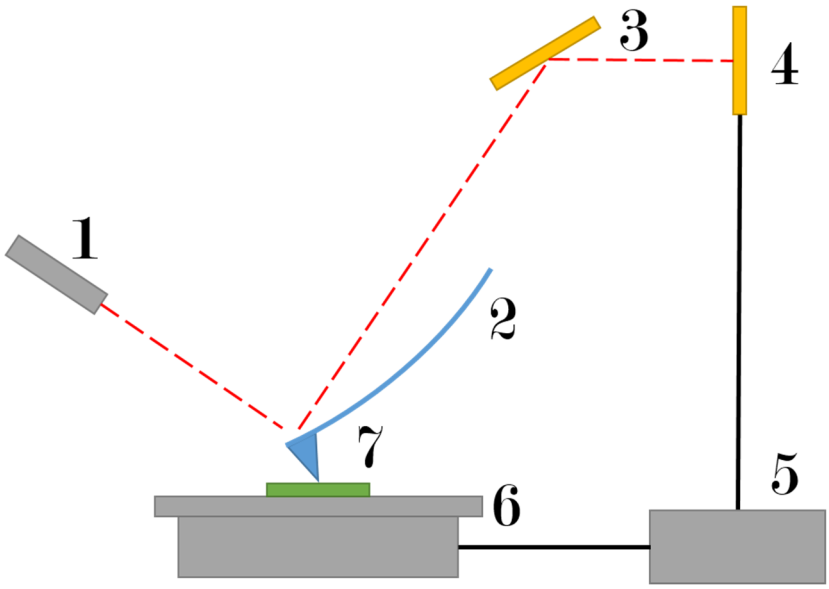

Figure 15 AFM Schematic.

1: Laser diode, 2: flexible cantilever, 3: mirror, 4: photodetector, 5: electronics and feedback control, 6: piezoelectric sample stage, 7: sample.

Instrumentation and typical parameters

Proteoliposomes samples were diluted to the desired concentring in a standard buffer of 20 mM HEPES (pH 7.5) 40 mM NaCl. Samples were deposited onto freshly cleaved atomically flat mica and allowed to incubate for 30 minutes before x10 exchange washes with buffer to remove any particles in solution not adhered to the surface. AFM was performed in liquid using a Bruker Dimension FastScan AFM with FastScan D probes (Bruker, USA) in tapping mode. Tapping amplitude, gains and scanning speed were adjusted during imaging to achieve minimal imaging forces and optimal resolution. Analysis was performed using Nanoscope Analysis software (v 1.9).

Note on contributions: All AFM data were collected by my supervisor Dr Peter Adams and analysed by AMH.

2.8 Transmission electron microscopy

Theory

Electron microscopy is a technique that allows imaging below the classical diffraction limit of optical microscopy by using electrons instead of photons. Visible light has a diffraction limit dependent on the wavelength of light used as defined by the Abbe limit (Equation 15) (Tipler and Mosca, 2007).

$$d = \frac{\lambda}{2\, n\, sin\theta}$$

Equation 15 Abbe limit for optical microscopy: (d) resolution limit, (λ) wavelength of light, (n) refractive index of medium, (θ) half the lens convergence angle

When using visible light (average wavelength 550 nm) for microscopy measurements the theoretical highest resolution which can be achieved is 275 nm (with an nsinθ value of 1.0). This is too large to resolve nanomaterials such as lipid nanodiscs which are on the order of tens of nm in diameter.

The wavelength of massive particles, such as electrons, is defined by the de Broglie wavelength (Equation 16) which inversely dependent on particle momentum (p).

$$\lambda = \frac{h}{p}$$

Equation 16 de Broglie wavelength for massive particles. (λ) de Broglie wavelength, (h) Plank's constant, (p) particle momentum

Electrons travelling with higher momentum have a shorter de Broglie wavelength, therefore microscopes capable of accelerating electrons to higher momentums have higher resolution. Modern electron microscopes are capable of achieving atomic resolution with diffraction limits of ~1 Å. Transmission electron microscopy is one of the main modes of electron microscopy. Electrons are accelerated across a set potential before being directed through an aperture and lenses onto the sample. The electrons will either scatter upon interaction with atomic nuclei in the sample or pass through the chamber though another set of lenses onto a CCD detector. The image is therefore made up by measuring lower levels of transmitted electron insanity due to scattering from interaction with the sample. Negative staining is a technique where samples are 'stained' with electron dense heavy metals, such as uranyl acetate, which will bind to nano structures

causing them to scatter more of the incident electron beam and give enhanced contrast in the final images (Boekema, 1991).

Instrumentation and typical parameters

Nanodisc samples were prepared as described above and diluted x 10 in a buffer of 20 mM HEPES (pH 7.5) 100 mM NaCl. 5.0 µL of diluted nanodisc sample was deposited onto glow discharge carbon grids and incubated for 30 s (Grids made in-house at the University of Leeds Astbury Centre EM Facility). Samples were then exchanged washed with 20 mM HEPES (pH 7.5) 100 mM NaCl and 5 µL of 1 % uranyl acetate was added for a further 30 s incubation. Sample and buffer were then removed from the carbon grid which was left at room temperate until completely air dry. TEM was performed using a FEI T12 transmission electron microscope (FEI Tecnai T12, USA) at a range of magnifications. Analysis of particle sizes was performed manually using ImageJ.

Note on contributions: All TEM data were collected by my colleague Damien Batchelor and analysed by AMH.

3 Results: Enhancing the Spectral Range of Light-Harvesting Proteins Using Lipid-Linked Chromophores

3.1 Motivation and Background

"Bio-hybrid" materials are those which combine synthetic and biological components and "bio-inspired" materials are those where biological principles may be applied to entirely synthetic or non-native systems. Such "bio-hybrid/ bio-inspired" nanomaterials have great potential for combining the most desirable aspects of biomolecules and the contemporary concepts of nanotechnology to create highly efficient light-harvesting materials. Biological light-harvesting proteins can be employed in devices for their high absorption efficiency to transfer energy to complex nanomaterials such as quantum dots (Werwie et al., 2012). Conversely, nanomaterials can be utilised to enhance the effective absorption of biological systems (Liu et al., 2015, Li et al., 2019). Light-harvesting proteins have the potential to be utilised for solar energy capture by interfacing them with surfaces to transfer absorbed energy to provide electrical current with an quantum yield comparable to that of photovoltaic devices (Kamran et al., 2014).

Light-harvesting proteins are optimized to absorb and transfer solar energy with remarkable efficiency but have a spectral range that is limited by their natural pigment composition. LHCII has a heterotrimeric structure with each monomer containing fourteen chlorophyll (shown in Figure 16 (D)) and four carotenoid molecules (Standfuss et al., 2005). This combination of pigments gives the protein complex a high absorption coverage across the visible spectrum aside from the 'green gap' of minimal absorption between 520–620 nm.

Several studies have 'filled' this green gap with complementary chromophores which absorb strongly in this spectral region and transfer energy to the chlorophyll within LHCII via Förster Resonance Energy Transfer (FRET). This was first demonstrated by covalently attaching chromophores to LH membrane proteins isolated in detergents, the

chosen chromophores including synthetic organic compounds (Gundlach et al., 2009, Harris et al., 2014a, Yoneda et al., 2015, Springer et al., 2012), and quantum dots (Schmitt et al., 2012, Werwie et al., 2012). FRET has also been demonstrated between non-covalently coupled chromophores incorporated into lipid bilayers (Sahin et al., 2015, De Leo et al., 2014, Lukashev et al., 2016), or polymer micelles (Adams et al., 2015a, Orf et al., 2017, Collins et al., 2016). LHCII has previously been integrated into model membranes, e.g., lipid vesicles (Tutkus et al., 2018, Moya et al., 2001, Natali et al., 2016, Seiwert et al., 2018, Zhou et al., 2009, Crisafi and Pandit, 2017), or lipid nanodiscs (Crisafi and Pandit, 2017, Pandit et al., 2011). These studies have been perform to understand the protein biophysical properties but have not been exploited to enhance its spectral range. Adding chromophores to the lipid membrane has several advantages compared to covalent modification of light-harvesting proteins: (i) lipids provide a more native environment for membrane proteins than detergent, (ii) membranes readily adsorb to hydrophilic solid supports so would be compatible with surface-based nanotechnologies, (iii) non-covalent systems allow greater flexibility to change the chromophore concentration (or type), (iv) membranes allow the potential to co-assemble other components to make for a modular system (e.g. other photosynthetic proteins or any small amphiphiles). This chapter presents the results of the development of model membranes ("proteoliposomes") in which the absorption range of the membrane protein Light-Harvesting Complex II (LHCII) is effectively enhanced by the addition of lipid-tagged Texas Red chromophores.

3.2 Experimental design: concept for interfacing LHCII with other dyes using lipid bilayers

The small organic chromophore Texas Red (Titus et al., 1982) was chosen as an ideal candidate for an energy donor to LHCII in membranes because of its complementary spectral properties, high extinction coefficient, and amenability to assemble into lipid bilayers by tethering it to a lipid head group (TR-DHPE, as purchased); its structure is shown in Figure 16 (F) (Adams et al., 2015b). The absorption of Texas Red is quite broad with a maximum at 591 nm (Figure 16 (A) – solid red) fitting well into the 'green gap' of minimal LHCII absorption (Figure 16 (A) – solid green). The TR fluorescence emission peak at 610 nm has extensive overlap with the LHCII Chl *b* absorption Figure 16 (A – dashed red), thus the excited state of TR is energetically close to chromophores within

the intended acceptor LHCII. The non-radiative energy transfer between donor and acceptor molecules can be described by Förster Resonance energy transfer (FRET) as discussed in detail in section 1.1.3. The Förster distance between donor and acceptor is the distance where energy transfer is 50 % efficient, defined in Equation 17, and is dependent on the spectral overlap (J – factor), relative orientation of donor and acceptor molecules (κ) and the refractive index of the optical medium (n) (Förster, 1965). The J factor is calculated from the overlap of Texas Red fluorescence emission and LHCII absorption as shown in Figure 16 (A) (Grey shaded area). Relative orientation of the transition dipoles of donor and acceptor molecules is assumed to be random, equating to a value of 2/3; this assumption is made as lipid-tagged Texas Red moves relative to the lipid it is tagged to in addition to the lipid diffusing freely in the bilayer relative to the reconstituted LHCII (Skaug et al., 2011). The refractive index (n) of the optical medium is assumed to be halfway between that of water (1.33) and lipid tails groups (1.55) (Sahin et al., 2015), with a value of 1.45. The Förster distance can be calculated for the system if the donor quantum yield (φ), 0.93 for Texas Red in ethanol (Lord et al., 2007), is taken into account using Equation 17 (the fluorescence of Texas Red in solvents vs liposomes is discussed in section 3.3.8). The Förster distance for Texas Red to LHCII energy transfer was calculated as 71.5 Å.

$$R_0^6 = 8.79\ x\ 10^{-5}\ J\ k^2\ n^{-4} \varphi Å$$

Equation 17 Calculated FRET R_0 for Texas Red to LHCII energy transfer

Therefore, high efficiency donor-to-acceptor FRET would be feasible if the chromophores can be arranged into close spatial proximity within proteoliposomes as shown in the concept schematic shown in Figure 16 (B). The effect of membrane reconstitution on energy transfer between Texas Red and LHCII is assessed by changes in absorption (solid lines in Figure 16 (A)), steady-state fluorescence emission (dashed lines in Figure 16 (A)) and time-resolved fluorescence (Figure 16 (C+E)) of LHCII and Texas Red in proteoliposomes. In this chapter, energy transfer between lipid-tagged Texas Red and LHCII in proteoliposomes is quantified by forming a range of proteoliposome samples with ranges of LHCII and Texas Red concentrations.

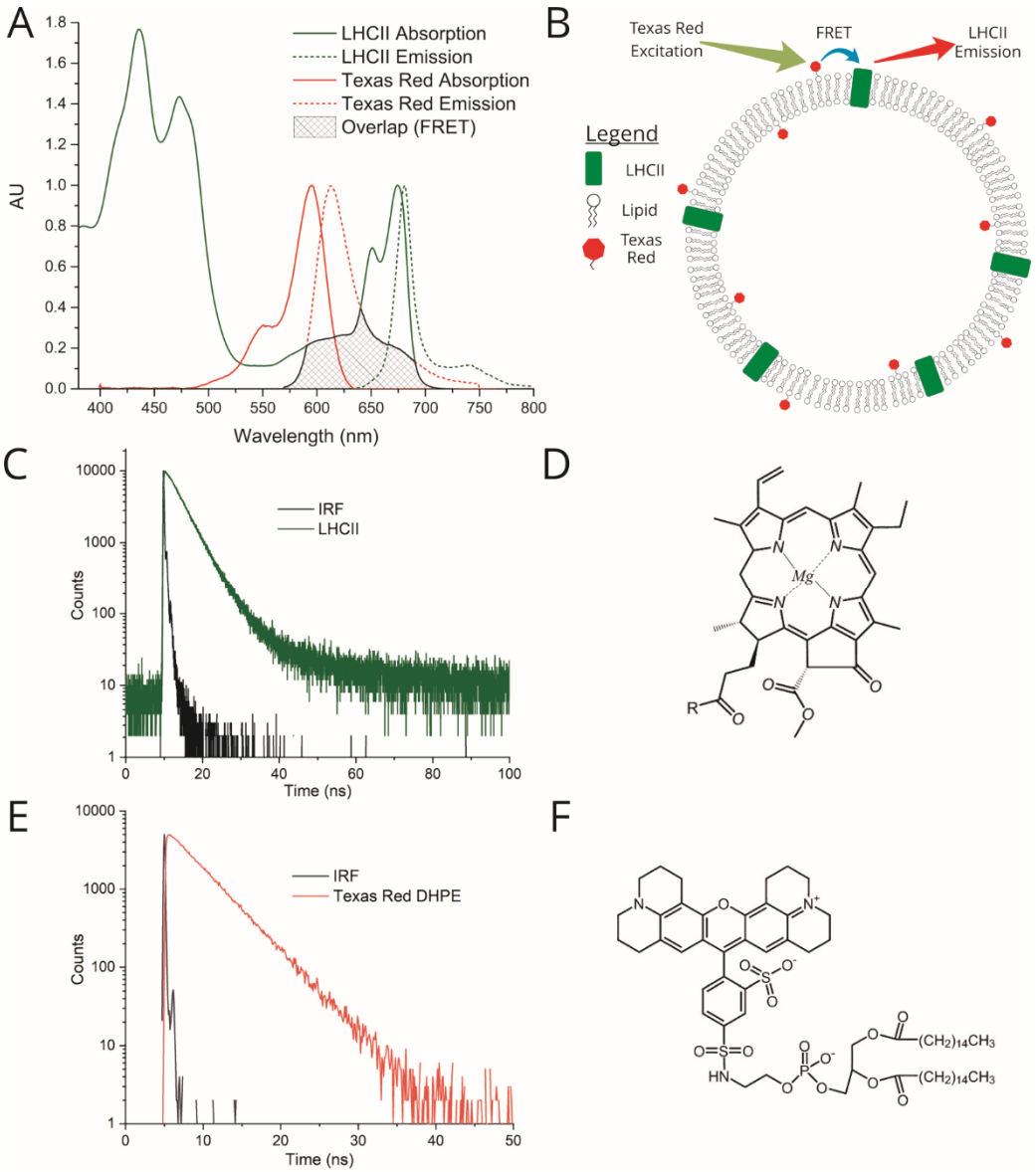

Figure 16 Spectra and schematic demonstrating the concept of interfacing lipid-tagged Texas Red with membrane reconstituted LHCII in proteoliposomes

(A) Ensemble solution-based spectroscopy performed on dilute samples of isolated LHCII or TR-DHPE in a detergent suspension: absorption (solid line) and fluorescence emission (dotted line) spectra. LHCII spectra normalized to 1.0 at Chl *a* absorption maximum (~675 nm) and Texas Red normalised to 1.0 at absorption maximum (~591 nm) for visual clarity. (B) Schematic concept of proteoliposomes with energy transfer direction and wavelengths indicated (not to scale). (C) Time resolved fluorescence data from LHCII trimers in a buffer of 0.03 % w/v α-DDM, 10 mM HEPES, pH 7.5 (absorbance ~0.1 at 675 nm). Taken using an Edinburgh Instruments F980 fluorescence spectrometer with 475 nm pulsed laser at 0.5 MHz. Instrument response function (IRF) taken using colloidal silica beads. (D) Chemical

structure of TR-DHPE (Texas Red 1,2-dihexadecanoyl-sn-glycero-3-phosphoethanolamine) (E) Time resolved fluorescence data from Texas Red DHPE in a buffer of 0.1 % w/v α-DDM, 10 mM HEPES, pH 7.5 (absorbance ~0.1 at 590 nm). Taken using QuantaMaster fluorescence spectrometer with supercontinuum pulsed laser at 0.5 MHz, excitation set to 540 nm (5 nm slit) and 610 nm emission (1 nm slit). Instrument response function (IRF) taken using colloidal silica beads. (F) Chemical structure of chlorophyll *a*, where R = $C_{20}H_{40}O$ (phytol).

3.3 Incorporation of LHCII and Texas Red into proteoliposomes

3.3.1 LHCII purification

First it was necessary to prepare the light-harvesting protein required. LHCII trimers were purified directly from spinach leaves using an established procedure (Adams et al., 2018); full details are in section 2.2.1. Briefly, spinach leaves were macerated, filtered and chloroplasts isolated through centrifugation. Isolated chloroplasts were then osmotically lyzed using a high sucrose buffer before several centrifugation and wash steps to allow thylakoid membranes to be isolated. Thylakoid membranes were solubilised with α-DDM detergent and loaded onto an 8-13 % continuous sucrose gradient and ultra-centrifuged for 36 hours to isolate LHCII trimers and monomers by weight. Clear bands which can be collected for further purification are shown in Figure 17 (A). After LHCII trimers were collected Fast Liquid Protein Chromatography (FLPC) was used with a Size Exclusion Chromatography (SEC) column to further purify proteins by size to separate LHCII trimers, monomers and any other contaminants. Clear peaks in UV absorption at 280 nm in chromatography traces indicate populations of trimers and monomers being eluted from the column, Figure 17 (B). Fractions were collected in between the full-width-half-maximum of the trimer peak before further concentration and buffer exchange into 20 mM HEPES (pH 7.5) 0.03 % α-DDM to be used in proteoliposome formation.

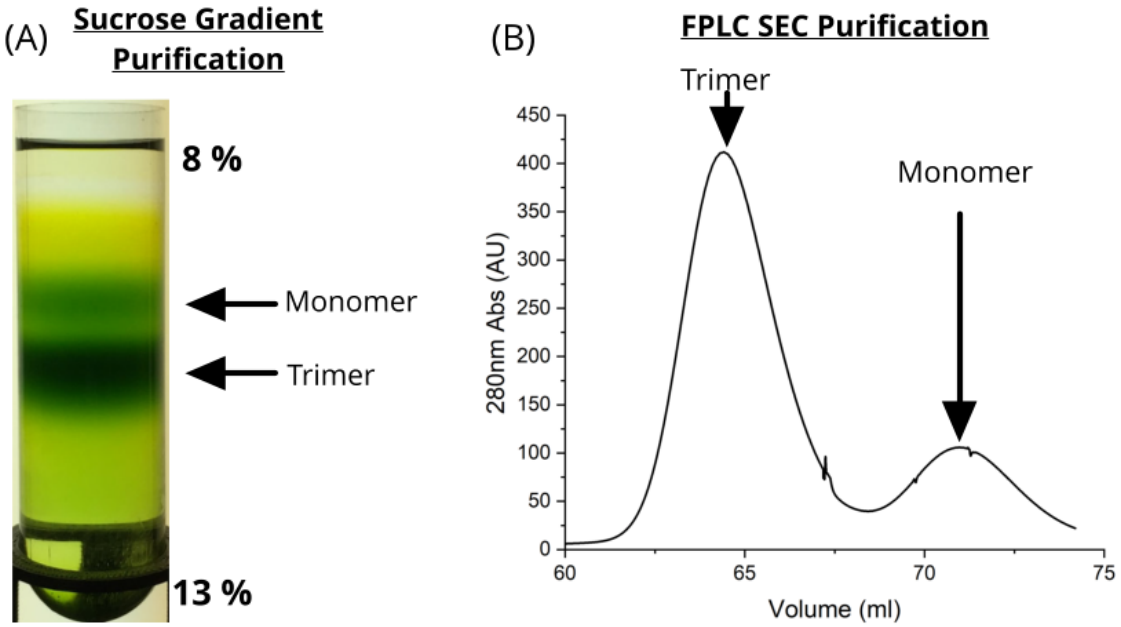

Figure 17 Purification of LHCII

(A) Photograph of post-centrifugation sucrose gradient with LHC-II monomer and trimer bands clearly visible. (B) Chromatogram of solution being eluted from FPLC SEC column (absorption at 280 nm, blue line).

Gel electrophoresis indicates a high protein purity and the natural trimeric state. Figure 18 shows both SDS-PAGE (denaturing) and clear native PAGE electrophoresis on LHCII trimers before FPLC and the monomer and trimer fractions post-FPLC. Clear single bands at 22 kDa on SDS-PAGE gels confirm the presence of single protein monomers post-denaturing with minimal contaminants. SDS-PAGE gels with UV sensitive Sypro Ruby stain clearly show the removal of contaminants after the FPLC purification stage. Clear native PAGE shows the presence of a significant population of LHCII monomers and dimers which are removed during FPLC purification. Post-FPLC LHCII trimers were used in the formation of proteoliposomes as discussed in the following sections.

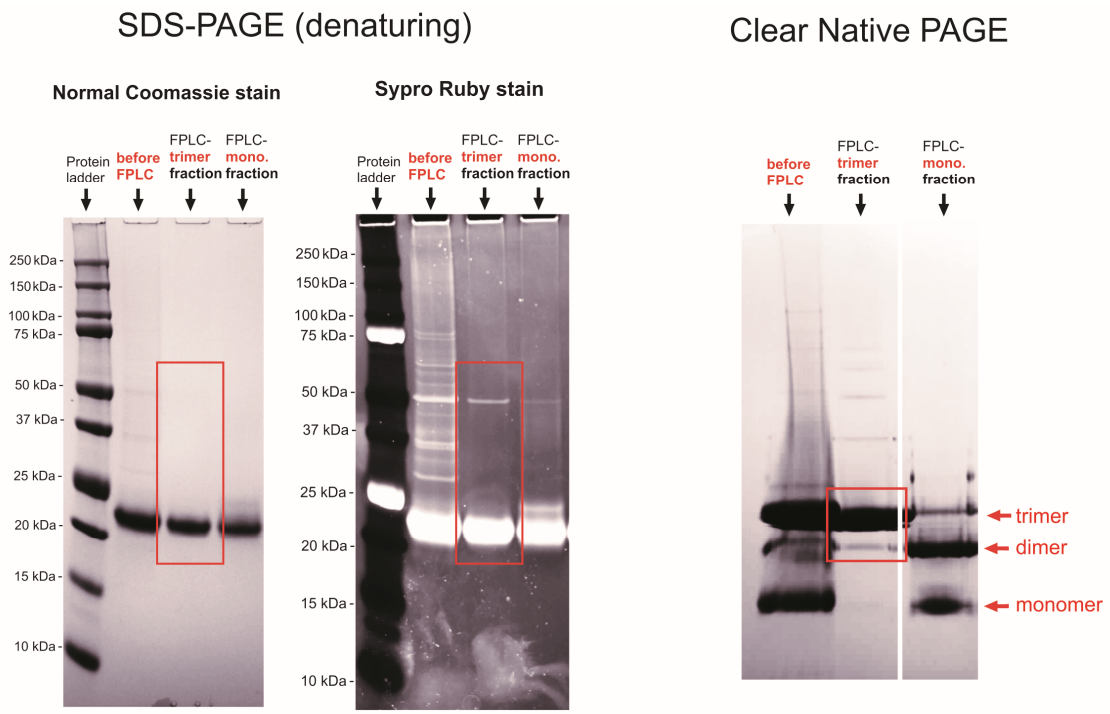

Figure 18 Gel electrophoresis of purified LHCII

SDS-PAGE gel with either Coomassie (left panel) or SYPRO-RUBY stain (middle panel). Gel lanes show, in order: protein standard, LHCII "before FPLC" (containing impurities, i.e., before size exclusion chromatography), purified trimeric LHCII (i.e., trimer fractions after size exclusion chromatography), purified monomeric LHCII (monomer fractions after size exclusion chromatography). Native-PAGE gel (right panel) was run at 4°C and then stained with Coomassie. Native gel lanes show, in order: LHCII "before FPLC", purified trimeric LHCII, and purified monomeric LHCII, as above.

3.3.2 Proteoliposome formation

In order to provide a native environment for LHCII reconstitution into the model membrane a mixture of plant lipids was used. Plant thylakoid lipids MGDG, DGDG, SQDG, Soy PG, the synthetic lipid DOPC, and the fluorescently-tagged lipid Texas Red DHPE were used for proteoliposome formation. The standard thylakoid lipid mixture used for all samples contained 35 % MGDG, 20 % DGDG, 12 % SQDG, 8 % Soy PG and 25 % DOPC (% wt/wt), adapted from Grab et al. (2016). TR-DHPE was added as required to aliquots containing the standard lipid mixture before drying. Lipid mixtures

were prepared by solubilising dry lipids with a 2:1 chloroform: methanol and mixing to obtain the desired ratios and final mass, then subsequently dried under dry nitrogen gas flow and placed in vacuum desiccator to remove any residual traces of solvents (full lipid prep procedure in 2.3.1). Lipid aliquots were either used immediately or stored under argon gas at -80 °C until use.

Aliquots of dry thylakoid lipid mixture (as prepared above) were solubilised with 0.5 % α-DDM, 20 mM HEPES (pH 7.5) at room temperature to form a micellar lipid-DDM solution. This was to ensure that lipids and protein could be homogenously mixed in lipid micelles before detergent removal. LHCII and NaCl were added to achieve a buffer of 1 mM total lipid, 0.2 % α-DDM, 20 mM HEPES (pH 7.5), 40 mM NaCl and the desired LHCII concentration. The lipid-DDM-protein mixture was then incubated with Bio-Beads to gradually remove the detergent and allow proteoliposome formation via self-assembly. Full protocol for proteoliposome formation is shown in section 2.3.3.

Next, it was useful to establish the size of the assemblies, which could be done via their migration through gradients of a polysaccharide concentration. Analytical ultracentrifugation was performed on a selected proteoliposome sample and an LHCII in detergent control to determine if homogenous populations of proteoliposomes had formed and to identify the presence of any non-reconstituted LHCII. A standard quantity of each samples was loaded onto 5-20 % continuous Ficoll gradients before ultracentrifugation at 200 kG for 10 hours. Note, Ficoll has a similar density to sucrose but aqueous solutions of Ficoll have a much lower osmolality, making it a gentler medium for isolation of vesicles whilst avoiding osmotic lysis. Figure 19 shows a clear single band of proteoliposomes at 8 % Ficoll concentration suggesting a single population. The absence of any protein at the bottom of the gradient, as seen in the LHCII-only sample, suggests that all LHCII has been reconstituted into the proteoliposomes as un-reconstituted LHCII aggregates in solution.

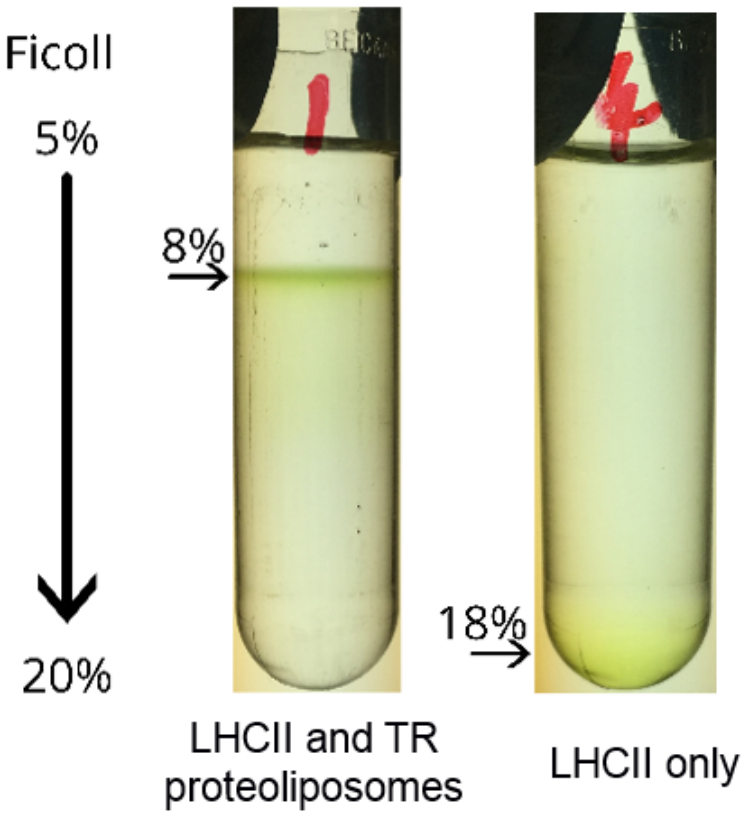

Figure 19 Analytical Ficoll gradients of proteoliposomes and LHCII in detergent

Analytical continuous 5-20 % Ficoll gradients (Left) Representative proteoliposomes sample (0.7 µM LHCII, 8 µM Texas Red, 1 mM total lipids) showing a clear single population and no aggregates of LHCII; (Right) LHCII in detergent at a 0.7 µM concentration showing clear sedimentation of LHCII not reconstituted into proteoliposomes.

3.3.3 De-composition of absorption spectra

To accurately calculate the concentration of both LHCII and Texas Red actually achieved in proteoliposome samples, rather than assuming all starting material was retained, a careful manual graphical analysis of absorption spectra was performed. All absorption spectra for proteoliposomes were collected as described in 2.4.2. Absorption spectra were "baselined" to give an absorbance of zero at 800 nm as expected in these samples, to remove any differences in noise (e.g. detectors, slight differences in cuvettes, etc.). All absorption spectra were then corrected for dilution by multiplying by dilution factor.

LHCII and TR content were calculated with separate de-compostions and calculations, as described individually below.

LHCII content was estimated from the Q_y peaks of LHCII, before any spectral de-composition (de-composition was unnecessary because there is no significant overlap of absorption from Texas Red >630 nm). LHCII content assessed from the integrated area from 635-700 nm, with LHCII concentration then calculated as:

$$\boldsymbol{LHCII} = \int_{635nm}^{700nm} \frac{\boldsymbol{Area}}{\boldsymbol{6.73x10^6}} \boldsymbol{M}$$

Equation 18 LHCII extinction coefficient and concentration calculation

(N.B., the constant 6.73×10^6 M^{-1} cm^{-1} is the integrated area which represents 1 mole/L in a 1-cm path length cuvette measured from a control sample of dilute LHCII in 0.03 % α – DDM detergent)

Protein content was calculated using the area under the peak, rather than peak height, to ensure that the slight peak broadening which occurred did not lead to a loss of relative absorption used in calculations. Absolute LHCII concentration in control samples was determined by extracting chlorophylls from LHCII in an 80 % acetone solution and measuring the absorbance at 663 and 646 nm. Using the empirical relationship (Porra et al., 1989): **Chl *a* + Chl *b* total (in µmol/L) = 19.54 $A_{646.6}$ + 8.26 $A_{663.6}$**
This allowed LHCII concentration to be quantified as 1/42 of this (there are 42 chlorophylls per LHCII trimer (Standfuss et al., 2005)).

Before quantification of concentration of Texas Red (TR), the component peaks within absorption spectra were de-composed because LHCII overlaps throughout the TR absorption range. To obtain the TR-only component, a representative LHCII absorption spectrum (originally collected from LHCII in detergent or in liposomes) was normalised to the test sample absorbance at ~675 nm (LHCII Chl *a* Q_y peak) and then subtracted, to give a result as shown in Figure 20 below.

Texas Red content was assessed on these de-composed spectra from the peak height at 591nm with TR-DHPE concentration then calculated as:

$$TR-DHPE = \frac{Peak\ Height}{85,000} M$$

Equation 19 Texas Red DHPE extinction coefficient and concentration calculation

(Note., the constant 85000 M^{-1} cm^{-1} is the extinction coefficient which represents 1 mol/L in a 1-cm path length (Titus et al., 1982)). Here, peak height was used to determine Texas Red content (as opposed to integrated area) because Texas Red did not undergo any spectral broadening or shifts in all proteoliposome samples measured.

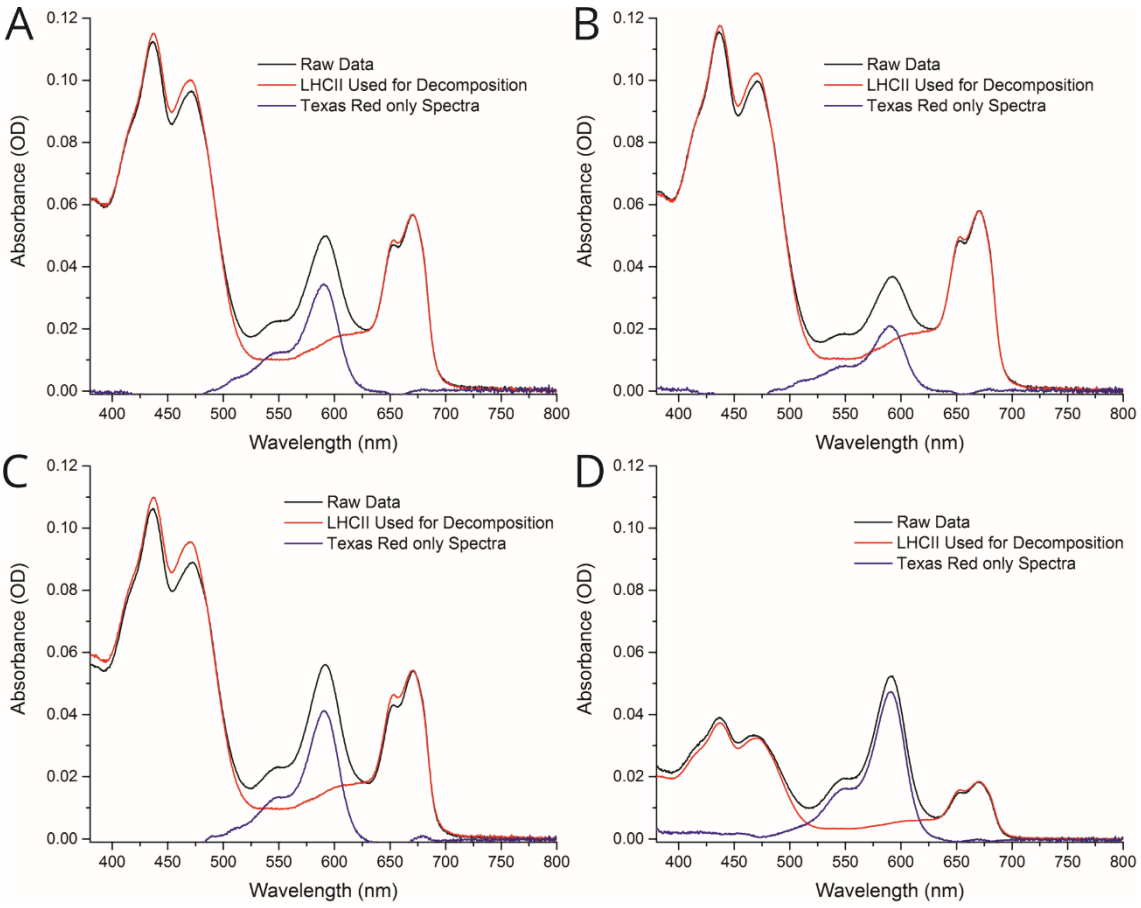

Figure 20 De-composition of LHCII and Texas Red absorption spectra

Example of the de-composition of absorption spectra as described in the text. Representative proteoliposome samples are shown (A) ~0.55 µM LHCII, 11.2 µM Texas Red. (B) ~0.55 µM LHCII, 6.0 µM Texas Red. (C) 1.18 µM LHCII, ~6.5 µM Texas Red. (D) 0.49 µM LHCII, ~6.5 µM Texas Red. (A-D) all samples at 1 mm total lipid; raw absorbance data are shown with spectra cut off at y=0.

3.3.4 LHCII and Texas Red can be reproducibly and controllably co-reconstituted into proteoliposomes

In order to assess the successful reconstitution of both LHCII and Texas Red into proteoliposomes and the relative changes in fluorescence intensity due to Texas Red to LHCII energy transfer the concentrations of both need to accurately calculated. Ensemble absorption spectroscopy (data collected as in 2.4.2) was used to determine the LHCII and Texas Red composition for each proteoliposome sample. Absorption spectra for samples with varying LHCII and Texas Red concentrations are displayed in Figure 21 (A) and (B), respectively. Spectral de-composition analysis, as described in 3.3.3, was used to isolate LHCII and Texas Red components of spectra. The concentration of both components in each sample was calculated from optical density and extinction coefficient, also described in 3.3.3 using the Beer-Lambert law (Lakowicz, 2006) as shown in Equation 6. The Beer-Lambert law allows chromophore concentration to be calculated by its absorption and distinctive extinction coefficient.

$$\boldsymbol{A = \varepsilon l c}$$

Equation 10 Beer-Lambert law relating, A: Sample absorbance, Ɛ: Molar extinction coefficient of relevant component, l: optical path length of absorption spectroscopy measurement, c: Molar concentration of relevant component.

Incorporation yields of both LHCII and Texas Red (TR) were consistently high, between 75–85 % and 80–90 %, respectively (% of starting material successfully retained). Samples prepared to have a constant Texas Red concentration, Figure 21 (A), had relatively similar TR concentrations of 5.0–8.4 μM (0.5–0.84 % of total lipid composition) with a LHCII range from 0.16 to 2.84 μM (2.4–30.5 % of total mass). Samples prepared to have a constant LHCII concentration, Figure 21 (B), had very similar LHCII concentrations of 0.52–0.61 μM (8.6–9.4 % of total proteoliposome mass) with a TR range from 0.9 to 12.3 μM (0.09–1.2 % of total lipid composition). Table 2 shows the measured absorbance of samples and the calculated concentrations of LHCII and Texas Red. Generation of this proteoliposome composition range demonstrates the modularity of the system with reasonable control over the incorporation of both LHCII and Texas Red. This range of samples will allow the effect of donor-acceptor separation on energy transfer efficiency to be quantified. It will also allow the effective enhancement of LHCII absorption due to energy transfer from varying amount of Texas Red to be measured.

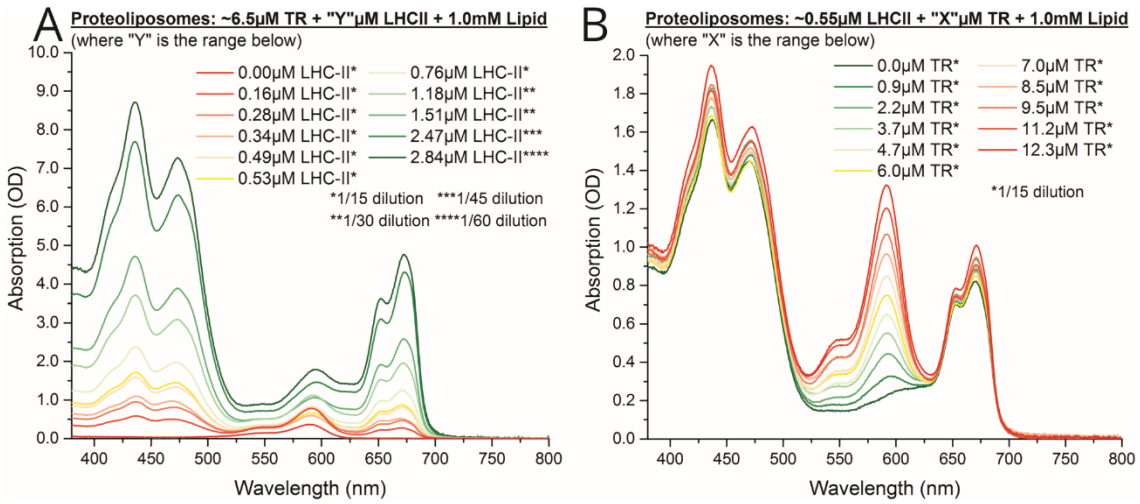

Figure 21 Ensemble absorption spectra of proteoliposomes with varying LHCII and Texas Red concentrations

Proteoliposome series with constant Texas Red and varying LHCII concentrations. (B) Proteoliposome series with constant LHCII and varying Texas Red concentrations. Samples were diluted prior to measurement and graphs are displayed after multiplication by these factors (annotated *). All measurements taken using an absorption spectrometer as described in 2.4.2 in a buffer of 20 mM HEPES (pH 7.5) 40 mM NaCl.

Initial concentrations		LHCII Absorbance	Calculated LHCII Concentration		TR Absorbance	Calculated TR Concentration	
LHCII (μM)	TR (μM)	Integrated area (635-800nm) dilution corrected	LHCII (μM)	(wt/wt% LHCII/ total)	OD at 591nm dilution corrected	TR (μM)	(mol/mol lipid%)
0.7	0.0	34.91	0.52	7.4	0.000	0.0	0.00
0.7	1.4	35.45	0.53	7.5	0.079	0.9	0.09
0.7	2.8	38.35	0.57	8.1	0.186	2.2	0.22
0.7	4.2	36.97	0.55	7.8	0.313	3.7	0.37
0.7	5.6	37.53	0.56	7.9	0.399	4.7	0.47
0.7	7.1	36.34	0.54	7.7	0.514	6.0	0.60
0.7	8.5	37.48	0.56	7.9	0.599	7.0	0.70
0.7	9.9	38.50	0.57	8.1	0.721	8.5	0.85
0.7	11.3	37.98	0.56	8.0	0.807	9.5	0.95
0.7	12.7	36.68	0.54	7.7	0.954	11.2	1.12
0.7	14.1	40.99	0.61	8.6	1.047	12.3	1.23
0.00	6.8	0.00	0.00	0.0	0.364	4.3	0.43
0.20	6.8	10.93	0.16	2.4	0.710	8.4	0.84
0.35	6.8	19.19	0.28	4.2	0.656	7.7	0.77
0.50	6.8	23.10	0.34	5.0	0.453	5.3	0.53
0.60	6.8	33.09	0.49	7.0	0.618	7.3	0.73
0.70	6.8	35.50	0.53	7.5	0.424	5.0	0.50
0.90	6.8	50.94	0.76	10.4	0.429	5.0	0.50
1.40	6.8	79.74	1.18	15.4	0.672	7.9	0.79
2.75	6.8	102.01	1.51	18.9	0.466	5.5	0.55
2.80	6.8	166.12	2.47	27.5	0.448	5.3	0.53
3.50	6.8	191.46	2.84	30.5	0.682	8.0	0.80

Table 2 Measured absorbance of LHCII and Texas Red in proteoliposome samples (black), and calculated concentrations in samples (red).

3.3.5 Spectral shifts at low lipid: protein ratios suggest LHCII-LHCII interactions promote stability

The aim of co-reconstituting lipid-tagged Texas Red and LHCII into proteoliposomes is that the additional energy from Texas Red will be transferred into an intact and functional LHCII trimer. Changes in protein conformation often manifest as shifts in absorption and emission spectral shape/ peak position as interactions between pigments are altered with disruptions to protein structure. Assessing the presence or absence of shifts in these spectra can be used to determine whether proteins are native or not: zero shift suggests exactly the same (native) environment for the chromophores (and therefore suggests a

similar 3-D protein conformation). Whereas a shift of a few nm indicates a subtle change in conformation and shifts of >5 nm are assumed to indicate more significant and unacceptable protein conformational changes. When reconstituting LHCII into proteoliposomes at a range of concentrations, a subtle blue shift in the chlorophyll (Chl) Q_y absorption peak (~675nm) compared to isolated LHCII in α-DDM detergent micelles was observed. Similar blue shifts are often observed in other studies but are often not explicitly stated (Johnson and Ruban, 2009). Figure 22 (A) shows ensemble absorption spectra of the proteoliposome series with varying LHCII concentration focusing on the Q_y absorption maximum of Chl *a* and Chl *b*; spectra are normalised at 1.0 at the Chl *a* maximum to allow for fair comparison between samples. The blue shift of Chl *a* absorption maximum is between 1-3 nm, as shown in Figure 22 (A), with larger shifts occurring at lower protein: lipid ratios. This indicates slight changes in the local environment of the chlorophylls (e.g. protein conformation) during membrane reconstitution. It was important to quantify those shifts, for full transparency, and to show how any such shifts compared to other studies.

Figure 22 (B) shows the LHCII fluorescence emission spectra (selective LHCII excitation at 473 nm) in the sample series with varying LHCII concentration, all normalised to 1.0 at the maximum (~681 nm) to allow fair comparison. The positions of LHCII emission maximum when reconstituted into proteoliposomes are shifted by no more than 1 nm compared to isolated LHCII trimers in α-DDM detergent micelles. A single fluorescence emission peak at ~681.5 nm represents emission from lowest energy Chl *a* indicating the highly-connected chlorophyll network within trimeric LHCII is intact. When reconstituted into proteoliposomes there is a slight broadening of the fluorescence emission peak of LHCII which varies with protein concentration. Broadening of the peaks increases at lower protein: lipid ratios to a maximum of 13 % (increase in total emission area with peak maximum normalised to 1.0) compared with isolated LHCII trimers in α-DDM detergent micelles. This suggests that up to 13 % of chlorophylls have an altered membrane environment. Whilst not ideal this is entirely in line with emission spectra broadening observed in other proteoliposome studies where LHCII appears to be destabilised at low protein concentrations (Adams et al., 2018, Pandit et al., 2011, Natali et al., 2016). The minimal changes in emission spectra between samples, Figure 22 (B), and good agreement of fluorescence excitation and linear absorption spectra for LHCII-

only proteoliposomes, discussed in 3.4.1, suggests that the pigments within the protein are well connected.

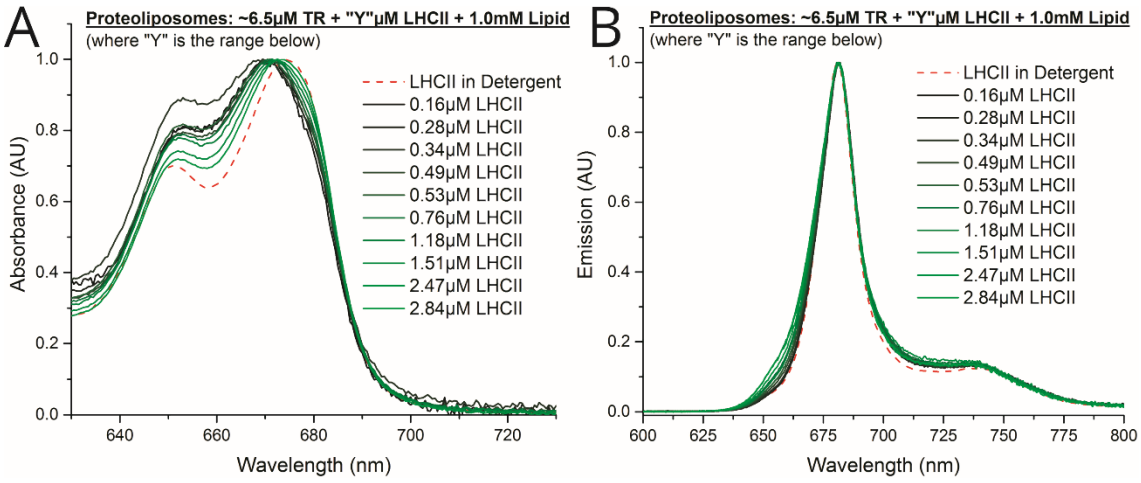

Figure 22 Absorption and emission spectra of LHCII reconstituted into proteoliposomes at different concentrations of Texas Red and LHCII

(A) Ensemble absorption spectra of proteoliposome series with constant Texas Red and varying LHCII concentration. Spectra shows Qy absorption peak maximum for Chl *a* and Chl *b* to highlight shifts in absorption peak shape and position with varying LHCII concentration. Spectra are normalised to 1.0 at the Chl *a* absorption maximum (~675 nm) for visual clarity. (B) Steady-state fluorescence emission spectra of proteoliposome series with constant Texas Red and varying LHCII concentration showing broadening in emission spectra at varying LHCII concentrations. Samples were excited at 473 nm (Xenon lamp source) to selectively excite LHCII-only. Spectra are normalised to 1.0 at the Chl *a* emission maximum (~681 nm) for visual clarity.

3.3.6 LHCII fluorescence emission is quenched at high protein concentrations in proteoliposomes due to LHCII-LHCII interactions

It was necessary to carefully quantify the magnitude of LHCII self-quenching within proteoliposomes in order to accurately distinguish this effect from the enhancement of LHCII emission due to energy transfer from Texas Red. The phenomenon of LHCII self-quenching is known to occur when LHCII is clustered. It has previously been observed in 3-D aggregates (Standfuss et al., 2005), natural thylakoids (Robert et al., 2004) and LHCII reconstituted into proteoliposomes (Moya et al., 2001, Crisafi and Pandit, 2017, Natali et al., 2016). The effect increases as protein to lipid ratios are increased and consequently LHCII-LHCII separation reduced. Steady-state fluorescence emission spectra were measured on samples of LHCII isolated in α-DDM detergent micelles and proteoliposomes with a range of LHCII concentrations. Texas Red was present in these samples at a constant concentration of ~6.5 μM. This does not affect the measurement as selective LHCII excitation at 473 nm was used which does not overlap with Texas Red absorption. Fluorescence emission 'per mol' of LHCII was calculated in order to easily compare quenching between samples. This relative fluorescence is calculated using the absolute concentration of LHCII in the sample, obtained from absorption data as described in section, 3.3.3 and the steady-state fluorescence emission. This allows one to account for sample to sample differences in yield and provide a more meaningful value of fluorescence emission which takes the concentration of the fluorescent component into account. Figure 23 (A) shows the relative emission of LHCII is reduced from 2.51 x 10^{15} counts / mol when isolated in detergent (red dashed line) to 1.82 x 10^{15} counts / mol when reconstituted into proteoliposomes at the lowest protein concentration tested of 0.16 μM (dark green line), representing a 28 % decrease in emission intensity (all samples with 1 mM total lipid). Figure 23 (A) also shows that the level of LHCII fluorescence further decreases as protein concentration is increased in proteoliposomes (darker to lighter green lines).A lowest relative LHCII emission of 5.06 x 10^{14} counts / mol was observed for the highest protein concentration of 2.84 μM LHCII representing a 79.8 % decrease.

The quenching of LHCII fluorescence emission is also observed as a decrease in fluorescence lifetime through independent time-resolved measurements. Time correlated single photon counting (TCSPC) was used to measure the fluorescence decay of LHCII

isolated in α-DDM detergent micelles and proteoliposomes with a range of LHCII concentrations. Texas Red was present in these samples at a constant concentration of ~6.5 μM. This does not affect the measurement as selective LHCII excitation at 475 nm was used which does not overlap with Texas Red absorption. Fitting measured decay curves to exponential decay functions allows the fluorescence lifetime of LHCII to be calculated as described in 2.4.4. Figure 23 (B) shows the fluorescence lifetime of LHCII is reduced from 3.96 ns when isolated in detergent (solid red line) to a maximum of 2.82 ns when reconstituted into proteoliposomes (solid dark green line). This decrease is measured at the lowest protein concentration of 0.16 μM (1 mM lipid) and represents a 31.2 % decrease in lifetime. Figure 23 (B) shows that LHCII fluorescence lifetime decays faster (steeper decay gradient) with higher protein concentration in proteoliposomes (Dark to light green). The shortest LHCII lifetime calculated was 0.90 ns for the highest protein concentration sample of 2.84 μM (1 mM lipid) representing a 78.0 % decrease in lifetime. A table of LHCII fluorescence lifetime components in proteoliposomes is shown in Table 3.

Steady-state and time-resolved fluorescence measurement of LHCII reconstituted into proteoliposomes, shown in Figure 23 (A) and Figure 23 (B), respectively, clearly show a relationship between LHCII concentration and the level of quenching. Figure 23 (C) shows the relative emission of proteoliposomes reconstituted with LHCII at different concentrations, with 100 % defined as steady-state fluorescence emission and fluorescence lifetime of 'unquenched' LHCII isolated in α-DDM detergent micelles. The levels of quenching calculated with the steady-state and concentration independent time-resolved techniques are in good agreement across all samples. The quenching of LHCII is attributed to LHCII-LHCII interactions which become more prevalent as distance between proteins decreases at higher protein concentrations.

Sample	Lifetime Components						LHCII Lifetime	
LHCII Concentration (μM)	τ_1 (ns)	β_1	τ_2 (ns)	β_2	τ_3 (ns)	β_3	$T_{Average}$ (ns)	X^2
Isolated in DDM	3.96	0.09	-	-	-	-	3.96	1.10
0.16	1.73	0.04	3.62	0.05	-	-	2.82	1.22
0.28	1.09	0.03	3.04	0.06	11.26	0.00	2.52	1.17
0.34	1.05	0.05	2.70	0.05	9.69	0.00	1.96	1.15
0.49	1.03	0.04	2.76	0.06	9.82	0.00	2.15	1.11
0.53	0.93	0.04	2.45	0.05	8.30	0.00	1.84	1.00
0.76	0.94	0.04	2.39	0.05	8.77	0.00	1.84	1.00
1.18	0.88	0.05	2.23	0.05	9.61	0.00	1.61	1.00
1.51	1.08	0.06	2.37	0.03	-	-	1.54	0.90
2.47	1.10	0.07	2.27	0.03	-	-	1.42	0.88
2.84	0.62	0.08	1.52	0.04	-	-	0.90	0.92

Table 3 LHCII fluorescence lifetime components in proteoliposomes. τ_n: Lifetime components, and β_n: lifetime amplitudes, where *n* represents the number of different components. $T_{Average}$: Amplitude weighted average lifetime. X^2: chi-squared value for goodness of fit to real data.

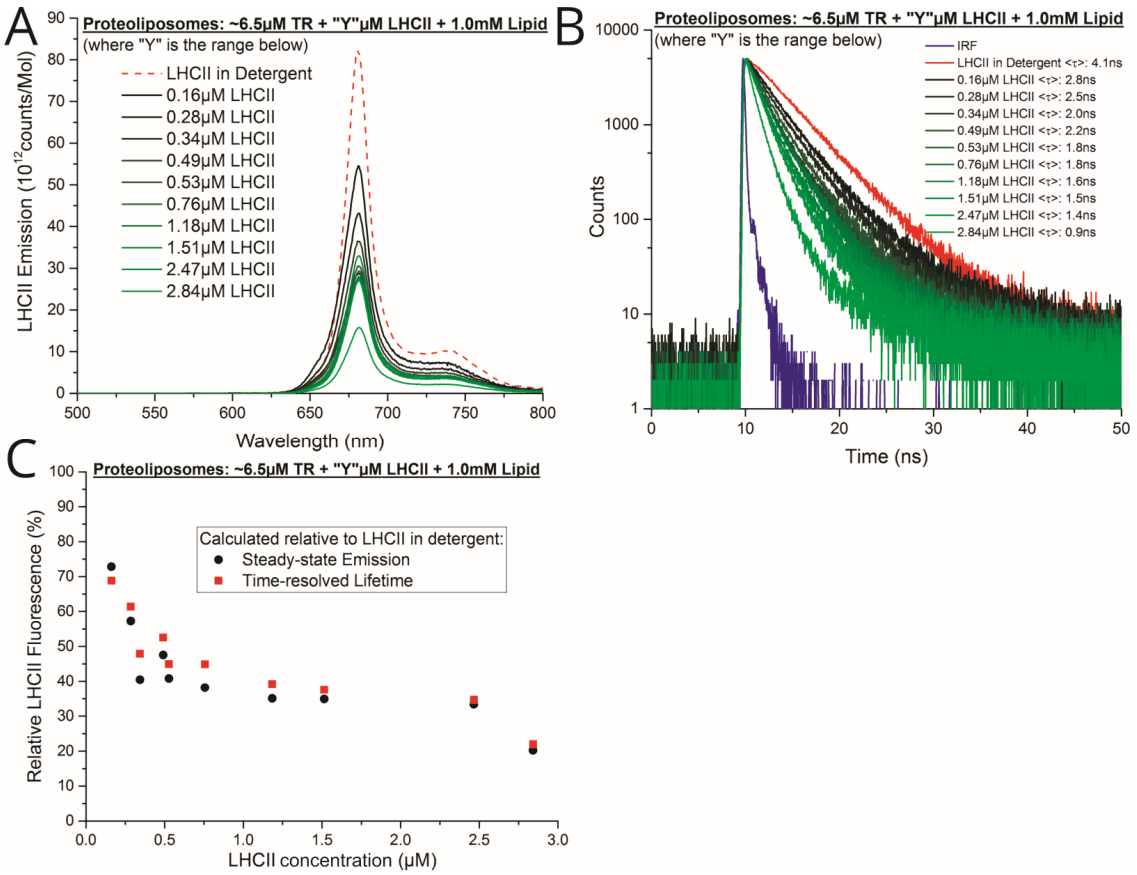

Figure 23 Steady-state and time-resolved florescence emission of LHCII reconstituted into proteoliposomes at different concentrations

(A) Steady-state fluorescence emission spectra of proteoliposome series with constant Texas Red and varying LHCII concentration. Samples were excited at 473 nm (Xenon lamp source) to selectively excite LHCII-only. All emission spectra are normalised to LHCII concentration giving a value of emission per mole to show relative quenching at different concentrations. (B) Time resolved fluorescence data from LHCII trimers in a buffer of 0.03 % w/v α-DDM, 10 mM HEPES, pH 7.5 (absorbance ~0.1 at 675 nm). Taken using Edinburgh Instruments F980 fluorescence spectrometer with 475 nm pulsed laser at 0.5 MHz. Amplitude weighted lifetime (<τ>) of LHCII calculated from each decay curve is displayed in legend. Instrument response function (IRF) taken using colloidal silica beads. (C) Graph showing relative LHCII quenching in proteoliposome series with constant Texas Red and varying LHCII concentration (1 mM lipid with 6.5 μM TR). Values are relative to steady-state emission and time-resolved lifetime of LHCII in detergent.

3.3.7 LHCII concentration directly affects the size of proteoliposomes formed

Incorporation of light-harvesting antenna proteins into model lipid membranes does not always result in homogenous populations of proteoliposomes. Sub-populations are likely to occur within samples with varying concentrations of incorporated proteins and proteoliposome sizes (Tutkus et al., 2018). We wished to confirm the consistent formation of proteoliposomes in each sample produced by the detergent removal method as described in 2.3.3. If populations of proteoliposome are formed consistently then the interpretation of Texas Red to LHCII energy transfer is simpler than with a heterogeneous population. This is because it can be assumed that the numbers of incorporated LHCII trimers per-proteoliposome are similar. Dynamic light scattering (DLS) was utilised to assess the hydrodynamic radius of proteoliposomes in solution formed with a range of LHCII concentrations. Briefly, dynamic light scattering utilises a laser which passes through a sample and is scattered in all directions due to diffracting upon interaction with the particles. The diffracted light forms a speckle pattern which is measured with a detector. As particles move in the sample, due to Brownian motion, the speckle pattern will also change. The spectral pattern is imaged in nanosecond intervals and changes are analysed by an autocorrelation function which describes the timescales of pattern change. Smaller particles will move faster than larger ones in solution due to Brownian motion and therefore have a different calculated autocorrelation function. These autocorrelation functions can then be used to estimate hydrodynamic radius of the particles in solution (see section 2.6 for full description) (Stetefeld et al., 2016).

Dynamic light scattering data shows that proteoliposomes formed via the detergent removal method, as described in 2.3.3, have a size dependence directly related to the concentration of LHCII. The average hydrodynamic radius of proteoliposomes with different LHCII concentrations is shown in Figure 24. Liposomes with no protein present have a hydrodynamic radius of 49 ± 3 nm which increases to 116±5 nm at the highest protein concentration of 2.84 μM LHCII (all samples at a total lipid concentration of 1 mM). This shows that the reconstituted LHCII in the proteoliposomes causes larger proteoliposomes to form. This is attributed to the protein locally restricting membrane curvature of the proteoliposomes (Lambrev and Akhtar, 2019).

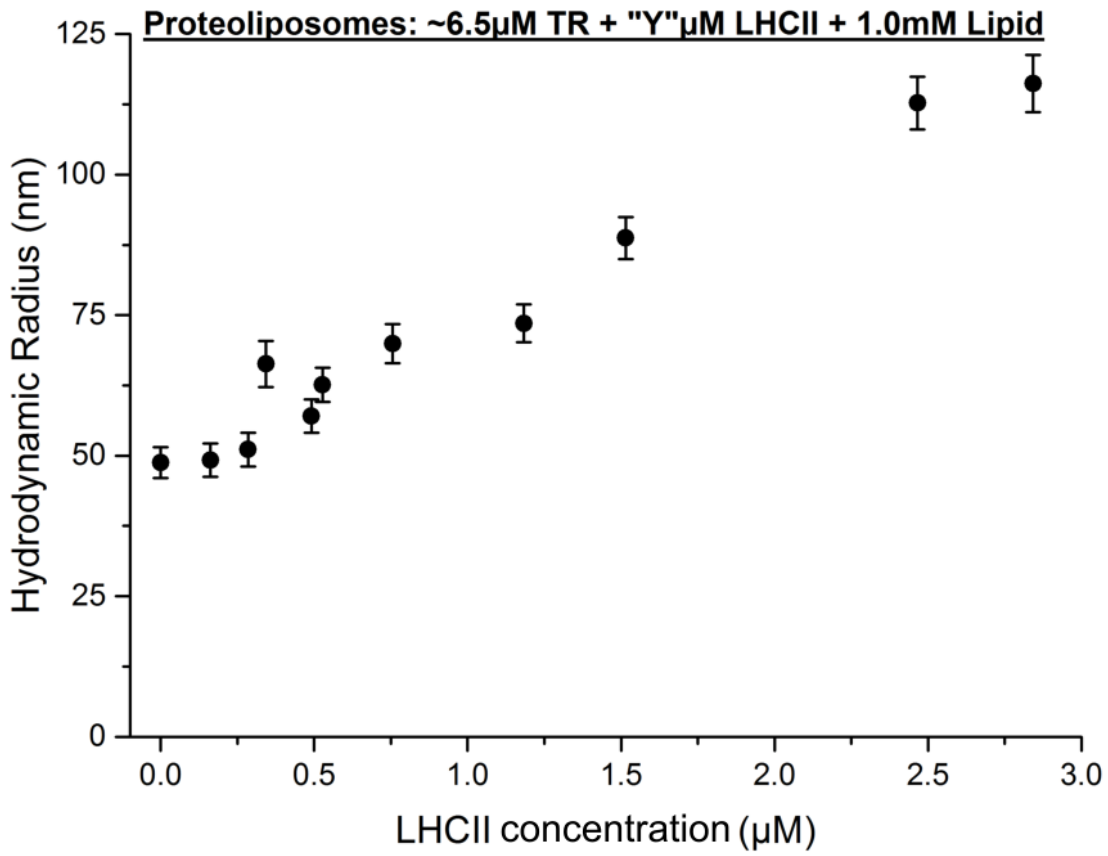

Figure 24 DLS data on proteoliposomes with LHCII reconstituted at different concentrations

Graph showing proteoliposome hydrodynamic radius (z-average) measured via Dynamic Light Scattering (DLS) against LHCII concentration. DLS measurements were taken with backscatter collected at 173° with a 633 nm excitation laser. Samples are from proteoliposome series with constant Texas Red and varying LHCII concentration (1 mM lipid with 6.5 µM TR). Error bars shown represent standard deviation.

Using the measured hydrodynamic radius of proteoliposomes, quantified concentrations of LHCII and Texas Red, and known lipid and protein surface area, the average number of lipids and LHCII trimers incorporated into proteoliposomes can be calculated. Measured proteoliposome radius and calculated average numbers of lipids, LHCII trimers, and Texas Red are shown in Table 4. Inter-particle separation of LHCII trimers, lipids and Texas Red molecules is also shown. Assumptions made are lipid area of 0.5 nm^2 and LHCII area of 40 nm^2 (Standfuss et al., 2005). This shows the number of proteins

increases from 4 per proteoliposome and an average LHCII-LHCII separation of 55.9 nm at the lowest concentration of 0.16 µM LHCII, to 352 per proteoliposome and average LHCII-LHCII separation of 14.7 nm at the highest concentration of 2.84 µM LHCII. This demonstrates the significant change in LHCII-LHCII separation in samples which drives the substantial changes in levels of LHCII quenching reported in the previous section.

Sample Description		Radius	Lipids				LHCII		
LHCII (µM)	TR (µM)	(nm)	no. lipids	no. TR-DHPE	TR-TR separation (nm)	L:P ratio	no. LHCII	LHCII-LHCII separation (nm)	LHCII coverage (%)
0.00	4.28	48.8	27802	12	34.2	-	-	-	-
0.16	8.35	49.2	27238	23	25.0	6162	4	55.9	2.4
0.28	7.72	51.1	28979	22	26.2	3510	8	42.4	4.2
0.34	5.33	66.3	50430	27	31.2	2916	17	38.7	5.1
0.49	7.28	57.1	35927	26	27.1	2036	18	32.5	7.1
0.53	4.99	62.6	44128	22	32.5	1897	23	31.4	7.7
0.76	5.04	69.9	54543	28	32.6	1322	41	26.5	10.9
1.18	7.91	73.5	56845	45	26.8	845	67	21.5	16.5
1.51	5.48	88.7	83417	46	32.2	660	126	19.2	20.8
2.47	5.27	112.7	123660	65	34.5	406	305	15.6	31.9
2.84	8.02	116.2	131504	105	27.9	352	374	14.7	36.0

Table 4 Comparison of estimated proteoliposome size and composition

3.3.8 Effect of solvent (chloroform, detergent, lipids) and concentration on Texas Red fluorescence activity

Both the steady-state and time-resolved fluorescence emission of Texas Red are used to quantify Texas Red to LHCII energy transfer in proteoliposomes. Energy transfer from Texas Red to LHCII will result in a quenching of Texas Red fluorescence emission intensity and lifetime. It is therefore crucial to have an accurate 'baseline' of Texas Red fluorescence to allow energy transfer efficiency to be calculated accurately. Steady-state and time-resolved fluorescence emission spectra of Texas Red were measured for control samples omitting LHCII in order to determine a value for fully emissive Texas Red (no quenching due to energy transfer). These values for "relative TR fluorescence" were used as a baseline to calculate the Texas Red quenching due to FRET in the energy transfer efficiency (ETE) equations. TR-DHPE was measured in two "isolated" forms of (i) in chloroform (black solid line), (ii) in DDM detergent micelles (red solid line), and compared to (iii) TR-DHPE reconstituted into liposomes at a series of concentrations. Each sample of isolated TR-DHPE was measured at different dilutions and the final results averaged (n=3). Six individually prepared samples of TR-DHPE in liposomes at different concentrations were measured. Slight differences in the magnitude of Texas Red fluorescence emission 'per mole' and amplitude-weighted lifetime were measured (Figure 25 (A + B)): in detergent 1.59×10^{12} counts / mol and 5.09 ns, in chloroform 1.56×10^{12} counts / mol and 4.14 ns. In liposomes a concentration dependency was observed; fluorescence emission decreases from 1.88×10^{12} counts / mol and 4.43 ns to 1.21×10^{12} counts / mol and 3.58 ns as Texas Red molar concentration increases from 0.43 % to 1.03 % (Figure 25 (C + D)). Differences in fluorescence when in chloroform, micelles, or liposomes are attributed to different local solvent environments, supported by slight shifts in the emission peak maximum wavelength. Self-quenching of TR-DHPE in liposomes at higher concentrations is a known effect that has been quantified (Titus et al., 1982). When calculating the efficiencies of energy transfer in proteoliposome samples the unquenched emission and lifetime used are always from Texas Red-only liposomes with a similar Texas Red concentration as in the proteoliposomes in question; this takes the effect of Texas Red self-quenching into account.

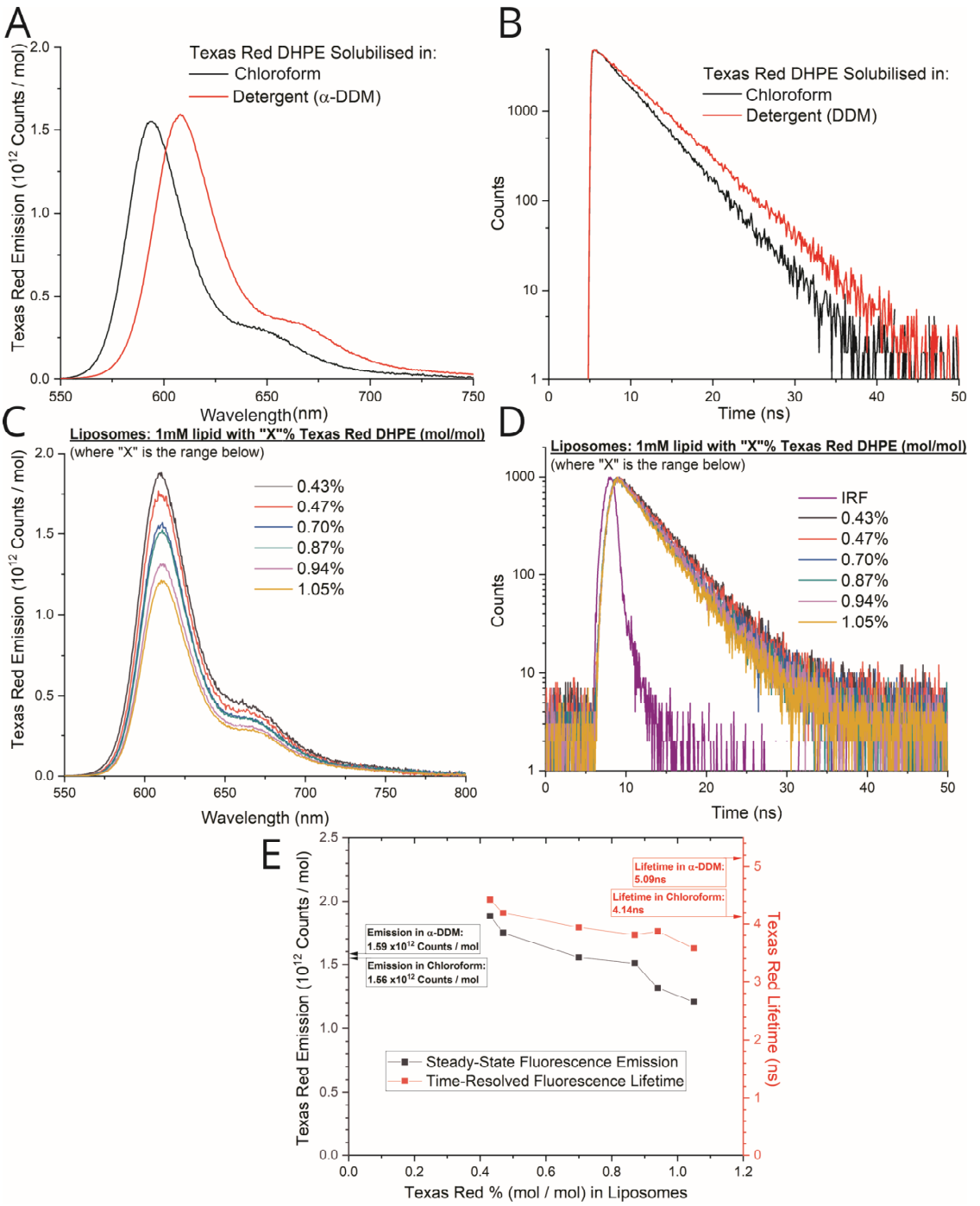

Figure 25 Steady-state and time-resolved fluorescence of Texas Red in solvent, detergent, and reconstituted into liposomes at different concentrations

(A) Steady state fluorescence emission spectra of Texas Red (540 nm xenon lamp excitation) solubilised in detergent micelles and in chloroform. All emission spectra are normalised to Texas Red concentration giving a value of emission per mole to show relative quenching in different environments. (B) Time resolved fluorescence data of Texas Red (540 nm pulsed laser excitation) solubilised in detergent micelles and in chloroform. (C) Steady state fluorescence emission spectra of Texas Red (540

nm xenon lamp excitation) in liposomes at different concentrations. All emission spectra are normalised to Texas Red concentration giving a value of emission per mole to show relative quenching. (D) Time resolved fluorescence data of Texas Red (540 nm pulsed laser excitation) in liposomes at different concentrations. (E) Graph showing the relative fluorescence emission and lifetime of Texas Red DHPE in detergent micelles, chloroform and in liposomes at different concentrations.

3.3.9 Further interpretations of initial spectroscopy data

It is worth providing some physical interpretations at this juncture, before presenting the effects of energy transfer from Texas Red to LHCII. In the section 3.3, the incorporation of LHCII into proteoliposomes has been characterised with focus on the changes in LHCII fluorescence observed when reconstituted into the bilayer. Absorption and normalised fluorescence emission data in section 3.3.5 show that the local environment for chromophores which make up LHCII is subtly changed when reconstituted into proteoliposomes at low concentrations. This change is manifested as broadening of absorption and fluorescence emission peaks in the spectral data. While these subtle changes are reported in the literature (Moya et al., 2001) we can speculate that the reason for similar absorption peaks (which are assumed to represent LHCII being closer to its native conformation) when LHCII was reconstituted at high concentration in proteoliposomes is that in the natural thylakoid membrane LHCII is part of a closely packed protein superstructure (Croce and van Amerongen, 2011). These protein-protein interactions may provide a stabilising effect for LHCII through attractive interactions such as van der Waals forces. It is also possible that during the self-assembly process there is some damage to the LHCII in the transition from detergent micelles to being reconstituted into the lipid bilayer which is exaggerated by higher lipid: protein ratios. This could be in the form of chromophore rearrangement or loss. Despite the observation of these slight changes in absorption and fluorescence spectra the minimal shifts of peak position by 1-4 nm in absorption and < 1 nm in emission are evidence of highly connected system of pigments within the protein. LHCII reconstituted into proteoliposomes was therefore considered to be fluorescently active (i.e., minimal change to the chlorophyll arrangement and the retention of inter-pigment energy transfer).

Dependence of LHCII fluorescence quenching on LHCII concentration within proteoliposomes was discussed in section 3.3.6. Analysis of both steady-state and time-resolved fluorescence of LHCII showed a clear decrease in both fluorescence intensity and lifetime when concentration was increased in proteoliposomes. The self-quenching of LHCII at higher concentrations is due to more frequent and shorter inter-LHCII interactions occurring as the average LHCII-LHCII distance is decreased. This LHCII-LHCII separation dependent self-quenching is thought to be a photo-protective mechanism observed in vivo in chloroplasts (Robert et al., 2004) and can be replicated in vitro in LHCII crystals (Standfuss et al., 2005), aggregates (van Oort et al., 2007), or proteoliposomes (Moya et al., 2001, Crisafi and Pandit, 2017, Natali et al., 2016). A state with quenched fluorescence emission is not only present in plant light-harvesting proteins but is also observed in the bacterial antenna protein LH2 (Schlau-Cohen et al., 2013, Schorner et al., 2015). Quenching of fluorescence in antenna proteins has a crucial role in nature to protect plants from photo-damage, which occurs when the photon absorption rate higher than can be utilised for the photochemical reactions of photosynthesis (Ruban, 2017b). The excess excitation energy is dissipated as heat within the antenna proteins through dissipative pathways where energy is redirected to alternative chromophores, such as carotenoids, which do not transfer energy to the reaction centres when performing their dissipative function (Ruban et al., 2007). These pathways form both on a single protein level, as proteins switch to a quenched state, and are affected by larger scale rearrangements such as aggregation (Duffy and Ruban, 2015). LHCII fluorescence quenching does not only occur within multiple interacting proteins but also in isolated LHCII trimers which can 'switch' from high to low emissive states (Krüger et al., 2014). The switching between quenched and non-quenched states in isolated LHCII proteins suggests that the energy required for the conformational change is low (Liguori et al., 2017). The conformational change results in the opening of a pathway for energy to be dissipated as heat not present in the non-quenched conformation (Schlau-Cohen et al., 2015). It is possible that forces exerted on proteins during aggregation make the shift to the quenched conformation more likely, resulting in an overall higher level of quenching for the system. The level of quenching due to LHCII-LHCII interactions observed in this study is in good agreement with similar proteoliposome studies. Natali et al. (2016) report a decrease in lifetime of LHCII reconstituted into proteoliposomes from 3.49 ns to 0.97 ns as lipid to protein ratio decreases from 7000:1 to 230:1. Here we show a decrease from 2.82 ns to 0.90 ns as the ratio decreases in a comparable range from 6162:1 to 352:1.

Crisafi and Pandit (2017) report a similar level of quenching to 80-50 % of LHCII isolated in detergent when reconstituted into proteolipids at lipid to protein ratios of 10000:1 to 1000:1. This is similar to the levels of quenching observed here of 75 – 40 % in the range of 6162:1 to 1316:1. The level of LHCII self-quenching is quantified for all proteoliposome samples to allows the enhancement of emission due to energy transfer Texas Red to be quantified taking the initial level of LHCII emission quenching into account.

The concentration of LHCII in proteoliposomes formed via the detergent removal method, described in 2.3.3, was found to directly relate to the size of proteoliposomes, 3.3.7. Higher concentrations of LHCII reconstituted into proteoliposomes produced proteoliposomes with a larger hydrodynamic radius as measured by light scattering. It has been suggested that photosynthetic membrane proteins such as LHCII have an effect on the local structure of lipid bilayers by limiting membrane curvature (Lambrev and Akhtar, 2019). Non-bilayer forming lipids, such as MDGD, that are at high concentration in native thylakoid membranes are known to form lamellar structures in the presence of LHCII (Simidjiev et al., 2000). It is therefore expected that proteoliposomes formed with a high proportion of native thylakoid lipids, as shown here, would form larger diameter proteoliposomes with the high concentrations of LHCII minimising curvature.

3.4 Energy transfer from Texas Red to LHCII in proteoliposomes

3.4.1 LHCII Fluorescence excitation spectra and linear absorption analysis shows how much energy absorbed in the system is transferred to LHCII

Comparison between fluorescence excitation spectra and linear absorption (1 – Transmission) spectra can indicate the connectivity of chromophores within light-harvesting proteins such as LHCII. In a system where all chromophores are well connected we would expect the two spectra overlap perfectly; energy absorbed at any wavelength will result as fluorescence emission proportional to the energy absorbed creating matched absorption and fluorescence spectra. This technique can also be used to determine the energy transfer efficiency between donor and acceptor molecules undergoing FRET. Fluorescence excitation spectra were collected for proteoliposome

samples with constant LHCII and varying Texas Red concentration (Figure 26 (A)) and samples with constant Texas Red and varying LHCII (Figure 26 (B)). Fluorescence excitation spectra were collected by selectively collecting LHCII emission at 686 nm and scanning over a range of excitation wavelengths as described in 2.4.3.

Sample transmission, defined as the fraction of the incident beam intensity which is transmitted through the sample, and can be obtained from absorbance of a sample, which is measured as described in 2.4.2. Logarithmic absorption (absorbance) is the standard absorbance spectroscopy measurement made due to being proportional to sample concentration. Using the relationships shown in Equation 20, linear absorption is calculated by 1 – the sample transmission.

$$\boldsymbol{T = \frac{I_T}{I_0} = 10^{-Abs}}$$

Where logarithmic absorption is the standard measurement made by the instrument:

$$\boldsymbol{Abs = \log_{10}\left(\frac{I_0}{I_T}\right)}$$

And linear absorption is defined as:

$$\boldsymbol{L\,Abs = 1 - T}$$

Equation 20 Transmission (T) as calculated from sample Absorbance (Abs). T: Sample transmission, Abs: Sample absorbance. Linear Absorption (L Abs)

The excitation spectra and linear absorption are both normalised to fluorescence excitation and absorption maxima at ~675 nm for LHCII to allow a comparison between them to be made. If the excitation spectrum is lower than the linear absorption at a particular wavelength there is less than 100 % energy transfer from photons observed at that wavelength to the 'terminal' fluorescent molecules. The ratio of excitation to linear absorption over the donor region is therefore directly related to energy transfer efficiency. In Figure 26 (A+B) the excitation spectra (dashed line) is closely overlaid with the linear absorption (solid line) for all regions of LHCII emission due to the strong connectivity of the chromophores in the protein. The excitation spectrum is below the linear absorption in the region of Texas Red absorption due to an imperfectly connected system with under 100 % energy transfer efficiency from energy absorbed by Texas Red to LHCII emission.

The observation that most excitation spectra are only slightly below their corresponding linear absorption suggests a well-connected system where energy absorbed at any wavelength is transferred to the same final fluorescent component. The close overlap of excitation and linear absorption in an LHCII proteoliposome sample (Figure 26 (B) solid and dashed black lines respectively) is indicative of intact and fluorescently active LHCII.

The energy transfer efficiency between Texas Red and LHCII can be quantified by comparison between acceptor fluorescence excitation and linear absorption over the region of donor absorption (with acceptor only contributions to excitation and linear absorption spectra subtracted). This relationship is shown in Equation 21.

$$ETE = 1 - \frac{(1 - T_D) - Ex_D}{(1 - T)}$$

Equation 21 Energy transfer efficiency as calculated by comparison of linear absorption and acceptor fluorescence excitation spectra. T_D: Donor transmission maximum (~590 nm), Ex_D Donor fluorescence excitation maximum (~590 nm). Both linear absorption and excitation spectra had the LHCII component removed as described in 3.3.3 for absorption data.

As the LHCII to Texas Red ratio increases, as shown in Figure 26 (A), there is a significant increase in the ratio of TR excitation to linear absorption of Texas Red. This indicates an increase in Texas Red to LHCII energy transfer efficiency from 64 % at the lowest LHCII concentration of 0.16 μM to 90-100 % at the highest LHCII concentrations. Analysis of samples with constant LHCII and varying Texas Red concentration do not show significant variation in the ratio of linear absorption and excitation in the Texas Red region of the spectra. This results in a calculated energy transfer efficiency consistently between 87-100 % with no dependence on Texas Red concentration. Figure 26 (C+D) show the calculated energy transfer efficiencies for each sample.

This method gives a good indication of the energy transfer efficiency between Texas Red and LHCII. However, the de-composition of LHCII and Texas Red components in absorption and fluorescence excitation spectra is significantly less accurate than de-composing fluorescence emission spectra, especially when the LHCII to Texas Red ratio is high. However, comparison between linear absorption and LHCII fluorescence excitation spectra show that the chromophores within LHCII are well connected and that

a significant proportion of energy absorbed by Texas Red is transferred to LHCII in all samples with both components.

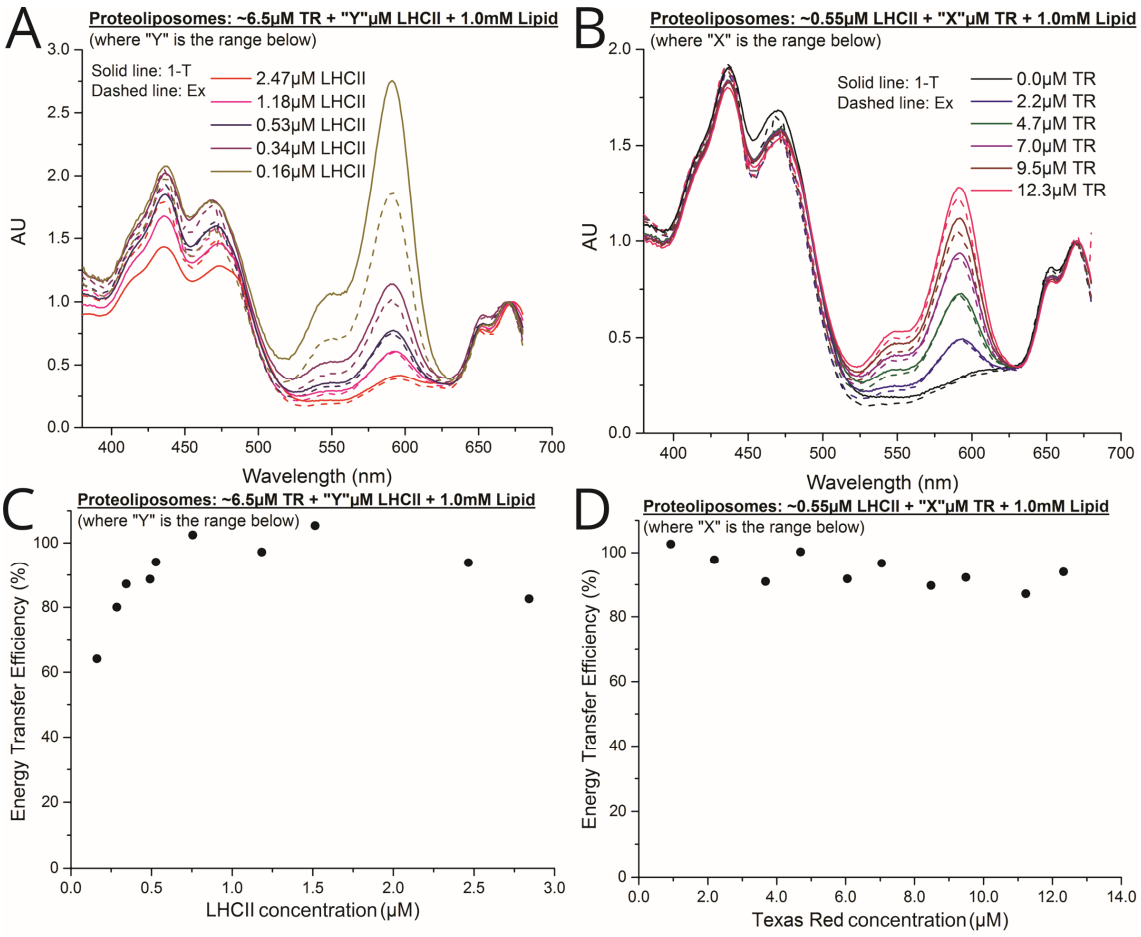

Figure 26 Linear absorption and excitation spectra of Texas Red-LHCII proteoliposomes

Representative LHCII fluorescence excitation (Ex – emission collected at 686 nm) and linear absorption (1-T) spectra for proteoliposomes: (A) constant Texas Red sample series, (B) constant LHCII sample series. Both spectra normalised to 1.0 at Chl *a* absorption peak (~675 nm) to allow comparison. (C+D) calculated energy transfer efficiency from data displayed in (A) and (B) respectively using Equation 21.

3.4.2 Emission de-composition

In the next section, fluorescence intensity change for Texas Red and LHCII will be quantified across a range of proteoliposome samples. Before quantification of relative fluorescence intensity, overlapping LHCII and Texas Red emission peaks were "de-composed" for combined samples in order to isolate either component. To obtain the LHCII-only component, a representative Texas Red emission spectrum (originally collected from Texas Red-only liposomes) was normalised to the measured sample's emission at 610 nm (Texas Red emission peak) and then subtracted, as shown in Figure 27 (A+B).

To obtain the Texas Red-only component, a representative LHCII emission spectrum was normalised to 83.3 % of the measured sample emission at 681 nm, as shown in Figure 27 (C+D). This representative LHCII spectrum was removed from the combined spectra to produce a de-composed spectrum where the value of emission at 681 nm is 17.7 % of Texas Red maximum at 610 nm, the expected value for pure isolated Texas Red. All emission spectra were then corrected for dilution by multiplying by the pre spectroscopy dilution factor. Positive residuals in the 650-700 nm region of all de-composition are attributed to the slight broadening of the LHCII emission peak at different concentrations in proteoliposomes as outlined in 3.3.5.

Whilst it may be somewhat convoluted this method of isolating the fluorescence emission intensity of each component allowed us to quantify the relative changes of each component. This is entirely necessary for the next analysis. Other de-composition methods could be applied in future. For example, least-squared fitting can be used to assign skewed Gaussians to emission spectra allowing different components to be isolated (Rooney and Lee, 1986).

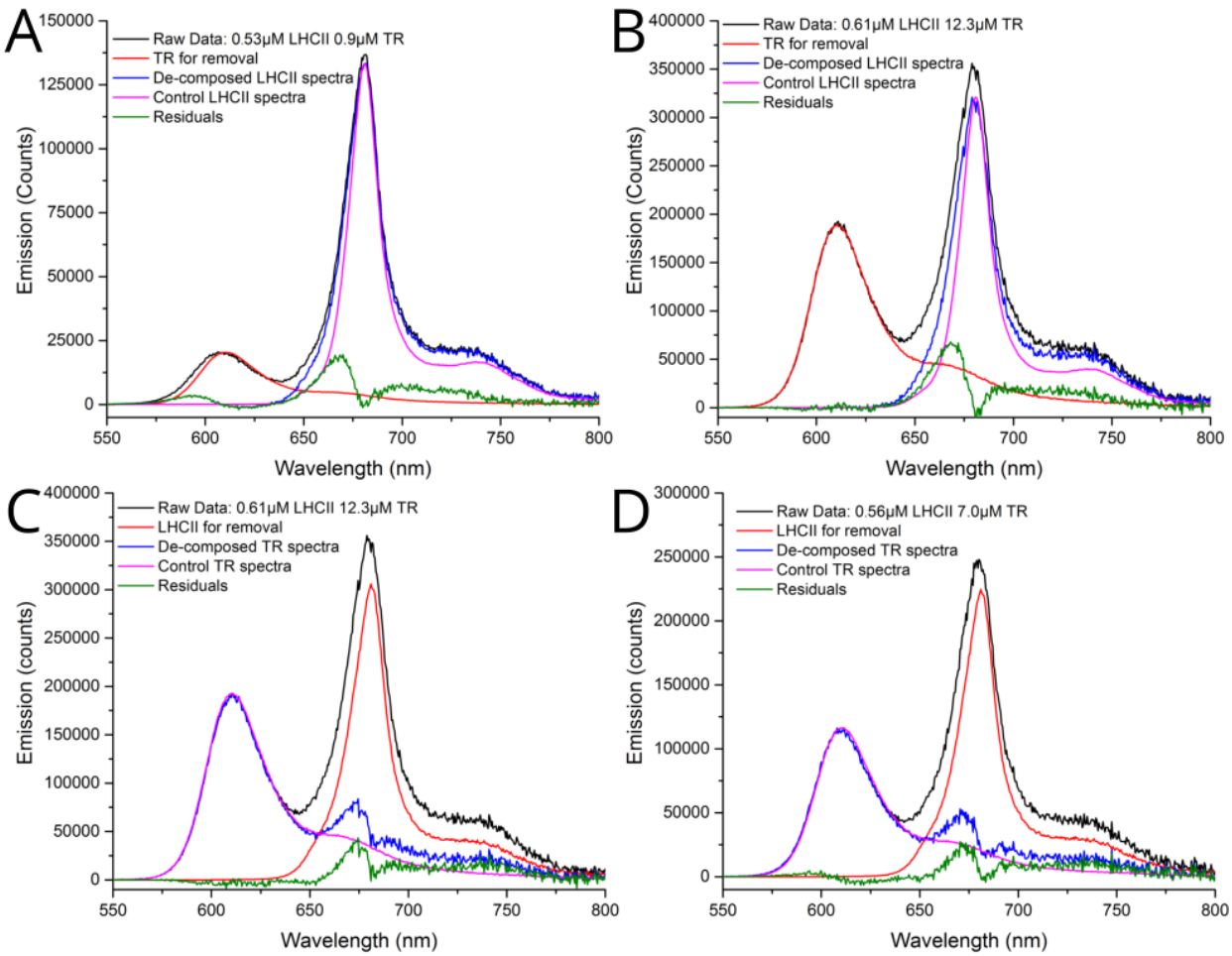

Figure 27 De-composition of LHCII and Texas Red fluorescence emission spectra

Example of the de-composition analysis of emission spectra for a representative proteoliposome sample (LHCII and TR concentrations stated in legend, all with 1 mM total lipids). (A-B) Removal of TR emission, (C-D) Removal of LHCII emission.

3.4.3 Texas Red emission is quenched as LHCII concentration increases suggesting an increasing energy transfer efficiency

If donor to acceptor energy transfer is taking place in Texas Red-LHCII proteoliposomes then Texas Red fluorescence should be quenched due to a statistically relevant number of excited states following this alternative non-radiative transfer pathway to LHCII rather than fluorescing. To estimate the energy transfer efficiency from Texas Red to LHCII the relative fluorescence of Texas Red in the combined system (donor + acceptor) was compared to a Texas Red-only system omitting LHCII (Texas Red-tagged lipids at 1 % within DOPC liposomes).

Texas Red quenching was assessed by measuring its fluorescence emission with selective excitation (540 nm Xenon source 1 nm bandwidth) and calculating relative Texas Red emission per mol to allow quantitative comparison between proteoliposome samples with constant Texas Red and varying LHCII concentration. As shown in Figure 28 (A), the Texas Red absorption component is relatively consistent between samples while the LHCII absorption increases incrementally (red to green colour scale of spectra indicates increasing LHCII concentration in samples). Knowledge of the actual achieved concentration in each sample allows the fluorescence data to be converted into a more meaningful form: "relative TR emission", defined as Texas Red emission per mole (Figure 9(B)). The relative fluorescence emission of Texas Red as LHCII concentration within proteoliposomes is increased is shown in Figure 28 (B). Fluorescence emission of Texas Red is reduced from 1.88 $x10^{12}$ counts / mol at the emission maximum (~610 nm) with no LHCII to 3.67 $x10^{10}$ counts / mol at the highest LHCII concentration of 2.84 μM. This represents a 98 % reduction in emission per mol of Texas Red suggesting almost all Texas Red molecules are transferring excitation energy to LHCII rather than emitting energy as fluorescence.

Sample description		Relative TR Emission
LHCII (μM)	TR (μM)	Counts / mol
-	4.30	1.88E+12
0.16	8.40	6.68E+11
0.28	7.70	4.08E+11
0.34	5.30	4.45E+11
0.49	7.30	2.53E+11
0.53	5.00	2.72E+11
0.76	5.00	2.00E+11
1.18	7.90	8.76E+10
1.51	5.50	9.76E+10
2.47	5.30	6.52E+10
2.84	8.00	3.67E+10

Table 5 Texas Red emission intensity in proteoliposomes with varying LHCII concentration

Quenching of Texas Red fluorescence was also quantified independently via time-correlated single photon counting (TCSPC) fluorescence measurements with selective Texas Red Excitation (540 nm pulsed laser, ~ 100 ps pulse width). Similarly to the analysis of steady-state fluorescence data, an increase in the rate of decay of the excited state (increase in the steepness of the decay curve) of the Texas Red in the presence of LHCII is indicative of a population of excited states being transferred to an acceptor molecule rather than fluorescing. Figure 28 (C) shows the time-resolved fluorescence data of Texas Red in proteoliposome samples with constant of Texas Red and varying LHCII concentration, as shown in Figure 28 (A). Fluorescence decay curves reveal a trend of increasingly steep exponential decay with increasing LHCII concentration. The fitted mean fluorescence lifetimes of Texas Red are shown in Table 6, calculated as in 2.4.4, and also shown in the Figure 28 (C) legend. The decrease of Texas Red fluorescence lifetime from 4.4 ns in the absence of LHCII to 0.72ns at the highest LHCII concentration of 2.84 μM suggests that the LHCII is causing the excited state lifetime of Texas Red to be reduced due to energy transfer.

Sample description		Lifetime Components						TR Lifetime	
LHCII (μM)	TR (μM)	τ_1 (ns)	β_1	τ_2 (ns)	β_2	τ_3 (ns)	β_3	$\tau_{Average}$ (ns)	X^2
-	4.30	4.4	1.00	-	-	-	-	4.43	1.0
0.16	8.40	4.9	0.11	1.2	0.16	3.1	0.7	2.98	0.7
0.28	7.70	0.6	0.25	4.1	0.19	2.3	0.6	2.21	0.6
0.34	5.30	3.7	0.42	1.7	0.38	0.5	0.2	2.34	0.6
0.49	7.30	0.6	0.47	4.1	0.11	2.2	0.4	1.65	0.7
0.53	5.00	1.8	0.42	3.8	0.22	0.4	0.4	1.70	0.6
0.76	5.00	0.4	0.47	1.6	0.37	3.8	0.2	1.40	0.8
1.18	7.90	1.9	0.29	4.6	0.05	0.4	0.7	1.05	1.0
1.51	5.50	1.5	0.29	3.8	0.11	0.3	0.6	1.02	1.2
2.47	5.30	2.0	0.33	0.4	0.63	5.3	0.0	1.15	1.0
2.84	8.00	0.4	0.82	14.4	0.00	2.1	0.2	0.72	0.9

Table 6 Texas Red lifetime components in proteoliposomes with varying LHCII concentration. τ_n: Lifetime components. β_n: Lifetime amplitudes. $\tau_{Average}$: Amplitude weighted average lifetime. X^2: chi-squared value for goodness of fit to real data.

Graphical analysis of steady-state fluorescence intensity and time-resolved fluorescence lifetime data allows the efficiency of Texas Red to LHCII to be quantified for all samples. Energy transfer efficiency was calculated from both steady-state (ETE_{SS}) and time-resolved (ETE_{TR}) data using the standard questions (Fung and Stryrm, 1978, Förster, 1965) as shown in Equation 22 and Equation 23, respectively.

$$ETE_{SS} = 1 - \frac{F_{DA}}{F_D}$$

Equation 22 Energy transfer efficiency as calculated from steady-state data, F_{DA}: Donor fluorescence intensity in the presence of acceptor (i.e., with LHCII), F_D: Donor fluorescence intensity in the absence of acceptor (i.e., control sample omitting LHCII).

$$ETE_{TR} = 1 - \frac{\tau_{DA}}{\tau_D}$$

Equation 23 Energy transfer efficiency as calculated from time-resolved data, τ_{DA}: Donor fluorescence lifetime in the presence of acceptor, τ_D: Donor fluorescence lifetime in the absence of acceptor.

Figure 28 (D) shows that energy transfer efficiency increases non-linearly with LHCII concentration and is fitted to an exponential growth function. This is appropriate as efficiency is expected to saturate at high acceptor concentration as donor-acceptor

separation is minimised below the Förster distance. The full dataset showing Texas Red emission intensities, lifetimes and calculated energy transfer efficiencies is shown in Table 7. Steady-state and time-resolved data are in good agreement with the trend of increasing energy transfer efficiency and estimate a maximum of ~94 % and ~77 %, respectively. The discrepancy between energy transfer efficiency calculated via analysis of steady-state and time-resolved fluorescence quenching is attributed to a limitation in the minimum lifetime which can be measured in the time-resolved measurements due to instrument limitations. It should also be noted that while steady-state and time-resolved measurements are both used to determine the level of fluorescence quenching, they do not measure the same effect. Steady-state fluorescence measurements show changes to the effective quantum yield of the fluorophore, time-resoled fluorescence measurements indicate the length of the fluorophore's excited state lifetime. Energy transfer may not affect the steady-state and time-resolved fluorescence of the donor in an identical manner. The trend of increasing energy transfer efficiency is attributed simply to the reduction in average distance between Texas Red and LHCII as LHCII concentration is increased. This fundamental result suggests that our system is behaving as an ideal donor-acceptor FRET system, as discussed in more detail later.

Sample description		Relative TR Emission	Calculated TR $\tau_{average}$	ETE (steady-state)	ETE (time-resolved)
LHCII (μM)	TR (μM)	Peak height at 610 nm (540 nm Excitation)	(ns)	(%)	(%)
-	4.30	1.88E+12	4.43	N/A	N/A
0.16	8.40	6.68E+11	2.98	64.5	32.7
0.28	7.70	4.08E+11	2.21	78.3	50.1
0.34	5.30	4.45E+11	2.34	76.3	47.2
0.49	7.30	2.53E+11	1.65	86.6	62.8
0.53	5.00	2.72E+11	1.70	85.5	61.6
0.76	5.00	2.00E+11	1.40	89.4	68.4
1.18	7.90	8.76E+10	1.05	95.3	76.3
1.51	5.50	9.76E+10	1.02	94.8	77.0
2.47	5.30	6.52E+10	1.15	96.5	74.0
2.84	8.00	3.67E+10	0.72	98.0	83.7

Table 7 Texas Red fluorescence emission, lifetime, and calculated energy transfer efficiency in proteoliposomes with varying LHCII concentration

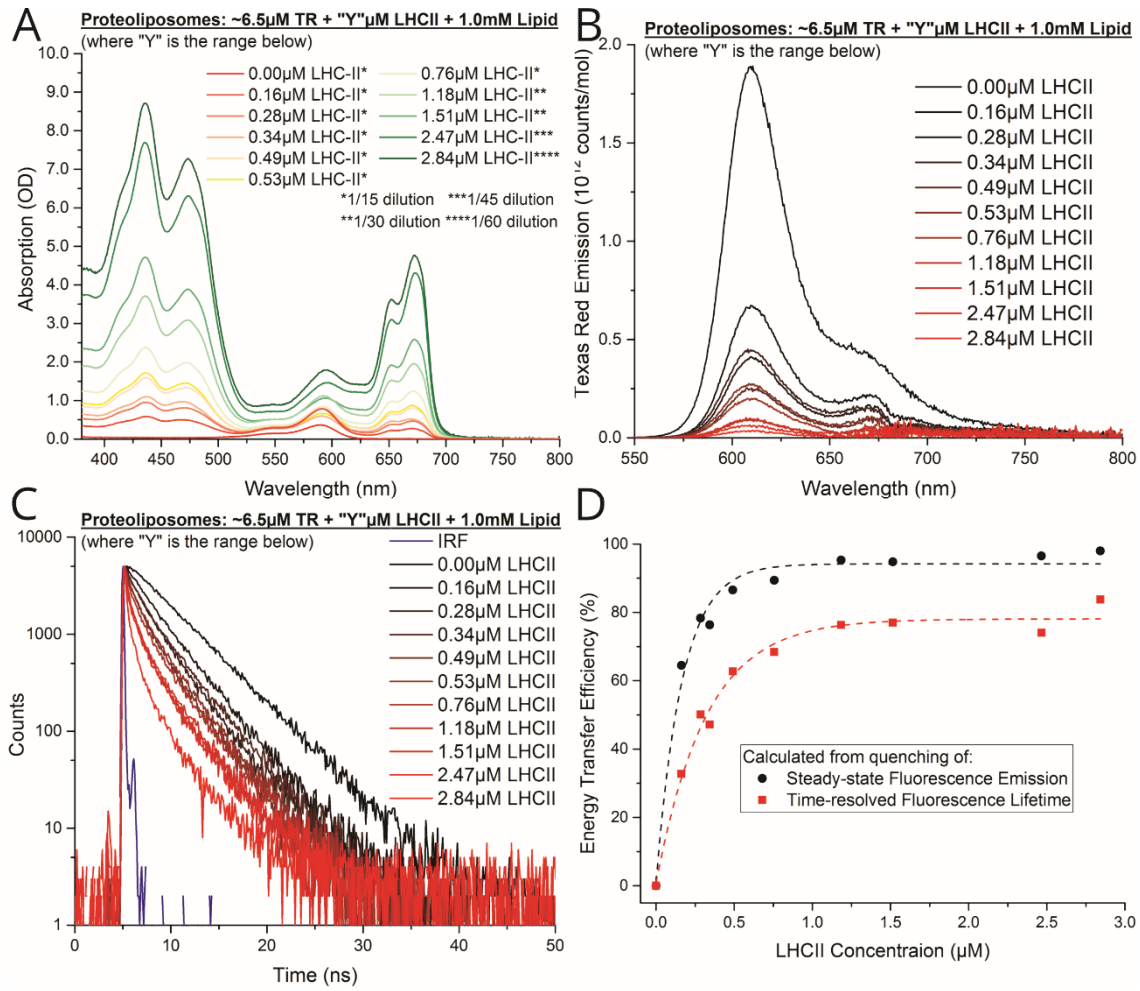

Figure 28 Steady-state and time-resolved fluorescence of Texas Red reconstituted into Texas Red-LHCII proteoliposomes with varying LHCII concentration

(A) Ensemble absorption spectroscopy of proteoliposome series with constant Texas Red and varying LHCII concentration. (B) Steady state fluorescence emission spectra of Texas Red (540 nm xenon lamp excitation) in proteoliposome sample series with constant Texas Red and varying LHCII concentration. All emission spectra are normalised to actual Texas Red concentration (the TR concentration calculated to be present in each sample from extinction coefficient and de-composition analysis of absorbance spectra, as in section 3.4.2) giving a value of emission per mole to show relative quenching at different LHCII concentrations. LHCII emission has been removed as described in 3.4.2 for visual clarity. (C) Time resolved fluorescence data of Texas Red (540 nm pulsed laser excitation) in proteoliposome sample series with constant Texas Red and varying LHCII concentration. Amplitude weighted lifetime (<τ>) of Texas Red calculated from each decay curve is displayed in legend. (D) Energy Transfer Efficiency (ETE) versus

LHCII concentration, calculated from proteoliposome series with constant Texas Red and varying LHCII concentrations. ETE is calculated from both steady-state and time-resolved data using the conventional relationship for FRET as described in Equation 22 and Equation 23 from donor emission and lifetime with and without acceptor.

3.4.4 LHCII fluorescence emission is enhanced due to energy transfer from Texas Red

If additional energy is transferred to LHCII from Texas Red in proteoliposomes, "enhancement" of LHCII fluorescence emission intensity would be expected in addition to the quenching of Texas Red fluorescence due to energy being transferred from one component to the other. When isolated LHCII is excited at 540 nm, where LHCII absorption is low, a minimal level of LHCII fluorescence is observed. Enhancement of LHCII fluorescence due to energy transfer from Texas Red was quantified by calculating relative LHCII fluorescence 'per mole LHCII' when excited at 540 nm (selective excitation for TR), for a series of proteoliposomes where we aimed for a constant LHCII and varying Texas Red concentration. As shown in Figure 29 (A), the LHCII Chl *a* and *b* Q_y peaks at 650-675 nm are largely consistent between samples while the Texas Red absorption peak at 591 nm increases incrementally. The accurate determination of LHCII concentration in 3.3.4 allowed slight sample-to-sample differences to be corrected for meaning the relative fluorescence of LHCII could be quantified. Qualitatively, in Figure 29 (B), LHCII emission is clearly enhanced with increasing TR concentration (from dark green to light green). The relative emission of LHCII excited at 540 nm increases from 1.03 $x10^{14}$ counts / mol in the absence of Texas Red to 2.96 $x10^{14}$ counts / mol at the highest Texas Red concentration in this series of 12.4 µM. Energy transfer efficiency between Texas Red and LHCII was found to be consistently between 70-80 % with no clear dependence on Texas Red concentration, as shown in Figure 29 (D). All data for calculated LHCII and Texas Red emission intensity and calculated FRET efficiencies is displayed in .

Relative fluorescence emission of LHCII reconstituted into proteoliposomes plotted against Texas Red concentration is shown in Figure 29 (C). In this representation of the

data LHCII self-quenching is taken into consideration. 100 % LHCII emission was calculated by taking the known phenomenon of concentration dependent LHCII self-quenching when reconstituted into proteoliposomes into account, described in 3.3.6. The relative self-quenching of LHCII in each proteoliposome sample is calculated by measuring LHCII fluorescence emission with selective LHCII excitation (473 nm) in comparison to LHCII isolated in detergent micelles as described in section 3.3.6. shows the values of relative LHCII emission before and after taking LHCII self-quenching into account. This allows the enhancement in LHCII fluorescence due to energy transfer from Texas Red to be assessed independently from the effects of LHCII-LHCII interactions and self-quenching. Within this range of Texas Red concentrations the enhancement of LHCII emission, when excited at 540 nm, was found to increase linearly with Texas Red concentration to a maximum of 314 % compared to LHCII-only proteoliposomes. Based on the relative number of Texas Red molecules and LHCII trimers in this sample, calculated by absorption spectroscopy, the ratio of Texas Red to LHCII is ~20:1. This translates to each Texas Red molecule effectively enhancing the emission of each LHCII trimer by ~10 %. This linear enhancement is somewhat counter-intuitive as we may expect that there would be some maximum (saturation) enhancement; this is investigated in the following section.

Sample description		ETE (steady-state)	Relative LHCII Emission	LHCII Emission Enhancement	LHCII Emission Enhancement
LHCII (μM)	TR (μM)	(%)	Integrated area 625-800 nm (540 nm Excitation)	Relative to LHCII isolated in detergent (%)	Relative to LHCII in proteoliposomes (%)
0.52	0.0	N/A	1.03E+11	43	100
0.53	0.9	82.6	1.33E+11	56	125
0.57	2.2	83.2	1.57E+11	66	150
0.55	3.7	86.3	1.76E+11	74	183
0.56	4.7	84.2	1.92E+11	81	206
0.54	6.0	87.4	2.10E+11	89	229
0.56	7.0	87.3	2.34E+11	99	253
0.57	8.5	89.5	2.47E+11	105	281
0.56	9.5	84.3	2.67E+11	113	271
0.54	11.2	90.4	2.93E+11	124	321
0.61	12.3	87.9	2.96E+11	125	314

Texas Red and LHCII fluorescence emission intensity, calculated energy transfer efficiency and LHCII enhancement in proteoliposomes with varying Texas Red concentration

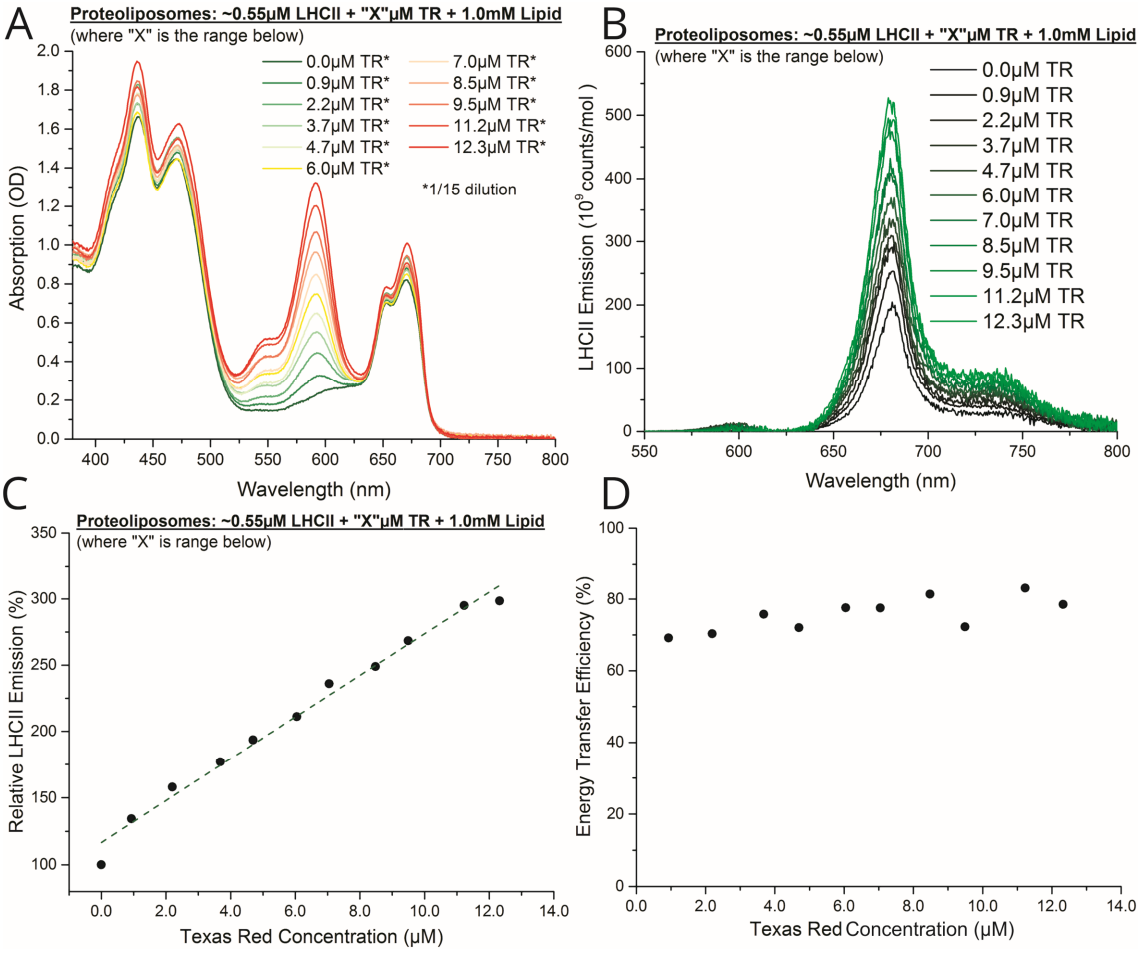

Figure 29 Steady-state fluorescence emission intensity of LHCII reconstituted into Texas Red-LHCII proteoliposomes with varying Texas Red concentration

(A) Ensemble absorption spectroscopy of proteoliposome series with constant LHCII and varying Texas Red concentration. (B) Steady state fluorescence emission spectra (540 nm excitation, 2 nm bandwidth) of LHCII in liposomes proteoliposome series with constant LHCII and varying Texas Red concentration. All emission spectra are normalised to LHCII concentration giving a value of emission per mole to show relative enhancement of fluorescence emission. Texas Red emission has been removed by digital de-composition (as described in 3.4.2) for visual clarity. (C) Relative LHCII emission versus TR concentration, calculated from proteoliposome series with constant LHCII concentration and varying Texas Red. Note, the known phenomenon of self-quenching of LHCII fluorescence, as described in 3.3.6, was quantified in control samples omitting Texas Red. Here, 100 % is defined as the baseline intensity of LHCII emission observed for proteoliposomes containing 0.55 μM LHCII and 1 mM total lipid (as this is the average LHCII content for this sample series). (D) Energy Transfer Efficiency (ETE) versus Texas Red concentration,

calculated from proteoliposome series with constant Texas Red and varying LHCII concentrations. ETE is calculated from steady-state emission quenching of Texas Red.

3.4.5 Proteoliposomes with high concentrations of Texas Red begin to show limit of LHCII enhancement

The previous section demonstrated that Texas Red to LHCII energy transfer results in a linear enhancement of LHCII fluorescence emission intensity up to a TR: LHCII ratio of 20:1. The limit of additional energy being transferred to LHCII from Texas Red in proteoliposomes was then investigated. A second series of proteoliposomes with constant LHCII and varying Texas Red concentration was formed in order to determine the maximum possible enhancement of LHCII fluorescence emission. Texas Red concentration was increased from 11.7 μM to 62.1 μM with LHCII concentration kept constant at ~0.7 μM, which represents a maximum TR: LHCII ratio of 86:1 compared to the maximum of 20:1 investigated in the sample set reported in 3.4.4. Ensemble absorption spectra of this proteoliposome sample set are shown in Figure 30 (A). At this high concentration of Texas Red labelled lipids (~6 % TR-DPHE of the total lipids, mol/mol %), Texas Red – Texas Red interactions, such as concentration dependent self-quenching and in-membrane aggregation are likely to occur as reported in section 3.3.8 and in other studies (Skaug et al., 2011). These effects could alter Texas Red to LHCII energy transfer and therefore higher concentrations of Texas Red were not investigated.

LHCII fluorescence emission when reconstituted into proteoliposomes containing high concentrations of Texas Red and excited at the lowest natural LHCII absorption of 540 nm is shown in Figure 30 (B). LHCII fluorescence emission clearly increases with Texas Red concentration from 9.01 $x10^{13}$ counts / mol in proteoliposomes with LHCII-only to a maximum of 3.28 $x10^{14}$ counts / mol at the highest Texas Red concentration of 62.1 μM. Across all samples energy transfer efficiency, calculated from quenching of Texas Red fluorescence emission, is 96-98 % consistent with the expected ETE for proteoliposomes with this LHCII concentration shown in section 3.4.3.

The trend for relative emission of LHCII against measured TR concentration, in proteoliposome samples with constant LHCII and high Texas Red concentrations is

shown in Figure 30 (C). At these high concentrations of Texas Red in proteoliposomes the fluorescence of LHCII no longer increases linearly. This suggests that there is a limit to the maximum emission 'per mol' of LHCII and that the protein is approaching its maximum fluorescence of 3.28 $x10^{14}$ counts / mol at the highest Texas Red concentration investigated here of 62.1μM. The exponential decay curve fitted in Figure 30 (C) suggests that LHCII would reach 99 % of its maximum possible enhancement of 3.40 $x10^{14}$ counts / mol at a Texas Red concentration of 93 μM in this proteoliposome system.

Relative fluorescence emission of LHCII in this proteoliposome series with high Texas Red concentrations can also be considered explicitly taking into account the measured level of LHCII self-quenching in each proteoliposome sample, as described in 3.4.4. Usually the self-quenching is very similar for a series containing similar concentrations of LHCII. However, here the level of self-quenching of LHCII significantly increases as the TR concentration increases. This suggests that somehow TR is promoting LHCII-LHCII interactions, is changing the local lipid environment, or that the excess energy being transferred into the system is causing LHCII to enter a photo-protective state. When this varying level LHCII self-quenching is considered, and the graph re-plotted as shown in Figure 30 (D), the enhancement of LHCII fluorescence emission in proteoliposomes increases almost linearly with the concentration of Texas Red. This shows that the amount of energy transferred to LHCII from each Texas Red molecule is not significantly affected by the total Texas Red concentration. The limitation of the system is instead the self-quenching of LHCII fluorescence that takes place when there are is a large number of Texas Red molecules transferring energy to LHCII.

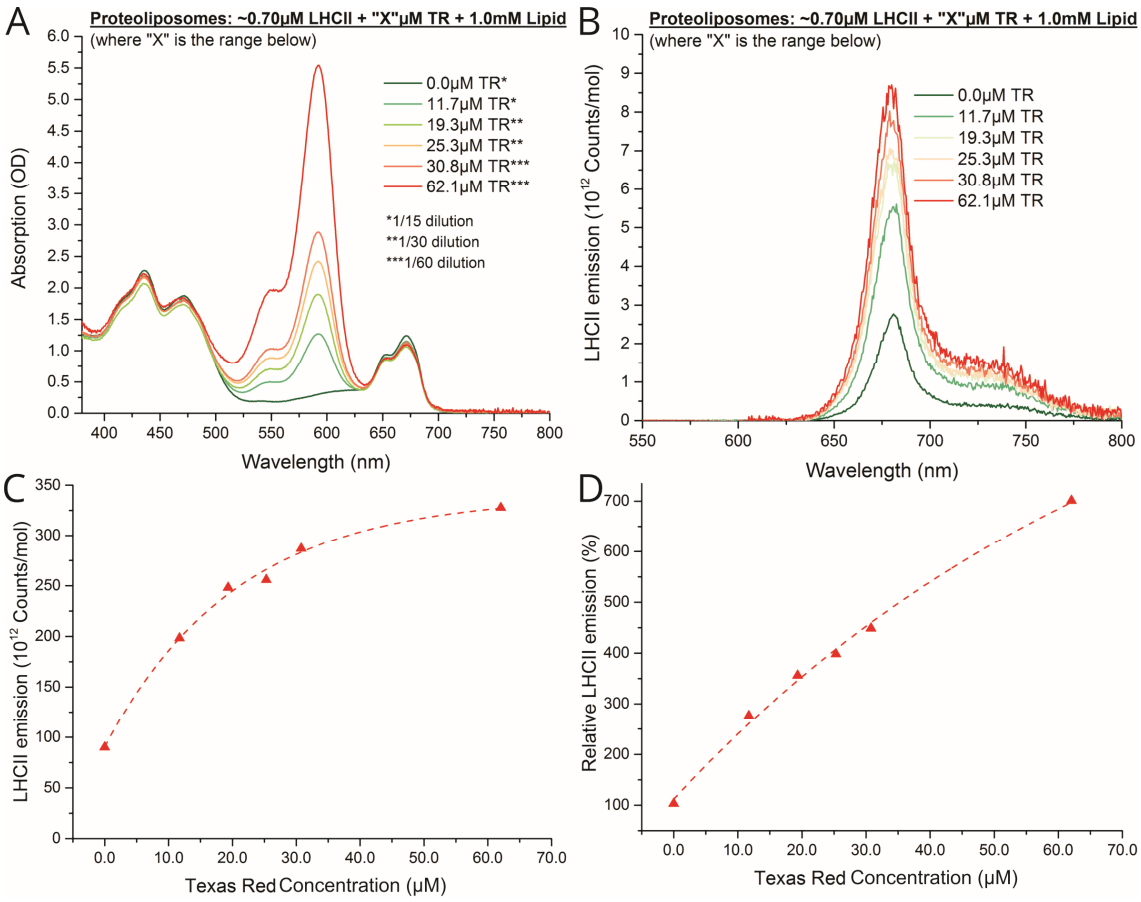

Figure 30 Steady-state fluorescence emission intensity of LHCII reconstituted into Texas Red-LHCII proteoliposomes with high Texas Red concentrations

(A) Ensemble absorption spectra of proteoliposome series with constant LHCII concentration and varying Texas Red concentration. Samples were diluted prior to measurement spectra displayed after multiplication by these factors (annotated *). (B) Steady state fluorescence emission spectra (540 nm xenon lamp excitation) of LHCII proteoliposome series with constant LHCII and varying Texas Red concentration. All emission spectra are normalised to LHCII concentration giving a value of emission per mole to show relative enhancement of fluorescence emission. Texas Red emission has been removed as described in 3.4.2 for visual clarity. (C) Graphical representation of data shown in (B) highlighting asymptotic nature of LHCII fluorescence emission increasing with Texas Red concentration. (D) LHCII emission versus Texas Red concentration, calculated from proteoliposome series with constant LHCII concentration and varying Texas Red. Note, the known phenomenon of self-quenching of LHCII fluorescence, as described in 3.3.6, was quantified for each sample using LHCII emission spectra (473 nm selective LHCII

excitation – 2 nm bandwidth). Here, 100 % is defined as the baseline intensity of LHCII emission calculated from the LHCII-only emission data

3.4.6 Solubilisation of proteoliposomes in detergent disrupts Texas Red-LHCII energy pathway and LHCII-LHCII interactions

All previous experiments studying the energy transfer from Texas Red to LHCII in proteoliposomes have assumed that changes in fluorescence intensity and lifetime in the combined system are due to interactions between Texas Red and LHCII. In order to confirm that this is the case the interactions between the fluorescent components were disrupted to demonstrate that the observed fluorescence quenching and enhancement effects were in fact due to the confined membrane architecture of proteoliposomes. The connectivity of LHCII and Texas Red in proteoliposomes can be destroyed by using a detergent which is normally used to isolate and purify the LHCII protein. This is expected to stop any energy transfer or inter-protein interactions from taking place as proteins and lipids are separated from each other as they enter into detergent micelles. Figure 31 shows the fluorescence emission spectra of a proteoliposome sample under selective Texas Red excitation (540 nm) before and after solubilisation in detergent. The detergent α-DDM is known to disrupt lipid bilayers at high concentrations (Knol et al., 1998) and will, after several minutes of mixing, isolate the majority of lipids and LHCII trimers into detergent micelles. The isolation of lipids and proteins is expected to limit any TR to LHCII energy transfer as they will be too spatially distant for efficient FRET to occur, it is also expected to disrupt any LHCII-LHCII interaction driven self-quenching.

As expected, the detergent treatment greatly diminished TR-LHCII and LHCII-LHCII interactions resulting in the regeneration of fluorescence of both components, as shown in Figure 31. Texas Red fluorescence emission intensity of detergent-solubilized proteoliposomes increased from 3 % to 75 %, as compared to a control sample of TR-DHPE prepared in detergent micelles. Relative LHCII fluorescence increased from 25 % to 87 % relative to LHCII isolated in detergent micelles. Fluorescence emission of both Texas Red and LHCII did not recover to 100 %, which may be due to photo-bleaching as spectroscopic measurements were being taken or to damage occurring when exchanging from the lipid bilayer to detergent micelles. This regeneration confirms that both LHCII

and Texas Red quenching occur due to interactions which are caused by the membrane architecture when reconstituted into proteoliposomes.

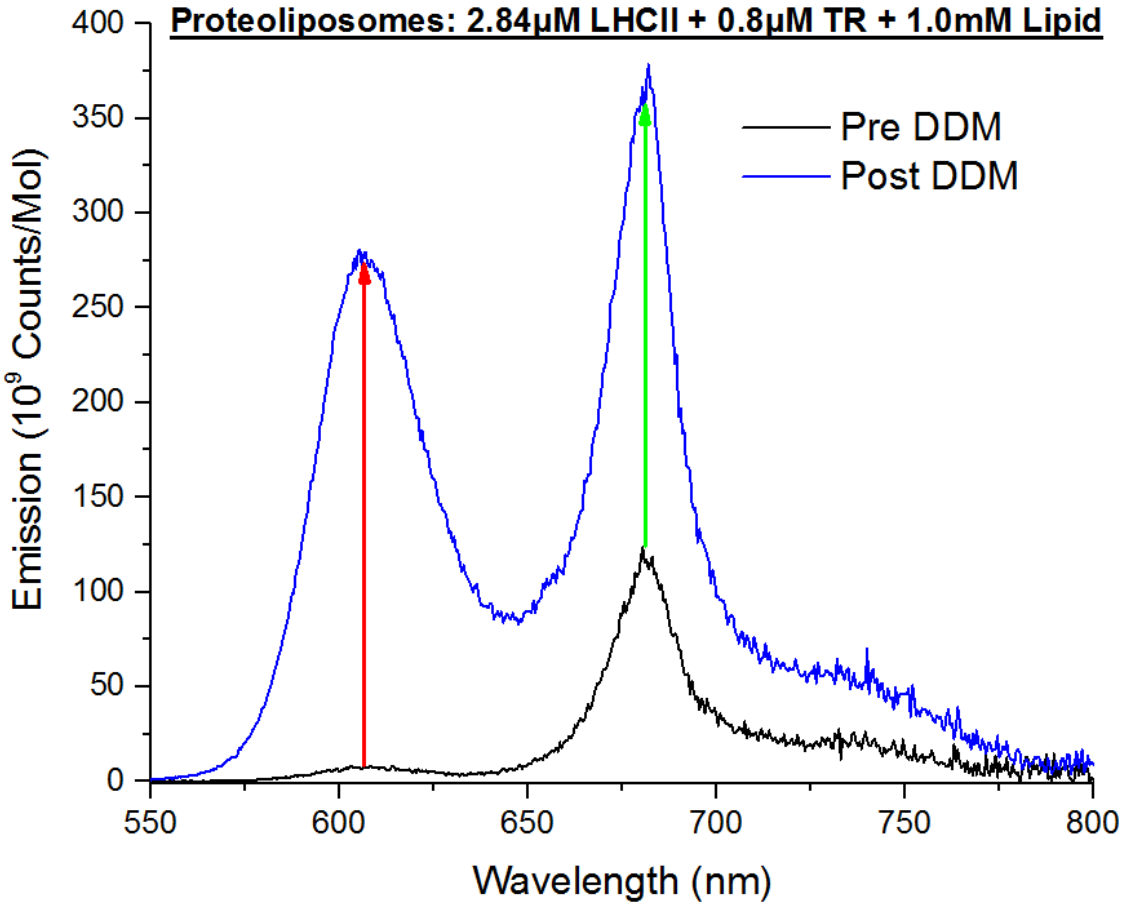

Figure 31 Change in LHCII and Texas Red steady-state fluorescence emission intensity upon destruction of proteoliposomes

Fluorescence emission spectra with selective Texas Red excitation (540 nm Xenon Source) for a representative proteoliposome sample before and after detergent solubilisation. Red and green arrows highlight the recovery of fluorescence emission for Texas Red and LHCII respectively. Emission spectra are normalised to Texas Red concentration giving a value of emission per mole.

3.4.7 Section summary and discussion

This chapter described the spectroscopic techniques used to investigate the energy transfer from the lipid tagged-chromophore Texas Red to LHCII. The characterisation of LHCII reconstituted into proteoliposomes in section 3.3 was crucial in allowing the energy transfer to LHCII to be quantified independently of LHCII self-quenching effects. Fluorescence excitation spectra in section 3.4.1 showed the effective enhancement of LHCII absorption range from 525-625 nm as increasing concentrations of Texas Red resulted in higher LHCII fluorescence when this region was excited. Comparison of LHCII fluorescence excitation spectra with linear absorption gave an estimate of energy transfer efficiency suggesting increasing efficiency with higher LHCII concentrations. This method of calculating energy transfer is often utilised when assessing energy transfer from a complementary chromophore covalently attached to a light-harvesting proteins (Yoneda et al., 2015, Harris et al., 2014b).

The efficiency of Texas Red to LHCII energy transfer was assessed in proteoliposomes. Both steady-state and time-resolved fluorescence measurements were used to quantify the quenching of Texas Red fluorescence due to energy transfer to LHCII in section 3.4.3. The decrease in Texas Red fluorescence emission intensity and lifetime as LHCII concentration was increased relates to an increase in energy transfer efficiency which was subsequently quantified using the standard FRET equations(Förster, 1965). This increase in energy transfer efficiency is attributed to a decrease in the average Texas Red to LHCII distance as the LHCII concentration within the lipid bilayer is increased. The increase in energy transfer efficiency towards a saturation point as donor concentration increases is because a higher donor concentration decreases the average donor-acceptor separation, becoming lower than the Förster radius of ~7 nm for a Texas Red/LHCII donor/acceptor pair. This result is consistent with theoretical modelling of a randomly distributed chromophores undergoing simple donor to acceptor FRET in a 2D bilayer system (assuming bilayer thickness of 3.5 nm and Förster radius of 7 nm, analogous to this system) (Subramanian et al., 2018). This suggests that both the LHCII and Texas Red are randomly distributed within the bilayer.

Texas Red effectively transferring energy to LHCII will result in an increase in excited stats of the protein which will manifest as increased fluorescence. An increase in LHCII

fluorescence emission when Texas Red was excited demonstrates the positive effect of Texas Red, as reported in sections 3.4.4 and 3.4.5. This enhancement of LHCII emission is due to the direct energy transfer from Texas Red when both components are reconstituted into proteoliposomes. If LHCII self-quenching is corrected there is a linear relationship between enhancement of LHCII emission and Texas Red concentration, which shows that each Texas Red molecule in the system is transferring energy to LHCII at a consistent rate. However, by quantifying the absolute fluorescence emission of proteoliposomes with very high Texas Red concentrations, in section 3.4.5, there is a limit to the enhancement possible from Texas Red energy transfer. The limitation of the maximum amount of LHCII fluorescence is most likely due to a form of photo-protective LHCII self-quenching. It could also be limited by lipid-tagged Texas Red aggregating at high concentrations in lipid bilayers (Skaug et al., 2011). Very small distances between Texas Red molecules could cause excessive self-quenching which would also limit the amount of energy available to be transferred to LHCII.

3.5 Concluding Remarks

In this chapter the effective absorption efficiency of LHCII has been more than threefold enhanced in the region of its natural minimal absorption. This is achieved by using a proteoliposome-based system incorporating the complementary lipid-tagged chromophore Texas Red DHPE. The concentration of both LHCII was varied from 0.16 μM to 2.84 μM and Texas Red from 0.9 μM to 62.1 μM, which shows the modularity of proteoliposomes as a medium for protein and lipid dye reconstitution. Future studies could incorporate a suite of different organic chromophores into lipid bilayers to interact with light-harvesting proteins and enhance their spectral range further. These could include lipophilic dyes which sit in the bilayer hydrophobic envelope (Klausner and Wolf, 1980), and/or quantum dots (Zheng et al., 2014). Energy transfer between TR and LHCII in proteoliposomes was highly efficient and comparable to systems utilising covalent attachment of chromophores to light harvesting proteins of 80-95 % (Gundlach et al., 2009, Harris et al., 2014a, Yoneda et al., 2015, Springer et al., 2012),and is consistent with theoretical modelling of a system that has a random distribution of chromophores throughout a 2D lipid bilayer undergoing simple donor-to-acceptor FRET (Subramanian et al., 2018). The results in this chapter demonstrate the modularity, consistency, and potential for highly efficient energy transfer of the self-assembled LHCII-chromophore

proteoliposome system. In the subsequent chapters the functionality of these proteoliposomes deposited onto surfaces both as individual particles and 'thick' multilayers will be discussed in addition to investigations into the dynamics of energy transfer between Texas Red and LHCII using ultrafast spectroscopy.

4 Results: Enhanced Absorption of LHCII in Surface Deposited Membranes

4.1 Motivation and background

Chapter 3 discussed development and characterisation of a proteoliposome system that significantly enhances the absorption cross section of the photosynthetic light-harvesting membrane protein LHCII using lipid-tagged chromophores. Absorption spectroscopy was utilised to assess the incorporation of LHCII and Texas Red into proteoliposomes, and the combination of steady-state and time-resolved fluorescence spectroscopic techniques allowed the calculation of the energy transfer efficiency. These methods focus on ensemble measurements of proteoliposomes in solution. This chapter will utilise microscopy techniques to assess individual proteoliposomes and their functionality when deposited onto solid surfaces.

Cuvette based absorption and fluorescence spectroscopy allows the composition and fluorescence state of Texas Red and LHCII reconstituted into proteoliposomes to be assessed in bulk, but they do not provide information regarding the population distributions or the composition of individual particles. As such, we investigated the degree of co-reconstitution of Texas Red and LHCII at the level of single proteoliposomes to assess the distribution (rather than merely the average) and to find whether sub-populations of irregular liposomes were present. Fluorescence microscopy is used to determine the co-localisation of LHCII and Texas Red within individual proteoliposomes when deposited onto a surface at low concentration. The distinct absorption and emission wavelengths of LHCII and Texas Red allow the fluorescence intensity of each component to be identified separately using a microscope configuration with dual-channel excitation and detection. Fluorescence microscopy is commonly used to determine co-localisation of probes in biomedical research (Dunn et al., 2011). It has also been utilised to quantify both the relative amounts both fluorescently tagged lipids and the naturally fluorescent photosynthetic membrane proteins in lipid bilayers (Tutkus et al., 2018). Fluorescence microscopy can also be used as a rough guide of the size of particles on a surface through

measurements of fluorescence intensity (Robson et al., 2018). It is possible to determine the size of single liposomes below the resolution limit of optical microscopy (~300 nm) by measuring the intensity of membrane reconstituted fluorescent dyes (Lohse et al., 2008, Larsen et al., 2011), or proteins (Tutkus et al., 2018). However, in Texas Red-LHCII proteoliposomes both components undergo significant changes in fluorescence intensity due to Texas Red to LHCII energy transfer, meaning that for this system the intensity of fluorescence cannot be used to determine proteoliposome sizes below the optical resolution. Fluorescence microscopy data can therefore only provide an indication of proteoliposome size, as the particles observed as diffraction limited spots can be assumed to be below ~300 nm in diameter.

Enhancing the effective absorption of a photosynthetic light-harvesting antenna with lipid tagged dyes relies on both tagged-lipids and proteins being evenly distributed in the membrane. If proteoliposomes are formed with significant aggregates of either Texas Red or LHCII energy transfer between them will be affected. Consequently, we determined the spread of Texas Red to LHCII energy transfer efficiencies within proteoliposome populations to identify the presence of Texas Red or LHCII aggregation. Fluorescence lifetime imaging microscopy (FLIM) allows both the fluorescence intensity and fluorescence lifetime of chromophores to be measured. Lifetime data provides additional information on the excited state of samples independent of the concentration deposited onto surfaces. FLIM can be used to determine the level of fluorescence quenching of light-harvesting proteins reconstituted into individual proteoliposomes (Natali et al., 2016). In this chapter, FLIM will be utilised to determine the fluorescence intensity and lifetime of both LHCII Texas Red reconstituted into proteoliposomes and deposited onto surfaces. The level of Texas Red fluorescence quenching due to energy transfer to LHCII is used to determine the efficiency of energy transfer on an individual proteoliposome level. This is analogous to the energy transfer efficiencies calculated for ensemble fluorescence spectroscopy data in section 3.4. This enables the distribution of energy transfer efficiencies to be determined over a population of proteoliposomes, as opposed to the ensemble averages calculated using cuvette-based spectroscopy.

The transfer of energy from lipid tagged Texas Red to LHCII must be retained when the system is deposited onto solid surfaces if it is to have future applications in light-harvesting devices. If the addition of complementary lipid-tagged chromophores to

enhance the effective absorption of LHCII has future light-harvesting device applications then it must be amenable to surfaces and retain functionality. As well as applications, having a stable and active membrane on a planar surface provides a platform which mimics the natural membrane, and is an excellent platform to assess the biophysics, because it allows high-resolution surface-based microscopy. Previous studies have shown that LH proteins attached to glass surfaces in nanoscale array patterns provide directional transfer of energy (Vasilev et al., 2014, Escalante et al., 2010), and that natural protein complexes can be coupled with electrodes to act as bio-photovoltaic devices (Kamran et al., 2014). Therefore we determined if lipid-tagged Texas Red to LHCII energy transfer was retained when proteoliposomes were deposited at high concentrations on surfaces. Energy transfer between donor and acceptor chromophores can be assessed by selectively photo-bleaching acceptor molecules and observing the recovery of donor florescence that was previously quenched by the energy transfer. Dual-channel fluorescence microscopy was used to locally photo-bleach LHCII in combined Texas Red-LHCII samples to observe fluorescence recovery of Texas Red attributed to the disruption of energy transfer. This technique has been employed previously to assess the efficiency of energy transfer between complex fluorescent nanomaterials, such as quantum dot conjugated proteins to determine the properties of quantum dot to protein energy transfer (Vinayaka and Thakur, 2011).

Next, we investigated the nanoscale architecture of Texas Red-LHCII proteoliposomes both individually and as ‘thick films’ that had been deposited onto solid surfaces. Here, thick films refer to disordered lipid/protein multilayers formed from the deposition of a high concentration of proteoliposomes onto a surface. The strategy of enhancing LHCII absorption in proteoliposomes relies on an even distribution of LHCII and Texas Red molecules within a model membrane. If proteoliposomes are able to form single bilayer thickness patches of membranes on solid surfaces it suggests that unilamellar proteoliposomes have been formed with minimal in solution-aggregation of lipids or proteins that could affect the efficiency of Texas Red to LHCII energy transfer. The nanoscale architecture of membrane ‘thick films’ will also be assessed to determine whether many layers of membranes can be densely packed onto solid surfaces, and if so whether this effects the efficiency of a protein based light-harvesting system (Ciesielski et al., 2010). Atomic force microscopy (AFM) is commonly used to study lipid bilayers due to its ability to map surface topography with sub nanometer resolution, and to probe

mechanical and chemical properties of samples through force measurements (Robson et al., 2018). AFM is also often used when studying reconstituted membrane proteins, such as photosynthetic light-harvesting proteins, as differences in membrane height can show the location and organisation of the proteins (Adams et al., 2018, Milhiet et al., 2006, Bahatyrova et al., 2004, MacGregor-Chatwin et al., 2019). AFM lithography can be harnessed to assess the thickness of soft materials such as lipid bilayers deposited onto hard surfaces, by etching away the 'soft' protein and lipid material to reveal the mica beneath allowing the depth of the layers to be determined (Lv et al., 2018) . In this chapter AFM is utilised to study the architecture of both individual and 'thick films' formed when proteoliposomes are deposited onto surfaces at low and high concentrations respectively.

Note on contributions: All proteoliposomes samples were prepared and spectroscopically imaged by AFM. All other data in this chapter were acquired by myself (e.g., epifluorescence). All FLIM data shown in this chapter were acquired by my colleague Sophie Meredith and data analysis was performed jointly. AFM data were collected by my supervisor Dr Peter Adams and analysed by AFM.

4.2 Characterising and investigating Texas Red to LHCII energy transfer in individual proteoliposomes

4.2.1 Initial sample choice and experimental design for microscopy acquisition

Three proteoliposomes samples were selected for FLIM characterisation, hereafter called 'high-LHCII', 'low-LHCII' and 'no-LHCII', selected to display the effect of different LHCII concentrations on Texas Red fluorescence and efficiency of energy transfer. These samples had initial concentrations of 2.84 μM LHCII + 9.4 μM Texas Red, 1.15 μM LHCII + 9.3 μM Texas Red and 6.5 μM Texas Red, respectively (all with 1 mM total lipid concentration), as determined by the absorption spectroscopy and graphical analysis described in section 3.3.3. When deposited onto surfaces the absolute concentrations of lipid, LHCII and Texas Red will change due to dilution and are therefore not a meaningful method of comparing samples. Ratios of lipids to fluorescent components are shown in Table 8. Samples were fully characterised by steady-state and time-resolved spectroscopy as described in 3.4. Energy efficiency was calculated as 96 % and 87 % from steady-state and time-resolved data for high-LHCII proteoliposomes and as 92 % and 81 % for low-LHCII proteoliposomes. This is consistent with other proteoliposome samples investigated in section 3.4 with higher LHCII concentration resulting in higher energy transfer efficiency due to a shorter average donor-acceptor separation.

Sample description	Calculated concentration		DLS Diameter	Lipid: protein	Lipid: dye	Dye: protein
	LHCII (μM)	TR (μM)	(nm)	ratio	ratio	ratio
High-LHCII	2.84	9.4	138	352	106	3
Low-LHCII	1.15	9.6	64	870	108	8
No-LHCII	0.00	6.5	52	-	154	-

Table 8 Ratios of lipids to fluorescent components in representative proteoliposome samples for FLIM analysis

Briefly, microscopy samples were prepared by diluting proteoliposomes, formed as described in section 2.3.3, and incubating onto piranha cleaned glass at a 1/50 dilution (20 μM Lipid). After initial incubation samples were washed to remove any excess proteoliposomes which were in solution to leave only particles absorbed onto the glass surface. All samples were images under a droplet of aqueous buffer. FLIM imaging was

performed using dual pulsed excitation lasers (sequential) and dual detectors to allow LHCII and Texas Red signals to be collected independently and simultaneously. LHCII was selectively excited at 485 nm and emission collected at 670-690 nm, Texas Red was selectively excited at 561 nm and emission collected at 620-635 nm, and the full microscopy set up is detailed in methods 2.5.2. Several adjustments had to be made to measurements to allow a fair comparison of LHCII and Texas Red signals. These corrections include taking into account background counts, spectral overlap, bleed-though of LHCII emission into Texas Red detector and vice versa, and the effect of different rates of fluorophore bleaching. All of these correction factors are described in the following sections as appropriate.

4.2.2 FLIM fluorescence intensity data shows co-localisation of LHCII and Texas Red within individual proteoliposomes

In order to assess the formation of Texas Red-LHCII proteoliposomes it is crucial to ensure that the majority of proteoliposomes contain both LHCII and Texas Red. The design of the proteoliposome system is that energy absorbed by lipid-tagged Texas Red is transferred to LHCII, which relies on the co-reconstitution of lipid-tagged Texas Red and LHCII into the same model membrane. Using ensemble spectroscopy the concentration of different fluorescent components can accurately be assessed but direct measurement of co-localisation is not possible. The co-reconstitution of LHCII and Texas Red in individual proteoliposomes was directly measured using dual channel fluorescence microscopy. The co-localisation of LHCII and Texas Red fluorescence signals in proteoliposomes was assessed using FLIM. Here, we used the FLIM microscope because it is our highest performance system (resolution, signal-to-noise), but focussed on the fluorescence intensity signal and not the time-resolved data (these were analysed independently, see section 4.2.3). Proteoliposome samples were prepared, and microscopy was performed, as described in the previous section. Proteoliposomes were analysed on an individual particle basis with the fluorescence intensity signal in both LHCII and Texas Red channels measured for each pixel. This signal was then corrected by subtracting background counts and detector bleed-through to give a ‘corrected signal’ for LHCII and Texas Red per pixel. Background signal is typically ~10 counts per pixel over the course of a measurement, 1.0 % of the “Texas Red channel” signal appears in

the “LHCII channel” and 7.5 % of the “LHCII channel” signal appears in the “Texas Red channel” due to overlaps in emission spectra. A representative image of ‘high-LHCII’ proteoliposomes used for co-localisation analysis is shown in Figure 32 with (A+B), (C+D) and (E+F) showing LHCII, Texas Red and composite florescence channels respectively. For each channel two images are shown with different intensity ranges, (A,C,E) LHCII: 2-25, Texas Red: 0-225 counts (B,D,F) LHCII: 2-75, Texas Red: 0-600 counts, to allow clear comparison. Qualitatively, it is clear that many of the green and red particles are overlapping suggesting co-localisation. This visual representation alone is inadequate and could under-represent the true co-localisation as some particles have significantly higher or lower overall signal than others.

A careful manual analysis of individual particles was performed where the total intensity from the pixels representing a single particle (manually chosen) was recorded and detector bleed-through and background signal was removed as described above. Representative data from this analysis is shown in Table 9. The maximum intensity for particles in each channel ranged from 18-250 (mean= 79) for LHCII and from 66-2610 (mean= 1010) for Texas Red. Analysis of the co-localisation of LHCII and Texas Red fluorescence intensity on individual proteoliposomes show at least 83 % and 80 % of proteoliposomes had significant signal from both Texas Red and LHCII emission channels, for low-LHCII and high-LHCII samples, respectively (n = 200). Significant signal was defined as x10 background counts for Texas Red intensity and x2 background counts for LHCII, giving thresholds of 100 counts and 20 counts for Texas Red and LHCII signals, respectively. This may underestimate the presence of LHCII as the signal is much lower and smaller vesicles with few LHCIIs may not be detected.

Fluorescence microscopy can be used to estimate the size of proteoliposomes deposited onto surfaces. Although the majority of proteoliposomes are beneath the optical resolution of light-microscopy (~50-120 nm in diameter as assessed by dynamic light scattering in section 3.3.7), microscopy can be used to determine if there are proteoliposomes larger than the diffraction limit of ~300 nm. It is difficult to determine if liposomes have remained intact when deposited onto a surface using fluorescence microscopy with this resolution limit. If proteoliposomes are intact then a double bilayer will be formed with a radius 2x larger than the radius of the proteoliposome in solution. Alternatively, proteoliposomes ‘burst’ onto the surface a single bilayer membrane patch

will form with x4 the radius of the intact proteoliposome in solution. Analysis of the full-width at half-maximum (FWHM) of fluorescence intensity across single particles was performed. This showed mean FWHM in the LHCII and Texas Red channels of 310±30 nm and 305±40 nm, respectively (for measuring n=20 representative proteoliposomes, similar to Table 9). Therefore, the majority of proteoliposomes in FLIM images are diffraction-limited spots with diameters under the resolution limit of 300 nm. This is in agreement with the likely diameters of ~50-120 nm calculated with DLS.

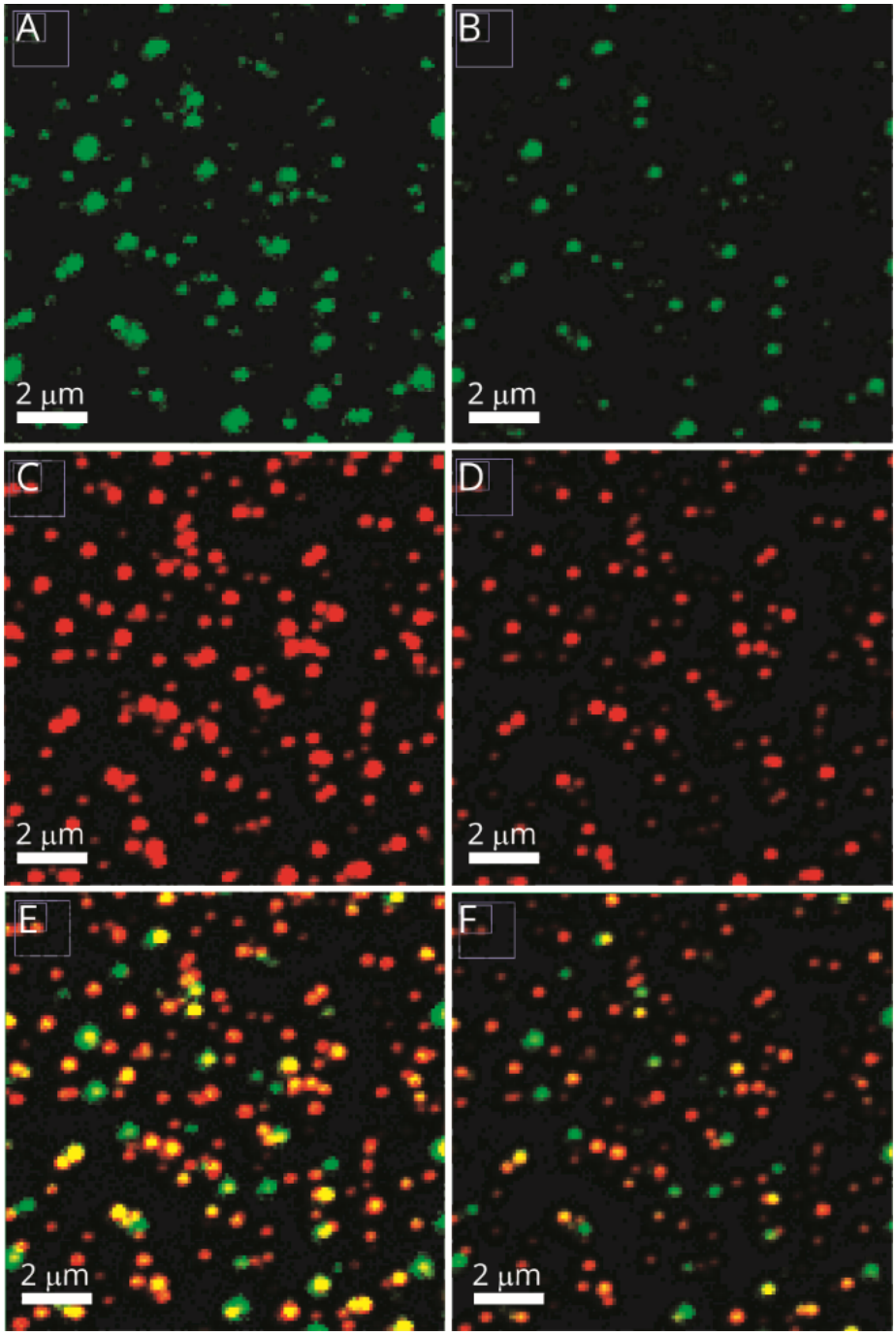

Figure 32 Representative dual-channel intensity only FLIM images of Texas Red-LHCII proteoliposomes deposited onto a glass substrate at low concentration

Confocal fluorescence microscopy images of a representative field from a "high-LHCII" proteoliposome sample (2.8 µM LHCII, 6.5 µM TR, 1 mM total lipid) deposited at low surface density. Panels show the fluorescence intensity in either the LHCII channel, TR channel, or a Composite (both overlaid). Panels (A,C,E) show a compressed intensity range (for clarity); panels (B,D,F) show the full intensity range. Yellow colour in the composite image indicates strong co-localisation of signals from LHCII and TR.

Particle number	Pixels in particle	LHCII Raw Signal	LHCII corrected Signal	Above LHCII threshold	TR Raw Signal	TR Corrected Signal	Above Texas Red threshold	Co-localised
#	#	Counts	Counts		Counts	Counts		
1	42	204	102	Yes	10572	10561	Yes	Yes
2	32	88	47	Yes	3903	3897	Yes	Yes
3	21	284	259	Yes	2364	2351	Yes	Yes
4	39	40	-10	No	4760	4756	Yes	No
5	30	111	78	Yes	3047	3041	Yes	Yes
6	20	115	100	Yes	1287	1281	Yes	Yes
7	23	67	43	Yes	2255	2251	Yes	Yes
8	34	40	15	No	2053	2049	Yes	No
9	63	563	430	Yes	13605	13578	Yes	Yes
10	57	1557	1484	Yes	7054	6986	Yes	Yes

Table 9 Representative LHCII and Texas Red emission intensity for co-localisation. If a particle was determined to have "corrected" LHCII signal > 20 counts and also TR signal >10 counts, then it was classified as co-localised

4.2.3 Single proteoliposome analysis by FLIM allows populations of Texas Red fluorescence lifetimes to be determined

Ensemble spectroscopic characterisation of Texas Red-LHCII proteoliposomes allows the efficiency of energy transfer between Texas Red and LHCII to be quantified for samples in bulk. However, these average measurements over millions of particles do not give any information on sample population distributions which may contain sub-populations exhibiting higher, or lower, levels of Texas Red to LHCII energy transfer. FLIM allows the fluorescence lifetimes of both LHCII and Texas Red to be determined in individual proteoliposomes absorbed onto glass surfaces. Proteoliposome samples were assessed using a dual excitation, dual detection system where LHCII and Texas Red fluorescence emission intensity and lifetime are collected independently. Representative FLIM images of the high-LHCII, low-LHCII and no-LHCII samples are shown in Figure 33 (A), (B) and (C), respectively, with two areas of each samples shown in both channels. Two sets of information are displayed in FLIM images: (i) the brightness of pixels is directly proportional to the intensity of fluorescence emission measured in that channel, (ii) the colour of the pixel represents the fluorescence lifetime measured, more red pixels have a longer lifetimes and blue pixels shorter.

In the no-LHCII liposome sample, shown in Figure 33 (A), there is very little signal in the LHCII channel. This minimal signal observed can be attributed to the spectral overlap of the emission filters and detectors (quantified overlap of <1 % of the Texas Red signal which is taken into account during subsequent analysis). In the Texas Red channel, the lifetime is usually high (3-4 ns) as is expected for non-quenched Texas Red; this is represented by the "red" colouration in the false-colour mapping of the FLIM images. In the proteoliposome samples, shown in Figure 33 (B+C), LHCII signal is clearly observed for both samples with a high degree of co-localisation with the corresponding Texas Red signal (99 % confidence that LHCII signal is above the Texas Red spectral overlap and noise thresholds, as discussed in section 4.2.2). The presence of LHCII in both of these samples was found to correspond to a quenching of the Texas Red fluorescence emission intensity and lifetime. This is observed qualitatively as the shorter lifetimes appear "bluer" in the FLIM false-colour mapping, as compared to no-LHCII sample (Texas Red-only liposomes). The sample with high-LHCII concentration on average appears to have shorter "bluer" Texas Red lifetimes and lower Texas Red intensities compared to the low-LHCII concentration sample. This provided an initial indication of the higher extent of donor quenching in the presence of a higher LHCII concentration. However, the variety of proteoliposomes and corresponding lifetimes within one field of view presents the need for a comprehensive single-particle analysis as discussed in the next section.

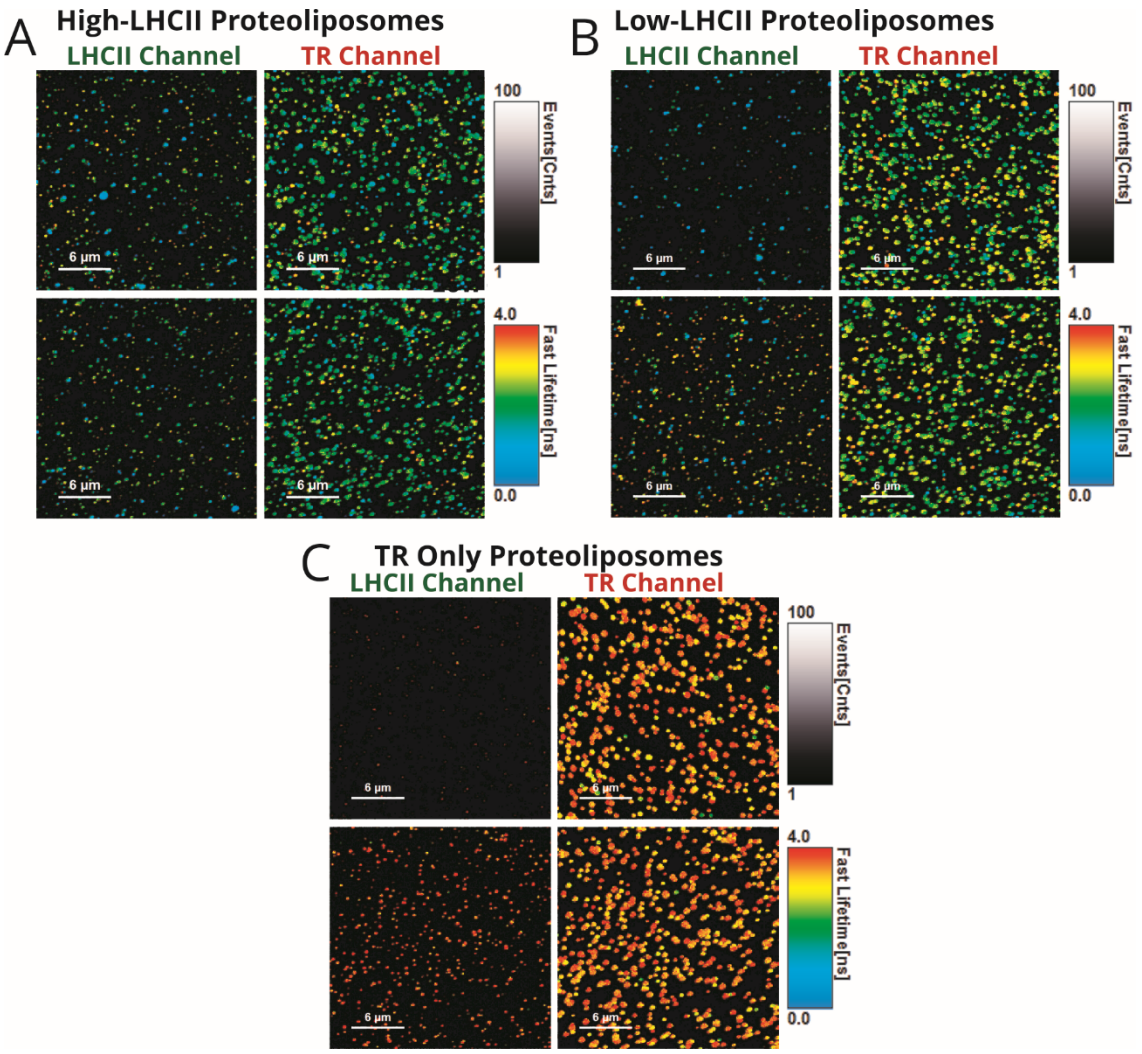

Figure 33 Representative dual-channel FLIM images showing both fluorescence intensity and lifetime data of proteoliposomes deposited onto a glass substrate at low concentration

Gallery of FLIM images showing fluorescence intensity (pixel brightness) and fluorescence lifetime (pixel colour) data for proteoliposome samples deposited onto glass coverslips. All samples contain 1 mM total lipid concentration and the following concentrations of LHCII and Texas Red calculated via absorption spectroscopy. (A) 'high-LHCII' 2.84 µM LHCII 9.4 µM Texas Red (B) 'low-LHCII' 1.15 µM LHCII 9.3 µM Texas Red (C) 'no-LHCII' 6.5 µM Texas Red (i.e. Texas Red liposomes). Two images of different imaged areas (top and bottom) are shown for each sample. The "fastFLIM" mode leads to a "FastLifetime" which is an estimate of the average fluorescent lifetime of a pixel based on the average 'time of flight' from excitation pulse to emission.

The intensities of LHCII and Texas Red signal from each particle were measured as described in section 4.2.2 to produce a "corrected signal" taking background noise and detector bleed-through into account. Only well-resolved proteoliposomes with sufficient signal to produce a good fit were selected for lifetime analysis (criteria of counts >500 and fit chi2 <1.2). This selection process may produce inherent bias as weakly emitting particles are not included. The Texas Red amplitude-weighted mean fluorescence lifetime ($T_{average}$) was calculated from a bi-exponential decay function fitted to the produced fluorescence decay curves of each defined proteoliposome particle (accumulated pixels). A_1, T_1 and A_2, T_2 represent the amplitude (A) and lifetime (T) of the two exponential components. The chi2 fit quality parameter is shown (chi2 <1.2 represents a good fit). The mean Texas Red fluorescence lifetime decreases from 3.26 ± 0.46 ns in control no-LHCII liposomes to 1.46 ± 0.53 ns and 1.79 ± 0.64 ns for high-LHCII and low-LHCII proteoliposomes respectively, with a standard image acquisition time. The intensity and lifetime of both LHCII and Texas Red components of representative proteoliposomes from the high-LHCII sample are displayed in Table 10. Figure 34(A) shows both intensity and lifetime FLIM data for an area of high-LHCII proteoliposomes. Figure 34(B) shows the bi-exponential decay fits used to calculate $T_{average}$ for each of the proteoliposomes highlighted in (A). These fluorescence lifetime measurements reveal the quenched state of Texas Red molecules independently of the emission intensity which is dependent on the concentration of fluorophore deposited onto the surface. This is used to allow energy transfer efficiency to be calculated on individual particles in the next section.

Particle number	Pixels in particle	TR A_1	TR A_2	TR T_1	TR T_2	TR $T_{average}$	TR χ^2
#	#	Counts	Counts	ns	ns	ns	
1	42	560	355	2.17	0.00	1.33	0.96
2	32	61	20	0.76	2.70	1.22	0.96
3	21	24	-87	2.30	0.03	0.84	1.01
4	39	894	243	2.44	0.00	1.90	0.97
5	30	102	96	2.70	0.74	1.76	1.04
6	20	180	17	0.93	3.00	1.20	0.71
7	23	155	345	3.20	1.30	1.91	1.17
8	34	74	6	1.40	4.70	1.60	0.76
9	63	570	1000	2.50	0.77	1.40	1.01
10	57	288	1200	2.40	0.67	1.00	1.06

Table 10 Examples of Texas Red lifetime analysis on single proteoliposomes

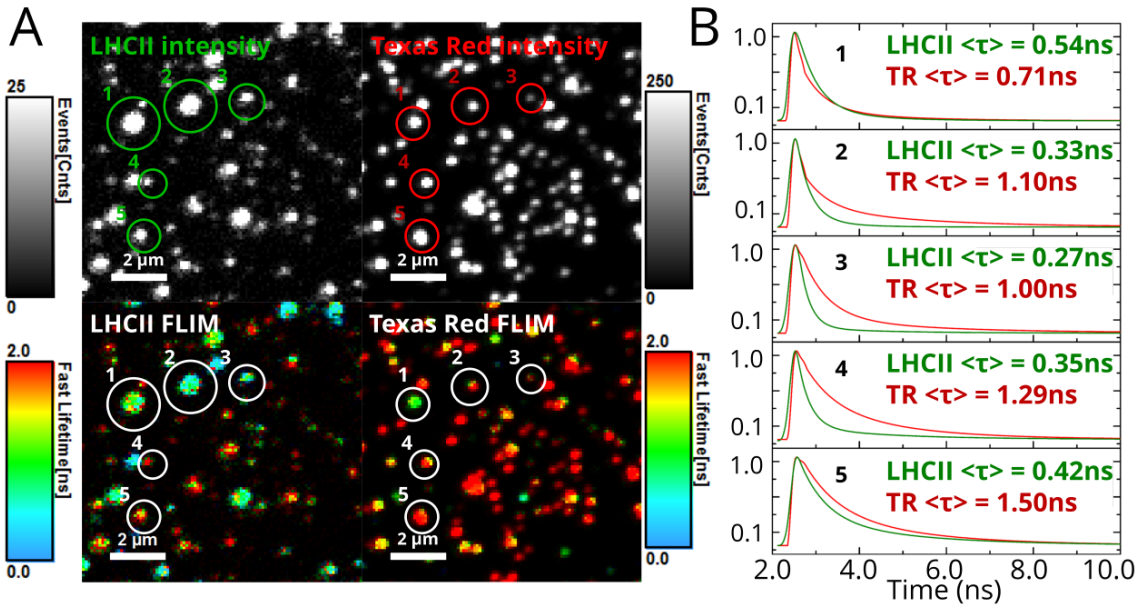

Figure 34 Representative dual-channel fluorescence intensity and lifetime FLIM images of single proteoliposome analysis

FLIM data from proteoliposomes deposited at a low surface density on glass coverslips, displaying both fluorescence intensity (brightness) and "fastFLIM lifetime" (colour scale). (A) Representative field from a high-LHCII proteoliposome sample (2.8 µM LHCII, 6.5 µM TR, 1 mM total lipid) imaged at high magnification, comparing fluorescence intensity (top) versus fluorescence lifetime (bottom) between LHCII and TR channels. Five representative particles have been indicated 1–5. The "fastFLIM" mode leads to a "FastLifetime" which is an estimate of the average fluorescent lifetime of a pixel based on the average 'time of flight' from

excitation pulse to emission. (B) Fluorescence decay curve fits from the individual proteoliposomes, as numbered in (A), annotated with the calculated mean amplitude-weighted lifetimes ⟨τ⟩ of each component. Here, the fluorescence data from the 20–30 pixels representing one proteoliposome were binned, a decay curve generated, and fit to a biexponential decay function.

4.2.4 Calculating energy transfer efficiency on a single proteoliposome level

Determining the fluorescence lifetime of Texas Red in each proteoliposome allows the energy transfer efficiency between Texas Red and LHCII to be calculated on a per-proteoliposome basis. First, the effect of different rates of LHCII and Texas Red photo-bleaching must be taken into account as other experiments show that a quenching of LHCII leads to an increase in Texas Red fluorescence (described in section 4.3). This effect is corrected for to provide a more reliable estimate for Texas Red lifetime and to allow accurate calculations of FRET efficiency to be made for individual proteoliposomes. The Texas Red mean lifetime was quantified over the entire field of proteoliposomes within the initial 170 s of an acquisition where the overall LHCII bleaching was relatively low (frames 1 – 50). This was compared to the mean lifetime measured over the full acquisition period in which LHCII had undergone a greater degree of bleaching (frames 1 – 500). From this, the Texas Red lifetime change due to LHCII photo-bleaching was determined to be: a 53 % increase for the high-LHCII proteoliposomes and a 52 % increase for low-LHCII proteoliposomes, shown as the "Ratio" in Table 11, below. Single-proteoliposome analysis was performed on the full 1-500 frames of data, which was necessary to provide a large enough photon count level to allow an adequate decay curve for a good fit to be made (typically 3000 counts with a range from 1000-10000). The data without any correction applied is shown in Figure 35 (A). These raw values for Texas Red mean lifetime were then adjusted by dividing by the appropriate value for Texas Red lifetime change due to LHCII photo-bleaching as defined above (0.52 and 0.53), to give an approximation of the mean Texas Red lifetime unbiased by photo-bleaching effects, the so-called "corrected lifetimes" shown in Figure 35 (B). The average measured raw Texas Red fluorescence lifetimes of 1.46 ± 0.53 ns and 1.79 ± 0.64 ns are reduced by the correction to 0.77 ± 0.28 ns and 0.89 ± 0.33 ns for high-LHCII and low-LHCII samples, respectively. Energy transfer efficiency (ETE) was then

calculated from the corrected Texas Red lifetime data, using the conventional relationship shown in Equation 23.

$$ETE_{TR} = 1 - \frac{\tau_{DA}}{\tau_D}$$

Equation 23 Energy transfer efficiency as calculated from time-resolved data, τDA: Donor fluorescence lifetime in the presence of acceptor, τD: Donor fluorescence lifetime in the absence of acceptor.

A FRET efficiency was calculated for each proteoliposome particles analysed in both high-LHCII and low-LHCII samples, which was used to produce a histogram of energy transfer efficiencies shown in Figure 35 (C). A mean energy transfer efficiency is determined of 71 ± 10 % and 77 ± 8 % (error is standard deviation) for "low-LHCII" and "high-LHCII" proteoliposomes (n= 175, n= 186), respectively. This result supports the hypothesis that samples with higher LHCII concentrations will have higher Texas Red to LHCII energy transfer efficiency due to statistically shorter donor-acceptor separation (P value < 0.001 for this data), in agreement with the ensemble spectroscopy of section 3.4. Furthermore, this shows that although within a population the energy transfer efficiency varies significantly between individual proteoliposomes, both samples exhibit sub-populations with over 90 % energy transfer efficiency. This variation in energy transfer efficiency is due to different numbers of LHCII trimers reconstituted into proteoliposomes within the population. The relatively tight distributions with standard deviations of ~ 10 % suggest a more homogenous population than reported in other proteoliposome FLIM studies (Natali et al., 2016).

	High-LHCII		Low-LHCII	
Frames #	TR $\tau_{average}$ ns	Error (ns)	TR $\tau_{average}$ (ns)	Error (ns)
1-50	0.713	0.018	0.712	0.026
1-500	1.335	0.008	1.36	0.007
Ratio	0.534	-	0.524	-

Table 11 The difference in measured TR lifetime over frames 1-50 vs 1-500

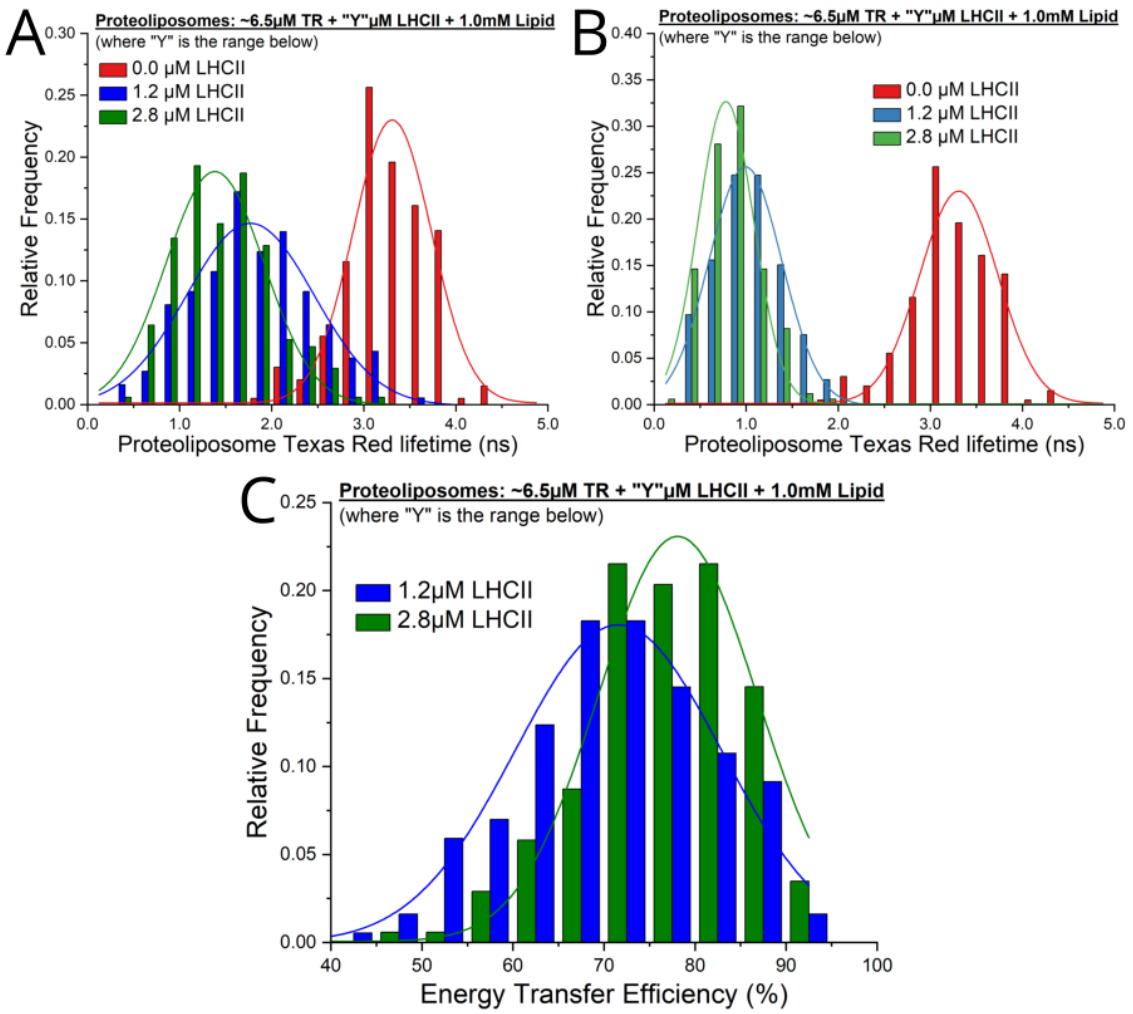

Figure 35 Histograms showing the distribution of Texas Red fluorescence lifetime and calculated energy transfer efficiency in proteoliposome samples

(A+B) Frequency distribution histogram of the mean T R fluorescence lifetime, comparing the low-LHCII proteoliposome, high-LHCII proteoliposome and TR liposome Frequency distribution histogram of the mean TR fluorescence lifetime, comparing the 'high-LHCII' proteoliposome, 'low-LHCII' proteoliposome and no-LHCII liposome samples (n = 175, 186 and 200, respectively). Only well resolved proteoliposomes with sufficient signal to produce a good fit were selected (counts >500; fitting $chi^2 < 1.2$). Gaussian distributions have been fitted to each of the spectra for visual clarity. (A) Uncorrected Texas Red lifetimes (B) Corrected Texas Red lifetimes (C) Frequency distribution histogram of the energy transfer efficiency, calculated as in Equation 23 using the data from Figure 35 (B). Gaussian distributions have been fitted to each of the spectra for visual clarity.

4.3 Photo-bleaching of LHCII results in the recovery of Texas Red fluorescence intensity and lifetime due to the disruption of energy transfer

4.3.1 Investigating energy transfer through selective acceptor photo-bleaching

An important principle in the design of Texas Red-LHCII proteoliposomes to enhance the effective absorption of LHCII by use of lipid-tagged Texas Red is the amenability of membranes to surfaces. It was therefore crucial to quantify the retention of efficient Texas Red to LHCII energy transfer for proteoliposomes deposited onto surfaces. When Texas Red to LHCII energy transfer is taking place there is a significant reduction of Texas Red fluorescence emission and a concomitant shortening of fluorescence lifetime compared to Texas Red in the absence of LHCII, as shown comprehensively for proteoliposomes in solution (via steady-state and time-resolved fluorescence spectroscopy in section 3.4). The level of Texas Red fluorescence emission and lifetime quenching are proportional to the efficiency of energy transfer. This effect has also been demonstrated with single proteoliposomes deposited onto a surface using FLIM in the previous section. Selective LHCII photo-bleaching allows the quenching of Texas Red due to energy transfer to LHCII to be indirectly assessed without the need of Texas Red-only controls. By intentionally photo-bleaching LHCII, using the appropriate excitation wavelengths, the protein becomes fluorescently de-activated and is no longer able to receive energy transferred from Texas Red via FRET. This results in the 'de-quenching' (i.e., fluorescence recovery) of Texas Red fluorescence as the alternative pathway for excitation energy has been removed, demonstrated in the Figure 36 schematic. It is useful to think: after LHCII has been completely photo-bleached, even combined TR+LHCII samples can be considered as "Texas Red-only" control samples (assuming no other effects acting on TR). One would predict that the higher the degree of Texas Red fluorescence recovery after LHCII photo-bleaching the higher the initial efficiency of energy transfer. This effect is shown in the following sections with FLIM on individual proteoliposomes and with epifluorescence microscopy on thick films of proteoliposomes. In this section dual channel fluorescence microscopy (both widefield epifluorescence and FLIM) probing both LHCII and Texas Red fluorescence provide a visual representation

of energy transfer through photo-bleaching experiments. These experiments allowed the photophysical functionality of proteoliposomes deposited onto surfaces to be assessed.

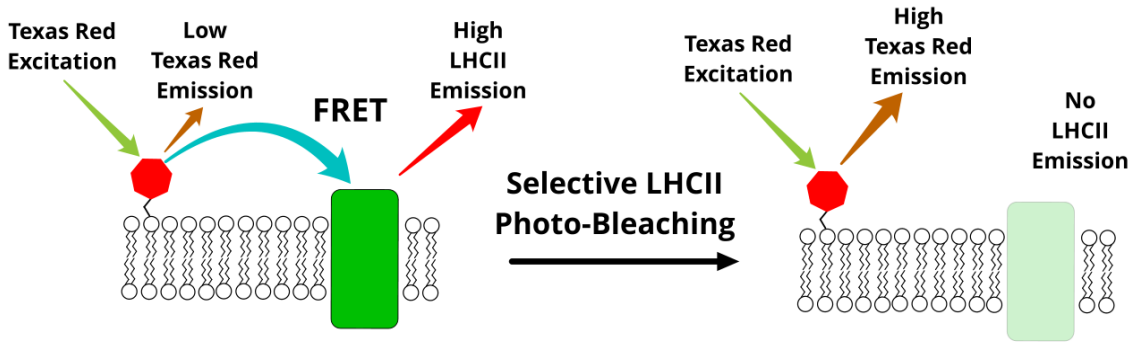

Figure 36 Schematic showing the mechanism for Texas Red de-quenching due to selective LHCII bleaching

4.3.2 De-quenching measurements on single proteoliposomes

In order to assess de-quenching as described above, a time-based analysis was performed on FLIM data already acquired on well-separated proteoliposomes (deposited at low density) onto glass coverslips, as described in 4.2. FLIM allows both the fluorescence emission intensity and fluorescence lifetime of Texas Red to be measured as LHCII photo-bleaches during the 500 frame acquisition. In the previous sub-sections, data were integrated over the total acquisition time. Here, images and subsequent numerical data are separated into a series of sequential time periods of 50 frames each. For each frame average values for LHCII and Texas Red fluorescence intensity and Texas Red fluorescence lifetime were calculated for all proteoliposomes. This was then averaged over each 50 frames to give one time-point.

Representative images of LHCII and Texas Red channels in frame 1, 250 and 500 for 'high-LHCII' proteoliposomes are shown in Figure 37 (A). LHCII intensity diminishes over time as Texas Red emission intensity simultaneously increases and also becomes 'redder' corresponding to a lengthening of lifetime. Qualitatively, high proportions of proteoliposomes in both exhibited significant recovery of Texas Red fluorescence intensity and lifetime with LHCII photo-bleaching. A quantitative analysis of fluorescence emission intensity shows 95 % and 90 % of proteoliposomes from 'high-LHCII' and 'low-LHCII' sample sets have an increase in the Texas Red lifetime of >125

% relative to its initial lifetime, after photo-bleaching of LHCII (i.e., more than a two-fold increase of the Texas Red lifetime). This suggests that >90 % of all proteoliposome samples contain both LHCII and Texas Red fluorescent components in agreement with co-localisation microscopy data shown in section 4.2.2. Figure 37 (B) and (C) show the reduction in LHCII fluorescence emission intensity and corresponding increase in Texas Red fluorescence emission intensity and lifetime averages, respectively. Over the 500 frames of LHCII photo-bleaching the normalised LHCII intensity decreases from 1.0 to 0.007 ± 0.012 and from 1.0 to -0.033 ± 0.006 for 'high-LHCII' and 'low-LHCII' samples, respectively (negative value attributed to imperfect background removal). The resulting increase in Texas Red fluorescence intensity is from 1.0 to 2.37± 0.14 and 1.79 ± 0.01, for 'high-LHCII' and 'low-LHCII' proteoliposomes. The calculated fluorescence lifetime of Texas Red increases from 0.73 ± 0.02 ns to 1.77 ± 0.02 ns for 'high-LHCII' and from 0.975 ± 0.02 ns to 2.18 ± 0.01 ns for 'low-LHCII'. The fluorescence lifetime of Texas Red does not fully recover to ~4 ns as observed in liposomes omitting LHCII. This may be due to a slight photo-bleaching of Texas Red as images are acquired and/or the incomplete photo-inhibition of LHCII.

Energy Transfer efficiency can be calculated using the standard equations introduced in section 3.4 when using spectroscopic methods. The efficiency is calculated using the fluorescence intensity (Equation 22) or lifetime (Equation 23) of donor molecules (Texas Red) in the presence and absence of an acceptor (LHCII).

$$ETE_{SS} = 1 - \frac{F_{DA}}{F_D}$$

Equation 22 Energy transfer efficiency as calculated from steady-state data, FDA: Donor fluorescence intensity in the <u>presence</u> of acceptor (i.e., with LHCII), FD: Donor fluorescence intensity in the <u>absence</u> of acceptor (i.e., control sample omitting LHCII).

$$ETE_{TR} = 1 - \frac{\tau_{DA}}{\tau_D}$$

Equation 23 Energy transfer efficiency as calculated from time-resolved data, τDA: Donor fluorescence lifetime in the <u>presence</u> of acceptor, τD: Donor fluorescence lifetime in the <u>absence</u> of acceptor.

Using the pre-photo-bleaching Texas Red fluorescence emission intensity and lifetimes as F_{DA} and $\tau_{DA,}$ respectively, and post-photo-bleaching Texas Red fluorescence emission intensity and lifetimes as F_D and τ_D, energy transfer efficiency can be calculated (i.e., comparing the final 50-frame-datapoint to the initial 50 frames). For 'high-LHCII' proteoliposomes the energy transfer efficiency is calculated as 58 % and 59 % from intensity and lifetime data, for 'low-LHCII' proteoliposomes the energy transfer efficiency is calculated as 44 % and 55 %. While these values of energy transfer efficiency are significantly lower than when calculated with cuvette-based spectroscopy (80-90 %) and by single proteoliposome FLIM analysis (70-80 %), the trend of higher energy transfer efficiency with higher LHCII concentration is consistent. The lower calculated transfer efficiency could be due to several factors: (i) Energy transfer from Texas Red to an LHCII complex which is photo-bleached leading to energy loss and reduced Texas Red fluorescence emission. (ii) Partial photo-bleaching of Texas Red, although Texas Red does not photo-bleach as easily as LHCII it does absorb in the wavelength range of selective LHCII excitation so some bleaching is expected. Texas Red photo-bleaching would result in a reduction of measured fluorescence emission intensity and a lower calculated energy transfer efficiency.

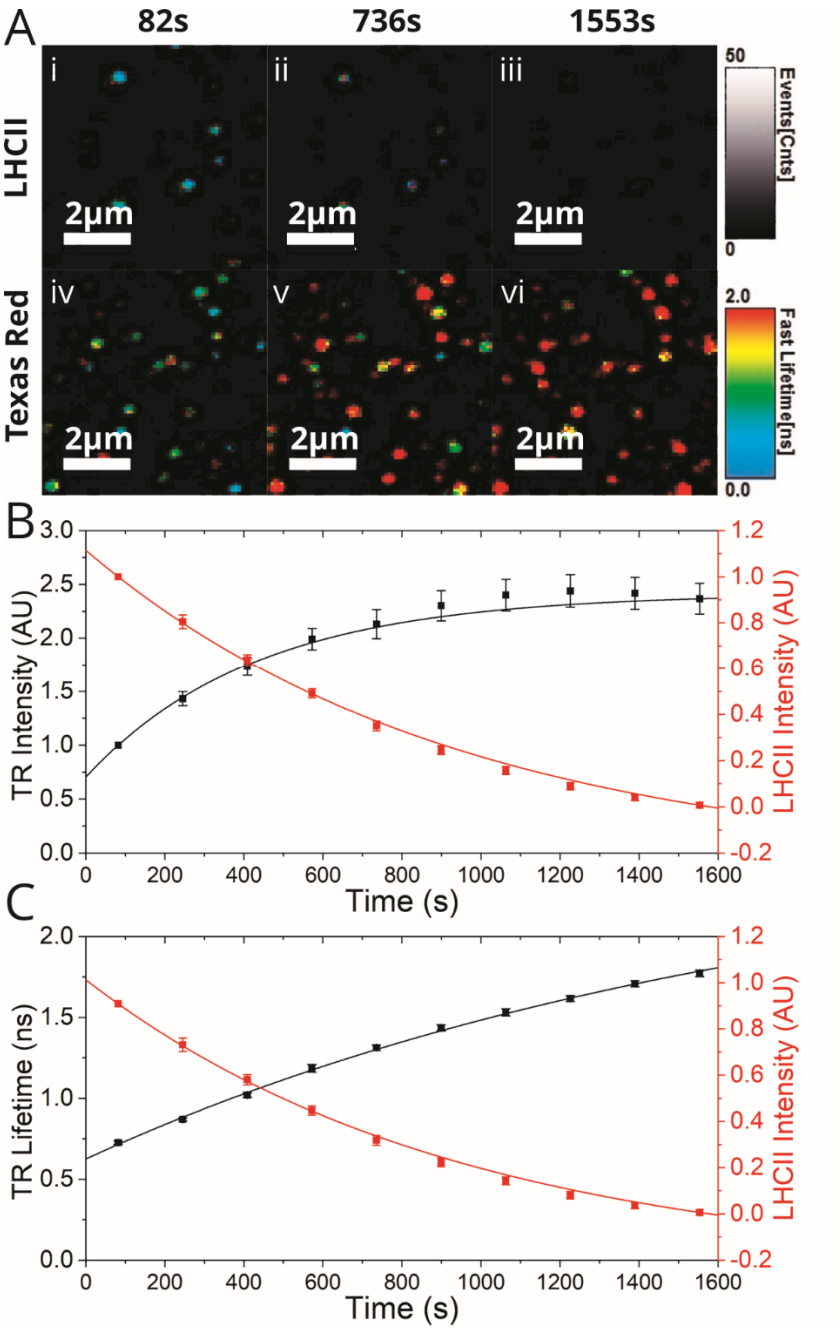

Figure 37 LHCII photo-bleaching and resulting recovery of Texas Red fluorescence emission intensity and lifetime in individual Texas Red-LHCII proteoliposomes deposited onto a glass substrate at low concentration

(A) Time-lapse series of FLIM images of proteoliposomes, displaying both fluorescence intensity (brightness) and "fastFLIM lifetime" (colour scale The "fastFLIM" mode leads to a "FastLifetime" which is an estimate of the average fluorescent lifetime of a pixel based on the average 'time of flight' from excitation pulse to emission. LHCII (i-iii) photo-bleaching occurs over time, which decreases the intensity and lifetime of Texas Red (iv-vi). Graph showing the total fluorescence intensity of the LHCII and Texas Red channels versus time, for the sequence from

(A). All intensity values were normalised to 1.0 relative to intensity of the first 50 frame average to allow easy comparison between LHCII and Texas Red.

4.3.3 Selective photo-bleaching of LHCII results in Texas Red fluorescence recovery giving direct evidence for energy transfer

We wished to assess the efficiency of Texas Red to LHCII energy transfer in proteoliposomes which were densely-packed, forming multiple layers of lipids and proteins. Thus, selective LHCII photo-bleaching experiments were also performed on proteoliposome samples deposited at high concentrations onto glass surfaces forming so-called 'thick films'. The de-quenching of Texas Red fluorescence when LHCII is photo-bleached allows energy transfer to be visualised. Briefly, proteoliposome samples were deposited onto piranha cleaned glass and incubated before exchange washing to remove any proteoliposomes in solution. Similar to FLIM, the epifluorescence microscope was set up with selective excitation and emission (using a carefully designed filter cube, see figure legend and 2.5.1 for details on sample preparation and microscopy set-up). Here, LHCII is photo-bleached by exposing a confined region of the sample to a high intensity of selective LHCII excitation as defined via an aperture. The effects are then observed in subsequent fluorescence images in both LHCII and Texas Red channels. Epifluorescence is lower resolution than our FLIM system and only measures fluorescence intensity (no lifetime information). However, it has much faster image acquisition, higher throughput, large field of view, and a manually operated aperture making it well designed for analysis of densely packed films. Therefore, the epifluorescence system was used to perform these photo-bleaching experiments on 'thick films' of membrane.

Epifluorescence photo-bleaching microscopy measurements were performed on proteoliposome samples with constant lipid and Texas Red concentrations (1 mM lipid, ~6.5 μM Texas Red) and varying LHCII concentration (0.16 - 2.84 μM. This is the same sample set used to determine the dependency of energy transfer efficiency on LHCII concentration by spectroscopic techniques in section 3.4.3. Representative images of a proteoliposome sample deposited onto a surface at high concentration in both LHCII and Texas Red channels before (i + iii) and after (ii + iv) selective LHCII photo-bleaching are shown in Figure 38 (A). Initial Texas Red and LHCII channel images, Figure 26 (A) (i+iii), show a high density of relatively evenly distributed particles on the surface. After

selective LHCII photo-bleaching for ~120 seconds, Figure 26 (A) (ii + iv), there is very low LHCII fluorescence intensity and an apparent increase in Texas Red fluorescence intensity. In the representative images the aperture was opened iteratively every 30 seconds (white labels 1 - 4) to demonstrate how varying the degree of LHCII photo-bleaching varies the Texas Red de-quenching. For measurements on all other samples a ~100 μm diameter area of the surface was exposed for photo-bleaching. Profiles of Texas Red fluorescence intensity after LHCII bleaching for representative images in the sample series with a range of LHCII concentrations are shown in Figure 26 (B). The profiles clearly show an increase in the level of Texas Red de-quenching at higher LHCII concentrations. As the Texas Red concentration is consistent between samples the increased de-quenching is attributed to a higher initial energy transfer efficiency. By quantitative analysis of the integrated fluorescence intensity of Texas Red in the bleaching area, before and after selective LHCII photo-bleaching, a value of Texas Red de-quenching can be obtained for each sample using Equation 24.

$$\boldsymbol{De-quenching}\ \% = \left(\frac{\boldsymbol{Emission_{Post-bleach} - Emission_{Pre-bleach}}}{\boldsymbol{Emission_{Pre-bleach}}}\right)\boldsymbol{x100}$$

Equation 24 De-quenching calculation

Figure 38 (C) shows the calculated value of Texas Red de-quenching for samples with varying LHCII concentrations. The level of de-quenching increases as the LHCII concentration in samples increases. This trend is conformation that the recovery of Texas Red fluorescence after LHCII photo-bleaching is related to energy transfer efficiency which was also shown to increase with LHCII concentration via spectroscopic analysis in 3.4. The Texas Red de-quenching shown here and energy transfer efficiency calculated with fluorescence spectroscopy are in good agreement. A maximum level of energy transfer efficiency is reached at ~1.0 μM LHCII (1 mM total lipid) where Texas Red – LHCII separation reaches a critical point. This retention of the same trends in energy transfer efficiency suggests that proteoliposomes are have the same photo-physics of Texas Red to LHCII energy transfer when deposited as ‘thick films’ on surfaces as they do in solution.

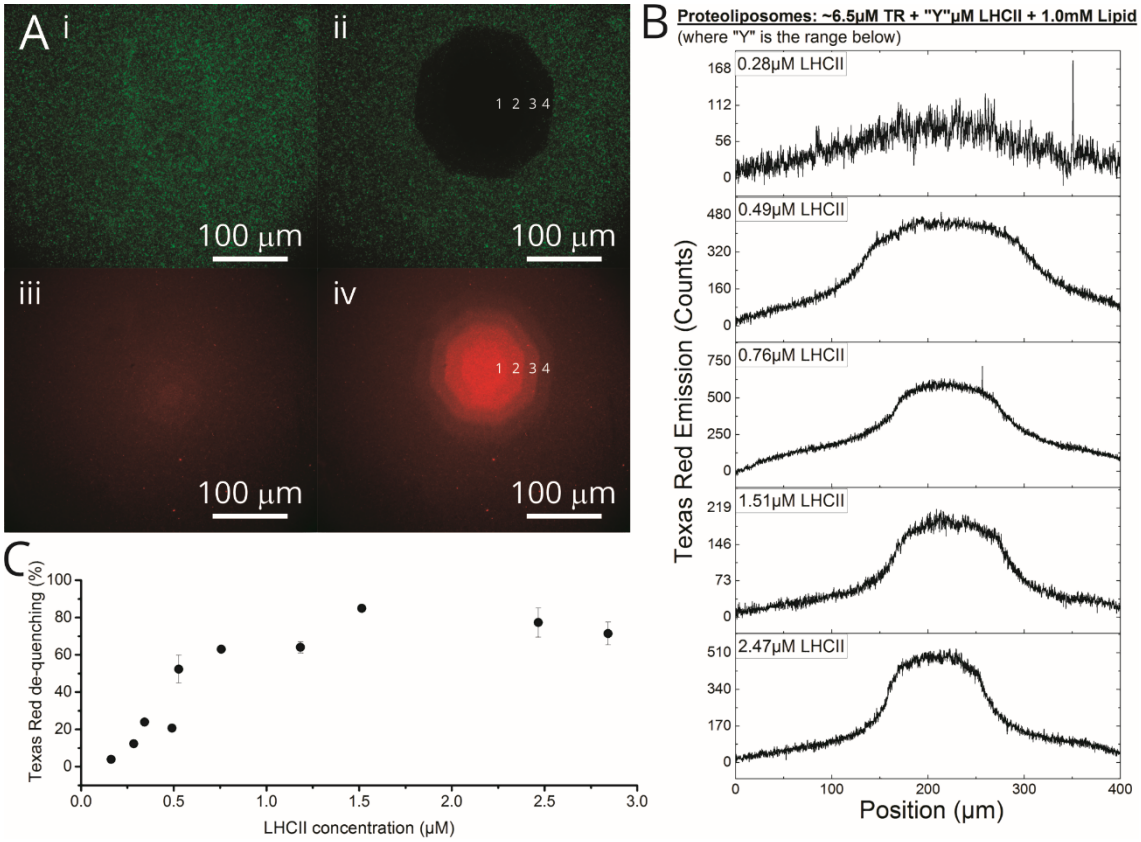

Figure 38 LHCII photo-bleaching and resulting recovery of Texas Red fluorescence emission intensity on 'thick films' of Texas Red-LHCII proteoliposomes deposited onto a glass substrate at high concentration

(A) Epifluorescence microscopy images of a representative proteoliposome sample (2.84 µM LHCII, 5.5 µM TR, 1 mM total lipid) deposited at high surface density onto glass substrate (x5 dilution). LHCII (i + ii) and Texas Red (iii + iv) channels were recorded sequentially using appropriate filter cubes before (i + iii) and after (ii + iv) photo-bleaching. Bleaching was performed with high intensity of LHCII excitation through an aperture, the degree of photo-bleaching was varied by iteratively opening the aperture in stages (numbered 1–4) in this example to highlight de-quenching of Texas Red. (B) Intensity profiles of Texas Red channel post LHCII bleaching from representative proteoliposomes sample series with varying LHCII and constant Texas Red concentrations. Surface profiles were taken from a line bisecting images with the bleached area in the centre. Y axis ranges were selected to demonstrate the increase in intensity relative to the background, not to the absolute values of counts which are dependent on the amount of material deposited onto the surface. (C) Graph showing degree of Texas Red de-quenching, as described in Equation 24, against LHCII concentration for samples with constant

Texas Red and varying LHCII concentration. For microscopy LHCII was excited at 450-570 nm and emission collected at 650-800 nm, Texas Red was excited at 540-580 nm and emission collected at 600-660 nm. All images were taken using an x40 air objective (NA 0.6), 1s exposure and appropriate ND filters inserted to maintain the maximum number of counts at a level for good detector signal-to-noise and linearity (10-75 % of detector saturation)

4.4 Atomic Force Microscopy on surface deposited membranes

4.4.1 Initial sample choice and characterisation for AFM

An important part of utilising lipid-tagged Texas Red to spectrally enhance LHCII in a proteoliposome-based system is the fact that membranes are inherently amenable to surfaces. The stable association of proteoliposomes on surfaces can allow one to investigate individual particles, and also 'thick films' of high-density membranes, at a higher resolution than can be achieved with optical microscopy. Atomic Force Microscopy (AFM) can be utilised to study the topography of proteoliposome samples deposited onto surfaces with sub-nanometer resolution. A representative proteoliposome sample containing both LHCII and Texas Red was used for all AFM imaging, which had an initial membrane composition of 1.18 μM LHCII, 8.0 μM Texas Red and 1 mM lipid (from absorption spectroscopy as in section 3.3.4). Energy transfer efficiency was estimated as 94 % and 75 % from steady-state and time-resolved fluorescence spectroscopy, respectively. These cuvette-based fluorescence techniques confirm that this is an appropriate energy-transferring sample to further characterise topographically. Briefly, to prepare for AFM the proteoliposome sample was diluted and deposited onto freshly cleaved mica to allow surface deposition at either low (x 100 dilution) or high (x 5 dilution) concentration to image either individual or densely packed 'thick films' of proteoliposomes. After a 30 minute incubation substrates washed with buffer to remove any non-surface adhered particles in solution.

4.4.2 Atomic force microscopy reveals domains of LHCII within proteoliposomes

In order to investigate the size and topography of individual proteoliposomes a representative sample was deposited at low concentration (x100) onto an atomically flat mica surface for characterisation. Figure 39 (A-E) shows AFM topographs of proteoliposomes at different magnification levels; individual proteoliposomes and or membrane patches can clearly be resolved. Single particle analysis was performed by selecting all individual particles over a threshold height of 0.5 nm and gathering statistics on average height and diameter. 0.5 nm was selected as a threshold in order to select any lipid or protein particle material on the surface above the height of the atomically flat mica. The image shown in Figure 39 (B) was used for this analysis, particles over the threshold height are highlighted in blue in Figure 39 (C). The average size of particles was found to be 54.7 ± 30.8 nm (standard deviation), with an average height of 4.8 ± 2.2 nm (standard deviation) (n=1100). This suggests that proteoliposomes have ruptured onto the surface forming patches of single bilayer thickness. Size characterisation measurements made using dynamic light scattering (DLS), as shown in section 3.3.7, determined the average hydrodynamic diameter of proteoliposomes in this samples to be 74 ± 3 nm. Based on this measurement one would expect the diameter of single-bilayer patches on the surface to be ~300 nm, far larger than observed here. This discrepancy may be due to: (i) as proteoliposomes rupture onto the mica surface and form single bilayer patches there is a significant degree of fragmentation; (ii) Smaller proteoliposomes are more likely to deposit onto the surface; this may be caused by smaller particles moving faster in solution due to Brownian motion and therefore being more likely to collide with the mica. Both of these explanations suggest that patches of membrane imaged here are not representative of the size distribution of proteoliposomes in solution. However, information about the composition of proteoliposomes can be extracted from these measurements on membrane patches. A zoomed-in image of a single membrane patch reveals protrusions ~10 nm in diameter as shown in Figure 39 (E). The height profile shown in Figure 39 (F) demonstrates the change in topography across the proteoliposome that we speculate to represent patches of protein. These could represent the increased height of membrane reconstituted LHCII trimers. Analysis of the LHCII area coverage in this single patch shows ~11 % of the membrane has a height of over 5 nm, very roughly in agreement with the 16.5 % LHCII membrane coverage expected for

this samples as assessed in 3.3.7. Even at this low resolution, the presence of these protrusions at relatively high density and at greater height than an empty lipid bilayer is evidence that LHCII is reconstituted into the lipid membrane of proteoliposomes and therefore co-reconstituted alongside the lipid-tagged Texas Red.

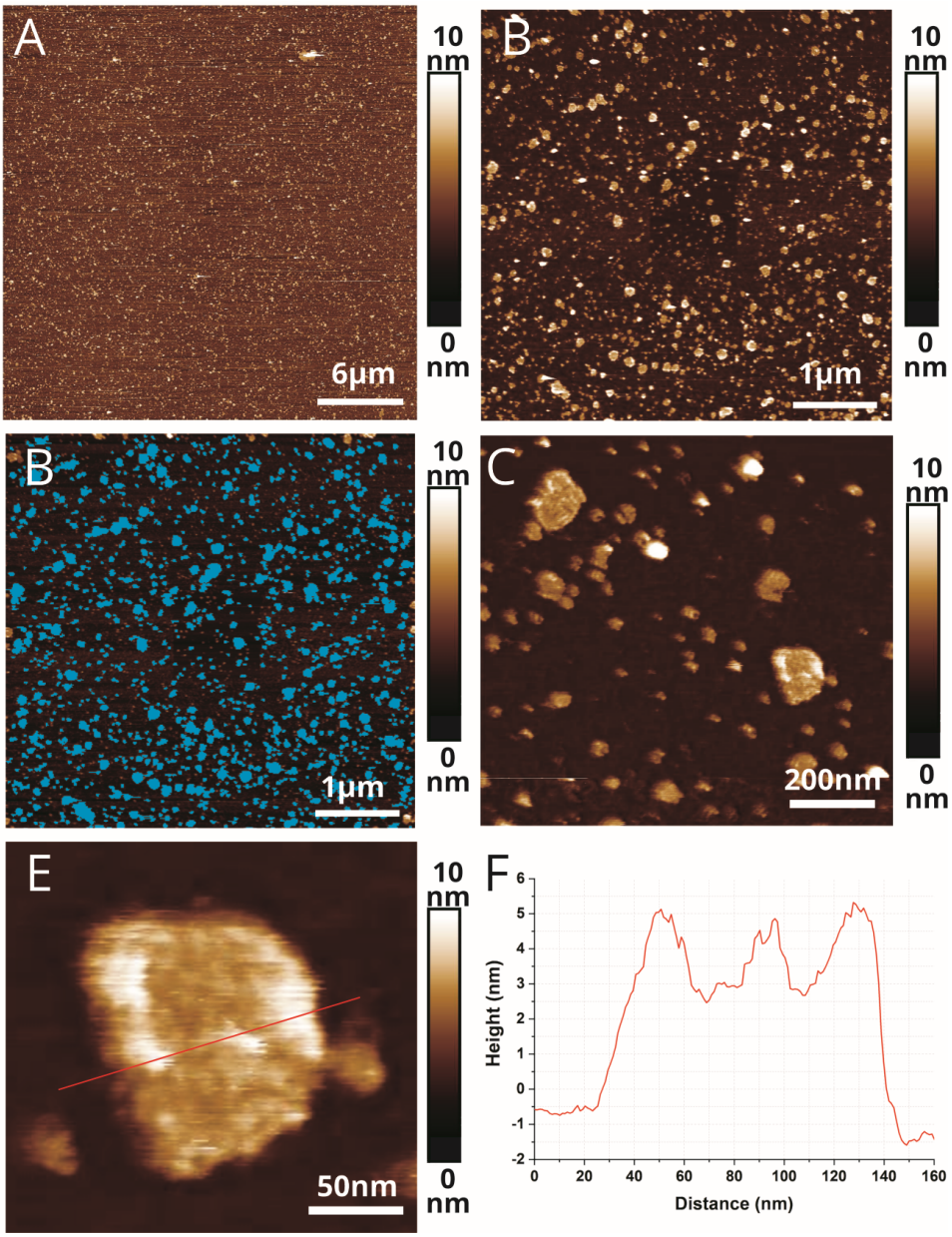

Figure 39 AFM topographs of proteoliposomes deposited at low concentration onto a mica substrate

(A-F) AFM topographs of representative proteoliposome sample (1.18 µM LHCII, 5.5 µM TR, 1 mM total lipid) deposited onto mica surface at low concentration. (C) Blue area indicates particles above a 0.5 nm threshold applied to (B) used for single particle analysis. (E) Zoomed in image of an individual proteoliposome showing domains of LHCII aggregates. (F) Height profile across proteoliposome shown in

(E) indicated by red line. Diluted samples are deposited onto freshly cleaved mica for imaging; this atomically flat surface is essential to allow sub-nanometer features to be resolved. After an initial 30 minute incubation samples are exchange washed to remove proteoliposome in solution and membranes loosely associated with the mica surface. Imaging was performed in liquid. Full details of sample preparation and AFM setup in 2.7. Data was acquired by Dr P. Adams and analysed by A. Hancock.

4.4.3 Proteoliposomes can be deposited onto a surface to form a multi-bilayer 'thick film'

In the design of Texas Red-LHCII proteoliposomes a useful property was the prospective use of densely packed membranes deposited onto surfaces. This would be crucial for potential future light-harvesting applications where the enhanced absorption of LHCII due to energy transfer from Texas Red could be utilised. It was therefore important to determine that Texas Red-LHCII proteoliposomes were capable of forming densely packed films on surfaces and that efficient Texas Red to LHCII energy transfer is retained in these systems. A representative proteoliposome sample deposited at high concentration (x 5 dilution) onto a mica surface in order to produce a densely packed layer or 'thick film' of lipid and protein material as shown in Figure 40 (A). The thickness of the film was assessed by disrupting an area of the film by applying high scanning forces to reveal the mica layer beneath (i.e. AFM-tip lithography). This lithography is shown in Figure 40 (B) with the white arrowhead indicating the area of disrupted film and mica beneath. The height of this film varies between 10-30 nm across the image suggesting multiple layers of membranes stacked on top of each other. The 'rough' surface revealed after lithography and shown in the height profile (Figure 40 (E)) suggests that the mica has not been fully exposed by the AFM tip, it does however confirm that the film is at least 8 nm thick. Figure 40 (C + D) show Texas Red de-quenching measurements after selective LHCII photo-bleaching confirming that the proteoliposomes are optically functional with efficient Texas Red to LHCII energy transfer occurring when deposited as a 'thick film'.

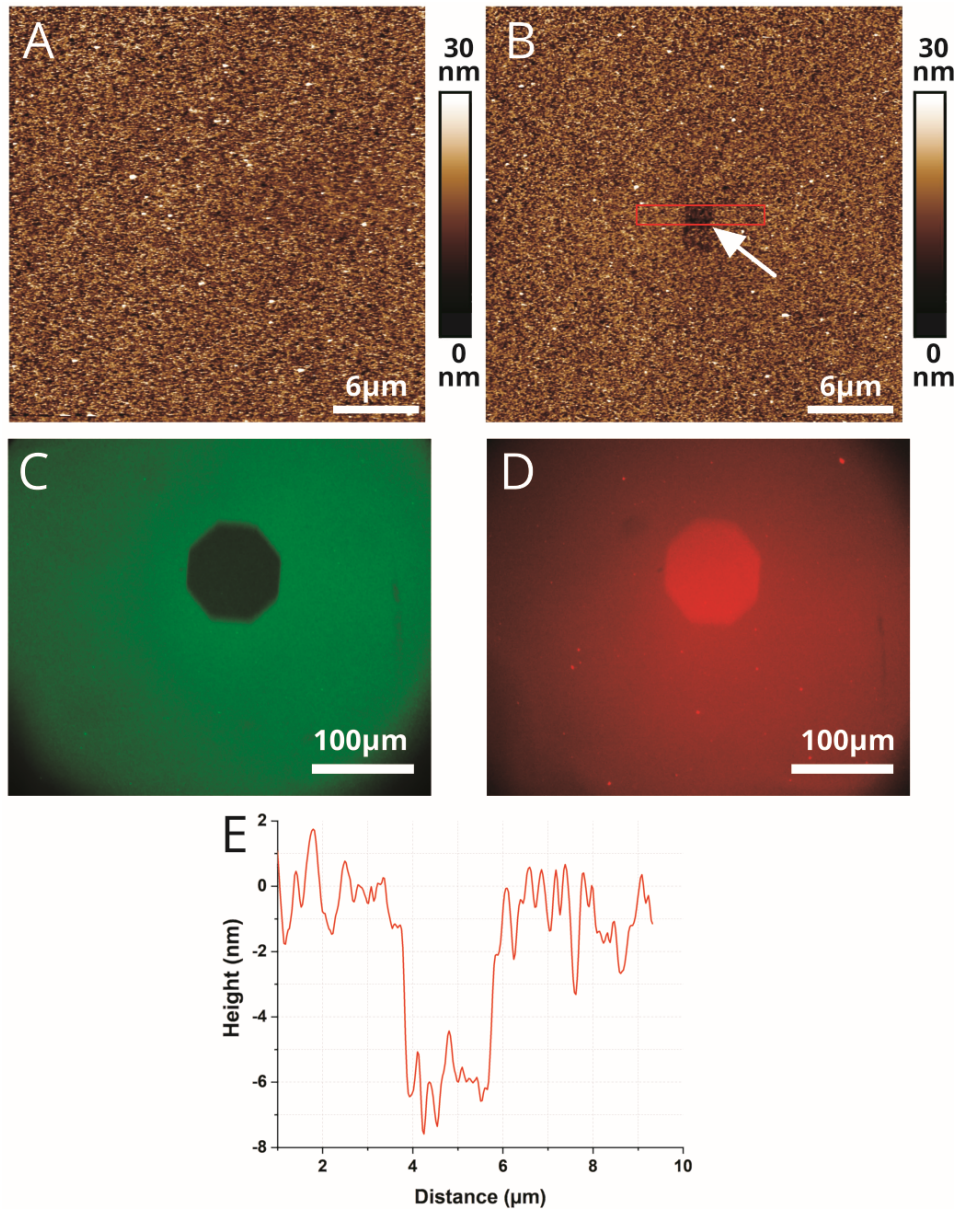

Figure 40 AFM topographs of proteoliposomes deposited at high concentration onto a mica substrate forming a membrane 'thick film'

(A + B) AFM topograph of representative proteoliposome sample (1.18 µM LHCII, 5.5 µM TR, 1 mM total lipid) deposited onto mica surface at high concentration (x 5 dilution). White arrow in (B) indicates region of film disruption by AFM tip lithography. (C + D) Epifluorescence microscopy images of 'thick film' sample. LHCII (C) and Texas Red (D) channels were recorded sequentially using appropriate filter cubes after photo-bleaching. Bleaching was performed by exposing a region of the sample of ~100 µm width (as defined by an adjustable aperture) to a high intensity of light passed through the LHCII excitation filter. (E) Step-height profile of AFM lithography area indicated in (B) with red box.

4.5 Section summary and discussion

In this chapter, proteoliposomes containing LHCII and lipid-tagged Texas Red were investigated using microscopy techniques, and surfaces functionalised with proteoliposomes at low and high concentrations were assessed to image individual particles and 'thick films' respectively. The characterisation of proteoliposomes deposited onto surfaces was complementary to spectroscopic techniques, discussed in Chapter 3, and was used to evaluate the co-localisation of chromophores. The system also allowed the assessment of Texas Red to LHCII energy transfer in both individual proteoliposomes and 'thick films'. Characterisation was performed using a combination of wide-field epifluorescence microscopy (measuring fluorescence intensity), fluorescence lifetime imaging microscopy (FLIM) (measuring fluorescence intensity and lifetimes), and Atomic Force Microscopy (AFM) (studying topography).

FLIM measurements were made on representative proteoliposome samples which covered a suitable range of Texas Red to LHCII energy transfer efficiencies: samples termed 'high-LHCII', 'low-LHCII' and 'no-LHCII' corresponding to concentrations of 2.84 μM LHCII, 1.15 μM LHCII and zero LHCII, respectively all containing similar (6-9 μM) Texas Red and 1 mM total lipids. Co-localisation analysis determined that at least 80 % of the proteoliposomes had significant signal from both LHCII and Texas Red for both 'high-LHCII' and 'low-LHCII' samples. Photo-bleaching experiments suggested an even higher potential co-mixing with 90-95 % of proteoliposomes exhibiting significant increase of in Texas Red fluorescence over the course of imaging. This was attributed to disruption of the energy transfer pathway from Texas Red to LHCII. The FLIM data also revealed that all individual particle images appear as diffraction-limited spots, suggesting that all particles are beneath the Abbe diffraction limit (~300 nm) in agreement with the DLS data. Both techniques suggest that there were no undesirable large aggregates of proteins/lipids, which can skew datasets. AFM was also used to determine the size of proteoliposomes deposited at low concentrations onto a mica surface, providing average widths and heights of ~60 nm and ~5 nm respectively. AFM was used to localise light-harvesting membrane proteins reconstituted into lipid bilayers (Adams et al., 2018); here we are able to resolve nanometer domains of LHCII reconstituted into proteoliposomes and estimate the surface coverage of protein within the membrane.

Analysis of single proteoliposomes by FLIM allowed fluorescence lifetimes to be calculated on a per-proteoliposome basis. This technique of single proteoliposome lifetime analysis via FLIM has previously been used to determine the level of LHCII quenching in proteoliposomes, allowing the relationship between LHCII-LHCII interactions and self-quenching to be assessed (Natali et al., 2016). Here, we measure the quenching of an energy donor molecule (Texas Red) allowing us to calculate the efficiencies of energy transfer on a per-proteoliposome level (Förster, 1965, Natali et al., 2016). Energy transfer efficiency for low-LHCII and high-LHCII samples are 71 ± 10 % and 77 ± 8 %, respectively. This estimation of ETE is ~10-15 % lower than the values calculated by ensemble fluorescence spectroscopy (81 % and 87 %, from section 3.4), possibly due to unaccounted for photo-bleaching effects or a certain population of proteoliposomes being more amenable to surface deposition. For example, the presence or absence of LHCII in proteoliposomes will affect the surface charge of the bilayer due to charged groups on the protruding portion of the protein (Standfuss et al., 2005), which will effect proteoliposome interaction with the glass surface. Overall, the result is consistent with the previous hypothesis that higher LHCII concentrations in proteoliposomes result in higher average energy transfer efficiency due to shorter average donor-acceptor separation (Subramanian et al., 2018). An important result of these single proteoliposome measurements is that >90 % of proteoliposomes are exhibiting Texas Red to LHCII transfer with at least 50 % efficiency. This means that that sub-populations of 'empty' liposomes omitting LHCII widely reported in the literature (Tutkus et al., 2018) are avoided in our formation procedure. It also implies that generally, Texas Red molecules are in close proximity to LHCII allowing the intended enhancement of absorption cross-section to take place.

De-quenching measurements give an indication of the efficiency of Texas Red to LHCII energy transfer when deposited onto surfaces by disrupting the energy transfer pathway (Wang et al., 2010). Energy transfer efficiencies of 44 % and 58 % were estimated for low-LHCII and high-LHCII samples from fluorescence intensity data and of 55 % and 59 % from lifetime data. These values are not completely quantitatively accurate as Texas Red photo-bleaching is not taken into account and we cannot ensure that LHCII is completely optically inactive after photo-bleaching. The result does however confirm that the energy transfer from Texas Red to LHCII is occurring with high efficiency and is dependent on LHCII concentration as previously demonstrated. This technique has been

employed previously to assess the efficiency of energy transfer between complex fluorescent nanomaterials, such as quantum dots, conjugated to proteins in order to determine the properties of quantum dot to protein energy transfer (Vinayaka and Thakur, 2011). We are unable to experimentally confirm the mechanism of the LHCII chlorophyll photo-bleaching due to high-intensity illumination. However, we speculate that the almost complete quenching of LHCII fluorescence is due to direct damage to the chlorophyll molecules from singlet oxygen. When under high-intensity illumination there will be a build-up of excitons in chlorophyll molecules of LHCII resulting in the formation of long-lived and highly reactive triplet chlorophyll states (Krieger-Liszkay, 2005). Triplet chlorophylls can react with oxygen to form highly reactive singlet oxygen states. Once formed, singlet oxygen will reduce any covalent bond in its immediate vicinity causing the bond to break (Krieger-Liszkay, 2005); this will cause molecular damage as the structure is irreparably changed. The fluorescence of chlorophyll is highly dependent on its structure and damage to important bonds in the head group could lead to a complete loss of fluorescence, therefore, we assume this is the mechanism for LHCII photo-bleaching.

Lipid based films have applications in nanotechnology from drug delivery to light-harvesting (Kang et al., 2018) so it is interesting to assess the how the proteoliposomes developed here behave when deposited as films. Texas Red to LHCII energy transfer was measured for proteoliposomes deposited at high concentrations as ‘thick films’ on glass surfaces, via de-quenching measurements. AFM lithography can be used to determine the thickness of ‘soft’ lipid/protein films by etching away the film to reveal the ‘hard’ surface beneath (Lv et al., 2018). The thickness of proteoliposome films formed here was found to be 10-30 nm suggesting several layers of membrane stacked on top of one another. Selective LHCII photo-bleaching and Texas Red de-quenching measurements were performed on ‘thick-films’ of proteoliposomes with a range of LHCII concentrations. It was found that the level of fluorescence recovery of Texas Red is strongly dependent on the LHCII concentration. This is again supportive of higher LHCII concentrations resulting in higher energy transfer efficiencies and importantly confirms that the energy transfer occurs when samples are deposited onto surfaces at a range of LHCII concentrations. While we do not have control over discrete ordered multilayers of lipid bilayer that have previously been formed by utilising stabilising polymers between

bilayers (Grab et al., 2016, Heath et al., 2016), we have demonstrated that the lipid-dye-protein system is optically active on surfaces when deposited as disordered multilayers.

The retention of optical functionality when the proteoliposomes are deposited onto surfaces as films is crucial if the concept of enhancing photosynthetic light-harvesting proteins with complementary lipid-tagged chromophores is to have any applications in functional devices. One benefit of proteoliposomes is the potential to incorporate additional proteins or alternative hydrophobic components alongside light-harvesting proteins, such as chromophores tagged to lipids as shown here. As an extension of this system, one could incorporate photosynthetic reaction centres that are capable of charge separation and electron transfer into proteoliposomes. Bacterial reaction centres have previously been adsorbed onto nanowires (Yaghoubi et al., 2017), graphene (Csiki et al., 2018), and gold electrodes (Friebe and Frese, 2017) while retaining photochemical functionality. The reaction centres act as bio-photovoltaic solar devices by taking advantage of the electrons expelled by the protein to generate photo-current (Kamran et al., 2014). Plant based light-harvesting proteins can also be patterned accurately onto surfaces (Vasilev et al., 2014). Such systems are also capable of long range energy propagation (Escalante et al., 2010). All of the applications of light-harvesting proteins into solar bionanotechnology could be enhanced by the additional incorporation of complementary lipid-tagged chromophores. FLIM analysis has shown that individual proteoliposomes can provide a Texas Red to LHCII energy transfer efficiency of over 90 %. The high efficiency is due to the small distances of Texas Red to LHCII separation and is comparable to what can be achieved with direct chemical attachment (Yoneda et al., 2015) or genetically encoded complementary chromophores (Grayson et al., 2017). There are several advantages of interfacing lipids within the bilayer as opposed to directly to the protein. (i) An abundance of lipid area around the protein for chromophore incorporation means many more chromophores can interact with the protein than if using specific binding sites. (ii) No chemical modification of the protein is required. (iii) Proteins can remain reconstituted into bilayers as they are in native system with inter protein energy transfer possible (e.g. to reaction centres). (iv) It has also been shown that model membranes containing electron transferring proteins can also be deposited onto electrodes with efficient electron transfer possible between membrane layers and onto electrodes (Heath et al., 2017).

5 Results: Energy Transfer in Texas Red-LHCII Nanodiscs

5.1 Motivation and background

Chapters 3 and 4 discuss the enhancement of the effective absorption cross-section of the light-harvesting protein LHCII using the lipid-linked chromophore Texas Red DHPE in a proteoliposome system. Chapter 3 focused on the spectroscopic characterisation of the system on an ensemble level, revealing the composition of proteoliposomes, stability of LHCII, and energy transfer efficiency. Chapter 4 utilised microscopy techniques to characterise proteoliposomes deposited onto surfaces, showing the retention of retention of the energy transfer pathways in individual membrane vesicles and thick multilayer films and allowed a detailed population distribution analysis of the photophysical properties. In this chapter, the reconstitution of LHCII and lipid-tagged Texas Red tagged lipids into nanodiscs and the ultra-fast dynamics of energy transfer will be discussed.

Firstly, we wished to investigate the high-speed energy transfer kinetics from Texas Red to LHCII in the model lipid membrane system. This will allow the rate of energy transfer to be determined, which in turn enables quantification of the average separation between donor Texas Red molecules and LHCII. Assessing the range of donor-acceptor energy transfer will allow the proportion of Texas Red molecules transferring energy to LHCII to be determined. In addition to understanding the transfer kinetics in this specific system, quantifying the energy transfer from external chromophores into photosynthetic light-harvesting proteins may provide useful information on the function of natural systems. Inter-pigment energy transfer in photosynthetic systems often occurs between the same types of pigment, (e.g. chlorophyll *a* to chlorophyll *a*) and is very difficult to quantify spectroscopically as their absorption and emission spectra are very similar. Quantifying energy transfer from membrane incorporated and spectrally different chromophores (such as lipid-tagged Texas Red) could provide insight into the speed of inter-chromophore energy transfer between photosynthetic proteins in nature. To study the rate of energy

transfer spectroscopic techniques must be used that are capable of observing changes in chromophore excited states at the femto- to picosecond timescales.

Ultrafast spectroscopic techniques are defined as those studying timescales on the order of picoseconds, and sometimes down to hundreds of femtoseconds. They are fundamental for quantifying the timescales of inter-chromophore energy transfer in the complicated network of pigments that make up light-harvesting proteins. This technique has been used for characterising energy transfer in both bacterial and plant light-harvesting proteins. It has been employed to determine the rate of transfer between different bacteriochlorophylls in purple bacteria (Fidler et al., 2013), and also the rate of energy transfer from carotenoids to chlorophylls in LHCII (Croce et al., 2001, Cong et al., 2008). More recently ultrafast methods, such as transient absorption spectroscopy, allow the effect of changes in intrinsic protein structure on inter-chromophore energy transfer to be determined. These changes in local environment can be due to changes in local lipid composition (Son et al., 2020) or due to changing light conditions which trigger phenomena such as non-photochemical quenching (Akhtar et al., 2019). Ultrafast spectroscopy is not limited to investigating natural networks of chromophores from single proteins, it has also been used to determine rates of energy transfer between artificial and natural chromophores (Maiuri et al., 2013, Yoneda et al., 2015, Grayson et al., 2017). The timescale, efficiency, and pathways of energy transfer between complementary non-native chromophores and light-harvesting proteins can be determined using ultra-fast techniques. This has previously been achieved through the covalent attachment of chromophores to proteins and the protein-pigment system studied either isolated in detergent micelles (Yoneda et al., 2015), or incorporated into lipid bilayers (Yoneda et al., 2020b).

To separate the energy transfer pathway between Texas Red and LHCII from any energy dissipation pathways associated with LHCII self-quenching, which is concentration-dependent as discussed in section 3.3.6, model lipid membranes that avoid LHCII-LHCII interactions are required. To achieve a model membrane environment with minimal LHCII-LHCII interactions, and therefore minimal aggregation dependent fluorescence self-quenching, lipid nanodiscs are used (Moya et al., 2001). Lipid nanodiscs have been used extensively to study single membrane proteins in a lipid bilayer environment as they resemble biological membrane more closely than detergent micelles. This is

advantageous for both structural studies (Hagn et al., 2018) and to determine how the lipid environment can affect protein functionality (Schuler et al., 2013). Nanodiscs are comprised of several scaffold proteins that form a ring of known diameter that encapsulates a small section of lipid bilayer, which can then contain a reconstituted membrane protein (Rouck et al., 2017). In this environment both lipid-tagged Texas Red molecules and a single LHCII trimer can be co-reconstituted into a bilayer where they are confined in close proximity. For any given nanodisc, one may expect that Texas Red molecules will be closer on average than they may be in a proteoliposome. This may allow energy transfer to take place from multiple Texas Red molecules to a single LHCII trimer.

The lipid nanodisc used to reconstitute single LHCII trimers alongside a lipid mixture including Texas Red DHPE was the human-derived Apolipoprotein ApoE422k (Chromy et al., 2007). Several of these 22kD proteins are known to self-assemble into a discoidal structure encircling a circular section of lipid bilayer which can contain a reconstituted membrane protein as shown in Figure 41. ApoE422k can form nanodiscs with different numbers of scaffold proteins coming together to form final disc diameters ranging from 15-30 nm, depending on the initial lipid-to-ApoE422k ratio (Blanchette et al., 2008). Typically, nanodiscs of ~10-15 nm in diameter are used if one wishes to study a single reconstituted membrane protein. However, for the purpose of this study using such a small nanodisc would confine the Texas Red DHPE to within 1-3 nm of the LHCII and would be more challenging to study because, firstly, there would be a very limited number of lipids surrounding each protein (low numbers of TR and thus low signal). Secondly, using small discs would result in very short donor-to-acceptor distance (significantly below the expected Förster radius) which would be expected to yield such a high energy transfer efficiency that the Texas Red fluorescence would be entirely quenched. The intermediate degree of confinement from discs of 20-30 nm was decided upon as a good compromise between these factors. Larger (25-30 nm) nanodiscs allow Texas Red tagged lipids to be at distances from the central LHCII trimer greater than the expected Förster radius (over 6 nm) allowing different energy transfer efficiencies due to different donor-acceptor separations to be observed.

.

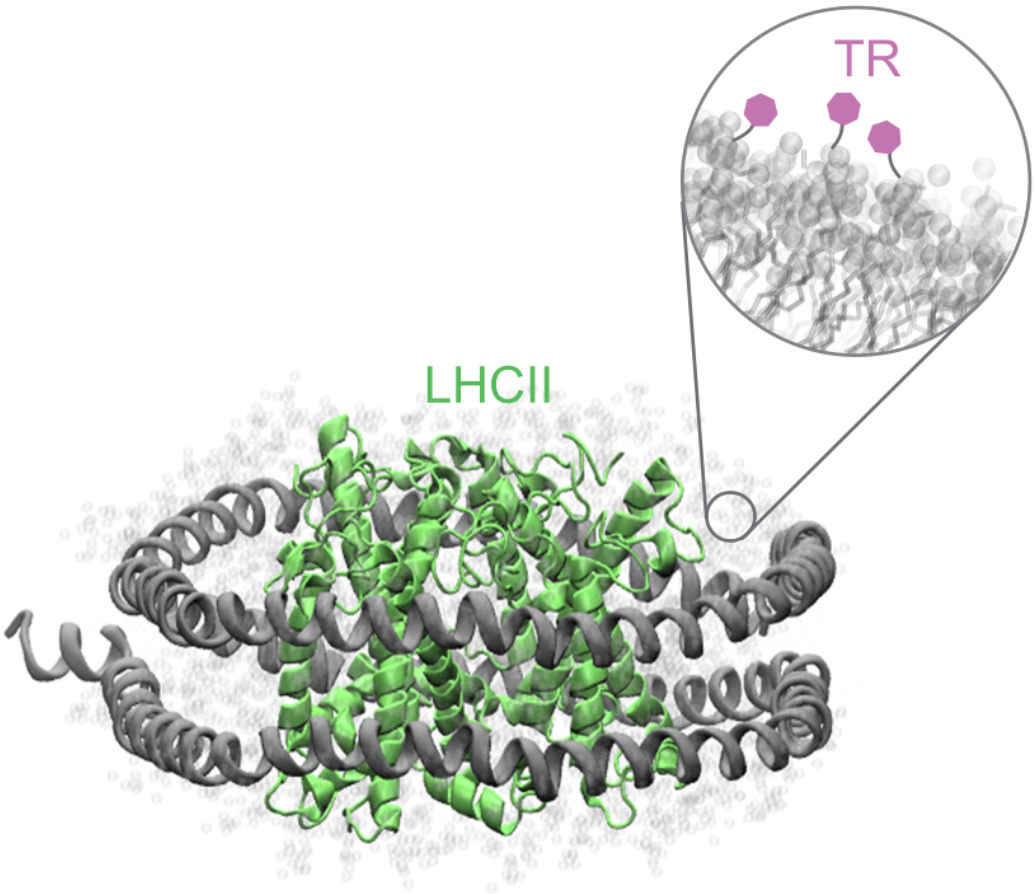

Figure 41 Schematic of LHCII and lipid-tagged Texas Red reconstituted into a lipid nanodisc.

(green) LHCII protein backbone, (dark grey) ApoE422k belting protein, (light grey) lipid molecules, (purple) Texas Red dye. This figure was produced by my collaborator Minjung Son, Department of Chemistry, MIT, USA.

5.2 Purification and formation of LHCII ApoE422k nanodiscs

5.2.1 Protein purification from plasmid

The ApoE422k membrane scaffold protein used to encapsulate LHCII and lipid-tagged Texas Red was purified from the plasmid pD451-SR provided by collaborators (Son et al., 2020). The plasmid included the gene for a fusion of the nanodisc peptide to a model protein, Thioredoxin-ApoE422k (termed the "full length fusion protein"), with 6x histidine residues included in ApoE422k segment (as an affinity tag), and a kanamycin antibiotic resistance gene. The plasmid was initially transformed into LB21 *E. coli* bacterial cells via heat shock and then grown on plates containing kanamycin to allow selection for bacterial colonies expressing the plasmid containing the antibacterial resistance gene. *E. coli* colonies expressing the gene were then used as a starter culture for a large volume bacterial growth. After large volume growth cells were lyzed to isolate the portion material and the Thioredoxin-ApoE422k protein separated using a Ni-NTA column (His-tag affinity column). Thioredoxin was then cleaved from ApoE422k with the enzyme Thrombin during overnight incubation. Finally, ApoE422k was separated from the sample by another Ni-NTA column purification. A full description of this process is described in methods 2.2.2. Approx. 100 mg of 22kD ApoE422k scaffold protein was purified per successful expression using 4 L of broth for the large-scale bacterial growth. SDS-PAGE was used to evaluate the purity of ApoE422k after purification, shown in Figure 42. A bright band at just below the 25 kD protein standard suggests that the sample is predominantly formed of the 22 kD ApoE422k subunits (80 % of the total intensity of bands in this lane, analysis performed with ImageJ macro).

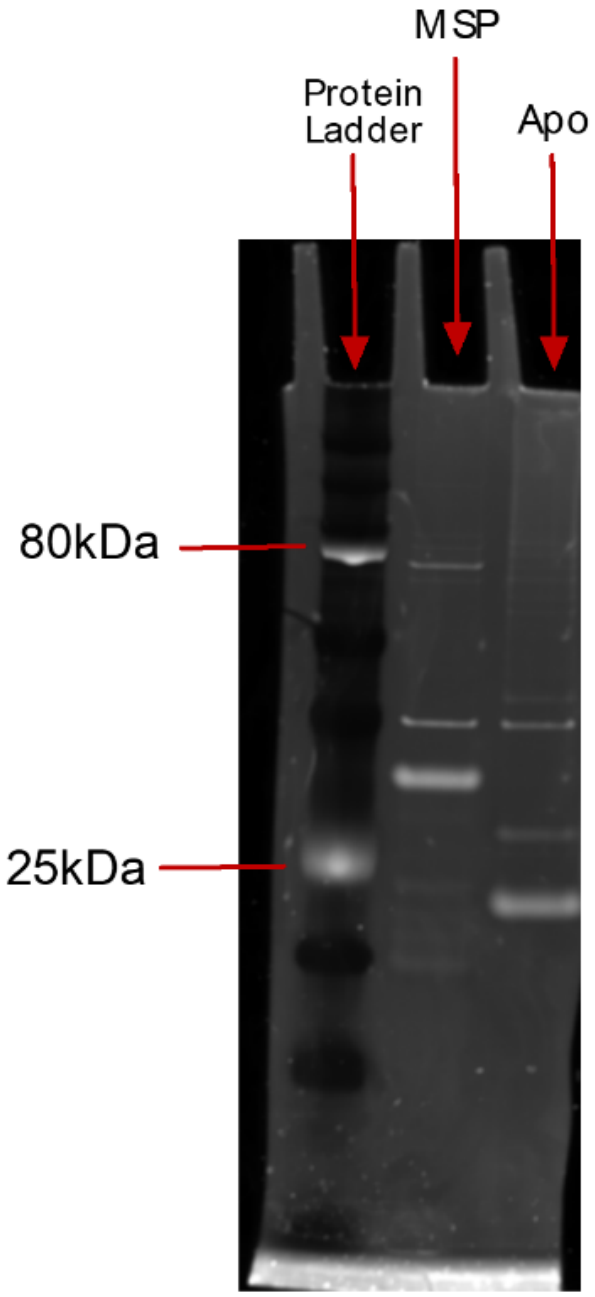

Figure 42 Gel electrophoresis of purified ApoE422k scaffold protein

SDS PAGE gel (Sypro ruby UV stain) of purified nanodiscs scaffold proteins. (Left column) Protein standard ladder, (Centre column) 40kD alternative membrane scaffold protein MSP1E3D1, (Right column) 22kD ApoE422k scaffold protein.

5.2.2 Assembly of LHCII and Texas Red nanodiscs

Lipid nanodiscs were assembled with a lipid: ApoE422k ratio of 240:1. This ratio was selected to form nanodiscs made up, on average, of 6-7 ApoE422k proteins forming a disc structure with a diameter of 25-30 nm containing ~1500 lipids and 1 LHCII trimer. This was designed to allow unimpeded lateral lipid diffusion within the lipid bilayer annulus around the protein with a width of 7.5-10 nm from the protein extremity to the ApoE422k disk edge (Blanchette et al., 2008). Soy Asolectin phospholipid mixture (lipid extract from soybeans, purchased from Sigma) was used in nanodisc formation. These lipids are commonly used for reconstituting LHCII into nanodiscs because they have been shown to result in similar spectral properties as when native thylakoid lipids are used but are significantly cheaper (Son et al., 2020). Soy Asolectin is made up of ~25 % lecithin(glycerophospholipid mixture), ~25 % cephalin, ~25 % phosphatidylinositol with the remaining 25 % made up of minor amounts of other phospholipids and polar lipids. LHCII trimers were extracted from spinach leaves and biochemically purified using the detergent α-DDM as previously described in 3.3.1 and published literature (Adams et al., 2018). The effect of reconstituting LHCII with these lipids is discussed below.

Lipids stocks used for the formation of nanodiscs and liposomes were initially prepared by solubilising a known mass of Soy Asolectin lipid mixture in a chloroform: methanol solution (5:2) and drying down to a thin film under ultra-pure nitrogen gas. Before drying, chloroform solubilised Texas Red DHPE was added to lipid stocks as required. A molar ratio of 75:1 Soy Asolectin: TR-DHPE was used to align with the middle of the proteoliposome TR:lipid ratio (1.3 % mol/mol) shown to exhibit efficient Texas Red to LHCII energy transfer. (Full protocol in section 2.3.1)

Before being used for nanodisc assembly, lipid stocks were brought to room temperature and incubated overnight in an α-DDM detergent solution (20 mM HEPES (pH 7.5), 100 mM NaCl, 0.5 % α-DDM) to solubilise lipids into detergent micelles. ApoE422k monomers, detergent solubilised lipids, and LHCII trimers were mixed in a 12.5: 3000: 1 ratio and incubated while shaking at 4°C for one hour. A two-fold excess of lipid and scaffold protein was used to minimise the formation of doubly LHCII loaded nanodiscs which could potentially exhibit LHCII-LHCII interaction driven energy dissipation. Absorbent Bio Beads were then added to sample and incubated for a further hour to

remove detergent and allow lipid LHCII nanodiscs to self-assemble. Nanodisc samples were then purified through a Ni-NTA affinity column to remove any material that was not incorporated into the His-tagged nanodiscs. Figure 43 displays a cartoon schematic visualising the stages of detergent removal and Ni-NTA purification of nanodiscs. Successful formation of nanodiscs was initially assessed from the elution UV chromatography trace the colour of eluted fractions after Ni-NTA purification. An observed pigmentation in eluted sample fractions of green (LHCII-only lipid nanodisc samples) and grey (LHCII + Texas Red samples) after deliberate disc elution was a first suggestion that binding and then elution was successful and that the majority of LHCII and Texas Red were within nanodiscs. The UV absorption trace shown in Figure 44 is measured as liquid leaves the column so is an effective measure of the amount of biological material being eluted. The initial (load) peak in the UV trace relates to the increased UV absorption of lipids and proteins which have not been reconstituted into the nanodiscs leaving the column. The flat (Equilibrate) section relates to the washing step which ensures all unbound material has left the column. The final (Elution) peak indicates the point where a high imidazole buffer is used to un-bind His tagged nanodiscs from the column, the sharp peak immediately after this is caused by the increased UV absorption of nanodisc sample and is collected. The increased UV baseline after elution is due to the high imidazole buffer having increased UV absorption, which does not affect the sample collection as the sharp peak due to the sample can be easily resolved. Samples were then dialysed into 20 mM HEPES (pH 7.5) 100 mM NaCl to remove any residual elution buffer before further spectroscopic characterisation (See methods 2.3.4 for full protocol).

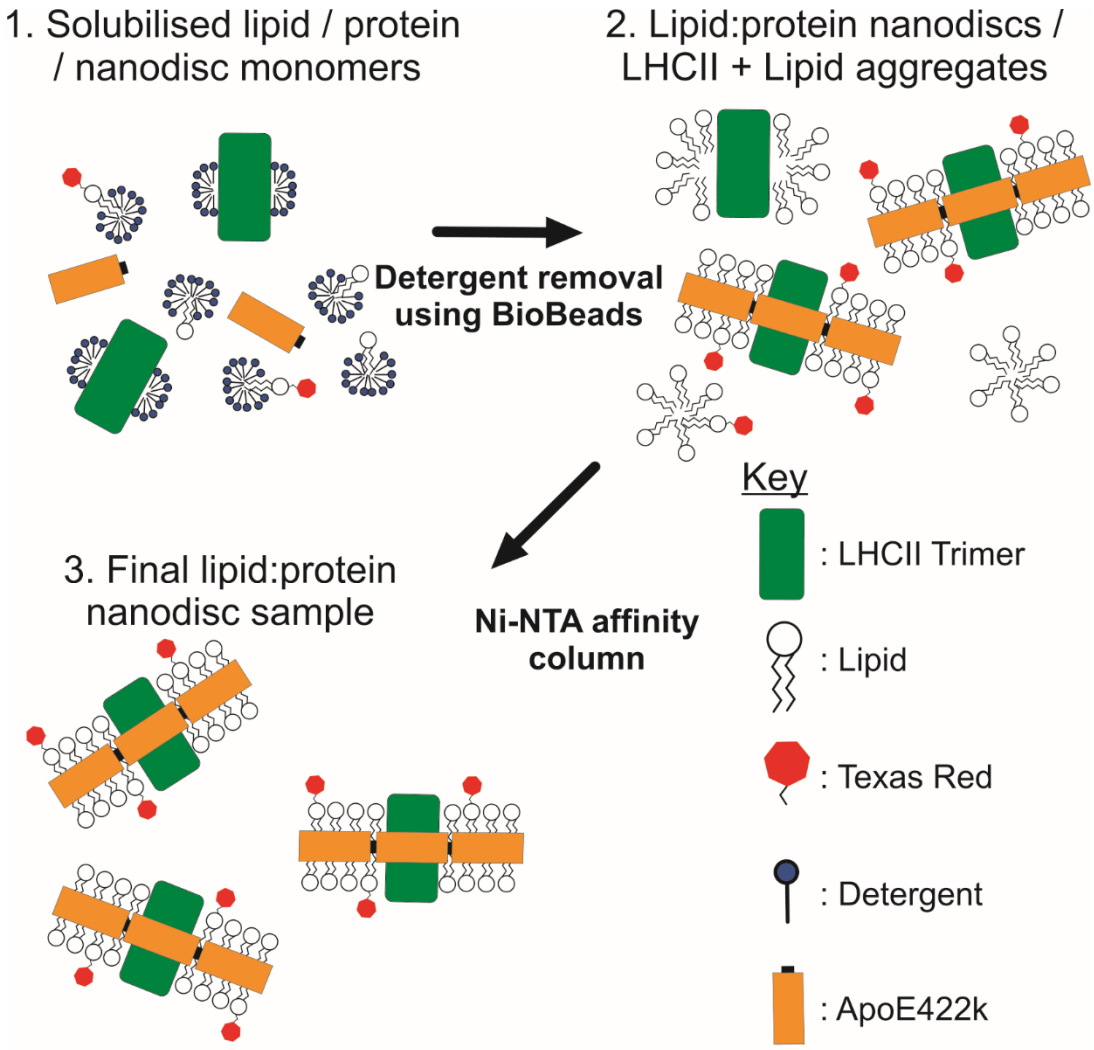

Figure 43 Concept schematic of ApoE422k lipid nanodisc formation (not to scale)

Lipid nanodiscs formation omitting LHCII was attempted using ApoE422k scaffold proteins and Soy Asolectin lipids as described previously. However, all attempts of forming discs without LHCII failed with minimal material coming through the Ni-NTA purification process. It is assumed that LHCII may have stabilising effect on lipid nanodiscs during self-assembly due to the large size of the discs and use of lipids which contain many non-planar bilayer forming lipids (Seiwert et al., 2018). Forming lipid only nanodisc samples was therefore not pursued as the Texas Red tagged lipid is expected to act similarly in liposomes as nanodiscs, therefore liposomes can be used as an appropriate control. Here, liposomes were formed via tip sonication in a buffer of 20 mM HEPES (pH 7.5), 100 mM NaCl as described in 2.3.2.

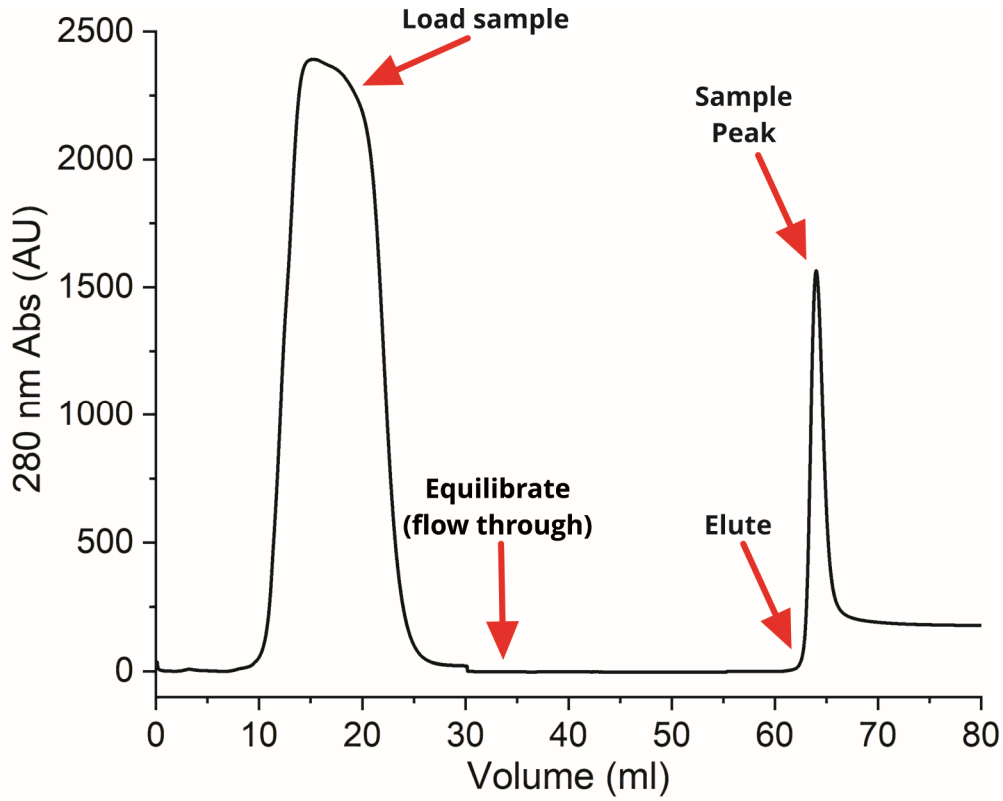

Figure 44 FPLC UV absorption trace of Ni-NTA purification of LHCII nanodiscs.

5.2.3 Size characterisation of nanodiscs

The size distribution of discs formed can be indicative of inconsistencies or failures in sample preparation. In order to investigate the dynamics of Texas Red to LHCII energy transfer in lipid nanodiscs it is essential to determine if they have formed as intended with a single LHCII protein incorporated into a confirmed bilayer area. The unintended formation of proteoliposomes or presence of large lipid or protein aggregates in samples will result in the dynamics of energy transfer in these systems being measured instead of those between freely diffusing Texas Red and single LHCII trimers as desired. The average diameter for nanodiscs with the ApoE422k: Lipid: LHCII ratio used (12.5: 3000: 1) was expected to be 25-30 nm with discs forming of 6-7 ApoE422k subunits. A distribution of disc sizes is expected as an x 2 excess of both ApoE422k and lipid was used to limit the formation of double or triple 'loaded' discs (2 or 3 proteins). A population of 'unloaded' discs without reconstituted LHCII are therefore expected to be formed which will have a smaller diameter (Blanchette et al., 2009).

Transmission Electron Microscopy (TEM) was employed to characterise a representative LHCII nanodisc sample and determine size distributions within the population. Highly diluted nanodisc samples were deposited onto copper mesh TEM grids and stained with 2 % uranyl acetate (full method in 2.8). TEM images of the representative nanodisc sample at different levels of magnification are shown in Figure 45 (A-D), and a histogram of manually measured nanodisc diameters (n=107) is shown in Figure 45 (E). The TEM images show a wide distribution of nanodisc diameters with an average of 21±7 nm (error value is calculated standard deviation). This value is slightly lower than the expected size of LHCII loaded nanodiscs of 25-30 nm. However, it is not unexpected due to the anticipated presence of 'unloaded' nanodiscs formed due to the excess of ApoE422k and lipids. The two peaks in the size distribution histogram are further evidence for two populations, one peak at 16 nm and one at 20 nm potentially represent 'unloaded' and LHCII 'loaded' nanodiscs, respectively. The absence of any significant proportion of large particles in the sample (>50 nm) suggests that the His-tag purification step is effective at removing any liposomes or proteoliposomes that may have formed during the detergent removal stage. This suggests that the vast majority of particles in the sample are individual lipid-nanodiscs.

All nanodisc samples were characterised with Dynamic Light Scattering to provide a size distribution for discs in solution and complement the TEM data (see 2.6 for full description). The size distribution for nanodiscs measured with DLS are shown in Figure 45 (F), LHCII-only nanodiscs (Green solid line), LHCII + TR nanodiscs (blue solid line) and Texas Red liposomes (red solid line) are displayed along with the z-average intensity diameters size of each (calculation in 2.6). These are 21 nm, 24 nm and 32 nm, respectively. These sizes are consistent with measurements from TEM on the representative nanodisc sample and do not suggest any large lipid or protein aggregates are present in solution. This size distribution samples suggests consistent formation of single nanodiscs.

Both DLS and TEM characterisation of nanodisc samples suggest an average nanodisc diameter of ~20 nm with most diameters falling within the range 15-30 nm. We speculate that this distribution is due to the presence of multiple populations of discs, unloaded (~15 nm), single LHCII loaded (~20-25 nm) and possibly double or triple LHCII loaded discs (~25-30 nm). Nanodiscs have previously been utilised to incorporate multiple proteins to

investigate interactions in a controlled membrane environment (Raschle et al., 2015). Although an excess of both lipids and ApoE422k scaffold protein was used to minimise the probability of multiple loaded discs the presence of this small sub-population is not entirely unexpected and known to occur in the formation of large nanodiscs. The sizes of nanodisc formed suggest that they contained of 4, 5 or 6 ApoE422k subunits which will form nanodiscs with diameters of 14.5 nm, 19 nm and 23.5 nm, respectively (Blanchette et al., 2008). The TEM images showed occasional particles of ~50 nm and very rare particles of ~100 nm. Crucially, the size characterisation studies did not show any significant evidence of very large (>100 nm) aggregates of proteins or lipids, meaning that Texas Red – LHCII interactions can be broadly considered to be between multiple Texas Red molecules and single LHCII trimers reconstituted into discs.

Note on contributions: All TEM data were collected by my colleague Damien Batchelor and analysed by AMH.

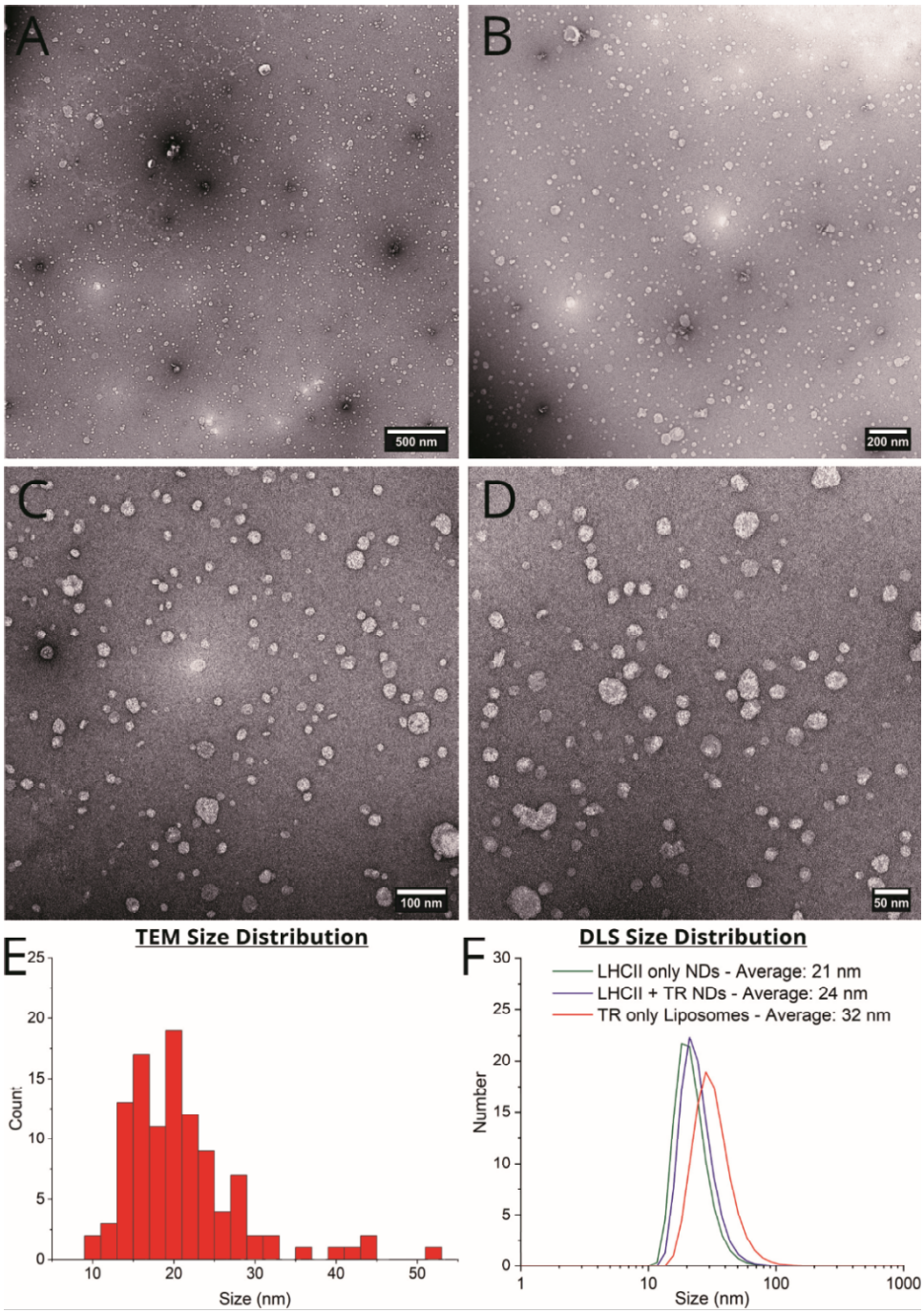

Figure 45 Negative stain TEM characterisation of LHCII lipid nanodiscs deposited onto copper mesh grids

(A-D) TEM images of LHCII lipid nanodiscs at different levels of magnification. (E) Size distribution histogram of nanodisc diameter in TEM images (n=107), images were analysed using ImageJ software 'measure' function and manually drawing profiles across the centres of particles in images. (F) DLS data for nanodisc and liposome samples (n=3 for each sample); the averages stated are the mean intensity weighted z-average hydrodynamic radius. Measurements were taken with backscatter were collected at 173° with a 633 nm excitation laser.

5.2.4 Absorption spectroscopy is used to determine sample composition

In order to effectively quantify Texas Red to LHCII energy transfer in lipid nanodiscs the relative composition of the fluorescent components must first be quantified. Ensemble absorption spectroscopy (data collected as in 2.4.2) was used to determine the LHCII and Texas Red composition in nanodisc and liposome samples. Normalised absorption spectra for these samples, LHCII lipid nanodiscs (solid green line), LHCII + Texas Red lipid nanodiscs (solid blue line), and liposomes with Texas Red (solid red line) are displayed in Figure 46. Spectral de-composition analysis, as described in previous chapters (section 3.3.3), allows the LHCII and Texas Red components of spectra to be isolated. The concentration of both components in each sample were calculated from measured optical density and extinction coefficients using the Beer-Lambert law (see section 4.2.1) (Lakowicz, 2006).

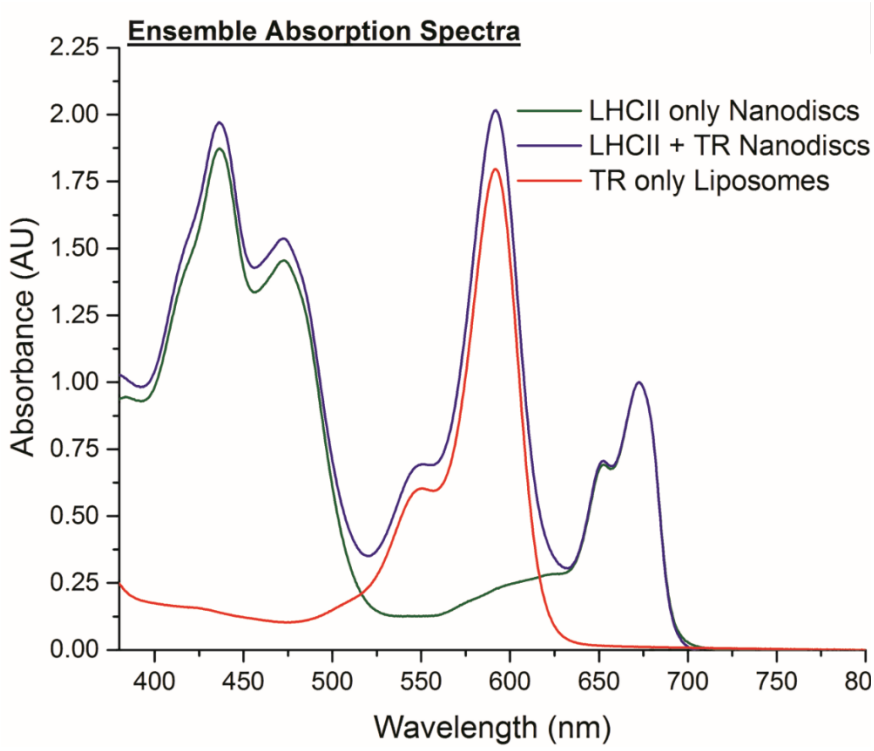

Figure 46 Absorption spectra of LHCII-only nanodiscs, Texas Red-LHCII nanodiscs and Texas Red-only liposomes

Absorption spectra of LHCII-only nanodiscs (solid green line), Texas Red-LHCII nanodiscs (solid blue line), and Texas Red-only liposomes (solid red line). All spectra normalised to 1.0 at Chl *a*, (~675 nm) or Texas Red (~591 nm) absorption peaks for

For the LHCII + TR nanodisc sample concentrations were determined to be 0.53 μM LHCII and 20.3 μM Texas Red. Assuming that the incorporation of untagged lipids and Texas Red DHPE are the same, nanodisc lipid concentration can be back-calculated from the initial lipid: TR ratio (75:1) as 1.52 mM lipid (1.3 % mol/mol TR-to-total lipid). This gives a Texas Red: LHCII ratio of ~40:1 in the sample with both components. All ratios of fluorescent components to lipids are displayed in Table 13. Due to using a 2x excess of lipid and nanodisc scaffold protein there is assumed to be a significant portion of lipid and Texas Red molecules not co-reconstituted into nanodiscs alongside LHCII. This makes quantifying the energy transfer efficiency difficult via analysis of donor quenching because fluorescence from Texas Red in these 'unloaded' nanodiscs would bias the overall signal.

The LHCII-only nanodisc sample was determined to have a LHCII concentration of 0.60 μM LHCII with 1.52 mM lipid (assuming the same lipid incorporation as the LHCII + TR sample). The Texas Red liposome sample had a Texas Red concentration of 55.9 μM with 4.19 mM lipid (1.3 % mol/mol TR-to-total lipid). The same lipid stock was used for Texas Red-only liposomes and Texas Red-LHCII to so that any changes in Texas Red fluorescence were due to energy transfer to LHCII and not concentration-dependent self-quenching of Texas Red (for discussion of this aspect, see section 3.3.8). Thus, these three fully-characterized samples were a good set for comparison as they contain a similar LHCII concentration in nanodiscs with or without TR (0.53 μM vs 0.60 μM LHCII) and the identical TR-to-lipid ratio in the sample with or without LHCII (75:1 = 1.3 % mol/mol).

Sample description	Calculated concentration		DLS Diameter	Lipid: LHCII	Lipid: TR	TR: LHCII
	LHCII (μM)	TR (μM)	(nm)	ratio	ratio	ratio
LHCII + TR nanodiscs	0.54	20.3	24	2817	75	38
LHCII only nanodiscs	0.60	0.0	21	2535	-	-
TR only liposomes	0.00	55.9	32	-	75	-

Table 12 Ratios of lipids to fluorescent components in nanodisc samples and liposome control

5.2.5 Comparison between LHCII reconstituted into proteoliposomes and nanodiscs

One of the purposes of using lipid nanodiscs to quantify the timescale of Texas Red to LHCII energy transfer was to minimise inter-protein energy dissipation associated with LHCII-LHCII interactions. The effect of LHCII aggregation was quantified for proteoliposomes in section 3.3.6. To confirm that nanodiscs minimise these aggregation driven effects the level of quenching in LHCII nanodiscs was also assessed and compared to proteoliposomes. The intactness and fluorescence properties of LHCII when reconstituted into lipid nanodiscs is also assessed via absorption and fluorescence spectroscopy, similar to the characterisation performed when LHCII was reconstituted into proteoliposomes (sections 3.3.5 and 3.3.6). To make a fair comparison between proteoliposomes and nanodiscs a proteoliposome sample with the same lipid: protein ratio as in the loaded nanodiscs was used (1500:1). The nanodisc and proteoliposome samples used in this comparison did not contain Texas Red so that the effect of the different membrane environments on LHCII can be easily determined independent of Texas Red.

When reconstituting LHCII into proteoliposomes small blue shifts in the Chl Q_y absorption peak (~675 nm), compared to isolated LHCII in α-DDM detergent micelles, were observed. Shifts of the absorption maximum could indicate a change in the local environment of the chlorophylls due to structural changes in the protein away from its native conformation. In proteoliposomes this shift appeared to be dependent on LHCII concentration and was between 1-3 nm, with larger shifts in proteoliposomes with a higher lipid: protein ratio. Figure 47 (A) shows the normalised absorption spectra of LHCII isolated in detergent micelles (black solid line), incorporated into lipid nanodiscs (red solid line) and incorporated into proteoliposomes (blue solid line). The Chl *a* absorption peak of LHCII in nanodiscs had a significantly lower blue shift (~1 nm) compared to ~3 nm in proteoliposomes (shifts relative to LHCII in detergent micelles). The Chl *a* to Chl *b* ratio (absorption peaks at 675 nm and 650 nm respectively) is also much closer to that of LHCII in detergent micelles when reconstituted into nanodiscs vs proteoliposomes. These smaller shifts in absorption peak position and spectral shape in nanodiscs suggest that they provide a more "native-like" lipid environment for LHCII than the proteoliposomes (at this lipid-to-protein ratio at least).

The phenomenon of LHCII self-quenching is known to occur when LHCII is reconstituted into both proteoliposomes and lipid nanodiscs (Moya et al., 2001). The level of self-quenching must be quantified in order to accurately determine the enhancement of LHCII emission due to energy transfer from Texas Red. LHCII fluorescence intensity and lifetime were assessed in nanodiscs and compared to when reconstituted into proteoliposomes. Figure 47 (B and C) show the comparison in steady-state and time-resolved fluorescence emission, respectively (colour scheme is the same as for absorption data). Tabulated values of LHCII quenching are shown in Table 13. The steady-state fluorescence emission of LHCII was reduced from 2.51 x 10^{15} counts / mol when isolated in detergent micelles to 1.78 x 10^{15} counts / mol in nanodiscs and to 1.06 x 10^{15} counts / mol when in proteoliposomes, as shown in Figure 47 (B) (total counts, from the integrated area under peak). Time-resolved fluorescence lifetime of LHCII calculated from decay traces shown in Figure 47 (C), calculated as described in 2.4.4, decreases from 4.1 ns when isolated in detergent micelles to 3.2 ns in nanodiscs and to 1.8 ns when in proteoliposomes. These measurements show that LHCII is significantly less quenched when reconstituted into nanodiscs compared to proteoliposomes at the same lipid: protein ratio. It seems that nanodiscs successfully minimize the known effect of LHCII-LHCII interaction driven self-quenching (Crisafi and Pandit, 2017).

Sample description	LHCII Absorbance	LHCII Conc	Relative LHCII Emission	Relative steady-state LHCII Emission	LHCII lifetime	Relative time-resolved LHCII Emission
	Integrated area (635-800 nm) dilution corrected	LHCII (μM)	Integrated area 625-800 nm (473 nm Excitation)	(%)	(ns)	(%)
LHCII in Detergent	793.56	0.01	2.51E+15	100.00	4.1	100.00
LHCII Nanodisc	40.66	0.60	1.78E+15	71.06	3.2	78.05
LHCII Liposome	34.91	0.52	1.06E+15	42.46	1.8	43.90

Table 13 Comparison of LHCII fluorescence in proteoliposomes and lipid nanodiscs

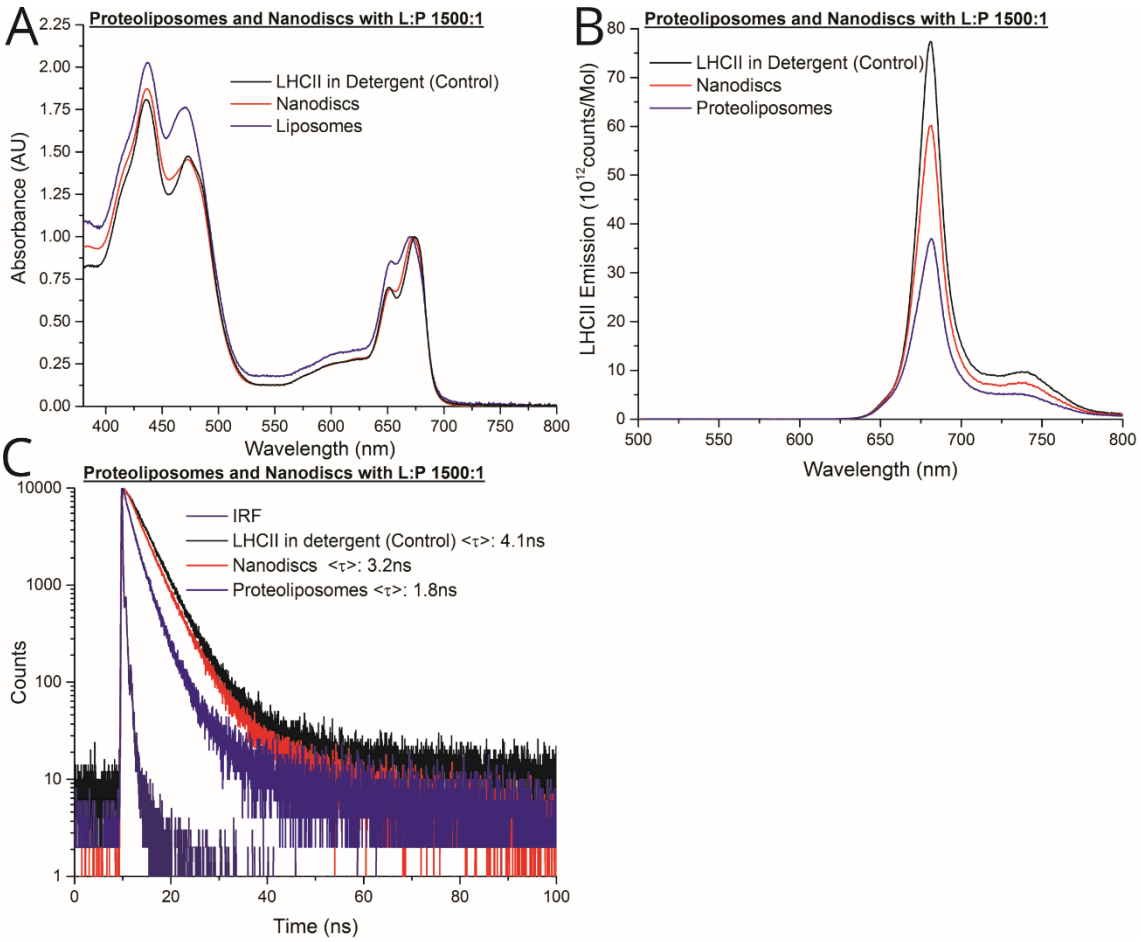

Figure 47 Absorption spectra, steady-state fluorescence emission intensity, and time-resolved fluorescence lifetime of LHCII isolated in detergent, in proteoliposomes, and in lipid nanodiscs

(A) Absorption spectra of LHCII reconstituted into liposomes and nanodiscs showing spectral shifts relative to LHCII in detergent. All spectra normalised to 1.0 at Chl *a* absorption peak (~675 nm) for visual clarity. (B) Steady state fluorescence emission spectra of LHCII (473 nm selective LHCII excitation – 2 nm bandwidth) reconstituted into proteoliposomes and nanodiscs relative to LHCII in detergent. All emission spectra are normalised to LHCII concentration giving a value of emission per mole to show relative quenching between systems. (C) Time resolved fluorescence data of LHCII (473 nm pulsed laser excitation – 10 nm bandwidth) reconstituted into proteoliposomes and nanodiscs relative to LHCII in detergent. Amplitude weighted lifetime (<τ>) of LHCII calculated from each decay curve is displayed in legend.

5.3 Calculation of the efficiency of Texas Red to LHCII energy transfer in nanodiscs

5.3.1 LHCII fluorescence excitation spectra and linear absorption analysis shows how much energy absorbed in the system is transferred to LHCII

We intended to quantify the dynamics of Texas Red to LHCII in a model nanodisc system where energy absorbed by Texas Red is efficiently transferred to LHCII in a system that is designed to limit any LHCII-LHCII interactions. It was therefore crucial to rigorously show that Texas Red to LHCII energy transfer is occurring in Texas Red-LHCII nanodiscs. Comparison between fluorescence excitation spectra and linear absorption (1 – Transmission) spectra can indicate the connectivity of chromophores within LHCII. One would expect perfectly overlapping spectra if all chromophores are well connected as energy absorbed by any chromophore in the system would manifest as fluorescence from the terminal chromophore. It can also be used to determine the energy transfer efficiency between donor and acceptor molecules undergoing FRET. Fluorescence excitation spectra were collected for LHCII nanodisc samples with and without Texas Red. Fluorescence excitation spectra were acquired by selectively collecting LHCII emission at 686 nm and scanning over a range of excitation wavelengths (described in 2.4.3). Linear absorption and the relationship to sample absorption was previously described in section 3.4.1

For LHCII reconstituted into nanodiscs without additional Texas Red, Figure 48 (green lines), the excitation and linear absorption spectra overlap almost perfectly (dashed and solid lines, respectively, normalised at 675 nm for comparison). This suggests a well-connected system where energy absorbed at any wavelength is transferred to the same final fluorescent component, representing intra-protein chlorophyll-to-chlorophyll and carotenoid-to-chlorophyll energy transfer. This is indicative of intact and fluorescently active LHCII when reconstituted into nanodiscs.

If the excitation spectrum is lower than the linear absorption there is less than 100 % energy transfer from donor to acceptor at that wavelength: for LHCII + Texas Red samples assessing the region of Texas Red absorption would represent Texas Red-to-

LHCII energy transfer. The ratio of excitation to linear absorption over the donor region is therefore directly related to energy transfer efficiency (ETE). Comparison between acceptor fluorescence excitation and linear absorption over the region of donor absorption (with acceptor only excitation and linear absorption subtracted) can be used to quantifiably estimate donor to acceptor energy transfer efficiency using the standard relationship shown in Equation 21 (Yoneda et al., 2015, Harris et al., 2014b).

$$ETE = 1 - \frac{(1 - T_D) - Ex_D}{(1 - T)}$$

Equation 21 Energy transfer efficiency as calculated by comparison of linear absorption and acceptor fluorescence excitation spectra. TD: Donor transmission maximum (~590 nm), ExD Donor fluorescence excitation maximum (~590 nm). Both linear absorption and excitation spectra had the LHCII component removed as described in 3.3.3 for absorption data.

In the Texas Red-LHCII nanodisc sample the ratio of linear absorption to LHCII fluorescence excitation over the region of Texas Red absorption indicates an energy transfer efficiency from 65 %, Figure 48 (blue lines). Due to the presence of 'unloaded' lipid nanodiscs which contain Texas Red but no LHCII, a proportion of the Texas Red linear absorption is from Texas Red molecules not interacting with LHCII. It is not possible to remove this component from the linear absorption spectra by de-composition meaning that the energy transfer efficiency for TR-LHCII-lipid nanodiscs is likely underestimated here.

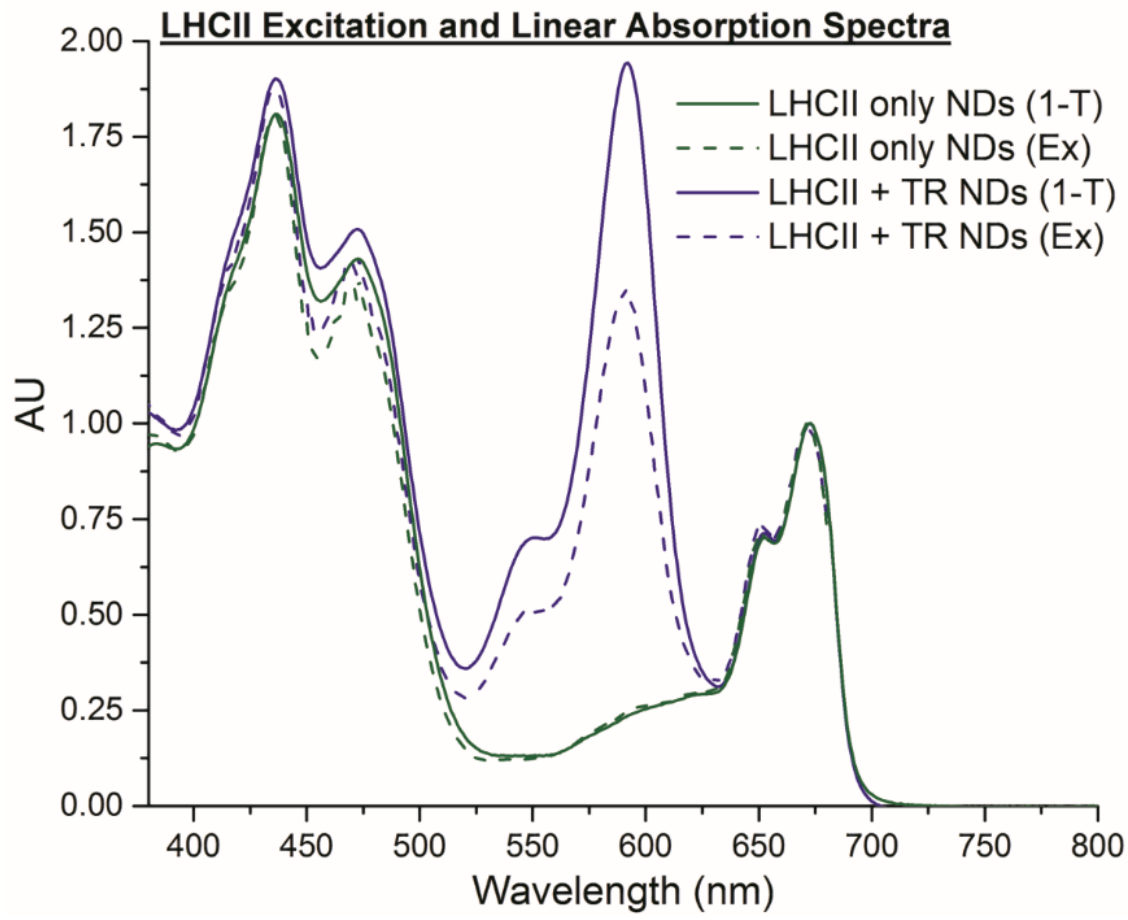

Figure 48 Linear absorption and excitation spectra of LHCII-only and Texas Red-LHCII lipid nanodiscs

LHCII fluorescence excitation (Ex – emission collected at 686 nm) and linear absorption (1-T) spectra for LHCII nanodiscs with and without Texas Red. Both spectra normalised to 1.0 at Chl *a* absorption peak (~675 nm) to allow comparison.

5.3.2 Calculation of excitation energy transfer efficiency from donor quenching

A more robust method of calculating the efficiency of energy transfer between Texas Red and LHCII is by measuring changes in the fluorescence emission of the donor (Texas Red) when the acceptor (LHCII) is present. The steady-state fluorescence emission and time-resolved fluorescence lifetime of Texas Red will be quenched if energy transfer to LHCII is occurring. This is due to a statistically relevant number of excitons in Texas Red taking the alternative non-radiative pathway of transferring energy to LHCII instead of

resulting in Texas Red fluorescence. The level of quenching is assessed by comparing the fluorescence emission and lifetime of Texas Red incorporated into liposomes omitting LHCII with the fluorescence emission and lifetime when incorporated into Texas Red-LHCII lipid nanodiscs.

Texas Red quenching was quantified by measuring its steady-state fluorescence intensity with selective Texas Red excitation (540 nm – 1 nm bandwidth) and using the known molar concentration, calculated from absorption data shown in Figure 49 (A), to convert spectra into 'emission per mole', Figure 49 (B). The reduction in fluorescence intensity of Texas Red when co-reconstituted into nanodiscs with LHCII is clearly shown in Figure 49 (B). Fluorescence emission intensity is reduced from 1.226 $x10^{12}$ counts / mol at the emission maximum (~610 nm) with no LHCII present (red solid line) to 4.68 $x10^{11}$ counts / mol when in nanodiscs with LHCII (blue solid line). This represents a reduction in fluorescence emission 'per Texas Red' of 62 %.

Quenching of Texas Red fluorescence due to energy transfer to LHCII was also independently measured via time-resolved fluorescence spectroscopy (TCSPC) by selectively exciting Texas Red (540 nm picosecond pulsed laser – 5 nm bandwidth) collecting emission (610 nm – 5 nm bandwidth). A reduction in the fluorescence lifetime of the Texas Red in the presence of LHCII is indicative of a population of excited states being transferred to an acceptor molecule rather than fluorescing. Figure 49(C) shows the time-resolved fluorescence decay curve of Texas Red incorporated into liposomes (solid red line) and incorporated into Texas Red-LHCII lipid nanodiscs (solid blue line). There is a clear steepening of the Texas Red decay curve when LHCII is present. The fitted mean fluorescent lifetime of Texas Red, calculated as in 2.4.4, decreases from a single exponential decay with time constant of 3.85 ns for Texas Red-only liposomes (red solid line) to a bi-exponential decay with a time constant of 2.26 ns when in Texas Red-LHCII lipid nanodiscs (blue solid line). This represents a reduction in Texas Red fluorescence lifetime of 41.3 %. The components of these decay fits are displayed in Table 14.

Sample description	Lifetime Components				TR Lifetime	
	τ_1 (ns)	β_1	τ_2 (ns)	β_2	$\tau_{Average}$ (ns)	X^2
TR only Liposomes	3.85	1.00	-	-	3.85	2.90
LHCII + TR Nanodiscs	0.82	0.51	3.57	0.49	2.26	1.40

Table 14 Texas Red lifetime components in Texas Red-LHCII nanodiscs and Texas Red-only liposomes

Graphical analysis of steady-state and time-resolved fluorescence intensity and lifetime data allows the observed trend of Texas Red fluorescence being quenched by LHCII to be quantified. Energy transfer efficiency was calculated from both steady-state (ETE_{SS}) and time-resolved (ETE_{TR}) data using the standard equations, as detailed in previous chapters.

($ETE_{SS} = 1 - \frac{F_{DA}}{F_D}$) and ($ETE_{TR} = 1 - \frac{\tau_{DA}}{\tau_D}$) (Equation 22 and Equation 23).

Texas Red fluorescence quenching measured via steady-state and time-resolved data lead to an estimated excitation energy transfer efficiencies of ~62 % and ~41 %, respectively.

A subpopulation of 'unloaded' nanodiscs in the LHCII+TR sample will mean that the values for quenched Texas Red fluorescence emission and lifetime will be overestimated. The true energy transfer efficiency for Texas Red molecules reconstituted into nanodiscs alongside LHCII is significantly higher than reported using the average Texas Red fluorescence measurements. The two Texas Red lifetime components identified by the bi-exponential decay in combined Texas Red-LHCII nanodiscs represent two populations of molecules, the shorter lifetime corresponding to Texas Red reconstituted into nanodiscs alongside LHCII and the longer component to Texas Red in 'unloaded' nanodiscs. The lifetime composts of the bi-exponential decay suggest that 49 % of Texas Red in the system is transferring energy to LHCII while the the remaining 51 % is not. This may be a combination of Texas Red molecules in 'unloaded' nanodiscs and Texas Red molecules at the periphery of loaded nanodiscs with too large a separation from LHCII for energy transfer to take place. The short component of Texas Red lifetime, 0.87 ns, suggests that this population has an energy transfer efficiency of 77 %.

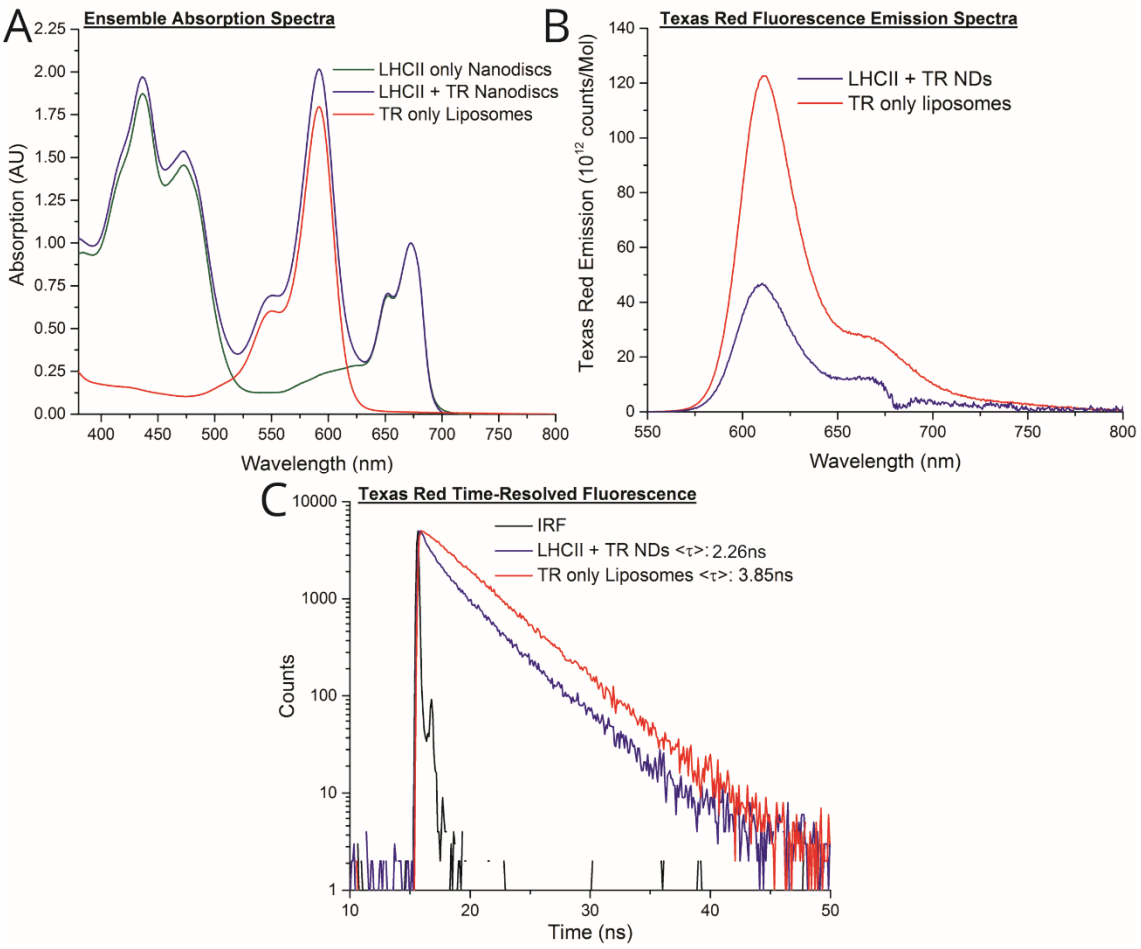

Figure 49 Steady-state fluorescence emission and time-resolved fluorescence lifetime of Texas Red reconstituted into Texas Red-LHCII lipid nanodiscs

(A) Absorption spectra of LHCII nanodiscs with and without Texas Red relative to LHCII in detergent; the spectrum of Texas Red liposomes is also displayed. All spectra normalised to 1.0 at Chl *a* absorption peak (~675 nm) for visual clarity. (B) Steady state fluorescence emission spectra (540 nm selective Texas Red excitation 1 nm bandwidth) of Texas Red in liposomes and nanodiscs with reconstituted LHCII. All emission spectra are normalised to Texas Red concentration giving a value of emission per mole to show relative quenching between systems. LHCII emission has been removed as described in 3.4.2 for visual clarity. (C) Time resolved fluorescence data of Texas Red (540 nm pulsed laser excitation – 5 nm bandwidth) reconstituted into proteoliposomes and nanodiscs in liposomes and nanodiscs with reconstituted LHCII. The amplitude weighted lifetime (<τ>) of Texas Red calculated from each decay curve is displayed in figure.

5.3.3 Calculation of enhancement of LHCII fluorescence due to energy transfer from Texas Red

Energy transfer from Texas Red to LHCII can be observed by an increase in the fluorescence emission of LHCII when Texas Red is selectively excited, as shown in chapters 3.4.3 and 3.4.5 for Texas Red-LHCII proteoliposomes.) This is also a way to directly measure the "benefit" to the protein due to the additional energy from Texas Red. When LHCII is excited at 540 nm, where LHCII absorption is low, a minimal level of LHCII fluorescence is observed. If energy is being transferred to LHCII from additional complementary Texas Red molecules an enhancement of LHCII fluorescence would be observed due to the additional energy being transferred from Texas Red. Enhancement of LHCII fluorescence due to energy transfer from Texas Red was quantified by calculating its relative fluorescence 'per mole' when excited at 540 nm in nanodiscs with and without Texas Red. Concentrations of LHCII and Texas Red were calculated as shown in 5.2.4 using absorption data from Figure 49 (A). The increase in LHCII fluorescence emission when excited at 540 nm is shown in Figure 50; the relative emission of LHCII increases from 1.54 $x10^{14}$ counts / mol in the absence of Texas Red (green solid line) to 4.00 $x10^{14}$ counts / mol with Texas Red present (blue solid line). This represents a 260 % enhancement in LHCII fluorescence when excited in the 'green gap' due to energy transfer from Texas Red. Tabulated values of LHCII enhancement are shown in Table 15. This level of LHCII enhancement in nanodiscs is significantly higher than in the 163 % enhancement in proteoliposomes containing a similar TR-to-lipid ratio, as described in section 3.4.5, due to minimised LHCII-LHCII interaction driven quenching.

This enhancement in LHCII fluorescence corresponds to each Texas Red molecule effectively enhancing the emission of LHCII by 4 % when excited at 540 nm. However, due to the presence of 'unloaded' nanodiscs containing Texas Red molecules which are not interacting with LHCII number of Texas Red molecules interacting with LHCII is overestimated. This means that the value of each Texas Red molecule effectively 'enhancing' the absorption of LHCII by 4 %, is also underestimated, and the true enhancement 'per mole' is likely higher for those TR which are actually co-reconstituted in nanodiscs with LHCII.

Sample description	LHCII Absorbance	LHCII Conc	TR Absorbance	TR Conc	Relative TR Emission	TR <T >	ETE (steady-state)	ETE (time –resolved)	Relative LHCII Emission	LHCII Emission Enhancement
	Integrated area (635-800 nm) dilution corrected	(μM)	OD at 591 nm dilution corrected	(μM)	Peak height at 610 nm (540 nm Excitation)	(ns)	(%)	(%)	Integrated area 625-800 nm (540 nm Excitation)	(%) relative to LHCII isolated in detergent micelles
LHCII Nanodisc	40.66	0.60	-	-	-	-	-	-	1.52E+14	96.82
TR Liposome	-	-	4.73	55.9	1.23E+12	3.85	-	-	-	-
LHCII + TR Nanodisc	35.88	0.53	1.72	20.3	4.68E+11	0.95	62.00	75.00	4.00E+14	255.45

Table 15 Spectroscopy data used to calculate Texas Red to LHCII energy transfer in nanodiscs

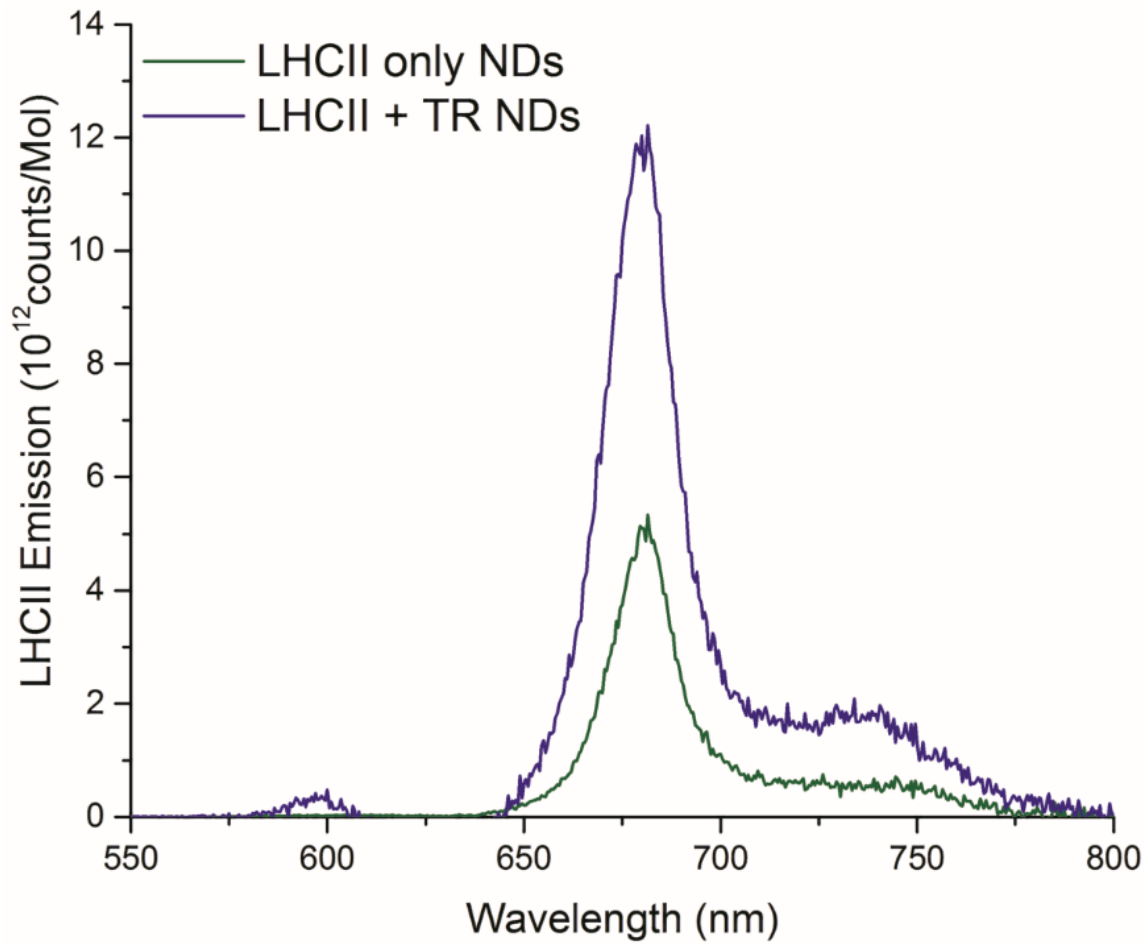

Figure 50 Steady-state fluorescence emission intensity of LHCII reconstituted into LHCII-only and Texas Red-LHCII nanodiscs

Steady state fluorescence emission spectra of LHCII (540 nm selective Texas Red excitation – 1 nm bandwidth) reconstituted into nanodiscs with and without Texas Red. All emission spectra are normalised to LHCII concentration giving a value of emission per mole to show relative enhancement between systems. Texas Red emission has been removed as described in 3.4.2 for visual clarity.

5.3.4 Discussion: interpretations of the initial nanodisc characterisation data

The characterisation of nanodisc samples described in the previous sections was performed before samples were shipped to collaborators for further time-resolved fluorescence spectra (TRFS) and transient absorption spectroscopy (TA) measurements. These advanced spectroscopy techniques were used to determine the timescale of Texas Red to LHCII energy transfer and are discussed in the following sections, but first it is worthwhile to discuss our initial findings of the sample quality. The detailed initial characterisation of both sample composition and of Texas Red to LHCII energy transfer was vital in confirming that nanodiscs had formed as intended so that the specific interactions between multiple Texas Red molecules and a single LHCII trimer could be investigated.

In the design of our lipid nanodiscs system, we had aimed to minimize the protein-protein interactions which are known to self-quench LHCII, to allow the energy transfer from Texas Red molecules to be studied without the complication of inter-protein energy dissipation. Comparison of LHCII fluorescence when reconstituted into proteoliposomes and lipid nanodiscs, with similar lipid: protein ratios, shows a decrease in emission intensity of 58 % in liposomes compared to 29 % in nanodiscs. Time-resolved fluorescence data shows a similar trend with the lifetime being quenched by 56 % in liposomes and 22 % in nanodiscs. Both steady-state and time-resolved quenching measurements are relative to LHCII trimers isolated in detergent micelles. This significantly lower level of LHCII self-quenching in nanodiscs compared to proteoliposomes is attributed to the minimised LHCII-LHCII interactions in the confined membrane area (Moya et al., 2001). This level of LHCII fluorescence quenching when utilising nanodiscs is consistent with other studies using the same lipid mixture and scaffold protein (Son et al., 2020) . This confirms that the goal of minimising LHCII-LHCII interactions in nanodiscs was successful and was a good starting place for the later ultrafast measurements to investigate Texas Red to LHCII energy transfer independent of LHCII self-quenching

In order to confirm that Texas Red to LHCII energy transfer was occurring in nanodiscs as intended, energy transfer from Texas Red to LHCII in nanodiscs was characterised

with the same fluorescence spectroscopy techniques as for proteoliposomes, as described in section 3.4. Texas Red to LHCII energy transfer efficiencies in nanodiscs calculated from three separate methods were 62 %, 41 % and 65 % (intensity, lifetime, excitation, respectively). The steady-state calculated energy transfer efficiency in nanodiscs, 62 %, is significantly lower than the 97 % calculated in a in a comparable proteoliposome sample (the same LHCII: Lipid: Texas Red ratio). This discrepancy is attributed to the presence of a population of 'unloaded' nanodiscs containing Texas Red molecules which are not interfaced with LHCII. These Texas Red molecules will be fluorescently unquenched and skew the steady-state and time-resolved values of Texas Red fluorescence emission resulting in a lower overall value of energy transfer efficiency being calculated. The "true" value for energy transfer efficiency for nanodiscs containing both LHCII and Texas Red can be estimated by not considering the 'un-quenched' lifetime component of the Texas Red bi-exponential lifetime decay fit. This results in an estimated energy transfer efficiency of ~77 % for the population of Texas Red modules with are interfaced with LHCII.

The absolute enhancement of LHCII fluorescence in nanodiscs was found to be significantly higher than for the equivalent proteoliposomes. This was likely due to low levels of fluorescence quenching associated with LHCII-LHCII interactions which are minimised in nanodiscs. LHCII fluorescence emission intensity, when excited at 540 nm, is enhanced to 255 % compared to a baseline of 'un-quenched' LHCII in detergent micelles when in nanodiscs containing Texas Red. This enhancement is only to 164 % in the equivalent proteoliposomes sample (the same LHCII: Lipid: Texas Red ratio). Like the proteoliposome system, enhancement of absorption using lipid tagged complementary chromophores is significantly higher than when covalently attaching chromophores. This is due to the potential of incorporating a much higher concentration of tagged-lipids around the protein within the bilayer compared to the number of available sites for covalent attachment directly to the protein (Yoneda et al., 2015). Enhancement of LHCII 'per Texas Red' is also calculated for the nanodisc system is 4 % 'per Texas Red' when excited at 540 nm. This is likely an underestimation due to the presence of 'unloaded' nanodiscs in the system. If one assumed that 50 % of the nanodiscs in the system are 'unloaded then the effective enhance of LHCII 'per Texas Red' rises to ~8 %, much closer to the enhancement of ~10 % 'per Texas Red' calculated in proteoliposomes with the same Texas Red: LHCII ratio.

Thus, we have found that efficient Texas Red to LHCII energy transfer is taking place in a significant population of nanodiscs in the sample. Size characterisation suggests that the sample consists of predominantly of disks either loaded with one LHCII trimer or are 'unloaded', consisting of lipid-only confined bilayer. Furthermore, the LHCII enhancement is much higher than observed in proteoliposomes due to minimised LHCII self-quenching attributed to minimised LHCII-LHCII interactions in the confined membrane area. Efficient Texas Red to LHCII energy transfer, previously shown in proteoliposomes, was successfully replicated in nanodiscs. Samples were taken forward for characterisation using advanced spectroscopic techniques to study the high-speed photo-physics of Texas Red to LHCII energy transfer. In these ultra-fast measurements, the issue of 'unloaded nanodiscs' is negated as signal from Texas Red molecules which are not transferring energy to LHCII can be distinguished between temporally.

5.4 Advanced spectroscopy techniques

5.4.1 Time resolved fluorescence spectra

We wished to more fully understand the excited state lifetimes of Texas Red-LHCII nanodiscs. Previously, lifetime measurements on LHCII and Texas Red had been made independently with narrow excitation and emission wavelengths for both. Time resolved fluorescence spectra (TRFS) measure the fluorescence decay rate in a across a range of emission wavelengths. This is comparable the TCSPC data shown in 5.2.5 and 5.3.2 for LHCII and Texas Red, respectively. All measurements were made using selective Texas Red excitation at 550 nm, as indicated in Figure 51, and have a significantly improved temporal resolution compared to previously reported TCSPC. This technique allows LHCII and Texas Red lifetimes in samples to be determined with a single measurement and also shows intermediate emission wavelengths. All measurements were performed at MIT by collaborator Minjung Son, Department of Chemistry, MIT, USA; full details of the measurement procedure included in 2.4.5.

Time resolved fluorescence spectra for Texas Red-only liposomes, LHCII-only nanodiscs, and Texas Red-LHCII nanodiscs are shown in Figure 52. The Texas Red-only map (Figure 52 (A)) clearly shows a maximum emission at 610 nm shortly after excitation (time = 0 s), followed by a steady decreases with time. The emission intensity against time is integrated over an area corresponding to the wavelength range of Em1 (560 - 600 nm) based on spectral interferometry, to produce a decay curve which represents Texas Red-only fluorescence decay, as shown in Figure 52 (D). This single exponential decay corresponds to a fluorescence lifetime of 3.94 ± 0.2 ns, in good agreement with our previous measurements on the fluorescence lifetime of Texas Red in liposomes omitting LHCII (non-quenched). Figure 52 (B) shows the decay map for LHCII-only nanodiscs: there is an emission maximum at 681 nm just after initial excitation (time = 0s) followed by a a clear decline in emission intensity. Figure 52 (E) shows the decay curve from the intensity vs time integrated over the Em2 wavelength range (>665 nm), based on spectral interferometry, which represents LHCII-only fluorescence. This bi-exponential LHCII decay has an associated fluorescence lifetime of 2.68 ± 0.06 ns, slightly shorter than shown in previous TCSPC measurements of LHCII-only nanodiscs (this chapter), but still suggests a relatively non-quenched LHCII.

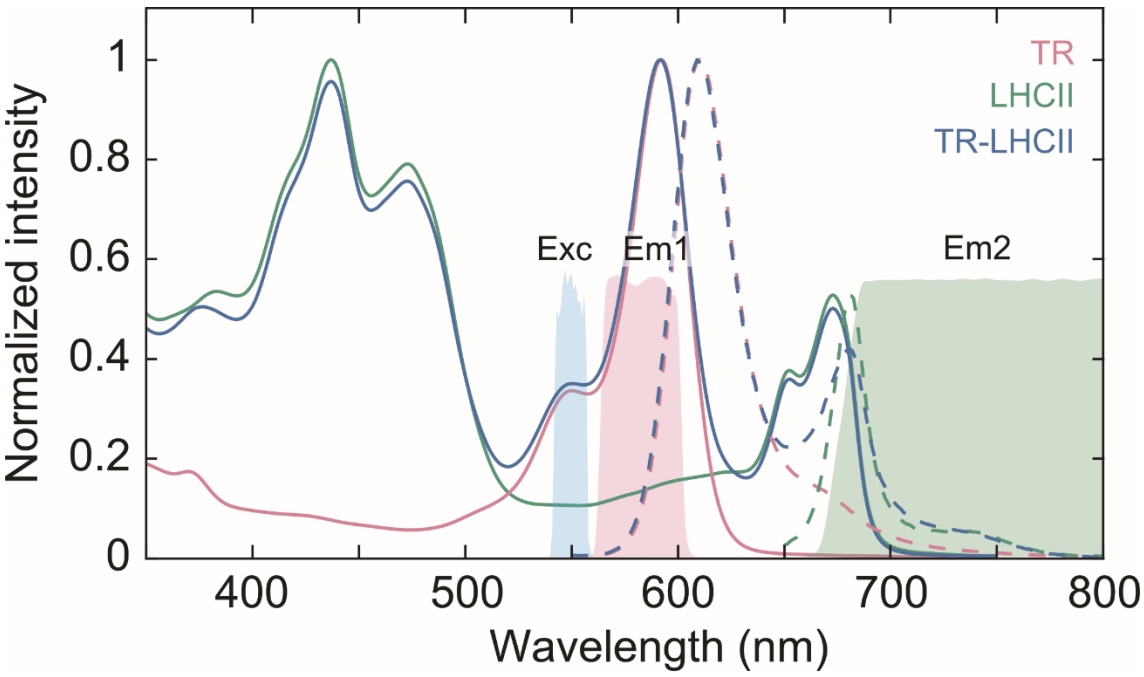

Figure 51 Experimental conditions for time-resolved fluorescence spectra measurements

Excitation spectrum (Exc) and the two emission filter ranges (Em1 and Em2) employed in the TCSPC measurements. The steady-state absorption (solid lines) and fluorescence (dashed lines) spectra of the samples are overlaid. This figure was produced by my collaborator Minjung Son, Department of Chemistry, MIT, USA.

The decay map for the combined LHCII +Texas Red nanodisc sample, shown in Figure 52 (C), reveals two fluorescent decay components with peak maximum at 610 nm and 681 nm corresponding to Texas Red and LHCII fluorescence decays, respectively. The Texas Red component, defined by the Em1 wavelength range of 560 – 600 nm, decays significantly faster in the combined LHCII + Texas Red sample than in Texas Red-only liposomes. Figure 52 (F, purple solid line) shows this decay curve for Texas Red (Em1); fitting this decay results in a bi-exponential fit with a corresponding average lifetime of 1.28 ± 0.03 ns. This decrease in Texas Red fluorescence lifetime can be used with Equation 23 to calculate the energy transfer efficiency.

$$ETE_{TR} = 1 - (\frac{\tau_{DA}}{\tau_D}).$$

All decay curve fitting components are shown in Table 16. The decrease in Texas Red fluorescent lifetime when in nanodiscs alongside LHCII corresponds to an energy transfer

efficiency of 68 %. The fluorescence lifetime of Texas Red calculated here (1.28 ns) is significantly shorter than when calculated with TCSPC earlier (2.26 ns). However, the distribution of the two lifetime components in the bi-exponential fit is broadly consistent from the two methods with ~50 % of the fitted lifetime amplitude representing unquenched Texas Red. The fluorescence decay of LHCII, defined by the wavelength range Em2 (>660 nm) in the combined LHCII + Texas Red nanodisc sample is shown in Figure 52 (F, green solid line). The decay curve fit corresponds to a bi-exponential decay with an average LHCII lifetime of 3.17 ± 0.13 ns. This longer lifetime, compared to LHCII-only nanodiscs, is attributed to an additional ~3.9 ns component not present in LHCII-only nanodiscs which arises due to overlap of the Em2 wavelength range with the Texas Red emission (i.e., Texas Red has an unquenched lifetime corresponding to the ~3.9 ns component and because some Texas Red signal overlaps into the LHCII channel may cause the lengthening of the calculated LHCII lifetime). There is no observable initial 'rise' in the LHCII decay due to a time delay in energy transfer from Texas Red, which suggests that the timescale of FRET is shorter than the systems temporal resolution of ~ 50 ps. The TRFS measurements allow the additional dimension of wavelength to be resolved and taken into account when considering the energy transfer process. The extra dimension (compared to TCSPC) allows processes which overlap in time but not wavelength to be separated in a manner that would not be otherwise possible.

Sample description	Emission range	Lifetime Components				Lifetime	
		τ1 (ns)	β1	τ2 (ns)	β2	$T_{average}$ (ns)	Error (ns)
TR Liposomes	Em1 (Texas Red)	3.94	1	-	-	3.94	0.20
LHCII Nanodiscs	Em2 (LHCII)	0.33	0.102	2.95	89.8	2.68	0.06
LHCII + TR Nanodiscs	Em1 (Texas Red)	0.32	0.588	2.64	41.2	1.28	0.03
LHCII + TR Nanodiscs	Em2 (LHCII)	2.60	0.664	3.92	33.6	3.17	0.13

Table 16 Fitting parameters for time resolved fluorescence data

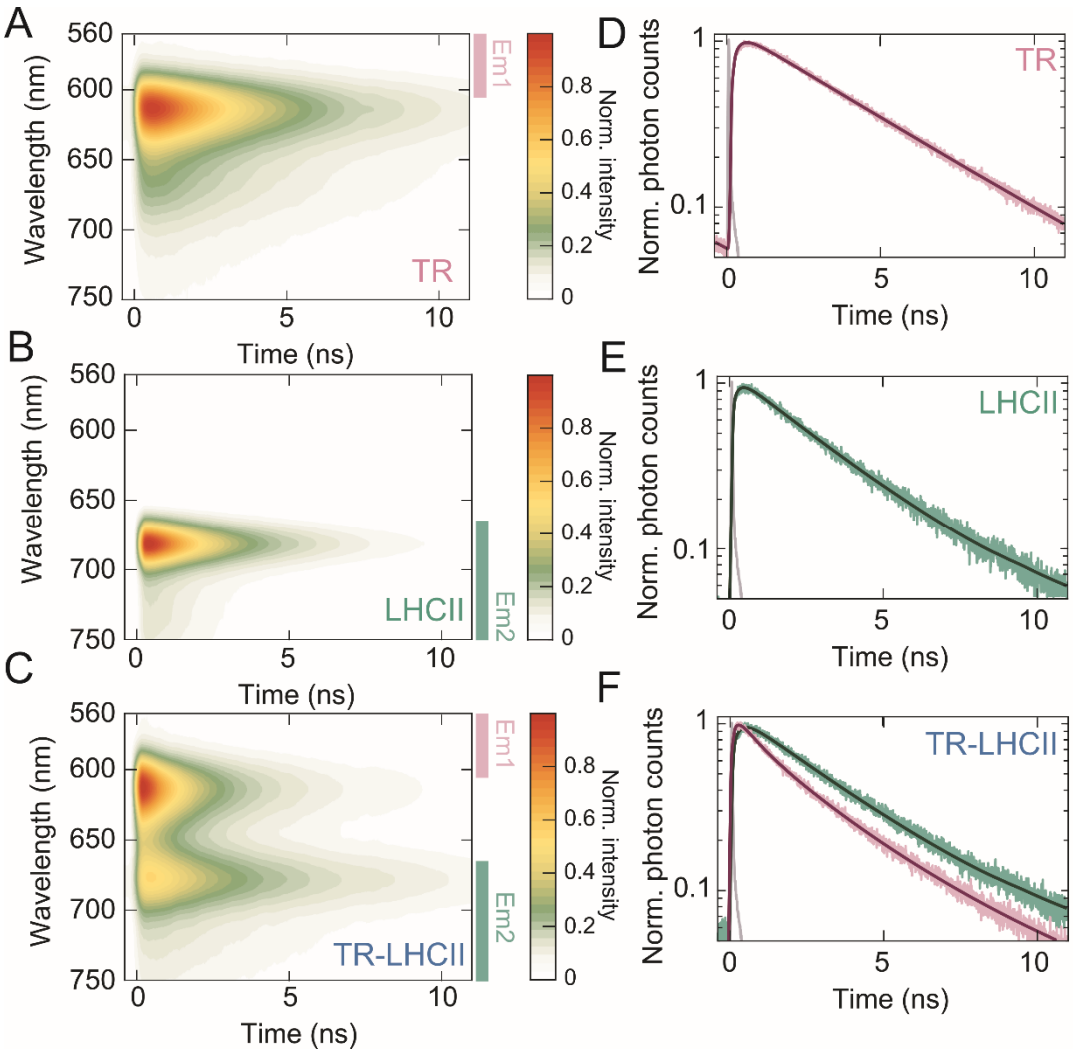

Figure 52 Time resolved fluorescence spectra data for LHCII-only nanodiscs, Texas Red-LHCII nanodiscs, and Texas Red-only liposomes

(A-C) Normalized TRFS of (A) TR-DHPE liposomes, (B) LHCII nanodiscs and (C) TR-LHCII nanodiscs. (D-F) Fitted decay traces of the TRFS shown in (A-C) for the emission ranges displayed, instrument response function (IRF) shown in grey. This figure was produced by my collaborator Minjung Son, Department of Chemistry, MIT, USA.

Note on contributions: all TRFS data were collected and analysed by my collaborators Minjung Son and Dr Muath Nairat from the group of Gabriela Schlau-Cohen, Department of Chemistry, MIT, USA. All samples were prepared and initially characterised by AMH before shipping.

5.4.2 Transient absorption spectroscopy

The transfer of energy from photons absorbed by lipid-tagged complementary chromophores to photosynthetic proteins is the key principle of effectively enhancing protein absorption in the nanodisc, or proteoliposome, system described in this thesis. Determining the route of exciton transfer into proteins and if specific populations of Texas Red molecules have different roles in energy transfer is integral to understanding the limitations and advantages of this system. We wished to quantify the ultra-fast nature of energy transfer from lipid-tagged Texas Red to LHCII in lipid nanodiscs. Transient absorption spectroscopy measurements allow the ultrafast (fs-ps) timescales of exciton dynamics to be investigated, as briefly outlined below.

Measurements are made by illuminating the sample with two pulses from the same laser source with a defined time interval. The absorption of the sample is measured at a range of wavelengths by the initial 'pump' pulse and again by the second 'probe' pulse. The difference in the absorption, or ΔAbs, at different pump/probe intervals across a range of wavelengths is used to produce TA maps which contain information on the evolution of the excited state(s) of a system with time. Two main components of transient absorption spectra produce a negative ΔAbs signal, which relates to a decrease in the sample absorption measured by the probe pulse compared to the initial pump. "Ground state bleaching" describes the effect observed where a molecule's ground electronic state has become de-populated. ΔAbs is reduced due to molecules being excited into higher electronic levels by the initial pump pulse, so fewer molecules in the ground state mean that the probe pulse cannot be absorbed as effectively as the pump resulting in lower measured absorption. "Stimulated emission" signal is caused by the probe pulse interacting with molecules already in electronic excited states due to the initial pump pulse. This interaction causes a photon to be emitted at the same wavelength of the incident photon. This effect manifests as reduced measured absorption (negative ΔAbs) because the incident and emitted photons are indistinguishable. Both ground state bleaching and stimulated emission are directly caused by molecules being in an excited state and produce a negative ΔAbs signal. Therefore, the negative ΔAbs signal indicates the excited state of molecules and, when plotted against time, can indicate the decay and transfer of excited states.

TA map data can be interpreted through global analysis to produce decay associated spectra (DAS). Here, common decay lifetimes are found across the system at a range of wavelengths and a plot is produced which indicates the strength of these different decay components against wavelength. DAS signals can be positive or negative. A negative DAS signal indicates a reduction in the excited state over time, similar to what is observed in TCSPC lifetime measurements after initial excitation at time = 0 s. A positive signal indicates an increase in the excited state corresponding to the state being populated after t = 0 s. This 'delay' in excited state population is indicative of an excited state reaction with energy being transferred from one component to another with a 'delay' in energy transfer associated with the timescale of energy transfer (van Stokkum et al., 2004). The amplitude of the DAS spectra is not representative of the actual amplitude of each component as it assumes all decays are happening simultaneously. A more accurate form of global analysis assumes that one decay evolves into the next in a series with the fastest decay being the most prominent as it relates to higher energy transfer efficiency. In these measurements the pump probe selectively excites Texas Red (500-600 nm) followed by a wide beam probe to measure both LHCII and Texas Red (500-700 nm) as described fully in section 2.4.6.

In order to provide benchmarks when investigating the Texas Red to LHCII energy transfer in the combined system TA spectroscopy measurements were made on liposomes containing only Texas Red and nanodiscs containing only LHCII. The TA map of Texas Red-only liposomes, Figure 53 (A + B), shows the ground state bleach/stimulated emission signal with peaks at 593 nm and 662 nm starting immediately after t = 0 s. This range of wavelengths is consistent with the vibronic band structure of excited states observed as emission intensity peaks in steady-state fluorescence spectroscopy data. Both peaks undergo a mono-exponential decay, demonstrated by the fitted time trace at 600 nm shown in Figure 54 (A, solid purple line) with a time constant of 1.17 ± 0.02 ns as obtained by global analysis of the TA map. Decay associated spectra are shown in Figure 54 (C) with a clear peak of 1.17 ns decay at 593 nm. Figure 53 (C + D) shows the TA map for LHCII-only nanodiscs, which shows a clear ground state bleach/stimulated emission signal at 675 nm associated with the population of the Chl *a* Q_y state. The decay can be fitted with global analysis as a mono-exponential with a time constant of 903 ± 8 ps. This decay can be clearly seen with the fitted time trace at 675 nm shown in Figure 54 (B, solid green line), the DAS is shown in Figure 54 (D) where the 903 ps lifetime

component is clearly seen to have a maximum intensity at 675 nm. The overall excited state lifetimes observed with TA for both Texas Red and LHCII have significantly lower values than those found with both TCSPC and TRFS measurements. The difference is attributed to the limited time range of transient absorption measurements (0-700 ps) meaning that the longer components are not collected.

The TA map for the LHCII + Texas Red nanodisc sample is shown in Figure 53 (E + F). Due to the overlap of LHCII and Texas Red absorption it is estimated (from absorption spectra) that ~20 % of the selective Texas Red excitation in fact directly populates the Q_x and Q_y states of the chlorophyll. The TA map shows two peaks of TA signal with associated wavelengths of 593 nm and 668 nm corresponding to the excited states of Texas Red and LHCII, respectively. Comparison between the 593 nm signal in the combined LHCII and Texas Red sample in Figure 53 (E) and in the Texas Red-only sample in Figure 53 (A) clearly shows a shortening of excited state lifetime in the presence of LHCII. This is also demonstrated by the normalised fitted time traces at 600 ns in Figure 54 (A), the sample with LHCII (solid blue line) has a far steeper decay compared to the Texas Red-only sample (solid purple line). Global analysis reveals a bi-exponential decay in the Texas Red region of the map, DAS shown in Figure 54 (E), with time constants of 3.7 ps and 128 ps. The LHCII region of the spectra shows a 'rise' in the excited state that is clearly visible in the emission map in Figure 53 (F) and the 675 nm fitted time trace in Figure 54 (B). The 'rise' is the delay in the LHCII excited state being populated state due to the timescale of energy transfer from the Texas Red. The LHCII 'rise' data is difficult to accurately assign due to the overlap of directly excited LHCII, directly excited Texas Red, and Texas Red to LHCII energy transfer. However, the DAS in Figure 54 (E) clearly shows a positive component of both the 3.7 ps and 128 ps components in the LHCII wavelength region that is not seen in the solely Texas Red or LHCII DAS. The 3.7 ps and 128 ps decay components are therefore assigned as the timescales of energy transfer from Texas Red to LHCII as they correspond to the new faster decays in Texas Red excited state and also the 'rise' in LHCII excited state population. They are significantly slower than internal Chl-Chl conversions which occur on fs timescales (Meneghin et al., 2017) and are consistent with previously reported ps timescales of energy transfer from synthetic chromophores to light-harvesting proteins (Yoneda et al., 2015). The final 1.03 ns decay component displayed in the DAS in Figure

54 (E, Green solid line) represents the much longer timescale of both LHCII and Texas Red decay after initial excited state population.

The presence of two distinct time components of Texas Red to LHCII energy transfer suggests that the energy transfer is heterogeneous in nature. This is expected due to the distribution of freely diffusing Texas Red tagged lipids in the membrane around LHCII with a range of donor-acceptor distances. The timescale of energy transfer can be used to calculate the average Texas Red – LHCII separation using the standard FRET equation for the rate of energy transfer (Förster, 1965). The rate of energy transfer at distance *r* (K_r) is simply the inverse of the timescale of energy transfer calculated from the TA data (τ_r), $K_r = 1/\tau_r$. Equations for calculating donor-acceptor separations from rate of energy transfer shown below (Equation 25):

$$K_r = \left(1/\tau_0\right)\left(R_0/r\right)^6$$

Which can be rearranged for r to:

$$r = \frac{R_0}{\sqrt[6]{K_r \tau}}$$

Equation 25 Rate of energy transfer to donor-acceptor separation relationship. K_r: rate of energy transfer, τ_0: unquenched donor lifetime, R_0 critical FRET distance ("Förster Radius" estimated as 7.15 nm for Texas Red and LHCII in section 3.2) r: donor-acceptor separation

The 3.7 ps and 128 ps timescales of energy transfer correlate to Texas Red – LHCII separations of 2.25 nm and 4.05 nm respectively.

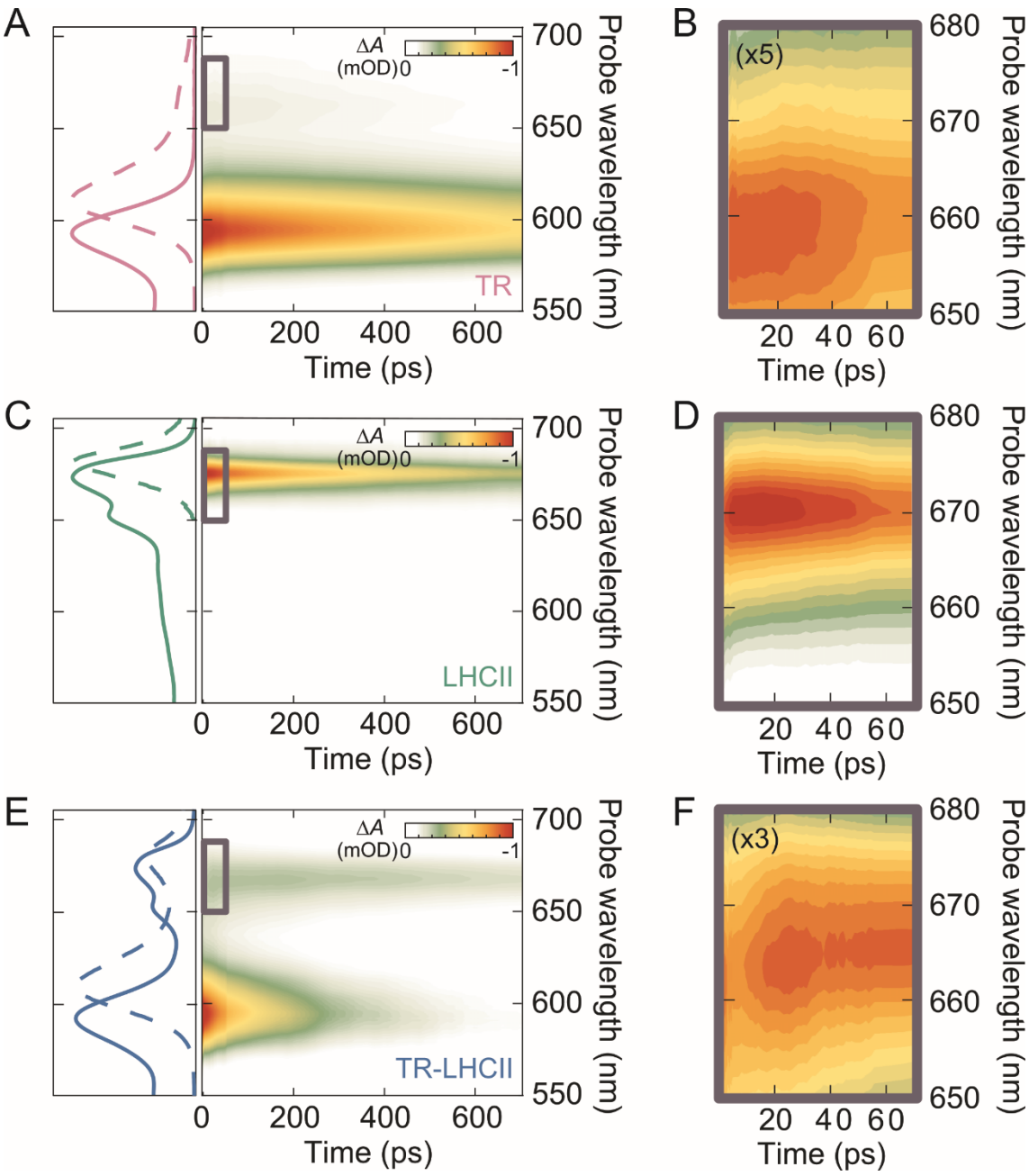

Figure 53 Transient absorption spectroscopy data for LHCII-only nanodiscs, Texas Red-LHCII nanodiscs, and Texas Red-only liposomes

Normalised TA maps of: (A-B) Texas Red-only liposomes, (C-D) LHCII-only nanodiscs, (E-F) LHCII + Texas Red nanodiscs. Steady state absorption (solid line) and fluorescence emission (dashed line) for each sample are shown to the left of TA maps. (B,D,F) are zoomed in TA maps in the Chl *a* Q_y region for the first 70 ps. (B) and (F) are multiplied by a factor of 5 and 3 respectively for visual clarity. This figure was produced by my collaborator Minjung Son, Department of Chemistry, MIT, USA.

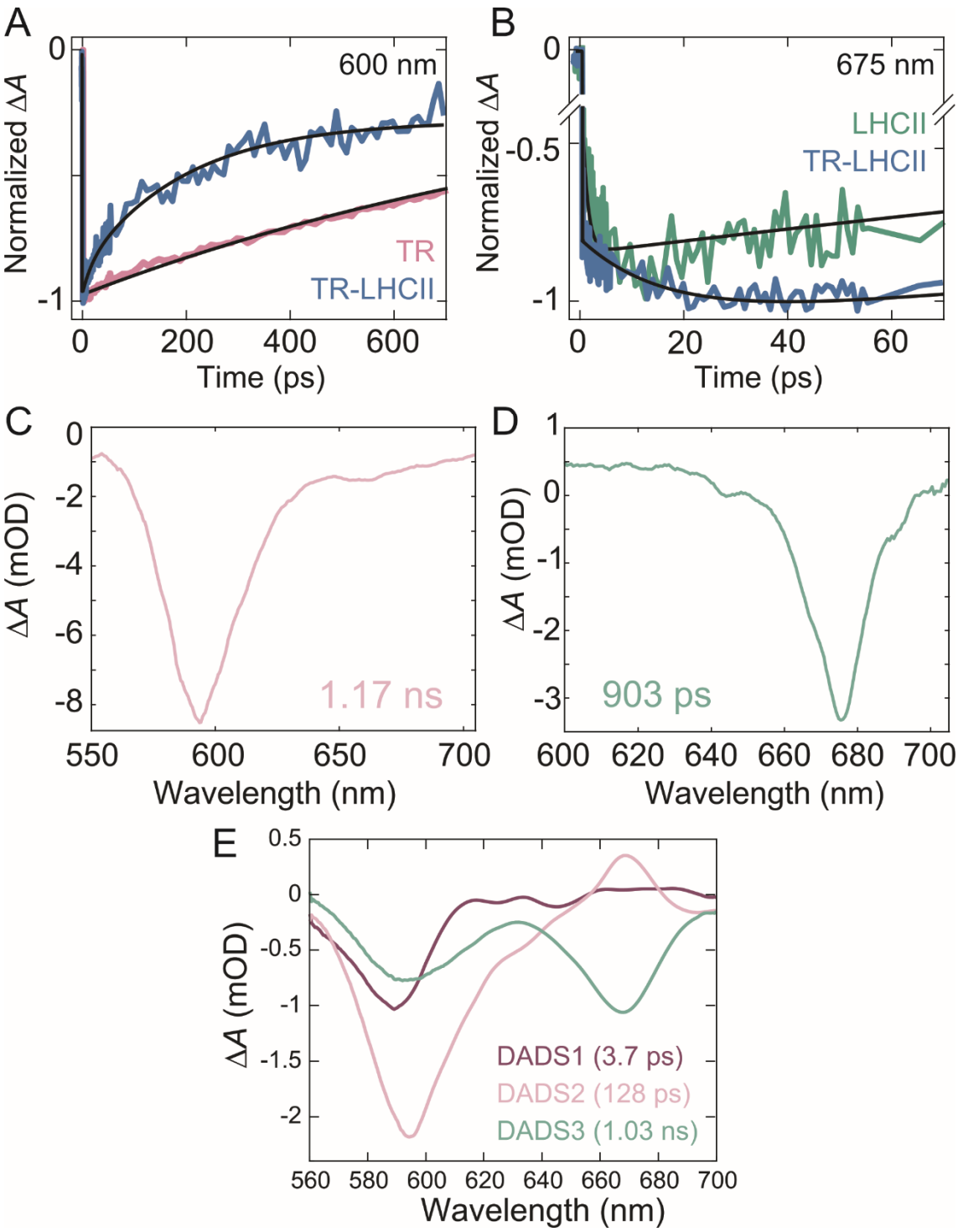

Figure 54 Spectral analysis of transient absorption data

(A+B) Normalised fitted time traces for transient absorption data. (A) Selective Texas Red data at 600 nm (B) Selective LHCII data at 675 nm (C-E) DAS global analysis plots from transient absorption data. (A) Texas Red-only liposomes, (B) LHCII-only nanodiscs, (C) LHCII + Texas Red nanodiscs. This figure was produced by my collaborator Minjung Son, Department of Chemistry, MIT, USA.

Note on contributions: all transient absorption spectroscopy data were collected and analysed by my collaborators Minjung Son and Dr Muath Nairat from the group of Gabriela Schlau-Cohen, Department of Chemistry, MIT, USA. All samples were prepared and initially characterised by AMH before shipping.

5.4.3 Further interpretations of advanced spectroscopy data

This chapter has demonstrated that the enhancement of the effective absorption cross section of the photosynthetic light-harvesting antenna LHCII, using Texas Red tagged lipids, can be applied to single LHCII trimers reconstituted into lipid nanodiscs for their several advantages, as discussed below. The enhancement of LHCII fluorescence emission is improved in nanodiscs compared to in proteoliposomes due to minimised LHCII-LHCII interactions which cause LHCII fluorescence quenching (Crisafi and Pandit, 2017, Son et al., 2020). Lipid nanodiscs also allowed advanced spectroscopy techniques to be used to investigate the ultrafast dynamics of energy transfer from Texas Red to LHCII. Nanodiscs therefore allow measurements on relatively isolated "single-proteins", as one may achieve by isolating membrane proteins in detergent micelles. However, they provide the distinct advantage of the natural lipid environment which in this case is utilised for incorporating Texas Red DHPE. Recently, ultrafast studies of LHCII within nanodiscs have shown that the photo-physics is different for LHCII isolated in detergent micelles versus when in lipid nanodiscs, effectively demonstrating the importance of the lipid bilayer (Son et al., 2020). Nanodiscs have the advantage over proteoliposomes for these measurements as the Texas Red chromophores are able to interact with single and relatively unquenched LHCII trimers as opposed to a network of several interacting proteins in proteoliposomes where protein-protein energy transfer complicates matters. Nanodiscs are also sufficiently small that they minimise visible light scattering, a common complication with techniques such as transient absorption spectroscopy.

We wished to investigate the high-speed photo-physics of Texas Red to LHCII energy transfer to understand more about the timescale and to determine if there were pub-populations of molecules with different roles in the system. TA spectroscopy revealed three main decay components. A single 1.04 ns component relates to the long decay of the Texas Red and LHCII excited states, and two shorter 3.7 ps and 128 ps components

present in both the Texas Red and LHCII regions which are not observed in control samples. The shorter timescales correspond to Texas Red to LHCII energy transfer. Using standard FRET equations relating energy transfer rate to donor–acceptor separation, the 3.7 ps and 128 ps components relate to Texas Red – LHCII separations of 2.25 nm and 4.05 nm, respectively. The occurrence of two apparent average distances for Texas Red to LHCII separation are feasible for the system with a ~20 nm diameter bilayer containing a 8 nm diameter reconstituted LHCII trimer, and a schematic of the system is shown in Figure 55. The calculated values represent the average separation of populations as there will be significant variation due to random diffusion of lipids in the bilayer. The two distances are assumed to represent two populations of Texas Red molecules transferring energy to the LHCII. The population with the smaller average separation represents Texas Red tagged lipids more tightly coupled to the protein with a high energy transfer efficiency. These interactions will be responsible for the majority of energy transferred to LHCII. The second population represents Texas Red molecules not associated with the protein with a far lower efficiency of energy transfer. TA data represents an average measurement over millions of particles meaning that details in the system are likely missed by these methods. Deeper theoretical modelling of the system could reveal even more accurate values by taking into account interactions between individual chromophores.

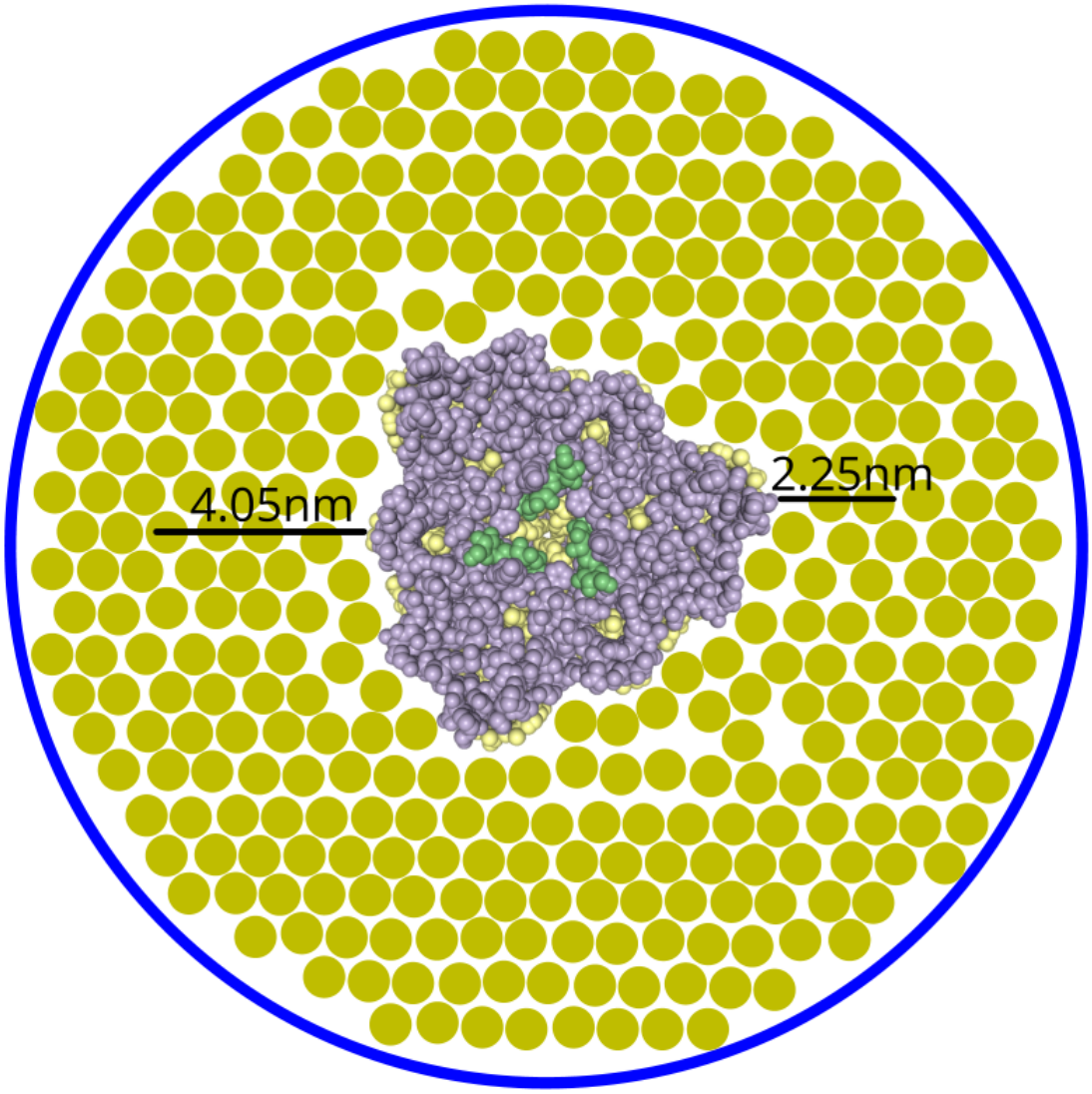

Figure 55 Schematic of LHCII trimer reconstituted into 20 nm diameter lipid nanodisc (top down view) with average donor – acceptor distances indicated

Transient absorption measurements have demonstrated that the timescale of energy transfer from lipid-tagged Texas Red to reconstituted LHCII trimers is on a similar timescale to energy transfer between antenna proteins in a natural photosynthetic membrane system (Akhtar et al., 2016). It has been demonstrated that LHCII – PSII energy transfer occurs on a 2 – 5 ps timescale, very similar to what is observed here (Sener et al., 2011, Sener et al., 2005). The fast timescale of energy transfer will account for the majority of energy transferred to the protein. This is comparable to other systems where light-harvesting protein have been interfaced with complementary chromophores by covalent attachment with time constants of 1-10 ps (Yoneda et al., 2015, Yoneda et al., 2020b). The advantage of this self-assembly driven method of interfacing the chromophores with LHCII is the lack of need for biochemical modification of the proteins

and an area for incorporating extra chromophores only limited by the close packing of membrane proteins and self-quenching of pigments at high concentration. Another advantage is the ability to use large lipid-tagged fluorescent molecules, such as Texas Red, with high extinction coefficients and strong dipole moments which allow non-radiative energy transfer to occur over relatively large distances. There is more to be learned about the molecular motions of the Texas Red molecules in the population closely associated with the LHCII. The Texas Red tag on lipids is known to flip in and out of the bilayer leaflet (Skaug et al., 2011), the exact position of the head group relative to the external chlorophylls of LHCII will have a significant effect on energy transfer taking place. Effects such as the 'flipping' of Texas Red and direct interactions between TR-DHPE and LHCII could be revealed by molecular dynamics simulations of the system. The system lends itself to potential incorporation of other complementary co-factors into the bilayer, which could include other types of dyes to more fully enhance the absorption range of LHCII. It could also be applied to light-harvesting proteins from other photosynthetic systems e.g. bacterial, or used to directly enhance proteins in vivo which perform the photochemistry of photosynthesis (Grayson et al., 2017).

6 Conclusions and Future Outlook

6.1 Conclusions

The three results chapters have detailed the development of self-assembled and modular systems to enhance the effective absorption cross-section of the photosynthetic antenna protein LHCII by incorporating it into model lipid bilayers alongside the complementary lipid tagged dye Texas Red – DHPE.

Chapter 3 initially investigated the effect of reconstituting trimeric LHCII into proteoliposomes on protein intactness and fluorescence state. This was essential to allow the quantification of Texas Red to LHCII energy transfer in subsequent sections. LHCII was reconstituted into proteoliposomes at different lipid: protein ratios; this showed a dependence of LHCII fluorescence intensity and lifetime which is quenched at higher protein concentration. LHCII fluorescence emission intensity and lifetime both decreased from ~70 % to ~ 20 % relative to completely 'unquenched' LHCII isolated in detergent as the lipid to protein ratio in proteoliposomes is decreased from 6162:1 to 352:1. This is in good agreement with other studies which report on LHCII-LHCII interactions being a cause for energy dissipation both in vivo (Robert et al., 2004) and in vitro membrane systems (Crisafi and Pandit, 2017, Natali et al., 2016). The lipid: protein ratio was also found to directly affect the size of proteoliposomes formed with higher concentrations of LHCII resulting in proteoliposomes larger diameter. Liposomes formed omitting LHCII were consistently ~ 50 nm in diameter and increase to ~116 nm at the highest protein concentration with a corresponding lipid: protein ratio of 352:1. This dependency of LHCII concentration is attributed to LHCII favouring lamellar bilayers and restricting the local curvature in membranes (Lambrev and Akhtar, 2019).

Texas Red to LHCII energy transfer in proteoliposomes was quantified by assessing the quenching of Texas Red fluorescence emission intensity and lifetime due to energy transfer. Energy transfer efficiency remained relatively constant between 80 - 90 % as Texas Red concentration is varied between 0.9 μM and 12.3 μM (if the amount of LHCII is constant at ~0.55 μM) and increased non-linearly from 65 % to a point of saturation at

98 % as LHCII concentration is increased from 0.16 μM to 2.84 μM (if the amount of Texas Red is constant at ~6.5 μM), all with 1 mM total lipid. These results are consistent with average donor-acceptor separation decreasing at higher acceptor concentrations in a randomly distributed 2D system (Subramanian et al., 2018). When excited in the region of minimal natural absorption LHCII emission intensity was shown to increase more than threefold with the highest concentrations of Texas Red compared to samples without TR. This increase was apparently linear at low Texas Red concentrations (~25 TR: LHCII) but began to saturate above this point. This limitation in LHCII enhancement is attributed to either a self-quenching effect of LHCII (Belgio et al., 2013), self-quenching effects of the Texas Red chromophores at high concentrations (Skaug et al., 2011) or, likely, a combination of both.

Chapter 4 focused on the characterisation of surface-deposited proteoliposomes containing both LHCII and Texas Red using microscopy techniques. A key design principle of the proteoliposomes system for enhancing LHCII absorption was the amenability of membranes to surfaces. In this chapter microscopy was used to both characterise proteoliposomes on surfaces and assess their functionality. First, the co-reconstitution of both LHCII and Texas Red into individual proteoliposomes and efficiency of energy transfer was quantified by dual-channel time-resolved fluorescence microscopy. Here, the observation of co-localized fluorescence from both LHCII and Texas Red within the same particles revealed co-reconstitution in proteoliposomes (> 90 %). Measuring the level of Texas Red fluorescence quenching in individual proteoliposomes allowed energy transfer to be determined on a single proteoliposome level, revealing population distributions. The distributions of energy transfer efficiency across samples suggested relatively consistent concentrations of reconstituted LHCII in individual proteoliposomes, an improvement compared to other studies (Natali et al., 2016, Tutkus et al., 2018) where the amounts of LH proteins incorporated by other assembly methods varied wildly from vesicle-to-vesicle. Energy transfer from Texas Red to LHCII was also assessed via microscopy-based de-quenching measurements (Wang et al., 2010) where LHCII was selectively photo-inactivated and the resulting recovery of Texas Red fluorescence quantified. These measurements reinforce other experiments showing high proportions of individual proteoliposomes exhibiting highly efficient Texas Red to LHCII energy transfer. De-quenching measurements also demonstrated that

energy transfer was retained in 10-30 nm thick membrane 'thick films' formed from proteoliposomes deposited at high concentration onto surfaces.

Chapter 5 aimed to measure the interactions between Texas Red and single LHCII trimers via ultrafast spectroscopy by utilising lipid nanodiscs as a small, confined area of lipid bilayer. Nanodiscs potentially have the advantages of minimising LHCII-LHCII interactions which are known to cause LHCII to enter a quenched state, of confining Texas Red molecules to within the Förster distance of LHCII, and of minimising any scattering effects allowing ultrafast spectroscopy to be performed. Texas Red and LHCII were successfully co-reconstituted into lipid-nanodiscs and energy transfer observed through Texas Red fluorescence quenching and LHCII emission enhancement; this enhancement of fluorescence was significantly higher than observed in proteoliposomes due to minimised LHCII aggregation induced quenching. TEM revealed that a high proportion of nanodiscs were likely to contain only 1 or 2 LHCII trimers. This was successful in achieving significantly less self-quenching of LHCII fluorescence compared to that observed for LHCII proteoliposomes, probably due to the small membrane area minimising LHCII-LHCII interactions in nanodiscs. Ultrafast (transient absorption) spectroscopy quantified the timescale of Texas Red to LHCII energy transfer, by analysing the 'delay' in LHCII reaching an excited state after Texas Red excitation (van Stokkum et al., 2004). This analysis revealed two significant time constants, one relating to a ~4 ps energy transfer and one to ~125 ps. These two time constants suggest that two populations of Texas Red molecules transfer energy to LHCII, one tightly energetically coupled to the protein providing the majority of transferred energy and a second uncoupled population representing the other Texas Red molecules diffusing laterally in the rest of the nanodisc area. The timescale of energy transfer from the closer population of lipid-tagged Texas Red is on the same time sale as energy transfer from LHCII to PSII in natural systems of 2-5 ps (Sener et al., 2005, Sener et al., 2011). This is attributed to the large extinction coefficient of Texas Red and high quantum yield making it an excellent energy donor in a FRET pair.

Overall in all 3 chapters, the enhancement achieved for the effective LHCII absorption in the 'green gap' of minimal absorption by use of lipid-tagged Texas Red is comparable to what has been reported in the literature with the direct attachment of complementary chromophores to light-harvesting proteins either by the use of chemical cross linkers

(Yoneda et al., 2020b, Springer et al., 2012, Gundlach et al., 2009) or genetic modification (Grayson et al., 2017). Self-assembly techniques have been used in the past to interface multiple chromophores which are capable of non-radiative energy transfer and to effectively enhance the absorption cross section of a single system. Previously, this has been realised using biological chromophores (Adams et al., 2015a) and full light-harvesting proteins (Harris et al., 2014a) in polymer micelles but has only been achieved in a lipid-based system using simple chromophores (Sahin et al., 2015). Here, we demonstrated the first instance of utilising a lipid-tagged chromophore to directly enhance the spectral properties of membrane reconstituted light-harvesting proteins in a self-assembled and surface amenable system. This system takes advantage of self-assembly driven formation and does not require chemical or biological modifications to the protein which are commonly utilised in artificially enhanced photosynthetic systems. It also has the advantage of being able to utilise larger, brighter, complementary dyes with high quantum yields (such as Texas Red). Many chromophores previously used to enhance the absorption of photosynthetic proteins are amino acid based and very small in size with low extinction coefficients and relatively weak transition dipole moments: this could significantly limit their potential for transferring energy to photosynthetic pigments. Whereas, Texas Red is a small organic molecule which is able to get spatially closer to an LH protein and it also has a strong absorption strength, reasons why the FRET efficiency and enhancement were found to be high, here. Model lipid membranes were demonstrated to be a highly modular platform with the potential to be adapted with different photosynthetic proteins and corresponding complementary dyes. This membrane-based system also has the benefit of being amenable to surfaces, an essential property for any future thin-film based device applications and a benefit as a minimal model system for studying the protein biophysics/photo-physics as it allows surface-based techniques.

6.2 Future work

A limitation in the potential use of the Texas Red dye in the enhancement of photosynthetic proteins for light-harvesting applications is its limited spectral absorption range. While Texas Red absorbs strongly at ~590 nm, the centre of LHCIIs natural ‘green gap’ of minimal absorption, it does not cover the entire range with absorption minima in the combined system centred at 525 nm and 625 nm. A further improved system could

involve the incorporation of multiple different lipid-tagged chromophores to fully bridge the gap of minimal chlorophyll absorption, which would require energy to be transferred via FRET between the pigments absorbing in the 500-650 nm range before reaching the antenna protein. In such as system, the overall efficiency of absorbing any given photon would potentially be higher due to the more significant spectral overlap between chromophores. It has been demonstrated that quantum dots with different spectral properties are able to both transfer energy to (Vinayaka and Thakur, 2011) and receive energy from (Werwie et al., 2012), a range of photosynthetic proteins (Werwie et al., 2018, Liu et al., 2019). It is also been shown that it is possible to encapsulate quantum dots within the hydrophobic envelope of lipid bilayers (Zheng et al., 2014). These nanoscale semiconductor particles have very strong absorption in the visible region and can be tuned to modulate the wavelength of fluorescence emission. If quantum dots could be reconstituted into membranes via self-assembly driven formation, they could potentially be ideal donors to photosynthetic proteins as an alternative to lipid tagged dyes. The potential for enhancing photosynthetic protein absorption is not limited to plant based organisms and has been demonstrated extensively in bacteria (Yoneda et al., 2020b, Grayson et al., 2017). Bacterial systems typically perform photochemistry with lower energy excitation relative to plants, bacterial reaction centres utilise reaction centre pigments absorbing at ~850 nm, as opposed to 680-700 nm in plants (Dahlberg et al., 2017). This means that a different range of dyes with a 'more red' absorption range must be utilised to effectively fill the absorption gap for bacterial systems. Another limitation of a lipid-based system of interfacing dyes with proteins is the relative instability of lipid bilayers over long periods of time. A hybrid polymer-lipid mixture has been shown to significantly enhance the lifetime of membrane protein activity and could potently be used to create long-lived photosynthetic membranes deposited onto surfaces (Seneviratne et al., 2018).

An interesting next step in this research would be to quantify the interactions of individual Texas Red molecules with LHCII. A disadvantage of this system of artificially enhancing the absorption of photosynthetic membrane proteins through self-assembly and lipid tagged dyes compared to systems where dyes are directly attached to proteins (Gundlach et al., 2009, Harris et al., 2014a, Yoneda et al., 2015, Springer et al., 2012) is that the location of Texas Red molecules relative to the photosynthetic pigments cannot be accurately controlled. It is therefore more difficult to determine exactly how dyes will

interact with the protein. Single molecule FRET measurements can be used to assess the energy transfer, and therefore interactions, between two chromophores incorporated into lipid bilayers (Nath et al., 2010). Single LHCII trimers could be reconstituted into nanodiscs with a low concentration of lipid tagged Texas Red and the fluorescence quenching of Texas Red and enhancement of LHCII tracked over time, which would allow variations in energy transfer due to the dynamics of the system to be assessed. This could give information on interactions between single Texas Red molecules and LHCII and be achieved with steady-state or time resolved fluorescence correlation microscopy (Ray et al., 2010). An alternative method of fully understanding Texas Red and LHCII interactions would be the use of molecular dynamics simulations. Recent advances in high-throughput simulations allow lipid bilayers to be modelled for extended periods of time, so it is possible to simulate the diffusion of different lipid molecules in a membrane and how they interact with membrane proteins (Yamamoto et al., 2016). Texas Red DHPE is known to be dynamic in the membrane with the dye 'flipping' from the outside to the inside of the bilayer, which could significantly affect Texas Red to LHCII energy transfer and could be investigated with these simulations (Skaug et al., 2011). Quantum chemistry simulations of energy transfer and dissipation in light-harvesting systems is also possible. These simulations could potentially be applied to our system to investigate both how the dynamics of Texas Red movement effect energy transfer and the 'route' of excitons from the Texas Red into LHCII and possibly other photosynthetic proteins (Balevicius et al., 2019).

A natural next step in this research would be to apply it to systems containing more photosynthetic proteins and effectively enhance the efficiency of the entire molecular machinery of photosynthesis. Hybrid thylakoid membranes have been formed which combine extractions natural of thylakoid membranes and model lipid bilayer forming lipids, these hybrid membranes are deposited onto surfaces and are capable of performing the key initial stages of photosynthetic including NADPH production (Yoneda et al., 2020a). These membrane have potential to include other proteins, such as ATP synthase, to fully replicate the key mechanisms of photosynthesis in vitro (Li et al., 2018). Texas Red tagged lipids could potentially be added into these systems to further enhance their productivity by way of proven protein absorption enhancement. Previous studies have shown that LH proteins deposited onto surfaces provide directional transfer of energy (Vasilev et al., 2014, Escalante et al., 2010) and can be coupled with electrodes to act as

bio-photovoltaic devices (Ravi et al., 2017, Ciesielski et al., 2010). It has been shown that it is possible to create multi-bilayer stacks of model membranes continuing photoactive LHCII both as discreet layers (Grab et al., 2016) and as membrane thick films, as in the present study. A potential future bio-hybrid device could make use of electronic energy propagation through membranes stacks to electrodes (Heath et al., 2017), and the high absorptivity of combined LHCII and complementary lipid tagged dyes, to create a highly effective light-harvesting system. The concept of using lipid incorporated dyes to enhance effective protein absorption beyond model membrane systems could be applied to full photosynthetic organisms. It has been demonstrated that some lipophilic dyes, which sit in the bilayer hydrophobic envelope, can be incorporated into pre-formed model lipid membranes (Lubart et al., 2020) and into natural biological membranes with high efficiency (Jensen and Berg, 2016). There are many variations of these dyes with different absorption emission wavelengths covering the entire visible spectrum meaning that they could be preferentially selected to transfer additional absorbed energy to specific photosynthetic systems. The dyes could be potentially be incorporated into natural systems already being harnessed to convert solar energy to useful chemical energy via photosynthesis. This includes the use of bacteria for carbon fixation (Milano et al., 2019), or green algae for biofuel production (Anemaet et al., 2010), both of which could be significantly boosted if the absorption range of the photosynthetic proteins was enhanced by additional complementary chromophores associated with the photosynthetic membrane. While this thesis has comprehensively demonstrated the potential for using lipid-tagged chromophores to spectrally enhance photosynthetic proteins, there are limitations which make scaling the system to industrial levels difficult. This includes the high commercial cost of biochemically purifying proteins and also producing the synthetic dyes. However, we have demonstrated the potential for using a model membrane platform to spectrally enhance photosynthetic proteins in a self-assembly driven system. The platform has also shown that it is possible to study in-membrane energy transfer from tagged lipid to proteins, which could be utilised in the future as a method of understanding the biophysics of energy transfer in complex natural membranes.

References

ADAMS, P. G., COLLINS, A. M., SAHIN, T., SUBRAMANIAN, V., URBAN, V. S., VAIRAPRAKASH, P., TIAN, Y., EVANS, D. G., SHREVE, A. P. & MONTANO, G. A. 2015a. Diblock copolymer micelles and supported films with noncovalently incorporated chromophores: a modular platform for efficient energy transfer. *Nano Lett,* 15**,** 2422-8.

ADAMS, P. G., SWINGLE, K. L., PAXTON, W. F., NOGAN, J. J., STROMBERG, L. R., FIRESTONE, M. A., MUKUNDAN, H. & MONTAÑO, G. A. 2015b. Exploiting lipopolysaccharide-induced deformation of lipid bilayers to modify membrane composition and generate two-dimensional geometric membrane array patterns. *Sci. Rep.,* 5**,** 10331.

ADAMS, P. G., VASILEV, C., HUNTER, C. N. & JOHNSON, M. P. 2018. Correlated fluorescence quenching and topographic mapping of Light-Harvesting Complex II within surface-assembled aggregates and lipid bilayers. *Biochimica et Biophysica Acta - Bioenergetics,* 1859**,** 1075-1085.

AKHTAR, P., DO, T. N., NOWAKOWSKI, P. J., HUERTA-VIGA, A., KHYASUDEEN, M. F., LAMBREV, P. H. & TAN, H. S. 2019. Temperature Dependence of the Energy Transfer in LHCII Studied by Two-Dimensional Electronic Spectroscopy. *J Phys Chem B,* 123**,** 6765-6775.

AKHTAR, P., LINGVAY, M., KISS, T., DEAK, R., BOTA, A., UGHY, B., GARAB, G. & LAMBREV, P. H. 2016. Excitation energy transfer between Light-harvesting complex II and Photosystem I in reconstituted membranes. *Biochim Biophys Acta,* 1857**,** 462-72.

ANEMAET, I. G., BEKKER, M. & HELLINGWERF, K. J. 2010. Algal photosynthesis as the primary driver for a sustainable development in energy, feed, and food production. *Mar Biotechnol (NY),* 12**,** 619-29.

BAHATYROVA, S., FRESE, R. N., SIEBERT, C. A., OLSEN, J. D., VAN DER WERF, K. O., VAN GRONDELLE, R., NIEDERMAN, R. A., BULLOUGH, P. A., OTTO, C. & HUNTER, C. N. 2004. The native architecture of a photosynthetic membrane. *Nature,* 430**,** 1058-1062.

BALEVICIUS, V., JR., WEI, T., DI TOMMASO, D., ABRAMAVICIUS, D., HAUER, J., POLIVKA, T. & DUFFY, C. D. P. 2019. The full dynamics of energy relaxation in large organic molecules: from photo-excitation to solvent heating. *Chem Sci,* 10**,** 4792-4804.

BAR-ON, Y. M., PHILLIPS, R. & MILO, R. 2018. The biomass distribution on Earth. *Proc Natl Acad Sci U S A,* 115**,** 6506-6511.

BELGIO, E., DUFFY, C. D. & RUBAN, A. V. 2013. Switching light harvesting complex II into photoprotective state involves the lumen-facing apoprotein loop. *Phys Chem Chem Phys,* 15**,** 12253-61.

BERERA, R., VAN GRONDELLE, R. & KENNIS, J. T. M. 2009. Ultrafast transient absorption spectroscopy: principles and application to photosynthetic systems. *Photosynthesis Research,* 101**,** 105-118.

BETTERLE, N., BALLOTTARI, M., ZORZAN, S., DE BIANCHI, S., CAZZANIGA, S., DALL'OSTO, L., MOROSINOTTO, T. & BASSI, R. 2009. Light-induced dissociation of an antenna hetero-oligomer is needed for non-photochemical quenching induction. *J Biol Chem,* 284**,** 15255-66.

BHADURI, S., ZHANG, H., ERRAMILLI, S. & CRAMER, W. A. 2019. Structural and functional contributions of lipids to the stability and activity of the photosynthetic cytochrome b 6 f lipoprotein complex. *J Biol Chem,* 294**,** 17758-17767.

BITOUNIS, D., FANCIULLINO, R., ILIADIS, A. & CICCOLINI, J. 2012. Optimizing Druggability through Liposomal Formulations: New Approaches to an Old Concept. *ISRN Pharm,* 2012**,** 738432.

BLANCHETTE, C. D., CAPPUCCIO, J. A., KUHN, E. A., SEGELKE, B. W., BENNER, W. H., CHROMY, B. A., COLEMAN, M. A., BENCH, G., HOEPRICH, P. D. & SULCHEK, T. A. 2009. Atomic force microscopy differentiates discrete size distributions between membrane protein containing and empty nanolipoprotein particles. *Biochim Biophys Acta,* 1788**,** 724-31.

BLANCHETTE, C. D., LAW, R., BENNER, W. H., PESAVENTO, J. B., CAPPUCCIO, J. A., WALSWORTH, V., KUHN, E. A., CORZETT, M., CHROMY, B. A., SEGELKE, B. W., COLEMAN, M. A., BENCH, G., HOEPRICH, P. D. & SULCHEK, T. A. 2008. Quantifying size distributions of nanolipoprotein particles with single-particle analysis and molecular dynamic simulations. *J Lipid Res,* 49**,** 1420-30.

BLANKENSHIP, R. E. 2014. Molecular Mechanisms of Photosynthesis. *Wiley-Blackwell*

BLANKENSHIP, R. E., TIEDE, D. M., BARBER, J., BRUDVIG, G. W., FLEMING, G., GHIRARDI, M., GUNNER, M. R., JUNGE, W., KRAMER, D. M., MELIS, A., MOORE, T. A., MOSER, C. C., NOCERA, D. G., NOZIK, A. J., ORT, D. R., PARSON, W. W., PRINCE, R. C. & SAYRE, R. T. 2011. Comparing Photosynthetic and Photovoltaic Efficiencies and Recognizing the Potential for Improvement. *Science,* 332**,** 805-809.

BOEKEMA, E. J. 1991. Negative staining of integral membrane proteins. *Micron and Microscopica Acta,* 22**,** 361-369.

BOUDIERE, L., MICHAUD, M., PETROUTSOS, D., REBEILLE, F., FALCONET, D., BASTIEN, O., ROY, S., FINAZZI, G., ROLLAND, N., JOUHET, J., BLOCK, M. A. & MARECHAL, E. 2014. Glycerolipids in photosynthesis: Composition, synthesis and trafficking. *Biochimica et Biophysica Acta (BBA) - Bioenergetics,* 1837**,** 470-480.

CARDONA, T., SEDOUD, A., COX, N. & RUTHERFORD, A. W. 2012. Charge separation in photosystem II: a comparative and evolutionary overview. *Biochim Biophys Acta,* 1817**,** 26-43.

CAVALIER-SMITH, T. 2000. Membrane heredity and early chloroplast evolution. *Trends in plant science,* 5.

CHAKRABORTY, T., CHAKRABORTY, I. & GHOSH, S. 2011. The methods of determination of critical micellar concentrations of the amphiphilic systems in aqueous medium. *Arabian Journal of Chemistry,* 4**,** 265-270.

CHROMY, B. A., ARROYO, E., BLANCHETTE, C. D., BENCH, G., BENNER, H., CAPPICCIO, J. A., COLEMAN, M. A., HENDERSON, P. T., HINZ, A. K., KUHN, E. A., PESAVENTO, J. B., SEGELKE, B. W., SULCHEK, T. A., TARASOW, T., WALSWORTH, V. L. & HOEPRICH, P. D. 2007. Different Apolipoproteins Impact Nanolipoprotein Particle Formation. *J Am Chem Soc,* 129**,** 14348-14354.

CIESIELSKI, P. N., FAULKNER, C. J., IRWIN, M. T., GREGORY, J. M., TOLK, N. H., CLIFFEL, D. E. & JENNINGS, G. K. 2010. Enhanced Photocurrent Production by Photosystem I Multilayer Assemblies. *Advanced Functional Materials,* 20**,** 4048-4054.

COLLINS, A. M., TIMLIN, J. A., ANTHONY, S. M. & MONTANO, G. A. 2016. Amphiphilic block copolymers as flexible membrane materials generating structural and functional mimics of green bacterial antenna complexes. *Nanoscale,* 8**,** 15056-15063.

CONG, H., NIEDZWIEDZKI, D. M., GIBSON, G. N. & FRANK, H. A. 2008. Ultrafast Time-Resolved Spectroscopy of Xanthophylls at Low Temperature. *J. Phys. Chem. B,* 112**,** 3558-3567.

CRISAFI, E. & PANDIT, A. 2017. Disentangling protein and lipid interactions that control a molecular switch in photosynthetic light harvesting. *Biochim Biophys Acta,* 1859**,** 40-47.

CROCE, R., MULLER, M. G., BASSI, R. & HOLZWARTH, A. R. 2001. Carotenoid-to-Chlorophyll Energy Transfer in Recombinant Major Light-Harvesting Complex (LHCII) of Higher Plants. I. Femtosecond Transient Absorption Measurements. *Biophysical Journal,* 80**,** 901–915.

CROCE, R. & VAN AMERONGEN, H. 2011. Light-harvesting and structural organization of Photosystem II: from individual complexes to thylakoid membrane. *J Photochem Photobiol B,* 104**,** 142-53.

CROCE, R. & VAN AMERONGEN, H. 2014. Natural strategies for photosynthetic light harvesting. *Nat Chem Biol,* 10**,** 492-501.

CSIKI, R., DRIESCHNER, S., LYULEEVA, A., CATTANI-SCHOLZ, A., STUTZMANN, M. & GARRIDO, J. A. 2018. Photocurrent generation of

biohybrid systems based on bacterial reaction centers and graphene electrodes. *Diamond & Related Materials,* 89**,** 286–292.

DAHLBERG, P. D., TING, P. C., MASSEY, S. C., ALLODI, M. A., MARTIN, E. C., HUNTER, C. N. & ENGEL, G. S. 2017. Mapping the ultrafast flow of harvested solar energy in living photosynthetic cells. *Nat Commun,* 8**,** 988.

DAUM, B. & KÜHLBRANDT, W. 2011. Electron tomography of plant thylakoid membranes. *J. Exp. Bot.,* 62**,** 2393-2402.

DE LEO, V., CATUCCI, L., FALQUI, A., MAROTTA, R., STRICCOLI, M., AGOSTIANO, A., COMPARELLI, R. & MILANO, F. 2014. Hybrid Assemblies of Fluorescent Nanocrystals and Membrane Proteins in Liposomes. *Langmuir,* 30**,** 1599-1608.

DEKKER, J. P. & BOEKEMA, E. J. 2005. Supramolecular organization of thylakoid membrane proteins in green plants. *Biochim Biophys Acta,* 1706**,** 12-39.

DEMCHENKO, A. P., MELY, Y., DUPORTAIL, G. & KLYMCHENKO, A. S. 2009. Monitoring biophysical properties of lipid membranes by environment-sensitive fluorescent probes. *Biophys J,* 96**,** 3461-70.

DEME, B., CATAYE, C., BLOCK, M. A., MARECHAL, E. & JOUHET, J. 2014. Contribution of galactoglycerolipids to the 3-dimensional architecture of thylakoids. *FASEB J,* 28**,** 3373-83.

DEMMIG-ADAMS, B. 1990. Carotenoids and photoprotection in plants: A role for the xanthophyll zeaxanthin. *Biochim Biophys Acta* 1020**,** 1-24.

DUFFY, C. D. P. & RUBAN, A. V. 2015. Dissipative pathways in the photosystem-II antenna in plants. *Journal of Photochemistry and Photobiology B-Biology,* 152**,** 215-226.

DUNN, K. W., KAMOCKA, M. M. & MCDONALD, J. H. 2011. A practical guide to evaluating colocalization in biological microscopy. *Am J Physiol Cell Physiol,* 300**,** C723-42.

ESCALANTE, M., LENFERINK, A., ZHAO, Y., TAS, N., HUSKENS, J., HUNTER, C. N., SUBRAMANIAM, V. & OTTO, C. 2010. Long-Range Energy Propagation in Nanometer Arrays of Light Harvesting Antenna Complexes. *Nano Letters,* 10**,** 1450-1457.

FENG, X., JIA, Y., CAI, P., FEI, J. & LI, J. 2016. Coassembly of Photosystem II and ATPase as Artificial Chloroplast for Light-Driven ATP Synthesis. *ACS Nano,* 10**,** 556-61.

FIDLER, A. F., SINGH, V. P., LONG, P. D., DAHLBERG, P. D. & ENGEL, G. S. 2013. Probing energy transfer events in the light harvesting complex 2 (LH2) of Rhodobacter sphaeroides with two-dimensional spectroscopy. *J Chem Phys,* 139**,** 155101.

FÖRSTER, T. 1965. Delocalized excitation and excitation transfer. *Modern Quantum Chemistry Istanbul Lectures,* 3**,** 93-137.

FRIEBE, V. & FRESE, R. N. 2017. Photosynthetic reaction center-based biophotovoltaics. *Current Opinion in Electrochemistry,* 5**,** 126-134.

FUNG, B. & STRYRM, L. 1978. Surface Density Determination in Membranes by Fluorescence Energy Transfer. *Biochemistry,* 17**,** 5241-5248.

GRAB, O., ABACILAR, M., DAUS, F., GEYER, A. & STEINEM, C. 2016. 3D-Membrane Stacks on Supported Membranes Composed of Diatom Lipids Induced by Long-Chain Polyamines. *Langmuir,* 32**,** 10144-10152.

GRAYSON, K. J., FARIES, K. M., HUANG, X., QIAN, P., DILBECK, P., MARTIN, E. C., HITCHCOCK, A., VASILEV, C., YUEN, J. M., NIEDZWIEDZKI, D. M., LEGGETT, G. J., HOLTEN, D., KIRMAIER, C. & NEIL HUNTER, C. 2017. Augmenting light coverage for photosynthesis through YFP-enhanced charge separation at the Rhodobacter sphaeroides reaction centre. *Nat Commun,* 8**,** 13972.

GROSSMAN, A. R., SCHAEFER, M. R., CHIANG, G. G. & COLLIER, J. L. 1993. The Phycobilisome, a Light-Harvesting Complex Responsive to Environmental Conditions. *Microbiological Reviews,* 57**,** 725-749.

GUNDLACH, K., WERWIE, M., WIEGAND, S. & PAULSEN, H. 2009. Filling the "green gap" of the major light-harvesting chlorophyll a/b complex by covalent attachment of Rhodamine Red. *Biochim Biophys Acta,* 1787**,** 1499-504.

HAGN, F., NASR, M. L. & WAGNER, G. 2018. Assembly of phospholipid nanodiscs of controlled size for structural studies of membrane proteins by NMR. *Nat Protoc,* 13**,** 79-98.

HANNA, M. C. & NOZIK, A. J. 2006. Solar conversion efficiency of photovoltaic and photoelectrolysis cells with carrier multiplication absorbers. *Journal of Applied Physics,* 100**,** 074510.

HARRIS, M. A., JIANG, J., NIEDZWIEDZKI, D. M., JIAO, J., TANIGUCHI, M., KIRMAIER, C., LOACH, P. A., BOCIAN, D. F., LINDSEY, J. S., HOLTEN, D. & PARKES-LOACH, P. S. 2014a. Versatile design of biohybrid light-harvesting architectures to tune location, density, and spectral coverage of attached synthetic chromophores for enhanced energy capture. *Photosynth Res,* 121**,** 35-48.

HARRIS, M. A., PARKES-LOACH, P. S., SPRINGER, J. W., JIANG, J., MARTIN, E. C., QIAN, P., JIAO, J., NIEDZWIEDZKI, D. M., KIRMAIER, C., OLSEN, J. D., BOCIAN, D. F., HOLTEN, D., HUNTER, C. N., LINDSEY, J. S. & LOACH, P. A. 2013. Integration of multiple chromophores with native photosynthetic antennas to enhance solar energy capture and delivery. *Chemical Science,* 4.

HARRIS, M. A., SAHIN, T., JIANG, J., VAIRAPRAKASH, P., PARKES-LOACH, P. S., NIEDZWIEDZKI, D. M., KIRMAIER, C., LOACH, P. A., BOCIAN, D. F., HOLTEN, D. & LINDSEY, J. S. 2014b. Enhanced light-harvesting capacity by

micellar assembly of free accessory chromophores and LH1-like antennas. *Photochem Photobiol,* 90**,** 1264-76.

HASSAN OMAR, O., LA GATTA, S., TANGORRA, R. R., MILANO, F., RAGNI, R., OPERAMOLLA, A., ARGAZZI, R., CHIORBOLI, C., AGOSTIANO, A., TROTTA, M. & FARINOLA, G. M. 2016. Synthetic Antenna Functioning As Light Harvester in the Whole Visible Region for Enhanced Hybrid Photosynthetic Reaction Centers. *Bioconjug Chem,* 27**,** 1614-23.

HEATH, G. R., LI, M., POLIGNANO, I. L., RICHENS, J. L., CATUCCI, G., O'SHEA, P., SADEGHI, S. J., GILARDI, G., BUTT, J. N. & JEUKEN, L. J. 2016. Layer-by-Layer Assembly of Supported Lipid Bilayer Poly-L-Lysine Multilayers. *Biomacromolecules,* 17**,** 324-35.

HEATH, G. R., LI, M., RONG, H., RADU, V., FRIELINGSDORF, S., LENZ, O., BUTT, J. N. & JEUKEN, L. J. C. 2017. Multilayered Lipid Membrane Stacks for Biocatalysis Using Membrane Enzymes. *Advanced Functional Materials,* 27.

HENSON, W. R., SHAH, V. B., LAKIN, G., CHADHA, T., LIU, H., BLANKENSHIP, R. E. & BISWAS, P. 2013. Production and Performance of a Photosystem I-Based Solar Cell using Nano-Columnar TiO2. *Conference paper*.

HOFFERT, M. I., CALDEIRA, K., BENFORD, G., CRISWELL, D. R., GREEN, C., HERZOG, H., JAIN, A. K., KHESHGI, H. S., LACKNER, K. S., LEWIS, J. S., LIGHTFOOT, H. D., MANHEIMER, W., MANKINS, J. C., MAUEL, M. E., PERKINS, L. J., SCHLESINGER, M. E., VOLK, T. & WIGLEY, T. M. L. 2002. Advanced Technology Paths to Global Climate Stability: Energy for a Greenhouse Planet. *Science,* 298**,** 981-987.

HORTON, P., RUBAN, A. V. & WALTERS, R. G. 1996. Regulation of Light Harvesting In Green Plants. *Annu. Rev. Plant Physiol. Plant Mol. Biol,* 47**,** 655–84.

JENSEN, K. H. & BERG, R. W. 2016. CLARITY-compatible lipophilic dyes for electrode marking and neuronal tracing. *Sci Rep,* 6**,** 32674.

JOHNSON, M. P., GORAL, T. K., DUFFY, C. D. P., BRAIN, A. P. R., MULLINEAUX, C. W. & RUBAN, A. V. 2011. Photoprotective energy dissipation involves the reorganization of photosystem II light-harvesting complexes in the grana membranes of spinach chloroplasts. *Plant Cell* 23**,** 1468-1479.

JOHNSON, M. P. & RUBAN, A. V. 2009. Photoprotective energy dissipation in higher plants involves alteration of the excited state energy of the emitting chlorophyll(s) in the light harvesting antenna II (LHCII). *J Biol Chem,* 284**,** 23592-601.

JOHNSON, M. P., VASILEV, C., OLSEN, J. D. & HUNTER, C. N. 2014. Nanodomains of Cytochrome b6f and Photosystem II Complexes in Spinach Grana Thylakoid Membranes. *The Plant Cell Online,* 26**,** 3051-3061.

JOUHET, J. 2013. Importance of the hexagonal lipid phase in biological membrane organisation. *Frontiers in Plant Science,* 4**,** 494.

KAISER, H., LINGWOOD, D., LEVENTAL, I., SAMPAIO, J., KALVODOVA, L., RAJENDRAN, L. & SIMONS, K. 2009. Order of lipid phases in model and plasma membranes. *PNAS,* 106.

KAMRAN, M., DELGADO, J. D., FRIEBE, V., AARTSMA, T. J. & FRESE, R. N. 2014. Photosynthetic Protein Complexes as Bio-photovoltaic Building Blocks Retaining a High Internal Quantum Efficiency. *Biomacromolecules,* 15**,** 2833-2838.

KANG, M., TUTEJA, M., CENTRONE, A., TOPGAARD, D. & LEAL, C. 2018. Nanostructured Lipid-based Films for Substrate Mediated Applications in Biotechnology. *Adv Funct Mater,* 28.

KLAUSNER, R. D. & WOLF, E. D. 1980. Selectivity of fluorescent lipid analogs for lipid domains. *Biochemistry,* 19**,** 6199-6203.

KNOL, J., SJOLLEMA, K. & POOLMAN, B. 1998. Detergent-Mediated Reconstitution of Membrane Proteins. *Biochemistry,* 37**,** 16410-16415.

KOURIL, R., OOSTERGETEL, G. T. & BOEKEMA, E. J. 2011. Fine structure of granal thylakoid membrane organization using cryo electron tomography. *Biochim Biophys Acta,* 1807**,** 368-74.

KRIEGER-LISZKAY, A. 2005. Singlet oxygen production in photosynthesis. *J Exp Bot,* 56**,** 337-46.

KRÜGER, T. P. J., ILIOAIA, C., JOHNSON, M. P., RUBAN, A. V. & VAN GRONDELLE, R. 2014. Disentangling the low-energy states of the major light-harvesting complex of plants and their role in photoprotection. *Biochimica Et Biophysica Acta-Bioenergetics,* 1837**,** 1027-1038.

KÜHLBRANDT, W., WANG, D. N. & FUJIYOSHI, Y. 1994. Atomic model of plant light-harvesting complex by electron crystallogtaphy. *Nature,* 367.

LAKOWICZ, J. R. 2006. Principles of Fluorescence Spectroscopy, *Springer US*

LAMBREV, P. H. & AKHTAR, P. 2019. Macroorganisation and flexibility of thylakoid membranes. *Biochem J,* 476**,** 2981-3018.

LARSEN, J., HATZAKIS, N. S. & STAMOU, D. 2011. Observation of inhomogeneity in the lipid composition of individual nanoscale liposomes. *J Am Chem Soc,* 133**,** 10685-7.

LI, G., FEI, J., XU, Y., LI, Y. & LI, J. 2018. Bioinspired Assembly of Hierarchical Light-Harvesting Architectures for Improved Photophosphorylation. *Advanced Functional Materials,* 28.

LI, M., KHAN, S., RONG, H., TUMA, R., HATZAKIS, N. S. & JEUKEN, L. J. C. 2017. Effects of membrane curvature and pH on proton pumping activity of single cytochrome bo3 enzymes. *Biochim Biophys Acta Bioenerg,* 1858**,** 763-770.

LI, X.-P., BJORKMAN, O., SHIH, C., GROSSMAN, A. R., ROSENQUIST, M., JANSSON, S. & NIYOGI, K. K. 2000. A pigment-binding protein essential for regulation of photosynthetic light harvesting. *Nature,* 403**,** 391-395.

LI, X., QIAO, S., ZHAO, L., LIU, S., LI, F., YANG, F., LUO, Q., HOU, C., XU, J. & LIU, J. 2019. Template-Free Construction of Highly Ordered Monolayered Fluorescent Protein Nanosheets: A Bioinspired Artificial Light-Harvesting System. *ACS Nano,* 13**,** 1861-1869.

LIGUORI, N., PERIOLE, X., MARRINK, S. J. & CROCE, R. 2015. From light-harvesting to photoprotection: structural basis of the dynamic switch of the major antenna complex of plants (LHCII). *Sci Rep,* 5**,** 15661.

LIGUORI, N., XU, P., VAN STOKKUM, I. H. M., VAN OORT, B., LU, Y., KARCHER, D., BOCK, R. & CROCE, R. 2017. Different carotenoid conformations have distinct functions in light-harvesting regulation in plants. *Nat Commun,* 8**,** 1994.

LIU, C., GALLAGHER, J. J., SAKIMOTO, K. K., NICHOLS, E. M., CHANG, C. J., CHANG, M. C. Y. & YANG, P. D. 2015. Nanowire-Bacteria Hybrids for Unassisted Solar Carbon Dioxide Fixation to Value-Added Chemicals. *Nano Letters,* 15**,** 3634-3639.

LIU, J., MANTELL, J., DI BARTOLO, N. & JONES, M. R. 2019. Mechanisms of Self-Assembly and Energy Harvesting in Tuneable Conjugates of Quantum Dots and Engineered Photovoltaic Proteins. *Small,* 15**,** e1804267.

LIU, Z., YAN, H., WANG, K., KUANG, T., ZHANG, J., GUI, L., AN, X. & CHANG, W. 2004. Crystal structure of spinach major light-harvesting complex at 2.72 A resolution. *Nature,* 428**,** 287-292.

LOHSE, B., BOLINGER, P.-Y. & STAMOU, D. 2008. Encapsulation Efficiency Measured on Single Small Unilamellar Vesicles. *J Am Chem Soc,* 130**,,** 14372–14373.

LORD, S. J., LU, Z., HUI, W., WILLETS, K. A. P., SCHUCK, J., LEE, H.-L. D., NISHIMURA, S. Y., TWIEG, R. J. & MOERNER, W. E. 2007. Photophysical Properties of Acene DCDHF Fluorophores: Long-Wavelength Single-Molecule Emitters Designed for Cellular Imaging. *J. Phys. Chem. A,* 111**,** 8934-8941.

LOURA, L. M. 2012. Simple estimation of Forster Resonance Energy Transfer (FRET) orientation factor distribution in membranes. *Int J Mol Sci,* 13**,** 15252-70.

LUBART, Q., HANNESTAD, J. K., PACE, H., FJALLBORG, D., WESTERLUND, F., ESBJORNER, E. K. & BALLY, M. 2020. Lipid vesicle composition influences the incorporation and fluorescence properties of the lipophilic sulphonated carbocyanine dye SP-DiO. *Phys Chem Chem Phys,* 22**,** 8781-8790.

LUBITZ, W., CHRYSINA, M. & COX, N. 2019. Water oxidation in photosystem II. *Photosynth Res,* 142**,** 105-125.

LUKASHEV, E. P., KNOX, P. P., GOROKHOV, V. V., GRISHANOVA, N. P., SEIFULLINA, N. K., KRIKUNOVA, M., LOKSTEIN, H. & PASCHENKO, V. Z. 2016. Purple-bacterial photosynthetic reaction centers and quantum‐dot hybrid‐assemblies in lecithin liposomes and thin films. *Journal of Photochemistry and Photobiology B: Biology,* 164**,** 73-82.

LV, Z., BANERJEE, S., ZAGORSKI, K. & LYUBCHENKO, Y. L. 2018. Supported Lipid Bilayers for Atomic Force Microscopy Studies. *Methods Mol Biol,* 1814**,** 129-143.

MACGREGOR-CHATWIN, C., JACKSON, P. J., SENER, M., CHIDGEY, J. W., HITCHCOCK, A., QIAN, P., MAYNEORD, G. E., JOHNSON, M. P., LUTHEY-SCHULTEN, Z., DICKMAN, M. J., SCANLAN, D. J. & HUNTER, C. N. 2019. Membrane organization of photosystem I complexes in the most abundant phototroph on Earth. *Nature Plants,* 5**,** 879-889.

MAIURI, M., SNELLENBURG, J. J., VAN STOKKUM, I. H., PILLAI, S., WONGCARTER, K., GUST, D., MOORE, T. A., MOORE, A. L., VAN GRONDELLE, R., CERULLO, G. & POLLI, D. 2013. Ultrafast energy transfer and excited state coupling in an artificial photosynthetic antenna. *J Phys Chem B,* 117**,** 14183-90.

MENEGHIN, E., LEONARDO, C., VOLPATO, A., BOLZONELLO, L. & COLLINI, E. 2017. Mechanistic insight into internal conversion process within Q-bands of chlorophyll a. *Sci Rep,* 7**,** 11389.

MILANO, F., PUNZI, A., RAGNI, R., TROTTA, M. & FARINOLA, G. M. 2019. Photonics and Optoelectronics with Bacteria: Making Materials from Photosynthetic Microorganisms. *Advanced Functional Materials,* 29.

MILHIET, P. E., GUBELLINI, F., BERQUAND, A., DOSSET, P., RIGAUD, J. L., LE GRIMELLEC, C. & LEVY, D. 2006. High-resolution AFM of membrane proteins directly incorporated at high density in planar lipid bilayer. *Biophys J,* 91**,** 3268-75.

MINAGAWA, J. 2011. State transitions--the molecular remodeling of photosynthetic supercomplexes that controls energy flow in the chloroplast. *Biochim Biophys Acta,* 1807**,** 897-905.

MIRKOVIC, T., OSTROUMOV, E. E., ANNA, J. M., VAN GRONDELLE, R., GOVINDJEE & SCHOLES, G. D. 2016. Light Absorption and Energy Transfer in the Antenna Complexes of Photosynthetic Organisms. *Chemical Reviews,* 117**,** 249-293.

MOYA, I., SILVESTRI, M., VALLON, O., CINQUE, G. & BASSI, R. 2001. Time-Resolved Fluorescence Analysis of the Photosystem II Antenna Proteins in Detergent Micelles and Liposomes. *Biochemistry,* 40**,** 12552-12561.

NATALI, A., GRUBER, J. M., DIETZEL, L., STUART, M. C., VAN GRONDELLE, R. & CROCE, R. 2016. Light-harvesting Complexes (LHCs) Cluster Spontaneously

in Membrane Environment Leading to Shortening of Their Excited State Lifetimes. *J Biol Chem,* 291**,** 16730-9.

NATH, A., TREXLER, A. J., KOO, P., MIRANKER, A. D., ATKINS, W. M. & RHOADES, E. 2010. Single-Molecule Fluorescence Spectroscopy Using Phospholipid Bilayer Nanodiscs. *Single Molecule Tools: Fluorescence Based Approaches, Part A.*

NIEDZWIEDZKI, D. M. & BLANKENSHIP, R. E. 2010. Singlet and triplet excited state properties of natural chlorophylls and bacteriochlorophylls. *Photosynth Res,* 106**,** 227-38.

NOGUEIRA, E., GOMES, A. C., PRETO, A. & CAVACO-PAULO, A. 2015. Design of liposomal formulations for cell targeting. *Colloids Surf B Biointerfaces,* 136**,** 514-26.

OLLIVON, M., LESIEUR, S., GRABIRLLE-MADELMONT, C. & PATERNOSTRE, M. 2000. Vesicle reconstitution from lipid-detergent mixed micelles. *Biochimica et Biophysica Acta,* 1508.

ORF, G. S., COLLINS, A. M., NIEDZWIEDZKI, D. M., TANK, M., THIEL, V., KELL, A., BRYANT, D. A., MONTANO, G. A. & BLANKENSHIP, R. E. 2017. Polymer-Chlorosome Nanocomposites Consisting of Non-Native Combinations of Self-Assembling Bacteriochlorophylls. *Langmuir,* 33**,** 6427-6438.

PANDIT, A., SHIRZAD-WASEI, N., WLODARCZYK, L. M., VAN ROON, H., BOEKEMA, E. J., DEKKER, J. P. & DE GRIP, W. J. 2011. Assembly of the major light-harvesting complex II in lipid nanodiscs. *Biophys J,* 101**,** 2507-15.

PORRA, R. J., THOMPSON, W. A. & KRIEDEMANN, P. E. 1989. Determination of accurate extinction coefficients and simultaneous equations for assaying chlorophylls a and b extracted with four different solvents. *Biochimica et Biophysica Acta,* 975**,** 384-394.

QIAN, P., SIEBERT, C. A., WANG, P., CANNIFFE, D. P. & HUNTER, C. N. 2018. Cryo-EM structure of the Blastochloris viridis LH1-RC complex at 2.9 A. *Nature,* 556**,** 203-208.

RASCHLE, T., LIN, C., JUNGMANN, R., SHIH, W. M. & WAGNER, G. 2015. Controlled Co-reconstitution of Multiple Membrane Proteins in Lipid Bilayer Nanodiscs Using DNA as a Scaffold. *ACS Chem Biol,* 10**,** 2448-54.

RAVI, S. K., YU, Z. M., SWAINSBURY, D. J. K., OUYANG, J. Y., JONES, M. R. & TAN, S. C. 2017. Enhanced Output from Biohybrid Photoelectrochemical Transparent Tandem Cells Integrating Photosynthetic Proteins Genetically Modified for Expanded Solar Energy Harvesting. *Advanced Energy Materials,* 7**,** 1601821.

RAY, K., MA, J., ORAM, M., LAKOWICZ, J. R. & BLACK, L. W. 2010. Single-molecule and FRET fluorescence correlation spectroscopy analyses of phage

DNA packaging: colocalization of packaged phage T4 DNA ends within the capsid. *J Mol Biol,* 395**,** 1102-13.

RICHTER, R. P., BERAT, R. & BRISSON, A. R. 2006. Formation of Solid-Supported Lipid Bilayers: An Integrated View. *Langmuir,* 8**,** 3497-3505.

ROBERT, B., HORTON, P., PASCAL, A. A. & RUBAN, A. V. 2004. Insights into the molecular dynamics of plant light-harvesting proteins in vivo. *Trends Plant Sci,* 9**,** 385-90.

ROBSON, A. L., DASTOOR, P. C., FLYNN, J., PALMER, W., MARTIN, A., SMITH, D. W., WOLDU, A. & HUA, S. 2018. Advantages and Limitations of Current Imaging Techniques for Characterizing Liposome Morphology. *Front Pharmacol,* 9**,** 80.

ROONEY, E. K. & LEE, A. G. 1986. Fitting fluorescence emission spectra of probes bound to biological membranes. *Journal of Biochemical and Blophystcal Methods,* 12**,** 175-189.

ROUCK, J. E., KRAPF, J. E., ROY, J., HUFF, H. C. & DAS, A. 2017. Recent advances in nanodisc technology for membrane protein studies (2012-2017). *FEBS Lett,* 591**,** 2057-2088.

RUBAN, A. V. 2016. Nonphotochemical Chlorophyll Fluorescence Quenching: Mechanism and Effectiveness in Protecting Plants from Photodamage. *Plant Physiol,* 170**,** 1903-16.

RUBAN, A. V. 2017a. Crops on the fast track for light. *Nature,* 541**,** 37.

RUBAN, A. V. 2017b. Quantifying the efficiency of photoprotection. *Philos Trans R Soc Lond B Biol Sci,* 372.

RUBAN, A. V., BERERA, R., ILIOAIA, C., VAN STOKKUM, I. H., KENNIS, J. T., PASCAL, A. A., VAN AMERONGEN, H., ROBERT, B., HORTON, P. & VAN GRONDELLE, R. 2007. Identification of a mechanism of photoprotective energy dissipation in higher plants. *Nature,* 450**,** 575-8.

SAHIN, T., HARRIS, M. A., VAIRAPRAKASH, P., NIEDZWIEDZKI, D. M., SUBRAMANIAN, V., SHREVE, A. P., BOCIAN, D. F., HOLTEN, D. & LINDSEY, J. S. 2015. Self-Assembled Light-Harvesting System from Chromophores in Lipid Vesicles. *J Phys Chem B,* 119**,** 10231-43.

SAKURAI, I., SHEN, J. R., LENG, J., OHASHI, S., KOBAYASHI, M. & WADA, H. 2006. Lipids in oxygen-evolving photosystem II complexes of cyanobacteria and higher plants. *J Biochem,* 140**,** 201-9.

SCHLAU-COHEN, G. S., WANG, Q., SOUTHALL, J., COGDELL, R. J. & MOERNER, W. E. 2013. Single-molecule spectroscopy reveals photosynthetic LH2 complexes switch between emissive states. *Proc Natl Acad Sci U S A,* 110**,** 10899-903.

SCHLAU-COHEN, G. S., YANG, H.-Y., KRÜGER, T. P. J., XU, P., GWIZDALA, M., VAN GRONDELLE, R., CROCE, R. & MOERNER, W. E. 2015. Single-molecule identification of quenched and unquenched states of LHCII. *The Journal of Physical Chemistry Letters,* 6**,** 860-867.

SCHMITT, F. J., MAKSIMOV, E. G., HÄTTI, P., WEIßENBORN, J., JEYASANGAR, V., RAZJIVIN, A. P., PASCHENKO, V. Z., FRIEDRICH, T. & RENGER, G. 2012. Coupling of different isolated photosynthetic light harvesting complexes and CdSe/ZnS nanocrystals via Förster resonance energy transfer. *Biochimica et Biophysica Acta - Bioenergetics,* 1817**,** 1461-1470.

SCHORNER, M., BEYER, S. R., SOUTHALL, J., COGDELL, R. J. & KOHLER, J. 2015. Multi-Level, Multi Time-Scale Fluorescence Intermittency of Photosynthetic LH2 Complexes: A Precursor of Non-Photochemical Quenching? *J Phys Chem B,* 119**,** 13958-63.

SCHULER, B. & EATON, W. A. 2008. Protein folding studied by single-molecule FRET. *Curr Opin Struct Biol,* 18**,** 16-26.

SCHULER, M. A., DENISOV, I. G. & SLIGAR,
S. G. 2013. Nanodiscs as a new tool to examine lipid-protein interactions. *Methods Mol Biol,* 974**,** 415-33.

SEIWERT, D., WITT, H., JANSHOFF, A. & PAULSEN, H. 2017. The non-bilayer lipid MGDG stabilizes the major light-harvesting complex (LHCII) against unfolding. *Sci Rep,* 7**,** 5158.

SEIWERT, D., WITT, H., RITZ, S., JANSHOFF, A. & PAULSEN, H. 2018. The Nonbilayer Lipid MGDG and the Major Light-Harvesting Complex (LHCII) Promote Membrane Stacking in Supported Lipid Bilayers. *Biochemistry,* 57**,** 2278-2288.

SENER, M., STRUMPFER, J., HSIN, J., CHANDLER, D., SCHEURING, S., HUNTER, C. N. & SCHULTEN, K. 2011. Forster energy transfer theory as reflected in the structures of photosynthetic light-harvesting systems. *Chemphyschem,* 12**,** 518-31.

SENER, M. K., JOLLEY, C., BEN-SHEM, A., FROMME, P., NELSON, N., CROCE, R. & SCHULTEN, K. 2005. Comparison of the light-harvesting networks of plant and cyanobacterial photosystem I. *Biophys J,* 89**,** 1630-42.

SENEVIRATNE, R., KHAN, S., MOSCROP, E., RAPPOLT, M., MUENCH, S. P., JEUKEN, L. J. C. & BEALES, P. A. 2018. A reconstitution method for integral membrane proteins in hybrid lipid-polymer vesicles for enhanced functional durability. *Methods,* 147**,** 142-149.

SHASHI, K., SATINDER, K. & BHARAT, P. 2012. A complete review on: Liposomes. *Int. Res. J. Pharm,* 3.

SIMIDJIEV, I., STOYLOVA, S., AMENITSCH, H., JA´VORF, T. S., MUSTA´RDY, L. S., LAGGNER, P., HOLZENBURG, A. & GARAB, G. Z. 2000. Self-assembly

of large, ordered lamellae from non-bilayer lipids and integral membrane proteins in vitro. *PNAS,* 97**,** 1473–1476.

SKAUG, M. J., LONGO, M. L. & FALLER, R. 2011. The impact of Texas red on lipid bilayer properties. *J Phys Chem B,* 115**,** 8500-5.

SON, M., PINNOLA, A., GORDON, S. C., BASSI, R. & SCHLAU-COHEN, G. S. 2020. Observation of dissipative chlorophyll-to-carotenoid energy transfer in light-harvesting complex II in membrane nanodiscs. *Nat Commun,* 11**,** 1295.

SPRINGER, J. W., PARKES-LOACH, P. S., REDDY, K. R., KRAYER, M., JIAO, J., LEE, G. M., NIEDZWIEDZKI, D. M., HARRIS, M. A., KIRMAIER, C., BOCIAN, D. F., LINDSEY, J. S., HOLTEN, D. & LOACH, P. A. 2012. Biohybrid Photosynthetic Antenna Complexes for Enhanced Light-Harvesting. *J Am Chem Soc ,* 134**,** 4589-4599.

STANDFUSS, J. & KUHLBRANDT, W. 2004. The three isoforms of the light-harvesting complex II: spectroscopic features, trimer formation, and functional roles. *J Biol Chem,* 279**,** 36884-91.

STANDFUSS, J., VAN SCHELTINGA, A. C. T., LAMBORGHINI, M. & KUHLBRANDT, W. 2005. Mechanisms of photoprotection and nonphotochemical quenching in pea light-harvesting complex at 2.5A resolution. *EMBO Journal,* 24**,** 919-928.

STETEFELD, J., MCKENNA, S. A. & PATEL, T. R. 2016. Dynamic light scattering: a practical guide and applications in biomedical sciences. *Biophys Rev,* 8**,** 409-427.

SUBRAMANIAN, V., ZUREK, N. A., EVANS, D. G. & SHREVE, A. P. 2018. Predictive modeling of broad wavelength light-harvesting performance in assemblies of multiple chromophores. *Journal of Photochemistry and Photobiology A: Chemistry,* 367**,** 105-114.

SWAINSBURY, D. J. K., PROCTOR, M. S., HITCHCOCK, A., CARTRON, M. L., QIAN, P., MARTIN, E. C., JACKSON, P. J., MADSEN, J., ARMES, S. P. & HUNTER, C. N. 2018. Probing the local lipid environment of the Rhodobacter sphaeroides cytochrome bc1 and Synechocystis sp. PCC 6803 cytochrome b6f complexes with styrene maleic acid. *Biochim Biophys Acta Bioenerg,* 1859**,** 215-225.

THEKAEKARA, M. P. 1973. Solar irradiance: total and spectral and its possible variations. *Applied Optics,* 14.

TIPLER, P. A. & MOSCA, G. A. 2007. Physics for Scientists and Engineers, *W. H. Freeman*.

TITUS, J. A., HAUGLAND, R., SHARROW, S. O. & SEGAL, D. M. 1982. Texas red, a hydrophilic, red-emitting flourophore for use with flourescein in dual parameter flow microfluorometric and fluorescence microscopic studies. *Journal of Immunological Methods,* 50**,** 193-204.

TRESSET, G. 2009. The multiple faces of self-assembled lipidic systems. *PMC Biophys,* 2**,** 3.

TUTKUS, M., AKHTAR, P., CHMELIOV, J., GORFOL, F., TRINKUNAS, G., LAMBREV, P. H. & VALKUNAS, L. 2018. Fluorescence Microscopy of Single Liposomes with Incorporated Pigment-Proteins. *Langmuir,* 34**,** 14410-14418.

VAN AMERONGEN, H. & CROCE, R. 2013. Light harvesting in photosystem II. *Photosynth Res,* 116**,** 251-63.

VAN AMERONGEN, H. & VAN GRONDELLE, R. 2001. Understanding the Energy Transfer Function of LHCII, the Major Light-Harvesting Complex of Green Plants. *J. Phys. Chem. B,,* 105**,** 604-617.

VAN GRONDELLE, R. 1985. Excitation energy transfer, trapping and annihilation in photosynthetic systems. *Biochimica et Biophysica Acta - Bioenergetics,* 3**,** 147-195.

VAN OORT, B., VAN HOEK, A., RUBAN, A. V. & VAN AMERONGEN, H. 2007. Aggregation of light-harvesting complex II leads to formation of efficient excitation energy traps in monomeric and trimeric complexes. *FEBS Letters,* 581**,** 3528-3532.

VAN STOKKUM, I. H. M., LARSEN, D. S. & GRONDELLE, R. V. 2004. Global and target analysis of time-resolved spectra. *Biochimica et Biophysica Acta,* 1657**,** 82-104.

VASILEV, C., JOHNSON, M. P., GONZALES, E., WANG, L., RUBAN, A. V., MONTANO, G., CADBY, A. J. & HUNTER, C. N. 2014. Reversible Switching between Nonquenched and Quenched States in Nanoscale Linear Arrays of Plant Light-Harvesting Antenna Complexes. *Langmuir,* 30**,** 8481-8490.

VINAYAKA, A. C. & THAKUR, M. S. 2011. Photoabsorption and resonance energy transfer phenomenon in CdTe-protein bioconjugates: an insight into QD-biomolecular interactions. *Bioconjug Chem,* 22**,** 968-75.

WANG, L., CHEN, T., QU, J. & WEI, X. 2010. Photobleaching-based quantitative analysis of fluorescence resonance energy transfer inside single living cell. *J Fluoresc,* 20**,** 27-35.

WEI, X., SU, X., CAO, P., LIU, X., CHANG, W., LI, M., ZHANG, X. & LIU, Z. 2016. Structure of spinach photosystem II-LHCII supercomplex at 3.2 A resolution. *Nature,* 534**,** 69-74.

WERWIE, M., DWORAK, L., BOTTIN, A., MAYER, L., BASCHE, T., WACHTVEITL, J. & PAULSEN, H. 2018. Light-harvesting chlorophyll protein (LHCII) drives electron transfer in semiconductor nanocrystals. *Biochim Biophys Acta,* 1859**,** 174-181.

WERWIE, M., XU, X., HAASE, M., BASCHE, T. & PAULSEN, H. 2012. Bio Serves Nano: Biological Light-Harvesting Complex as Energy Donor for Semiconductor Quantum Dots. *Langmuir,* 28**,** 5810-5818.

YAGHOUBI, H., SCHAEFER, M., YAGHOUBI, S., JUN, D., SCHLAF, R., BEATTY, J. T. & TAKSHI, A. 2017. A ZnO nanowire bio-hybrid solar cell. *Nanotechnology,* 28**,** 054006.

YAMAMOTO, E., KALLI, A. C., YASUOKA, K. & SANSOM, M. S. P. 2016. Interactions of Pleckstrin Homology Domains with Membranes: Adding Back the Bilayer via High-Throughput Molecular Dynamics. *Structure,* 24**,** 1421-1431.

YANG, C., BOGGASCH, S., HAASE, W. & PAULSEN, H. 2006. Thermal stability of trimeric light-harvesting chlorophyll a/b complex (LHCIIb) in liposomes of thylakoid lipids. *Biochim Biophys Acta,* 1757**,** 1642-8.

YONEDA, T., TANIMOTO, Y., TAKAGI, D. & MORIGAKI, K. 2020a. Photosynthetic Model Membranes of Natural Plant Thylakoid Embedded in a Patterned Polymeric Lipid Bilayer. *Langmuir,* 36**,** 5863-5871.

YONEDA, Y., GOTO, A., TAKEDA, N., HARADA, H., KONDO, M., MIYASAKA, H., NAGASAWA, Y. & DEWA, T. 2020b. Ultrafast Photodynamics and Quantitative Evaluation of Biohybrid Photosynthetic Antenna and Reaction Center Complexes Generating Photocurrent. *The Journal of Physical Chemistry C*.

YONEDA, Y., NOJI, T., KATAYAMA, T., MIZUTANI, N., KOMORI, D., NANGO, M., MIYASAKA, H., ITOH, S., NAGASAWA, Y. & DEWA, T. 2015. Extension of Light-Harvesting Ability of Photosynthetic Light-Harvesting Complex 2 (LH2) through Ultrafast Energy Transfer from Covalently Attached Artificial Chromophores. *J Am Chem Soc,* 137**,** 13121-9.

YUAN, P. & WALT, D. 1957. Calculation for Fluorescence Modulation by Absorbing Species and Its Application to Measurements Using Optical Fibers. *Analytical Chemistrty* 59**,** 2391-2394.

ZHENG, W., LIU, Y., WEST, A., SCHULER, E. E., YEHL, K., DYER, R. B., KINDT, J. T. & SALAITA, K. 2014. Quantum dots encapsulated within phospholipid membranes: phase-dependent structure, photostability, and site-selective functionalization. *J Am Chem Soc,* 136**,** 1992-9.

ZHOU, F., LIU, S., HU, Z., KUANG, T., PAULSEN, H. & YANG, C. 2009. Effect of monogalactosyldiacylglycerol on the interaction between photosystem II core complex and its antenna complexes in liposomes of thylakoid lipids. *Photosynth Res,* 99**,** 185-93.

ZHU, X. G., LONG, S. P. & ORT, D. R. 2010. Improving photosynthetic efficiency for greater yield. *Annu Rev Plant Biol,* 61**,** 235-61.